OPTICAL FIBER MODAL DOMAIN SENSORS FOR DYNAMIC STRAIN MEASUREMENT

by

K.D. Bennett

Dissertation submitted to the Faculty of the
Virginia Polytechnic Institute and State University
in partial fulfillment of the requirements for the degree of

DOCTOR OF PHILOSOPHY

in
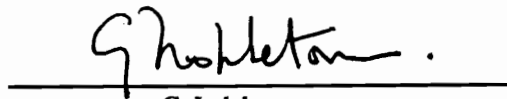
Electrical Engineering

APPROVED:

R.O. Claus, Chairman

J.C. Duke   _G. Indebetouw_

R.J. Pieper   _T.C. Poon_

January, 1990

Blacksburg, Virginia

OPTICAL FIBER MODAL DOMAIN SENSORS FOR DYNAMIC STRAIN MEASUREMENT

by

K.D. Bennett
Dr. R.O. Claus, Committee Chairman
Electrical Engineering
(ABSTRACT)

Modern engineering structures often incorporate new materials and complex designs for which existing techniques for nondestructive evaluation prove inadequate, especially for dynamic and in-service measurements. At the same time, optical fiber sensors have been identified as an ideal candidate for embedded and attached measurements of material parameters such as strain, temperature, or state of damage. In particular, sensors based on optical fiber modal interference phenomena have been shown to be capable of highly sensitive detection of static and dynamic strain.

This work reviews known applications of modal domain sensing to measurement science to date, and discusses the principles behind the method. A general expression for the intensity distribution emerging from a multimode fiber is formulated, covering both few mode and highly multimode fibers, and new expressions for their sensitivity to both radial and axial strain are derived. Optimized multimode fibers are seen to show an intrinsic phase sensitivity which rivals or even surpasses that of the single mode interferometer, especially in the case of applied radial strain. The use of modal domain sensors for real-time ultrasonic wave transduction is described as a particular application to NDE, with experimental results being presented with regard to acoustic emission monitoring as well as the detection and analysis of shock waves due to impact. Finally, optimization schemes and alternatives for such sensors are addressed, and recommendations for future work are raised.

ACKNOWLEDGEMENTS

TABLE OF CONTENTS

1.0 INTRODUCTION

1.1 NDE of Advanced Materials

The desire for greater efficiency in the manufacturing of metallic structures, as well as an ever-increasing emphasis on their performance reliability, led to many early advances in the field of measurement science. From the well established practices of penetrant inspection and x-ray analysis, to the more sophisticated eddy current and ultrasonic methods, nondestructive evaluation (NDE) still largely focuses on the mission of inspecting critical metal components for crack formation. However, the development of more exacting designs and new engineering materials has in many cases outpaced the development of adequate techniques to nondestructively test them [1]. For complex structures such as modern aircraft, which contain many high performance parts and assemblies requiring regular inspection, a reliable NDE maintenance program can involve excessive costs. Not only are there often considerable man hours and down time associated with such inspection procedures, in many cases the accuracy and consistency of the results are user-dependent [2]. In other situations, the procedures call for actions which themselves may jeopardize structural integrity by causing other, undetected damage.

In response to these concerns, recent trends in the area of structural analysis favor the development of in-service and real time monitoring schemes. Whereas nondestructive inspection is normally performed periodically in accordance with fatigue and time-to-failure predictions, an in-situ (or in the case of an aircraft, in-flight) monitoring system could allow conventional inspection to be performed only when the presence of critical damage is indicated. Furthermore, real time sensors could be used to make critical mission decisions, the typical example being that of an aircraft wing instrumented with an array of damage monitors. If the wing suffers critical damage, not only could the pilot be aware of the presence

and the extent of damage, the control computer could be triggered to reconfigure the flight surfaces of the plane to reduce further damage and risk, and to optimize continued operation.

In order for NDE to contain a predictive element, measurements must go beyond detecting the initiation of cracks. Most often, strain and temperature levels are to be monitored, and high resolution, high accuracy, and high dynamic range are all required. Also, in addition to making point measurements, it is desirable in many circumstances to know the strain integrated along a particular path, or the total strain in a large, macroscopically homogeneous section. Not only can insight be gained as to the dynamic properties of the whole component, such information could also be used in active control systems designed to initiate structural motion or damp unwanted movement. Other system requirements include the fact that the in-service environment is likely to be hostile to the measurement tools themselves, making readings impossible or unreliable. For example, elevated temperature and pressure can destroy conventional strain gages and either acoustic emission or standard ultrasonic transducers, while electromagnetic noise can render such devices unusable.

Another goal in present NDE research is to develop sensors which can interrogate the interior of structural components to determine areas where damage is most likely to form. This is especially true for the increasing number of parts formed from complex layered media, such as advanced composites, where internal interface conditions may vary from place to place. Many types of composite materials now exist for modern engineering structures, including glass or polymer fibers embedded in resins, as well as fiber reinforced ceramic and metal matrix composites. The merits of these various materials are now well established, and include high strength-to-weight and stiffness-to-weight ratios, outstanding corrosion resistance, and superior adaptability in part design. As structural members they may reduce part counts and display increased longevity over high technology metals, while their constituents are often created from abundant materials, making them potentially attractive from a financial point of view. Finally, the dielectric nature of glass and polymer

composites offers advantages considered paramount in importance for certain applications, such as offering low radar cross-sections.

The inhomogeneous and anisotropic internal structure of fiber reinforced composites presents new challenges to traditional NDE techniques, and is much more difficult to analyze than that of metal alloys. In these materials, location, type, and time of failure under various operating conditions are still not well understood, making predictions on system reliability based on periodic conventional NDE measurements tenuous at best. In addition, whereas breakdowns in metal components generally result from simple crack formation, failure mechanisms in composites can be much more complex and extensive, including fiber breakage, matrix cracking, fiber/matrix disbond, and ply delamination. Moreover, as in the case of impact damage, often the external appearance of the composite surface shows little flaw, though the internal damage is actually quite extensive.

The result of designing more elaborate structures, using new materials for an expanding variety of applications, and making more demands in terms of performance, efficiency, and reliability, has been to create a need for a new generation of measurement tools. Although headway is being made in acoustic, electromagnetic, thermographic, holographic, and other techniques, few are well suited to dynamic, in-situ, or internal measurements. An important new technology emerging in NDE involves the use of fiber optic sensors to address many of these needs.

1.2 Fiber Optic Sensors for Dynamic Strain Measurement

Optical fibers offer the same advantages to sensing systems as they do to telecommunications. First, extremely high signal bandwidth and low attenuation are achievable with fiber optic sensors as compared to even microwave-based devices. Second, the dielectric nature of optical waveguides inherently renders them much less sensitive to electrical noise than traditional signal carriers. This fact drives much of the development of such sensors, especially in view of mounting concern about both

electromagnetic interference and electromagnetic pulse weaponry. Their chemical structure also makes these sensors safe for certain types of corrosive or high temperature environments which conventional sensors cannot tolerate. Third, optical fibers can be made responsive to any number of parameters: electric, magnetic, or acoustic fields, mechanical displacement, velocity, acceleration, pressure, strain, chemical concentration, or temperature, to name just a few [3,4]. This often constitutes the point of separation between fiber sensor and communications applications. Whereas communications engineers wish to *reduce* a fiber's sensitivity to physical perturbations, sensor designers wish to increase and exploit it. Furthermore, because of their small size, and more particularly because of the small wavelength of light, optical sensors can demonstrate extremely high sensitivity and dynamic range.

Other benefits of fiber optic sensors stem from their geometric versatility. Glass fibers are thin and light, can be made flexible yet rugged, and can be incorporated into an endless variety of sensor configurations. This can include extrinsic designs, where light signals are captured by the fiber and are guided along its path to a photodetector, or intrinsic designs, where the signal light stays inside the fiber over its entire length until it exits at the photodetector; the transmission characteristics of the light within the fiber are changed by the parameter to be measured. Moreover, because of their common components, fiber sensors and fiber telemetry systems are highly compatible. Besides the obvious advantage of being able to construct all-fiber systems, this means that advances in communications technology often translate into enhanced capabilities in the sensor field.

When considering the measurement requirements for advanced structures, the inherent advantages and sensing capabilities of optical fibers make them an ideal candidate for use in real time monitoring. As attached sensors, fibers can readily be laid singly or in arrays to detect surface conditions or monitor the environment external to the structure. Furthermore, because of their small size and compatibility, especially with graphite fibers, optical fibers may be embedded in graphite/epoxy composites without introducing significant degradation in material properties. Thus, rather than relying entirely on external measurements,

internal inspection of the structure is enabled where damage is most likely to occur or where measurements are most critical. Also, the dielectric nature of the material is maintained over the structure, while the fibers provide their own signal paths.

Attached and embedded optical fibers also offer the possibility of providing for cradle-to-grave structural health monitoring, as embodied in the relatively new concept of "smart structures." Fibers placed in a composite laminate during layup may sense internal conditions such as pressure, temperature, and density during cure, implying that more accurate processing control and therefore more structurally sound composites may be achieved efficiently. Once in service, components containing optical fibers may be continuously monitored, with sensors potentially detecting all of the observables which are available through standard NDE methods and more. For structural materials, focus is often placed on the measurement of parameters used to evaluate integrity and fatigue. Optical fibers have been shown to be theoretically capable of measuring stress-induced strain on the order of 10^{-12} per centimeter of gage length, while reported values range to within a few orders of magnitude of theoretical [5-7]. The broad range of fiber optic sensor types and configurations offer to measurement science a new class of tools which may be able to fill in many gaps in conventional NDE. However, a number of developmental steps must be taken before these tools can be widely deployed.

1.3 Modal Domain Sensors

In the now well over ten years since research into fiber optic sensors began in earnest, workers have reported monitoring a host of mechanical and environmental observables by causing the observable to interact with one of the fundamental parameters of the light inside a fiber. These include the optical phase, intensity, wavelength, polarization, propagation time, and modal power distribution. It is well known that the most sensitive fiber transduction mechanism generally involves modulation of

the optical phase of the light in a single mode fiber with respect to that in a reference path, either external or contained within another fiber. In an alternate method, herein referred to as modal domain sensing (MDS), sensing is performed by causing the perturbation of interest to interact with a fiber which propagates more than one optical mode. In general, any two nondegenerate modes are affected differently since their phase velocities and path lengths differ; the phase difference between modes is employed to infer the amount of physical disturbance.

The most basic modal domain sensor consists of a single mode fiber operated slightly below its cut-off wavelength, such that only the two lowest order modes propagate. For ordinary communications grade fiber, this implies that the LP_{01} and LP_{11} modes are employed, generally resulting in a two lobe interference pattern in the output. It will be demonstrated analytically that as the fiber is axially strained, power in the output is transferred periodically from one lobe to the other. That is, a dual mode fiber can act as a strain sensor by monitoring the intensity of one or both output lobes. Highly multimode fibers may also be employed as modal sensors. Assuming the fiber is excited with coherent radiation, the output will consist of a complex pattern formed by the interference of all modes, commonly referred to as a speckle pattern. Disturbances on the fiber translate to local changes in refractive index and geometry, which alter the differential phase of the modes and thus modulate the speckle pattern. With dual mode fibers, signal recovery is most often accomplished by imaging a single lobe, or part of a lobe, onto a photodiode through a pinhole. With multimode fibers, however, it is usually the average modulation of several speckles that is detected to infer perturbations.

A number of modal domain sensor applications have been reported in the literature, starting with the dual mode fiber detection of acoustic waves in water by Layton and Bucaro [8], followed soon after by demonstrations of multimode fiber sensitivity to acoustic waves in air [9-11]. Higher frequency acoustic emissions have also been sensed using few mode fibers embedded in composite coupons [12], as have acoustic shock waves arising from impacts to both aluminum and composite panels [13,14]. MDS has been successfully applied to the measurement of vibrations in large flexible

structures, such as space station components [15,16], in addition to subsurface ground vibrations due to human activity on the surface [17,18]. Other researchers have demonstrated the measurement of alternating electric current [19], induced temperature fluctuations [20,21], and fluid flow [22], as well as simply induced axial strain [23]. Dual mode, few mode, and highly multimode fibers have all been employed successfully.

In order for modal domain sensors to be actively deployed in critical real world applications, a number of issues must first be addressed. One concern arises from the fact that most of the energy emerging from the fiber does not reach the detector, but is instead absorbed by a spatial filter in front of the detector. This leads to obvious needs for higher source power and output amplification to maintain signal integrity. Also important to obtaining the highest signal quality is the position of the detector in the output field; methods to readily find and maintain that position must be identified. This can present special complications in systems involving long wavelength radiation, in miniaturized or encapsulated devices, and particularly in sensors utilizing many modes. Instabilities due to mode coupling can present a problem, especially when higher order modes are desired at the exclusion of lower order modes which are allowed in the waveguide. Lead-fiber sensitivity is also of concern. That is, if a certain section of fiber is to be perturbed by a particular mechanism, care must be taken to assure that no disturbances on the rest of the fiber give rise to signals similar to that caused by the observable under study. This problem also affects conventional interferometers, and though a degree of stability is gained by having the interferometer paths within a single fiber, it can still be a major limitation to practical use. Finally, an issue which is common to all interferometry is that of the non-linear (periodic) nature of the output modulation with disturbance. This is of special interest when the sensor output is being fed into a control system, where signal non-linearities can be particularly troublesome.

1.4 MDS for Detection of Damage-Related Acoustic Waves

Although the smart structures concept incorporates a large variety of situations, the majority of smart structures themselves are still conceived for aerospace and naval applications. As mentioned above, ever higher performance standards are being demanded from parts, subassemblies, and systems, as well as entire vessels and aircraft. As a result, building, maintaining, and operating costs for these modern craft are climbing out of sight, while personnel are encountering greatly elevated operating risks. Hence more emphasis is being placed on total system reliability. This is evidenced by an increasing desire for the accurate, in-service detection of damage, upon which many mission decisions are predicated. In turn, it is hoped that this information can be used to make predictions about the remaining lifetime of the structure.

Damage in modern engineering structures can be caused by many factors, notably over-stressing, exposure to extreme environments such as chemically corrosive or high temperature conditions, or direct impact with objects ranging from reefs and ducks to torpedos and missiles. At present a number of methods exist for quantifying different types of damage, though few, if any, are suitable for in-situ, real time measurements. In many cases however, rather than focussing strictly on sensing damage itself, it would be desirable to detect the precursors to serious damage. If suitable monitors could be devised, parts or whole vessels may be taken out of service long before dangerous levels of damage are reached, thus avoiding either costly or even catastrophic failure.

In order for a real time measurement to be useful in predicting future performance, several steps must by taken. First, research must be conducted to establish the relationship between the type of damage and the lifetime of the component. By way of example, consider the measurement of acoustic emissions (AE) due to stress corrosion cracking (SCC) in a submarine component. The effect of stress corrosion cracking on component lifetime must be determined. In some cases, it may be necessary to know and to be able to simulate actual operating conditions; a certain amount of SCC is induced, and the part is subjected to realistic

loading, while time-to-failure data is collected. Obviously, a great deal of careful modelling and statistical analysis must be performed for these tests to be useful. Furthermore, if other types of damage or other factors such as time-in-service or loading cycle are found to affect lifetime and performance, then the nature of these effects must be assessed, as well as their relationship to SCC.

Next, a correlation between the type of damage and the measured quantity, here stress corrosion cracking and acoustic emission, must be ascertained. It can be imagined, for instance, that not all forms of SCC would necessarily give rise to what is traditionally classified as AE. Dependence on AE detection alone might therefore lead to erroneous conclusions about the level of SCC; some extrapolation or alternate measurements may be required. Likewise, many other mechanisms besides SCC could cause the rapid release of acoustic energy, such as small cracks occurring during normal loading conditions, over-loading, or impacts. Thus, though it is acoustic emissions which are monitored, not all AE events are indicative of SCC, or even of damage (as generally defined), and therefore may not be important as far as the operation of the submarine component is concerned.

Finally, there is the issue of the measurement itself. As with the monitoring of any physical quantity, the method of energy transduction must be examined with regard to its sensitivity, dynamic range, frequency response, accuracy, and repeatability. In addition, presuming that the final energy state is electrical, then signal processing techniques and instrumentation also play a part in determining the accuracy of the measurement with respect to the actual situation. So if, in our example, optical fibers are used to detect AE, then the relationship between the true emission (discovered by the most absolute means possible), and the signal output must be known in order to eventually make predictions about the performance of the part.

As with stress corrosion cracking, understanding the effect of impact damage on future performance requires engaging in the involved research process described above. In addition, a more detailed analysis would reveal many difficult questions waiting to be answered. What do we mean by

"damage?" How is it qualified? What types of impacts are there? What characteristics distinguish these types? What role do quantities such as impact energy, velocity, or surface area play in the amount of damage incurred? How are these quantities related to the different kinds of damage? Though these questions are important, and will be discussed briefly in the following chapters, they go beyond the scope of this work. Indeed, answering them for even a small range of engineering materials could be an enormous task. Nevertheless, it is also clear that even in order to begin investigations, a measurement tool is needed to sense impacts and provide an electrical signal which can be related to them.

In the discussion that follows, it is assumed that the primary observable resulting from a crack or an impact to structures is the generation and propagation of acoustic waves in the material. It is further assumed that for the amplitude and frequency range of these waves, conventional processing electronics presently exist which can faithfully record the most important features of the signals to be measured. Thus, only a transducer to convert mechanical energy to electrical energy is sought. In light of the previous sections, it is obvious that a variety of optical fiber sensors could undoubtedly be applied to this problem. However, by virtue of their relative simplicity and sensitivity, modal domain sensors appear to be a suitable candidate for acoustic wave detection and impact monitoring. Further justification for this notion will be presented in a subsequent chapter, where results of modal domain sensor experiments will be discussed.

1.5 Chapter Organization

As noted above, optical fiber modal domain sensors have been applied to an assortment of problems in nondestructive evaluation, and have been written about in numerous reports, papers, and master's theses [24-31]. However, it appears that no comprehensive review of MDS has been undertaken recently, especially in terms of their application to NDE, as well as the limitations of the method and potential solutions for overcoming them. It is hoped that this report will at least partially meet that need.

However, the major objective of the work described was to investigate the application of optical fiber modal domain sensors to the needs of nondestructive evaluation; specifically, to examine their use as embedded or attached to materials to perform structural health monitoring. In the chapters that follow, the theory and operation of modal domain sensors as a new NDE tool for dynamic strain monitoring will be developed.

The presentation is organized into seven chapters. In Chapter 1, the basic philosophy behind this work is introduced, including a justification for the application of fiber optic sensor technology to strain measurements. Chapter 2 continues with a review of prior research involving fiber optics in materials evaluation. While the general methods presented in this chapter are not the primary focus of the present work, they do serve to set it in proper perspective. Also, it is fair to say that even given the growing number of smart structures programs around the country (which often emphasize or exclusively center on fiber methods for materials evaluation), a significant portion of the new research has been performed by workers at the Fiber and Electro-Optics Research Center at Virginia Tech. Throughout the report, more than 25 publications or patents co-authored by the present writer are discussed as relevant to modal domain sensing and smart structures applications, as well as the results of much other unpublished investigation. References to this author's work and that of others are clearly marked where applicable.

Chapter 3 opens with a presentation of the theoretical principles of modal domain optical fiber sensors, starting with a review of the existence of modes in a dielectric waveguide. Single mode fiber interferometers are discussed next to lay the foundation for dual mode, few mode, and highly multimode sensors. In particular, the output intensity pattern for each of these sensor types is analyzed, and a new expression for the multimode fiber speckle pattern is derived. In Chapter 4, the issue of the sensitivity of optical phase in fibers to applied strain is raised. Corrections to the standard model are made first, and the new expressions for the sensitivity are applied to the cases of both axially and radially applied strain for each fiber type for the first time. Results of these theoretical considerations

suggest that multimode fiber sensitivity can compare well with that of single mode interferometers especially when subject to radial strain.

Chapter 5 reports the outcome of two particular applications of MDS to strain measurement which are believed to be unique to this work, that of acoustic emission detection, and real-time impact monitoring. In the Chapter 6, a number of considerations for optimizing modal domain sensors are raised. Source, fiber, and detection concerns are discussed in some detail, as are potential solutions to individual problems. In some cases, experiments were performed to assess the effectiveness of the solutions; these are reported, along with their results. In the final chapter, recommendations are made concerning future efforts, and conclusions are drawn.

2.0 STRUCTURAL HEALTH MONITORING

2.1 Introduction

Optical fiber waveguides have been developed over the past two decades for primary applications in high speed digital communications. Typical fiber waveguides used for communications consist of concentric silica glass core and cladding regions totaling 125 microns or more in diameter, surrounded by a protective polymer jacketing with a 250 micron outer diameter. Dopants added to the inner core glass during manufacture increase its index of refraction over that of the cladding, thus allowing for total internal reflection and the propagation of guided optical modes over long distances with low attenuation and low dispersion. Selection of core and cladding refractive indices and core diameter and geometry for a specific transmission wavelength allows a degree of control over the number and polarization of propagating modes in the fiber. In particular, a single mode is supported by a waveguide that has the combination of sufficiently small core and cladding index difference and small core diameter.

During the past ten years a variety of environmental sensors which employ such optical fibers as the sensing elements have been developed and demonstrated. Optical fiber sensors can be configured to measure environmental conditions such as strain, temperature, magnetic and electric fields, acoustic waves, and chemical concentrations by determining the induced changes in the intensity, phase, wavelength, polarization, time domain characteristics and modal content caused by such external phenomena. Such sensors may be broadly classified as either extrinsic devices in which guided light exits the fiber, interacts with the environment and subsequently re-enters the fiber, or intrinsic devices in which the propagating light remains within the fiber along its entire length. Intrinsic sensors offer the advantages of simplicity and potentially low

profile for embedding applications. Although most fiber sensors are instrumented to yield a measurement of a single parameter at a particular location along the fiber length, some multi-parameter, quasi-distributed and continuously distributed sensor devices have been recently reported which utilize either special waveguide properties or signal processing techniques [32].

The use of optical fiber sensors for the evaluation of advanced materials was proposed by Heyman in 1979 and subsequently demonstrated by Claus and Cantrell in 1980 [33]. In principle such sensors can be used to directly measure surface strain, temperature, and chemical concentrations and, if the fibers are embedded, such conditions can be determined internal to the medium. As cited in the first chapter, the advantages of optical fiber sensors for NDE are many. Fibers are relatively small and lightweight with respect to the active sensing elements of many systems, they may be configured to respond to a variety of environmental perturbations, have excellent sensitivity, linearity and dynamic range, and due to their all-dielectric nature are insensitive to electromagnetic interference.

This chapter will consider the use of optical fiber sensors during the entire life cycle of a material. First, the effect of embedding fibers upon the structural integrity of components will be considered. Next, the uses of fiber sensors will be described in order of their possible use during material life; specific sensor applications in composite cure cycle monitoring will be discussed, as will measurement of in-service conditions. Finally, methods for detecting acoustic wave precursors for material failure will be briefly reviewed.

2.2 Embedding Optical Fibers in Materials

Early research in the embedded fiber sensor area paralleled the development of optical fiber sensing systems for non-embedded applications and demonstrated the ability of different optical methods to measure particular internal phenomena [34]. In the early 1980's the potential usefulness of such techniques for the quantitative nondestructive

evaluation of advanced composite materials was recognized, with much work directed at the in-situ characterization of graphite-epoxy materials in particular. Subsequent work more fully developed the capabilities of the sensor systems to specifically permit multiparameter and distributed measurements. Much recent work has in addition attempted to integrate fiber sensor elements into systems for process control, vibration control, and damage location and possible identification. In this section, the process of embedding optical fibers will first be considered, followed by a brief discussion of the fiber-to-matrix interface, and the significant area of the effect of embedding fibers on the structural integrity of the host material.

2.2.1 The Fiber Embedding Process

The embedding of optical fiber in materials is limited not only by the properties of the fiber, but that of the processing conditions required for material fabrication as well. At present, for instance, laying optical fibers in particular locations and between specific plies during lay-up requires care and skill. Embedded fibers and leads must also be capable of withstanding the effects of applied stresses during fabrication. Otherwise, the large compressive stresses associated with the processing of materials such as graphite/epoxy or carbon-carbon composites may simply crush the fiber inside the specimen, or initiate cracks either internal or on the surface of the specimen. To date, our most successful method of curing graphite/epoxy samples without incurring damage to embedded sensors has been with the use of a hot plate press. At the lead-in/lead-out interfaces, where the fibers are subject to the greatest mechanical stress, various fiber protection schemes have been undertaken, including the addition at the panel edge of silicone rubber, heat shrink tubing, and damming material used to prevent resin flow. On the other hand, a standard procedure for autoclave processing has not yet been made public; indeed a number of engineers involved in such work complain of low survivability for sensors cured into composites in the autoclave.

The host material properties also affect embedding effectiveness. For example, a mismatch in the coefficients of thermal expansion of the fiber and the material may give rise to large shear strain concentrations at the fiber-to-matrix interface. This may result in fiber fracture due to stress-initiated cracking at a surface defect site, either during processing or while in service. Furthermore, due to the periodic graphite fiber bundle structure within composites and the regular surface patterns of the scrim cloth typically used as a backing during the curing of prepreg lay-ups, embedded fiber is inherently subject to some microbending. The geometry of this microbending is dependent upon the periodicity of the fiber bundles which are in contact with the optical fiber, and thus to the orientation of the adjacent ply layers. Total losses due to such microbending have been measured to be as much as 1 dB/m although losses of well less than 0.1 dB/m of embedded fiber are typical [35]. Alternatively, macro-bending-induced stresses caused by incorporation of fiber into a material in a serpentine geometry, using a technique such as that developed by Jackson, must be small enough so as not to compromise the long term integrity of the fiber [36].

Additional complications are created by the need to connect the embedded fiber sensor to the external transmitter and receiver instrumentation as well as, perhaps, to connect the fiber-embedded material to adjacent material components which combine to form a structure. First, the connector assembly must be integrated into the material during fabrication. In the case of advanced composites, this demands that the connector materials must be able to withstand the required processing temperatures and tool modifications that may be necessary for press or autoclave fabrication. Second, the mechanical alignment between optical fibers and thus between connectors must be maintained on the order of microns, because optical power losses are substantial if misalignment is on the order of one core diameter, typically ten microns for single mode fiber at 1300 nm and fifty microns for multimode fiber. In panels of material intended to be joined in a larger structure, the connectors may further need to be recessed to avoid the creation of surface anomalies. Although a few authors have discussed

options to the embedded fiber connectorization issue [37-40], many problems are far from being resolved.

2.2.2 The Fiber-to-Matrix Interface

The performance of optical fiber sensors for measuring internal material phenomena depends upon the effective boundary conditions at the fiber-to-host material interface. For example, it is often intended for embedded fibers to detect the strain existing in the host structure. In the ideal case, strain in the structure is completely transferred to the fiber through shear strain at the boundary between the two. However, evidence exists which suggests that weak bonding or highly elastic coatings on the fiber may in some cases lead to incomplete strain transfer: the structure deforms, while the fiber does not, or deforms to a lesser degree. Unless measurements are calibrated, this clearly could result in erroneous interpretation of the strain data.

In some cases it may appropriate or even necessary to remove the fiber jacketing prior to lay-up. This is especially true if the fiber is to sense the change in refractive index along its length as the part cures. Certainly removing the jacket will result in a reduction in fiber strength; generally coating is included to protect the fiber from dust and other foreign particles which can nick the glass and act as crack initiation sites. On the other hand, if the fiber is intended as an impact or damage monitor, this may be precisely the objective. At present however, there is no comprehensive study available documenting the strength characteristics of unclad, embedded fibers.

Regardless of the sensing method being employed, and the strength, thickness, and chemical properties of the fiber jacket, it is imperative that the fiber stay in intimate contact with the specimen along its entire length. It has been frequently documented with photomicrographs of sectioned parts however, that voids may form along the fiber during the fabrication process [37,40]. Voids can also exist due to cracks which may be created at an interface because of mechanical or thermal loading. It has been

demonstrated that the addition of extra resin along the fiber during lay-up can help alleviate voids, though resin-rich areas are often left instead [41].

2.2.3 Structural Effect of Embedded Fibers

Several investigators have studied the effect of embedded optical fibers upon the structural integrity of the host material. Jeglinski and Rytting, for example, report that unidirectional graphite-epoxy coupons, embedded with one or few unclad optical fibers oriented parallel to the graphite fiber tow direction, exhibit approximately a five percent reduction in their load to failure level over similar coupons which do not contain optical fibers [39]. Certainly the incorporation of optical fibers between ply layers in such a structure displaces graphite fibers, and as mentioned above, may cause the formation of voids, or nearly equivalently, of resin-rich regions, which in turn cause internal material geometry variations away from the interface. All of these effects vary as a function of optical fiber, its jacketing material, and adjacent ply orientation, as seen in Figure 2.1. Udd and co-workers have reported qualitative analysis of such effects for a variety of such orientations [40].

Measures [42] recently reported that tensile strength in $[0_2\{90\}0_2]$ Kevlar coupons were unaffected by an embedded array of fiber waveguides. Measurements of the ultimate compressive strength of 9 ply $[90_8]$ Kevlar/epoxy panels with and without three layers of embedded optical fibers (orthogonal to the material fibers) suggested the same conclusion. Similar work has indicated the embedded fiber grids do not have a detrimental influence on the resistance of the material to delamination [43].

In contrast, quantitative micromechanical analysis and measurement of the strain concentrations caused by embedded fibers has been reported recently by Czarnek et. al. at Virginia Tech [44]. Representative results of those measurements, obtained using Moire interference imaging methods, are given in Figure 2.2. This interferogram of the side of a symmetric cross-ply graphite/epoxy laminate, fabricated with a jacketed glass fiber waveguide embedded between and perpendicular to the center two plies,

may be interpreted visually to determine the two-dimensional residual strain field surrounding the fiber. A series of measurements similar to these but obtained for different levels of load on the composite specimen indicate strains of approximately 0.05 at the fiber-to-matrix boundary for an applied load equal to half the failure load of the eight-ply specimens tested. These large interface strain concentrations may pose significant limits on the long term structural integrity of materials containing embedded sensor fibers. As of yet, this issue has not received adequate attention in the smart structures community.

2.3 Fabrication - Cure Monitoring

The long term reliability of advanced composite material structures is dependent in part upon proper processing. As structural designs advance and more complicated geometrical composite assemblies are desired as integral units, the demands upon process engineering will increase. Embedded optical fiber sensors offer a possible means to extract information such as viscosity, modulus, compaction pressure, temperature and chemical changes during the cure process and as part of a real time process feedback control system. An idealized system would include fibers coated with appropriate materials so as to withstand the temperature and pressure of the cure environment (generally polyimide is used) and, in the case of autoclaved materials, a method to repeatably interface between the inside and outside of the autoclave. Most fundamental however, and most difficult, is to conceive and implement a sensing technique which will yield accurate, usable information regarding the state of cure within the sample.

Cure monitoring using fiber optrodes was pioneered by Levy, who employed tool mounted multimode fiber to interrogate the chemical conditions near the surface of the material to be cured [45]. By injecting source light into a small volume of material near the fiber-to-material interface at a specific wavelength, the fluorescence of the matrix material observed at another wavelength may be used to infer the chemical composition of the material and thus the degree of cure. Numerous other

authors have used similar distal end effects to monitor the chemical properties of materials [46]. One novel fiber concept, discussed by DiFrancia, employs a modified polymeric fiber cladding and coating to enhance the sensitivity of such schemes [47].

Other fiber sensor techniques also may be used in-situ to monitor conditions during composite cure. Reddy and co-workers, for example, demonstrated both differential interferometric and modal fiber methods for the measurement of strain, compaction pressure and heat flow during the cure process, and, for the first time, showed that distributed measurements of thermoset composite fiber cure process conditions were possible using a single sensor fiber length [48]. Figure 2.3 depicts a differential system in which heat flow in various laminates was monitored successfully, although it was recognized that random temperature fluctuations in non-laboratory environments may mask the resulting temperature-induced strain.

Drury reports the use of infrared spectroscopy to track the chemical state inside curing composites [49]. IR-transmitting fibers conduct light to a sapphire rod embedded in the sample. A certain amount of light leaks into the sample, is reflected back into the fiber, and sent to a spectral measurement system (a monochrometer/cooled detector combination, or an optical spectrum analyzer). As the chemistry of the resin changes during cure, differential absorption of the constituent wavelengths changes accordingly, indicating the degree of cure. Limitations exist due to the geometry of the sapphire rod, but presumably could be enhanced with the development of single crystal sapphire fibers, which could later be used to make in-service measurements.

More recently, Aframowitz has demonstrated an intensity-based fiber sensor to determine the point at which the composite matrix has been fully cured [50]. The technique makes use of an optically transmitting fiber fabricated from pre-cured resin, having an index of refraction slightly higher than that of the uncured epoxy into which it is embedded. As the material cures, its index rises to that of the sensor, cutting off more and more modes guided along its length. When at last the matrix index reaches that of the pre-cured fiber, input light is scattered into the part and

the sensor output is negligible. As of yet, it is unclear whether this approach will be as useful for quantitative measurements of the *degree* of cure as for final cure state. Unfortunately the monitor is not sensitive to different states of cure along its length, thus leaving in question the homogeneity of the part. Furthermore, after cure, conventional glass fibers which are used for lead-in and lead-out of the input light are left inside the part without the possibility of being employed for subsequent NDE measurements.

Another technique to monitor cure state of epoxy resins has been demonstrated at Virginia Tech using single mode fiber interferometry. Predicated on work done by Winfree and Parker [51,52], this method relies on ultrasonic pulse arrival time delays and amplitude differences to deduce acoustic velocity, attenuation, and dispersion information as a function of cure. We consider first the simplest case. Figure 2.4 depicts an ultrasonic transducer of dimension L insonifying a host material containing a single mode optical fiber embedded transverse to the direction of sound propagation. The source is modeled as launching a cylindrical, longitudinal sound wave at a single frequency, while the material thickness is considered thin enough that the length of the fiber traversed by the acoustic wave is also of length L. We also assume that the acoustic wavelength of the source is long compared to the diameter of the fiber. For ultrasonic transducers operating in the 1 MHz frequency range, and for typical composite materials, acoustic wavelengths are on the order of 1-10 mm. This is certainly greater than 10 times larger than the core of the average multimode fiber, and may be several hundred times larger for single mode fiber, so that the assumption appears to be justified.

Given these conditions, we may consider the fiber at any instant in time as surrounded around its radius by a hydrostatic radial pressure field. Two strain effects result. First, during the compression part of the cycle, the fiber diameter will be reduced over the length L. The amount by which it is reduced can be expressed in terms of the radial strain ϵ_r, and is calculated from mechanics by knowing the Young's modulus of the fiber and the amplitude of the acoustic pressure wave emitted by the source. The

latter can be derived from first principles using the material stress matrix, requiring only a knowledge of the material constants and the surface displacement of the piezoelectric crystal, but in practice is more easily obtained empirically.

The second observable strain effect is seen as an elongation of the fiber, arising from the Poisson effect. If the fiber were free to extend along its axis, then it would elongate by a length $\Delta L = L \, \varepsilon_z$. From Figure 2.4 however, it is clear that the fiber is at least partially constrained by the surrounding material. On the other hand, if intimate contact and adhesion is assumed between the fiber and host material, then complete strain transfer should be accomplished. Thus if the host material itself were unconstrained, then both it *and* the fiber would elongate by ΔL. Realistically however, the material will always be partially constrained at least at one surface, and complete strain transfer will not be possible. In this case the imparted strain will depend in part on the shear modulus of the material.

Furthermore, when we consider that the acoustic source generates time-varying compressional waves rather than static, then inertial effects must be accounted for. In this case, the mechanical vibration frequency spectrum of both the fiber and the host play a role, usually acting as a low pass filter, or alternatively, acting to attenuate the strain effect at high acoustic frequencies. Just how high is "high" and how much attenuation takes place will vary depending on material properties and geometrical layout. The extent of the effects is not well characterized in most real world situations.

The net effect of applied radial strain on the fiber is to change the phase of the light propagating within the fiber core. The exact mechanisms leading to phase change and the amount of change expected for a given level of strain is dealt with at length in Chapter 4. It suffices at this point to say that the phase change is related to the strain through a fairly simple expression involving either well known or easily calculated optical fiber parameters such as the index of refraction, radius, and the optical propagation constant. Of importance here is that the phase change is

directly proportional to not only the radial strain, but also the length L. Finally, we relax the assumption that the acoustic wave imparts only static strain, and again note that compressions and rarefactions are generated at the frequency of the acoustic source. When the embedded fiber is incorporated as the signal arm in an interferometer, phase changes lead to optical intensity variations which can be interpreted as acoustically induced strain; all are modulated in turn at the sound frequency.

In a real system, a high voltage pulse is sent to the electrodes of a piezoelectric transducer. Depending on the way the device is housed, the voltage rise produces an initial expansion, followed by mechanical ringing of the crystal at its resonant frequency. This produces a packet of sound waves which propagates into the material (assuming good acoustic impedance matching between the transducer and the sample), and across the fiber. A detector monitors the interferometer output and displays a modulation which directly follows the mechanical motion of the transducer.

The amplitude of the detected signal is a function of several factors, some of which have been mentioned above. First is the acoustic power which is generated by the source. We take that to be invariant throughout the course of an experiment, though in practice the height of an individual pulse may vary somewhat from pulse to pulse due to fluctuations in the driving electronics. This generally averages out over a number of cycles. Second is the bulk modulus, B, of the material (Young's modulus for the solid state), which couples the incident stress field to the amount of strain experienced by the material and the fiber, and is derivable in terms of the stiffness matrix components, or alternatively, the Lamé constants. It is the bulk modulus which acts in conjunction with the material equilibrium density ρ_0 to determine the velocity of sound in the medium: $V_s = \sqrt{B/\rho_0}$. In the case of a curing composite panel, the bulk modulus will vary widely from an initially intermediate value for a tacky, room-temperature lay-up, to a low value as the material softens, and again to a higher value as the material cures to a stiffened state. Note that at the same time the material

density also varies, and the net effect is that the velocity rises to a final high at the end of cure.

The third factor which determines fiber strain is the attenuation due to absorption of acoustic energy in the material. This is a frequency dependent effect which also changes as the material properties change during cure. Because of this effect, the distance between the source and the fiber is important. Though the fiber may move with respect to the source from slippage and compression during cure, the absorption over the small differential distance is considered insignificant, and is ignored. Finally we have the mechanical resonance effects mentioned earlier. These too are a function not only of frequency, but also of material state, encompassing shear modulus, Poisson's ratio, and density. The total response of all of these effects determines how the sensor will behave during cure.

In order to precisely predict the outcome of an experiment such as described above, it would be necessary to characterize all of the material properties and constants at every state in the cure cycle. Though this may not be an impossible task, it would certainly be cumbersome, and to our knowledge, it has not been done for the material at hand. Instead, experiments are performed to determine if the conglomerate fiber response offers features which can be used to infer the final cure state. These features include those mentioned above, such as attenuation, sound speed changes, or frequency dependent changes of either. These possibilities will all be discussed briefly below.

In the simplest system, a one-point attenuation measurement could be made with a set-up similar to what was described with regard to Figure 2.4. At time t_1 in the cure cycle, the output of a single fiber sensor might appear as depicted schematically in Figure 2.5, where the first signal in each trace represents the main bang of the transducer. At a later time t_2, it is expected that the signal amplitude would decrease due to changing material properties; the attenuation is inferred accordingly. Problems with interpreting this type of single point data arise however from the fact that other mechanisms could be responsible for such signal level changes other than cure state. Specifically, the very real problem of variable coupling into

the material arises, as well as the possibility of partial cancelling of acoustic power due to the summing of multiple reflections of ringing pressure waves at the transducer face. The latter phenomenon depends on the sound speed in the changing material and the material thickness, and is more pronounced for thin samples. It thus varies from sample to sample, and so could not be easily compensated for in a processing algorithm. It would be desirable for this system to make use of some type of referencing to avoid the need for constant calibration.

An alternate scheme makes use of two fiber sensors placed a distance apart, along the direction perpendicular to the sound propagation vector, with outputs represented in Figure 2.6. Now rather than a single amplitude compared against itself, we have two signals referenced against each other. If only amplitude ratios are considered, then source power or coupling variations are less of a concern. However, the obvious trade-off is the need for two sensors and any associated equipment. To avoid this need, we could configure a single sensor to pass through the sample twice, where only one trace is obtained, combining the two in the upper figure. An example of such a measurement will be discussed in the next section.

Drawbacks associated with this scheme have to do with the preferred method of acoustic excitation. As it is depicted, the sensor(s) passes through the sample at two different depths, presumably between different constituent plies. However, except for unusually thick lay-ups, the time delay Δt between fiber signals would be much shorter than the gated width of the ultrasonic pulse, meaning confusing signal overlap would occur. Also, the differential attenuation between two points spaced so close together would be small, reducing the signal to noise ratio. The alternative to this would be to lay the fiber passes laterally along the breadth of the lay-up, and launch acoustic waves into the sample at an edge. Although this is a viable technique and has been applied successfully by Miller et. al. [53], coupling sound into the edge of a panel and propagating to the center of a sample (where the sensor would presumably be ideally located) will always involve less power transfer than coupling across the panel plies. Furthermore, for all but the simplest of part geometries, edge excitation

could be complicated by panel curvatures, corners, and features, and may prove intractable.

Another possible measurement technique investigates the changes in the propagation velocity of sound as the host material cures. A preferred configuration would be just as described above, where now it is Δt which is of primary measurement importance rather than the amplitude ratio. As alluded to earlier, resulting velocity changes in curing neat resin and prepreg samples have been detected piezoelectrically and reported in the literature by Parker and Winfree from NASA Langley Research Center. However, though this is again a viable method, it is not ideal for embedded fiber sensors for all the same reasons as mentioned above. Furthermore, pulse spreading effects reduce the time resolution possible, and vary widely depending on excitation frequency and sample geometry.

A third measurement possibility derives its reference from the monitoring of two different acoustic frequency components rather than two different spatial locations. It was noted earlier that signal attenuation is frequency dependent through a number of mechanisms. In general it is safe to say that higher frequency components are attenuated more than lower frequencies, but the *amount* of attenuation is again dependent on exact material properties. Although not fully confirmed, it is believed that the differential attenuation characteristics at two specific frequencies will lead to a unique curve from which the cure end could be inferred.

A system to implement this idea appears in Figure 2.7. Two narrowband ultrasonic transducers with resonant frequencies f_1 and f_2 launch acoustic waves into the host material at times separated by Δt. At some time later, these pulses arrive at the embedded fiber, which strains as described above. The two received pulses are now separated in time by $\Delta t'$, which in general may be slightly different than Δt. The modulation frequency for each pulse is f_1 and f_2, respectively. Therefore, if a Fourier transform is performed on the time trace, a signal containing two strong peaks at f_1 and f_2 should appear, with their magnitudes indicating the amount of power detected at each frequency. If at a later time t_2 the material has changed, it is expected that the ratio V_1/V_2 will also have

changed. This is seen qualitatively in Figure 2.8a. It is hoped that a plot of this ratio over the cure cycle would yield information as to the cure state.

Though this system is easy to understand and offers potentially good frequency separation, it is troublesome to operate in that it requires two transducers. An alternative approach is to operate a single broadband transducer, which by definition emits acoustic energy over a range of frequencies. To analyze the fiber response, the FFT of the time trace is again performed, resulting an an output represented in Figure 2.8b. The magnitudes of the signal at two chosen frequencies are compared as before. It is noted that since energy here is spread over many unused frequencies, the signal to noise ratio for this embodiment would likely be lower than the two-transducer case.

2.4 In-Service Measurements

During the normal in-service lifetime of a structural material component numerous material properties may need to be monitored. Of primary importance is the measurement of strain, which may be either mechanically and thermally induced. Strain due to temperature changes, as well as some slowly varying mechanical processes is often termed "quasi-static." On the other hand, "dynamic" strain is vaguely applied to strain changes which occur at frequencies greater than several Hertz, such as exists during structural vibrations. Each of these cases will be dealt with separately as examples of in-service measurements which are presently in demand.

2.4.1 Quasi-Static Strain

Quasi-static strain measurements in particular have been the subject of much research during the past several years. These have typically been the first to be addressed in many research programs, partially because of their practical importance in real-world applications. The possibility of success

is also enhanced with quasi-static measurements, because the low bandwidth requirements allow the use of either highly sophisticated or else experimental signal processing schemes which operate at relative low frequencies. As a result, a number of different fiber sensor approaches have been taken for the measurement of strain, which will be reviewed below. Although modal domain sensing will be mentioned as appropriate, the bulk of the discussion regarding new applications of this method will appear in Chapter 5.

Single Mode Fiber Interferometry

The earliest strain monitors employing optical fiber sensors were interferometric in nature, appearing after the original paper on the subject by Butter and Hocker was published in 1978 [54]. Not long after, fiber optic interferometers were extended specifically to sensing applications in graphite/epoxy composites, notably by Claus, with sensitivities several orders of magnitude better than obtainable using conventional strain gages [33,55-57]. In addition to strain due to mechanical loading, as discussed in the previous section, absolute and differential fiber interferometry has been performed to monitor both thermally and acoustically induced strain, again achieving similar high levels of sensitivity.

By now the number of authors reporting the use of Mach Zehnder, Michelson, and Fabry-Perot interferometers for strain sensing is enormous. Though a large number deal more specifically with advancing interferometer stabilization and signal processing techniques, most could be readily applied to structures monitoring. By contrast, more and more researchers with a largely mechanical engineering background are beginning to apply fiber optic sensor methods, and specifically the single mode interferometer, to the problem of on-line strain measurement. In one notable example, a Mach-Zehnder configuration has recently been employed to accurately isolate strain in one dimension under the case of biaxial loading [58]. In another case, an interferometer was constructed using two incoherent optical sources and two multimode fibers; coherence was maintained by modulating the sources in phase at r.f. frequencies [59].

With one fiber embedded in a graphite/epoxy coupon, strains in the region of 1000 µstrain were recorded. Although this is far less sensitive than obtainable with optical interferometry, the advantages of simpler optical components may justify its use in some cases.

Differential Methods

Despite their advantages, interferometrically based sensors exhibit an ambiguity due to the fact that under normal conditions, mechanically induced and thermally induced strain are indistinguishable. However, several differential methods have been demonstrated recently which can be used to overcome such limitations. In the first two methods, two propagation conditions are used to solve for the two unknowns. For example, Meltz et. al. have shown that two propagation conditions may be created using an optical fiber having two single mode cores. Energy transfer between the cores occurs at a particular beat length along the fiber. Careful analysis of the energy transfer can yield both strain and temperature data [60].

Similarly, two modes propagating in a fiber having a low V-number will exhibit differential propagation effects. As explained earlier, such is the essence of modal domain sensors. In unpublished work performed in mid 1986, the present writer demonstrated the ability of few mode fibers to determine levels of quasi-static strain. As shown in Figure 2.9a, the fiber was attached to a [±45°] composite coupon, which was strained in a cantilevered fashion. A detector was placed so as to collect light from only one of the output lobes; the detector position was optimized to receive maximum intensity before load and some lesser amount upon load due to changes in the far field pattern. The average photodetector response resulting from two cycles of the loading micrometer screw appear in Figure 2.9b. Though further loading would likely have resulted in an upturn in intensity, it can be seen that at least for a limited dynamic range, monotonic operation can be achieved for the sensor. Duncan has suggested that such differential mode sensors operated at two distinct wavelengths simultaneously may give multiparameter measurement capability [30].

Extrinsic Methods

The alternative to measuring strain and temperature simultaneously is to monitor each independently. Murphy, for example, has developed an extrinsic device in which a single mode coupler is cleaved just to one side of the coupling region; on one fiber core is deposited a film of aluminum to mirror incoming light and provide a reference signal in a Michelson interferometer [61]. Light from the remaining core emerges, interacts with the straining sample, and is reflected back into the core to combine in the output arm with the mirrored light. Because the two interferometer paths have the same length in fiber and are in intimate contact, high sensitivity strain measurements can be made independent of temperature conditions.

In a simple intensity based scheme, Kriz developed a method which monitors the axial mismatch loss between the cleaved ends of two fibers facing each other from either side of a crack in a material [62]. By monitoring loss versus loading conditions, dynamic crack opening displacements were able to be determined in-situ. Needless to say however, this method was primarily intended as a laboratory-based tool, and was used to study stress corrosion crack dynamics.

Polarimetry

In contrast, polarimetric strain sensors are usually intrinsic. Sensing is performed by first injecting polarized light into the fiber; loading on the fiber is inferred by analyzing the polarization state of light emerging from a fiber, and measuring the amount of induced birefringence. Since these sensors generally make use of polarization preserving fiber, bending or twisting of the fiber generally does not upset the optimum bias point, as is often true with conventional interferometers. Furthermore, sensitivity of these devices depends in part upon the strain-birefringence relationship of the particular glass used to make the optical waveguides. Using this method, Meltz and Dunphy demonstrated excellent sensitivity to subsurface strains and stresses within orthotropic plates and symmetric cross-ply laminates [63]. The measurement of strain in cantilevered graphite/epoxy

beams was reported by Brennan, who used not only embedded polarimetric sensors, but also dual mode embedded sensors [64,16].

Time Domain Techniques

One problem suffered by all the sensors mentioned above is their general inability to make distributed measurements. As a result, for those involving intrinsic transduction mechanisms, certain sections of the fiber must be made insensitive to environmental fluctuations, while the sensing portion must be exposed to the observable. Often this approach is not highly effective, leading to relatively low signal to noise ratios, and is at best complicated to implement. Alternatively, it has been proposed that in order to sense quantities at different locations, an array of discrete sensors must be deployed, one for each location. Obviously such a scheme would entail greater complexity, duplication of parts, and expense.

One of the earliest routes taken towards single fiber distributed measurements made use of optical time domain reflectometry (OTDR) techniques. Light generated by a pulsed optical source is coupled into the fiber to be examined and propagates as one or more guided modes. As the light propagates along the fiber it is partially backscattered by anomalies in the waveguide structure. In otherwise unperturbed fibers, uniform Rayleigh backscatter caused by the intrinsic molecular structure of the component glasses results in an exponential decrease in optical power received at the front end as a function of time. Deviations from this anticipated baseline return signal may be interpreted as being caused by regions of local fiber perturbation, specifically local variations in fiber geometry or index of refraction or both. The location of such regions along the length of the fiber may be determined by measuring the round trip time of flight of an optical pulse from the source to the backscatter site and back to the detector.

In what appears to be the first application of OTDR to fibers embedded in materials, Claus, et. al. demonstrated the ability to locate and monitor regions of stress concentration arising from loads applied to host graphite/epoxy panels [65]. In this work, measurements were performed

using a communications OTDR unit having a spatial resolution (related to the temporal width of the excitation pulse) of 16 cm; the experimental setup and representative results are shown in Figure 2.10. Since then, refinements in commercially available OTDR instrumentation have increased the possible position resolution to nearly 100 µm, enabling distinctions to be made between strain levels which elongate the fiber such small distances. Employing such a unit, quasi-distributed strain was measured using in-line air gap splices as time (and therefore position) markers [66,67]. More recent advances take advantage of re-entrant loop techniques, and promise to better the current resolution limit by as much as two orders of magnitude [68].

2.4.2 Structural Vibration Measurements

Embedded or attached fiber sensors may also be used to monitor the vibration of structures. First, sensitive interferometers may be implemented as discrete sensors and used in a manner similar to that described above. Second, they may be designed to monitor strain integrated along the sensor length in order to infer axial deformation, bending, or structural mode shapes. For applications involving large structures which need to be controlled but which may be mechanically damaged during use, such distributed sensors have the advantage of possibly being able to gather mode shape information independent of the vibration node locations of the structure and the corresponding locations of discrete sensors.

Recently, the operation of two such line-integral strain sensor systems have been investigated in detail for the monitoring of structural vibration modes. The first, developed by Kush and Meffe used the interference between modes in a multimode fiber to infer structural mode shape amplitudes [69]. This basic idea was implemented in a number of configurations by Bennett, Ehrenfeuchter, and co-workers, using primarily few-mode fibers (V< 5) [70,71]. In their first modal domain fiber sensor, the optical modal content of the fiber was interrogated and processed to yield a measure of the dynamic Fourier coefficients of the mechanical vibrational

modes. A typical set-up and results of such a measurement are shown in Figure 2.11. A second technique, developed by Rogowski [72], uses an optical pulsed phase locked loop technique to monitor integrated strain in a vibrating beam. Results indicate that this method can resolve strains on the order of 0.1 microstrain. Current work by Rogowski compares the performance of the modal domain, optical phase locked loop and discrete resistive strain gage sensors. Additional research, aimed at dynamically measuring plate mode vibration amplitudes and phases due to the impingement of low frequency acoustic waves is presently ongoing at the Fiber and Electro-Optics Research Center at Virginia Tech.

The use of modal domain sensors in monitoring the slewing and vibration of large, flexible structures has led to the analysis of possible control system architectures that utilize the inherent and fundamentally different nature of fiber sensor output signals in feedback control systems. Conventional control systems accomplish such slewing tasks through the use of "point" sensors, that is, resistive strain gages which are much smaller in size than the structure to be controlled, that are generally attached at predetermined vibration anti-nodes. However, since the fiber strain sensors yield the strain integrated along the fiber path rather than strain at a point, control algorithms must be modified. The problem is further complicated due to the fact that for fiber elongations longer than the beat length between the participating modes, often as small as 100 μm, the signal output takes on the oscillatory nature characteristic of interferometers. However, it has been shown that this nonlinear sensor output will not lead to instabilities in the control system if the latter is appropriately designed [73]. In addition, this research is being complemented by the parallel development of embedded shape memory metal actuators which may be combined with embedded sensors to achieve total internal sensing and motion control maneuvers [74].

2.5 Material Degradation

When discussing in-service measurements on a given structure, a healthy condition is generally implied, where strain and temperature

measurements are expected to fall within the bounds of normal operation. In contrast, as the structure begins to degrade, either due to ordinary wear or to external events such as over-stressing or impacts, additional monitoring may be necessary in order to fully characterize the material state. The typical example is that of an acoustic emission emanating from a crack site, which may trigger an AE sensor, but go almost unnoticed by a conventional strain gage. Thus the mission of fiber sensors for NDE goes beyond making the types of measurements necessary under normal conditions; signals which are either precursors of damage, or which indicated material degradation has already occurred must also be captured and identified.

Prior work in fiber optic assessment of material damage has basically fallen into one of two categories. In the first, a straightforward, destructive approach has been taken which relies on the breakage of embedded or attached fibers. In the second, acoustic shock waves due to impact or to material cracking which leave the fiber in tact could be detected. In this section, fiber breakage sensors will first be reviewed. Acoustic wave monitoring will also be discussed, though recent measurements specifically concerning modal domain sensing will be left to Chapter 5.

2.5.1 Fiber Breakage -- Destructive Testing Methods

Optical fiber sensors based on partial or complete fiber breakage offer the potential advantages of simplicity and low cost. In the case of a single fiber running through a critical part or structural location, light from a low cost LED can be injected into the fiber, while the output can be detected using a low performance photodiode. A break in the light signal can be a reliable indication of damage in the part, as shown schematically in Figure 2.12a; such simple experiments have been performed in composite samples at the David Taylor Naval Research Labs, Virginia Tech, and the National Institute of Standards and Technology. If it is known that strain will be concentrated in a particular region containing the fiber, then it may even be possible to locate the damage. Similarly, if fibers of different tensile strength are embedded side by side, especially in a large specimen under

uniform load, the magnitude of the maximum strain experienced can be estimated by determining which fibers are still transmitting at any point in time. Perhaps the most comprehensive work embracing the idea of both embedded and attached fibers of various types for damage detection in composite materials to date has been performed at Messerschmitt-Bölkow-Blohm in West Germany for application to both railway and Airbus structures [75].

This idea can easily be extended to large two dimensional structures. Crane et. al. proposed a damage assessment system consisting of a mesh of optical fibers embedded orthogonally in composite materials [76]. This was to allow for determination of damage location by comparing the x and y coordinates of fibers transmitting no light, represented in Figure 2.12b. Another two dimensional system recently demonstrated by Measures, et. al. interrogates transverse leakage of light from broken fibers in semi-transparent Kevlar composites [77]. In this type of situation, data could be collected by a scanned detector array feeding a video image. Furthermore, backlighting the sample and subjecting it to visual inspection even revealed damaged areas which were undetected by C-scan [78]. Needless to say however, this technique is largely limited to non-opaque materials.

Other work has been aimed at making the fiber mesh method more readily applicable in a broad range of situations. For example, it is not always practical to embed an host of fiber optic lines in a test material. Instead, it may be more useful to embed them in a thin sheet of low modulus plastic which can conform to the surface of the workpiece [79]. However, these systems inherently involve a serious trade-off between complexity and resolution. Locating damage points with high resolution requires a fine mesh of fibers, increasing also the number of discrete components necessary for processing light in and out of the fibers. One methods to reduce the number of light sources would be to fan light out from source using a multi-port fiber coupler [80]. A similar approach might make use of single fibers and 2 x 2 couplers in combination with OTDR. This method would have the advantage of providing the location of the damage to within the resolution of the OTDR unit, as explained in Figure 2.13.

In order to eliminate the need for sophisticated OTDR electronics, a refinement has been designed, built, and tested in which a single source injects light into a multimode optical fiber, and in which only a single detector is required to collect the data [81,82]. Furthermore, this scheme partially processes the data optically and thus greatly reduces the computing time required to interpret the output. The design relies on a novel coupling method to ensure that each optical fiber path within the specimen receives a unique portion of the original input power. This is accomplished by fabricating a number of 1 x 2 couplers which do not have the standard 50-50% coupling ratio.

Figure 2.14a presents an example of the idea with a small four channel array, here depicted as embedded in a composite panel. A single input fiber passes through three couplers, resulting in four optical paths marked a-d, which cross through the panel as shown. In Figure 2.14b, the required splitting ratio for each coupler is seen boxed next to the coupler (in percent). In addition, the power in watts of each unperturbed line is shown, while the input optical power is assumed to be 15 mW (arbitrary). It is also assumed that if any fiber is broken, presumably due to damage incurred in the panel, it yields an output of 0 mW.

Since light intensities add linearly at a detector surface, if all fibers are in tact, a total power of 15 mW would be sensed by the detector. In addition, a tabulation of the output power total for all the combinations of broken or in-tact fibers results in Table 2.1. It is important to notice that for each of the sixteen possibilities, the outputs are unique, ranging in 1 mW intervals from 0 to 15 mW. It also might be noted that the couplers and broken fiber output need not be exactly as shown; slight variations throughout the system could be tolerated and still lead to unique values for each configuration of "good" and "bad" fibers.

In the sense given by the table, this system is essentially a digital to analog converter. An even simpler arrangement could be conceived to implement logical AND, NAND, OR, or NOR elements, which could be useful to monitor any number of processes or even perform computations. It is believed that any procedure which can be manipulated to express a Boolean output can be modelled in this way. In terms of the application at

hand, a digital interpretation of damage in designated areas of a panel may be obtained rapidly using a minimum of hardware.

Although it is a step in the right direction, problems still exist in the optical processing system. For one, it may have trouble distinguishing between strain induced loss in output and outright damage. The splitting of light most likely will need to be configured such that if light is lost due to strain, it does not yield the same output as if any one of the fibers had been broken. Similar consideration should be given to the possibility that a damaged fiber may still partially transmit light. However, it was discovered during actual demonstration of the concept that much of the ambiguity that existed due to non-ideal conditions could be accounted for by prudent choices of the preset threshold values in the computer data collection algorithm.

2.5.2 Detection of Ultrasonic Waves -- Nondestructive Testing Methods

One difficulty with the detection schemes above is that they all require a significant amount of damage to occur to the optical fiber before they will register. Using these methods, many types of damage, such as cracking and delamination could go completely unnoticed. Furthermore, they deal with an irreversible process by which light is partially or completely lost from the fiber. Thus sensitivity will also be lost to damage in locations where the lead-in fiber has already been destroyed. For these reasons, such sensors cannot be thought of as truly nondestructive, and can in no way predict damage or material failure. One approach to overcoming some of these disadvantages was successfully demonstrated by Claus and Wade, who used a grid array of optical fiber differential interferometers to derive strain fields integrated in the x and y directions [83]. Although this meant that a range of damage could be continuously monitored, the complexity of the system would make it impractical for most applications.

A more promising solution has been to apply fiber optic methods to the detection of acoustic waves arising from cracks or impacts. Acousto-optic transduction can be achieved by modulating any of the fundamental optical

field parameters within the fiber, such as phase, intensity, polarization, wavelength, or modal content. The first and major thrust in the development of acoustic sensors has been in the hydrophone area, where multiplexing of single mode interferometers has been employed to detect acoustic pressures with sensitivities at or near the "sea-state zero" level [84,85]. Intensity-based microbend loss hydrophones have also been developed [86] and direction sensing at frequencies in the kHz range has been demonstrated [87]. By now a number of research groups have worked towards the development of rugged, deployable hydrophone arrays; a good bibliography of important efforts over the last ten years appears in reference [85].

Underwater acoustic wave power measurements and the characterization of ultrasonic transducers have also been performed using polarimetric sensors [88]. Polarization preserving fibers were aligned in a sound field so that the waves were transverse to either one of the two polarization axes of the fiber. The sensor output was observed to be a linear function of the square root of the total power as recorded by a radiation force balance, or linearly proportional to the acoustic wave amplitude. Fibers were also scanned across the face of a 1 MHz plane transducer and a 10 MHz focussed transducer in order to map their respective beam profiles; the results were compared to similar measurements made with a PVDF hydrophone. It was noted that the fiber, whose dimensions are only a fraction of the acoustic wavelength for even high frequency sound, does not suffer from spatial averaging, and could thus give a more accurate representation of the spatial variation of ultrasonic fields than conventional devices.

In an example more relevant to the problem at hand, Dunphy and Meltz have reported using fiber optic polarimetry for the study of very rapid disturbances in composite materials which are thermally generated using high power pulsed CO_2 laser radiation [89,90]. The compressive stress wave thus produced impinged upon a highly birefringent (polarization preserving) fiber, inducing added birefringence. This was measured by monitoring the intensity of light in the two polarization states within the fiber. Acoustic perturbations in the GHz range were monitored with the

help of high speed transient recorders; it was suggested that in this way spatial/temporal stress wave dispersion measurements could be conducted with the use of multiple wavelengths.

Ultrasonic compressional wave signals from a piezoelectric source have also been detected using Mach Zehnder fiber interferometry. As mentioned earlier, measurements of ultrasonic velocity and attenuation have been performed during composite cure. This methodology is thought to be directly applicable to the newly emerging NDE discipline of acousto-ultrasonics, and certainly is of significance in laying a foundation for acoustic emission and impact shock wave detection.

As an example of the results obtainable with this type of measurement, Figure 2.15 depicts an aluminum bar measuring 2.5 x 5.1 x 42 cm, in which two holes were bored through laterally, 14 cm from one end and 7 cm from the other [91,92]. A continuous length of single mode fiber was threaded through both holes as shown, and the holes were well-filled with epoxy. The fiber was spliced into a single mode interferometer, and bulk waves with a center frequency of 2.25 MHz were injected into the side of the specimen so as to propagate across the fiber lengths using a transducer bonded at one end. High speed detection, filtering, gating, amplification, and signal averaging were applied to the interferometer output.

A typical oscilloscope trace is plotted in Figure 2.16. In this plot, the upper trace is strictly the acoustic response, that is, the main bang and the echo off of the back face of the bar. We note that the round-trip transit distance of the sound in the bar is 84 cm, and from the scope, the transit time is 134 μs. This leads to a longitudinal wave speed of $V_s \approx 6270$ m/s, which is reasonable for the alloy of aluminum used. Notice that 45 μs after the pulse is launched, a small reflection is received back from the first hole-epoxy-fiber combination, marked a1. That is, (2 x 14 cm)/6270 m/s = 45 μs, as expected. Again, at 112 μs = (2 x 35 cm)/V_s later, a small reflection a2 is received from the second fiber. The large end reflection is marked a3. Note that with each of the above pulses is associated a secondary pulse, always trailing by 8 μs. An adequate explanation for this has not yet been arrived upon, but it *is* an acoustically real phenomenon, and may have something to do with electrical pulse reflections inside the electronic system, or some

secondary transducer vibration. Also, it is noted that side reflections as well as reflection-generated shear waves may play a part.

The lower trace is the output of the photodiode after it has been rectified and filtered (enveloped detection), and amplified by a broadband receiver originally meant to amplify acoustic signals but here used for optically generated signals. The output was averaged 200 times over 2500 sample points by a LeCroy 9400 digital oscilloscope. The first, large pulse is an artifact of the previously mentioned noise source. When the laser beam is blocked from entering the fiber, the smaller peaks disappear, but the first one remains, indicating that it is not "real" signal. The smaller peaks, marked o1 - o5, correspond to the acoustic pulse traversing the fiber several times. Pulse o1 is the first crossing, correctly occurring 14 cm/V_s = 22 µs after the pulse initiation. As can be confirmed by simple arithmetic, o2 shows the sound pulse crossing the second pass of fiber, o3 occurs another 22 µs later when the pulse has reflected from the back end and crossed the second pass of fiber again, o4 shows the sound crossing the first pass, and o5 is after a reflection from the front surface and the first fiber pass is crossed again. Note now that not only are the associated pulses apparent as in the upper trace, but even finer structure can be seen.

2.6 Summary

Optical fiber sensors may be used to measure a wide range of physical observables in-situ. They offer the ability of being embedded or attached, and are characterized by small size and weight, an all dielectric profile, high sensitivity, good linearity and dynamic range, large bandwidth, and the opportunity for sensor signal multiplexing. Sensors have been applied to the monitoring of observables throughout the lifetime of an engineering structure, beginning with the strain and temperature effects which occur during the curing of composite materials. In addition, in-service measurements such as static and dynamic strain, structural vibrations, and thermal flow have all been performed using a variety of sensor configurations. Conditions associated with structural and material

degradation have been detected, such as acoustic emissions and low energy impacts. Future developments offer the promise of a class of devices broadly applicable to current problems in measurement science and nondestructive evaluation.

It is to be noted that a number of issues relevant to optical fiber environmental sensors remain to be resolved. At present, the effect upon long term structural reliability of embedding optical fiber within materials is unknown . Also unknown for both the case of embedded and attached sensors is the efficiency of strain coupling between the structure and the optical fiber. Finally, concerns such as optical fiber interconnection, methods to achieve full multidimensional distributed multiparameter sensing, and sensor multiplexing pose significant materials and signal processing challenges.
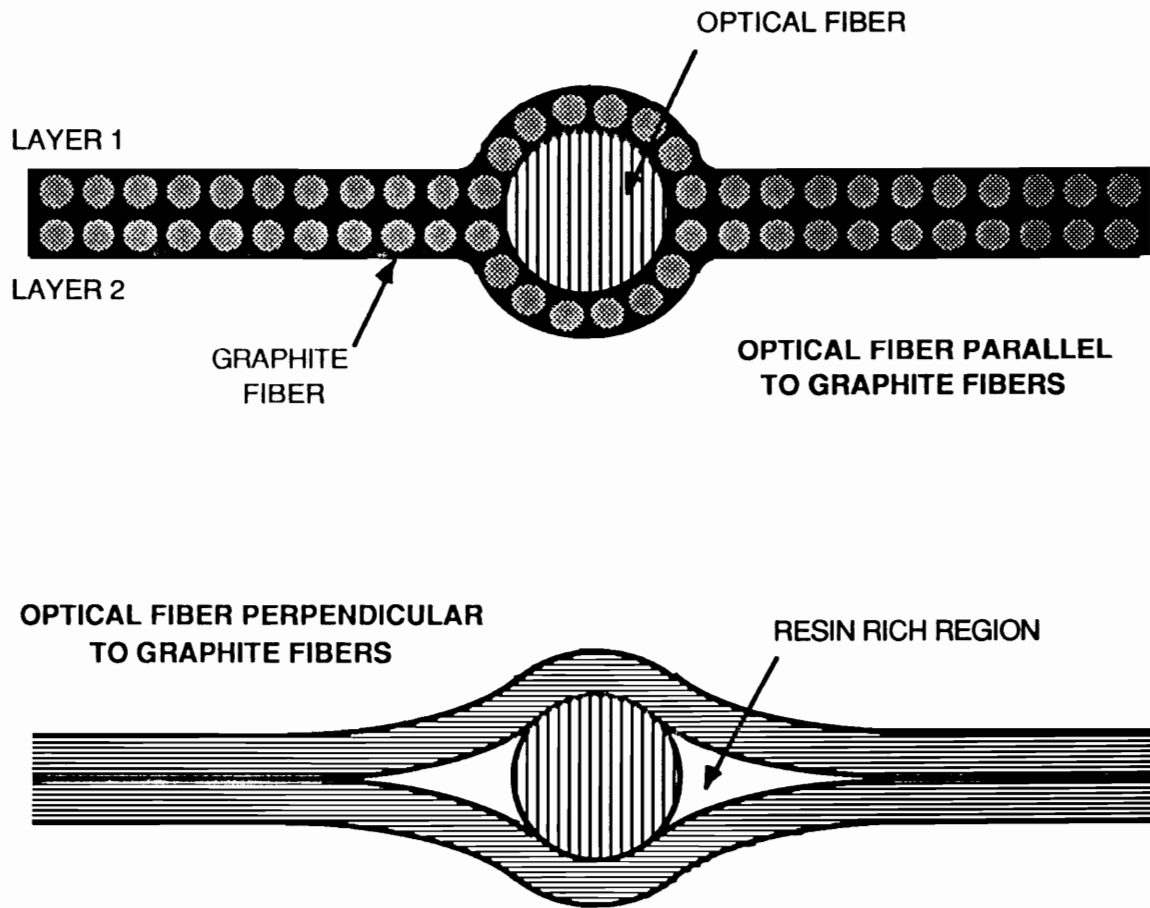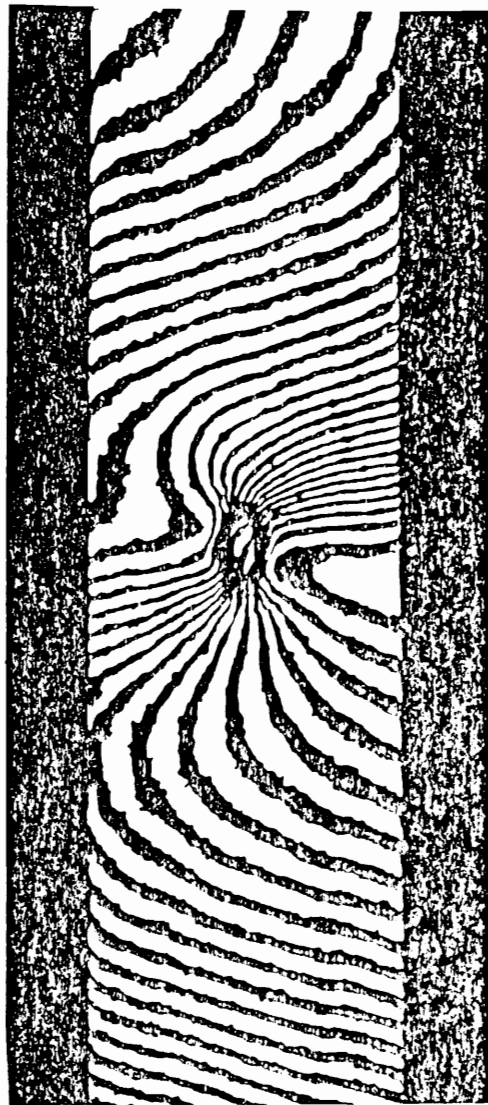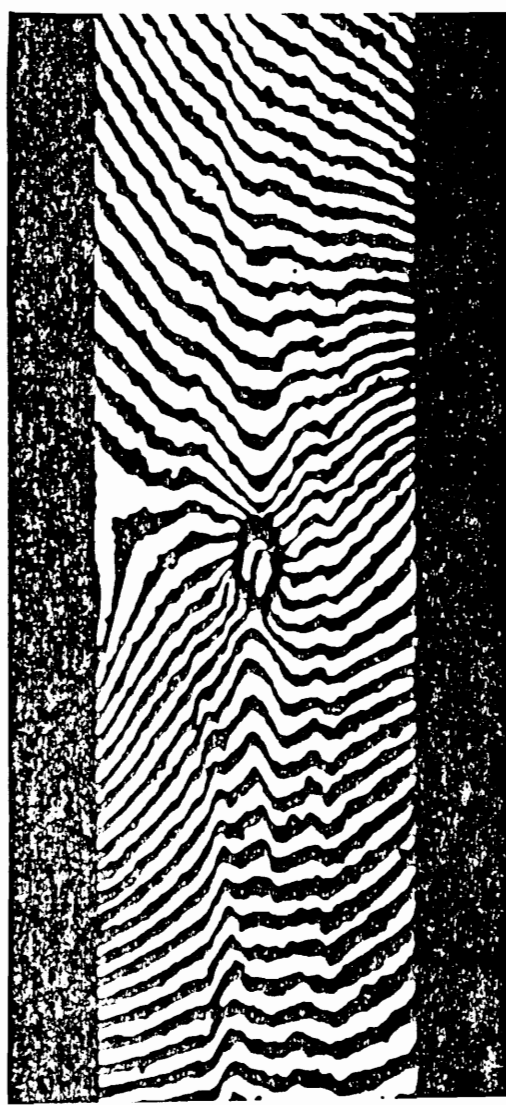
Figure 2.1. Representation of possible interface conditions between an embedded optical fiber and internal composite plies a) optical fiber parallel to graphite fiber, and b) optical fiber perpendicular to graphite fibers.

(U)   (V)

Figure 2.2. Moire interferogram depicting the u and v displacement fields in a side view of an eight ply graphite/epoxy panel with an embedded optical fiber. Specimen was loaded axially to half the calculated failure load [44].
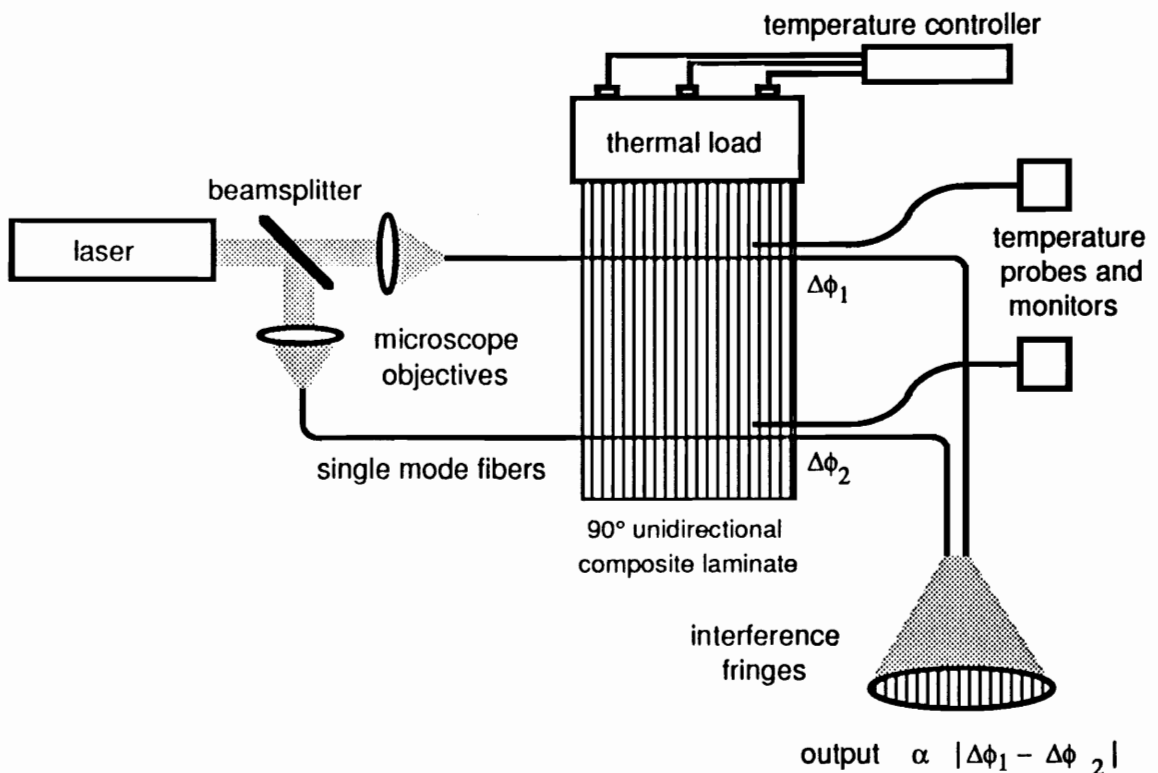
Figure 2.3. Fiber optic differential interferometric measurement of thermal flow in a 90° unidirectional composite laminate.
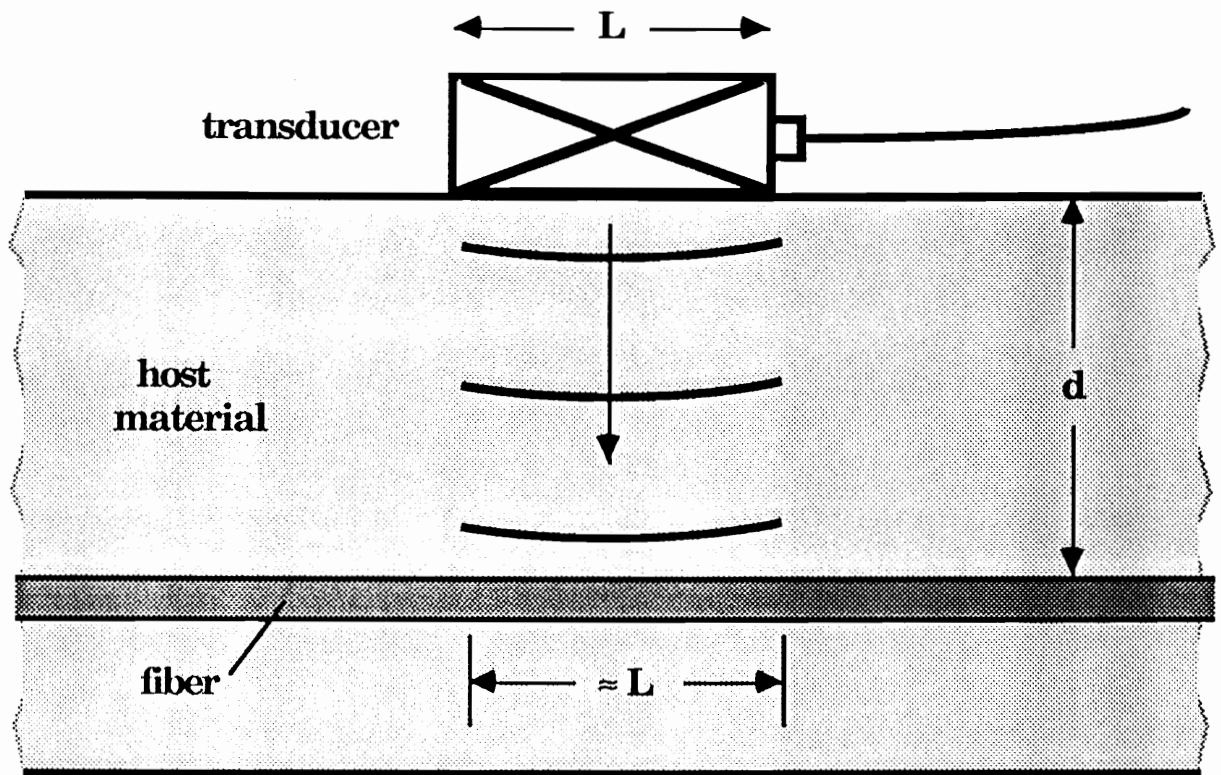
Figure 2.4. Schematic of an ultrasonic transducer insonifying an optical fiber embedded in a host material. Such a model is applicable to acousto-ultrasonics, and cure monitoring in particular. The modulus of the material can be inferred by measuring the attenuation of acoustic energy reaching the fiber as a function of cure.
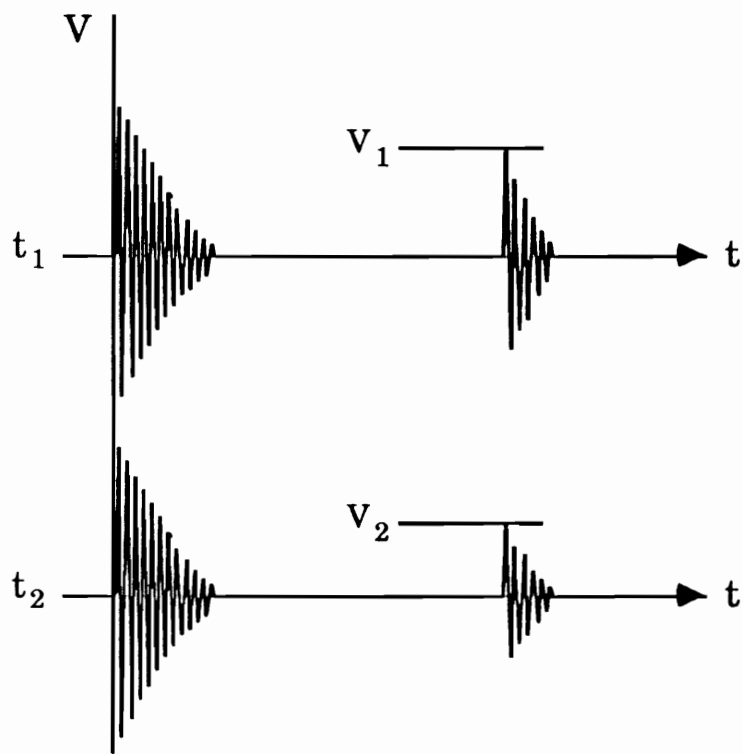
Figure 2.5. Possible sensor output for Figure 2.4 at two different times in the cure cycle. The first pulse in each trace represents the piezoelectrically transduced main bang, while the second pulse represents the optical response (not real data).
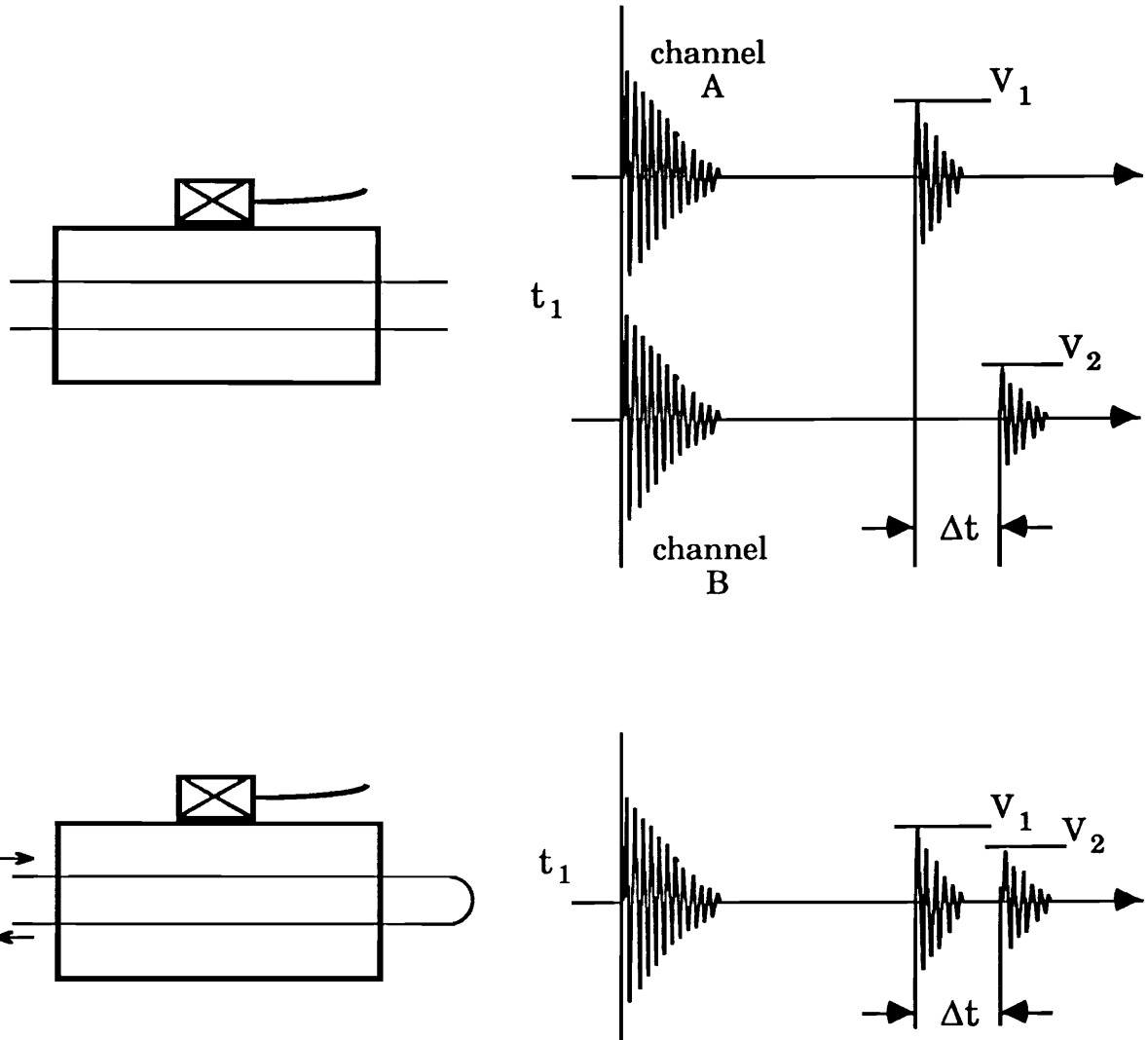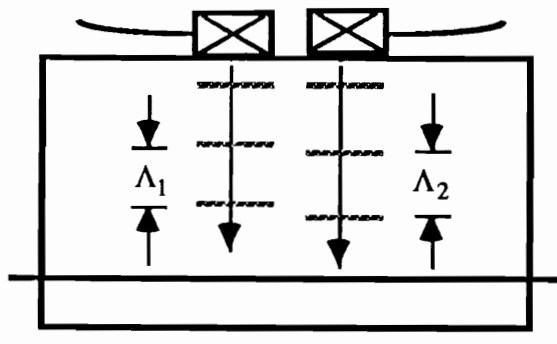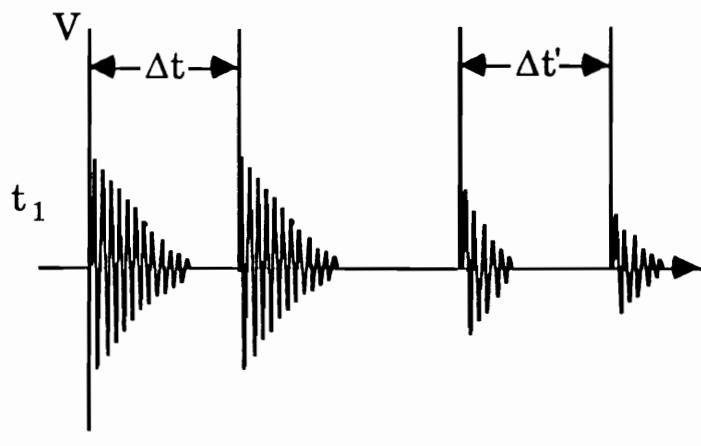
Figure 2.6. Two fibers could be embedded to yield both attenuation and velocity information as the sample cures. Alternatively, a single fiber could make two passes through the material.

(a)

(b)

Figure 2.7. a) Scheme for detection at two acoustic frequencies. (b) Possible output for the above. The sources are pulsed at times separated by Δt; the first two pulses represent piezoelectrically detected main bang signals, whereas the next two pulses would indicate optically detected strains in the material.
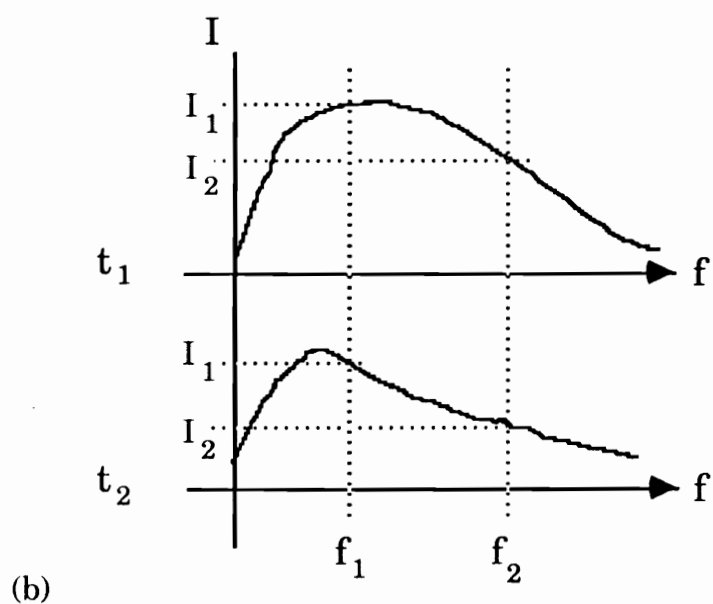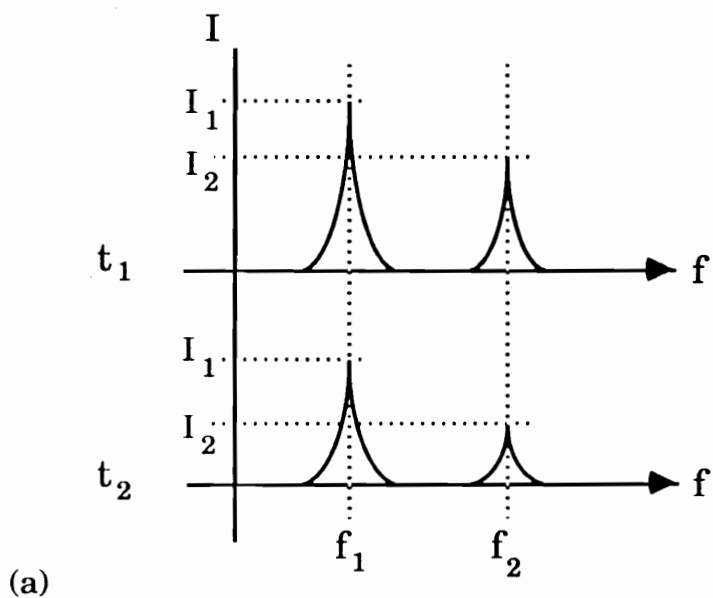
Figure 2.8 a) Example frequency spectrum associated with Figure 2.7b.
b) Example spectrum assuming a single broadband source.
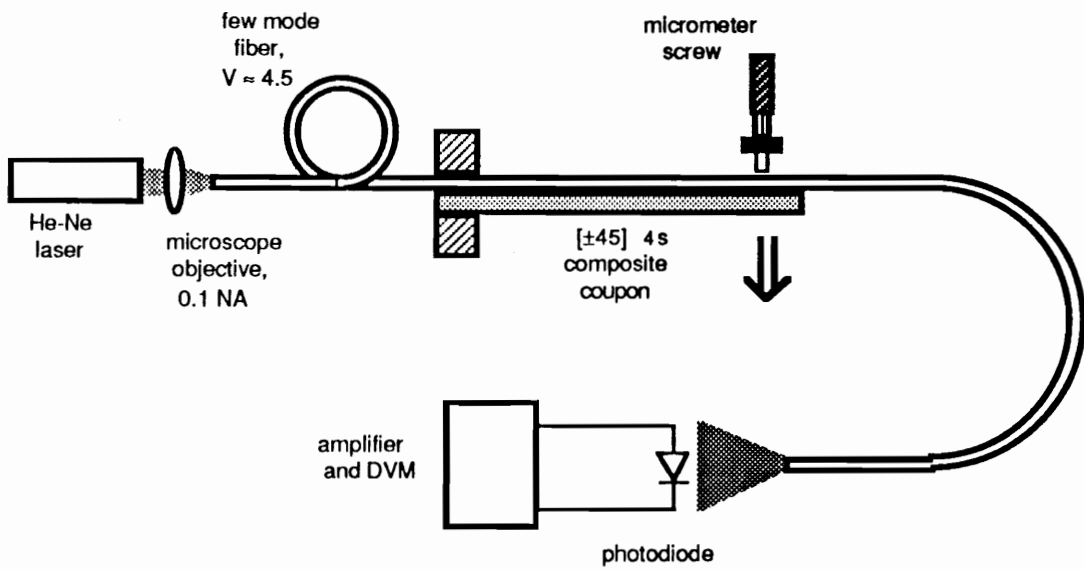
Figure 2.9b. Quasi-static strain measurement using few fiber sensor.

Intensity vs. Strain

few mode fiber on cantilevered beam
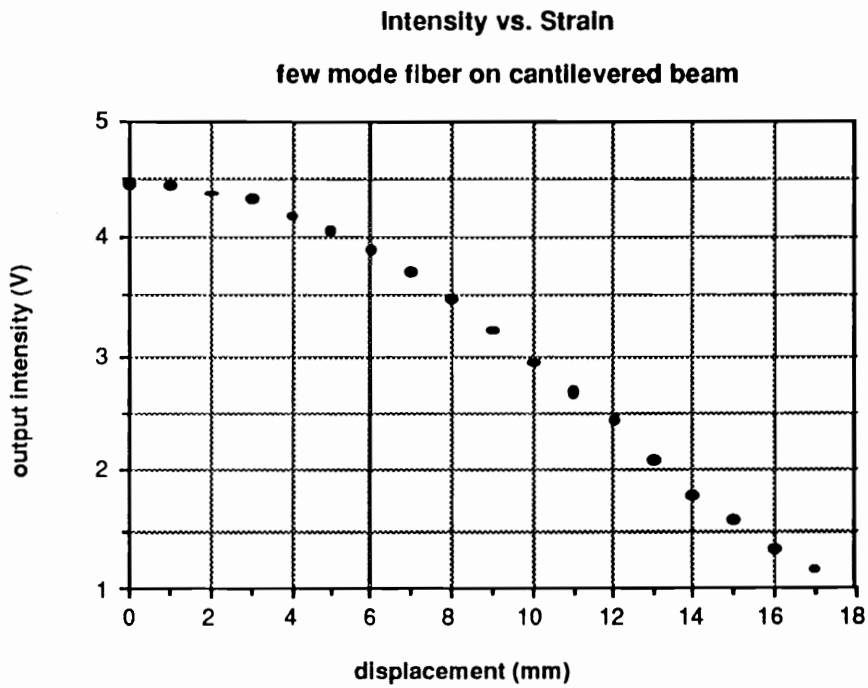
Figure 2.9b. Results of experiment outlined above (see text).
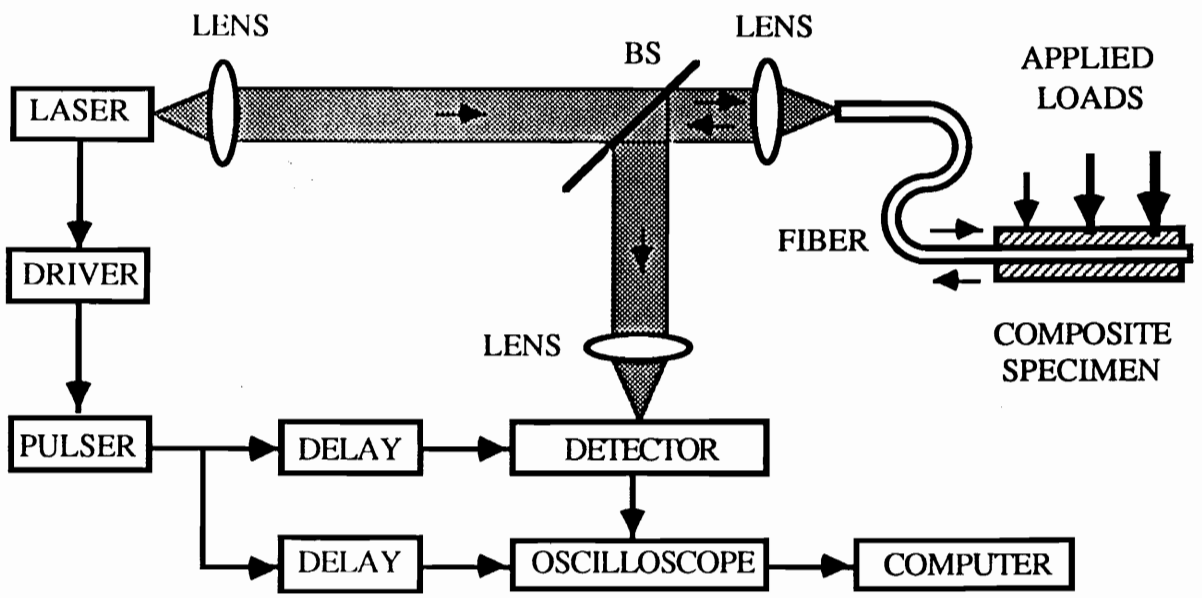
Figure 2.10a) Basic OTDR system used to measure strain due to loading.
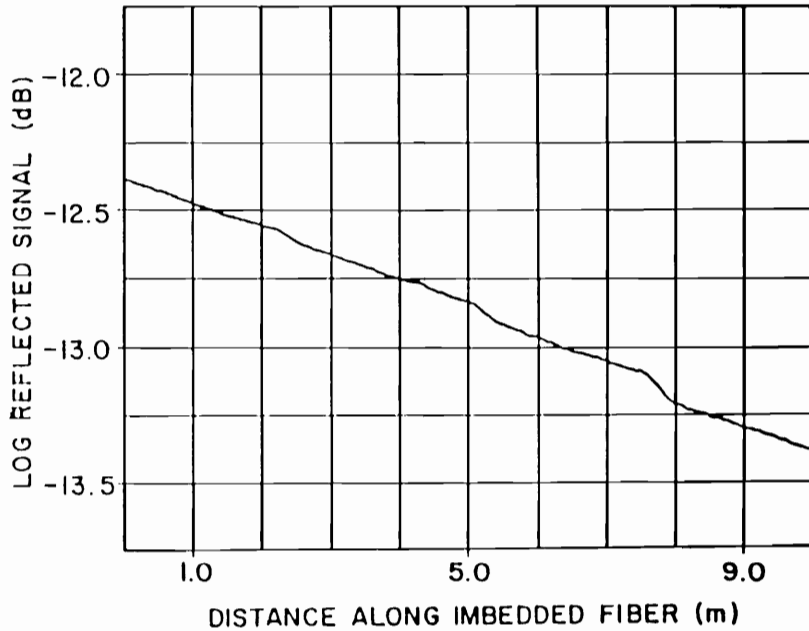
Figure 2.10b) Digitally averaged OTDR signal obtained for a composite specimen loaded at three locations along the fiber. Slope changes proportional to the respective loads (350, 700, and 1050 kPa) are observable at 2.2, 5.1, and 7.8 [65].
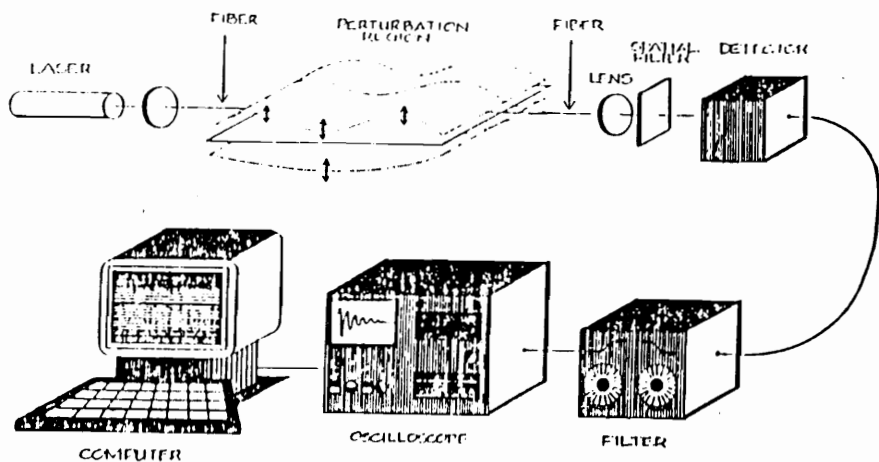
Figure 2.11a). Optical fiber modal domain sensing of mechanical vibrations. Experimental set-up [70].
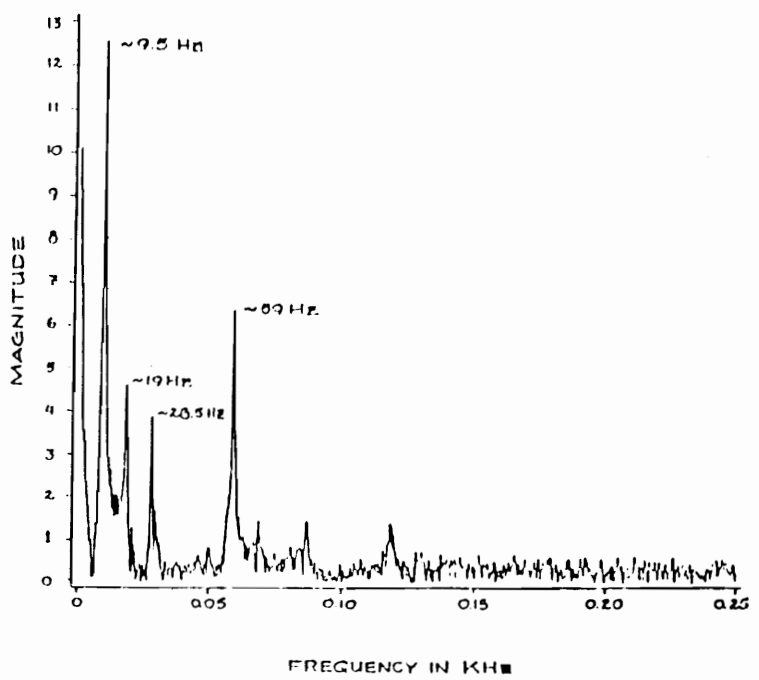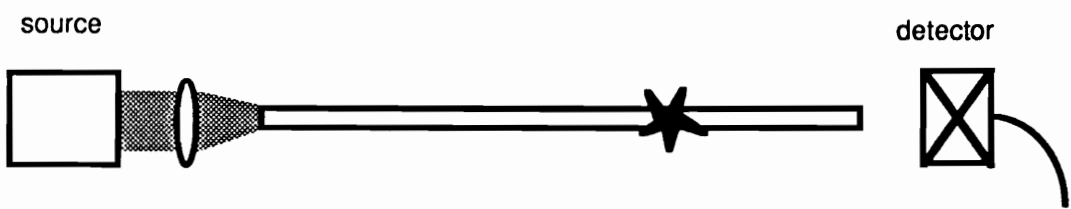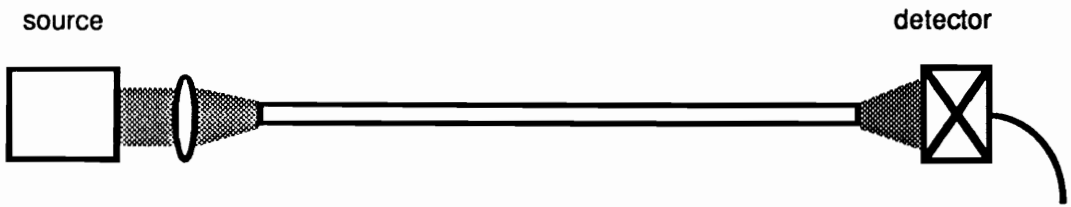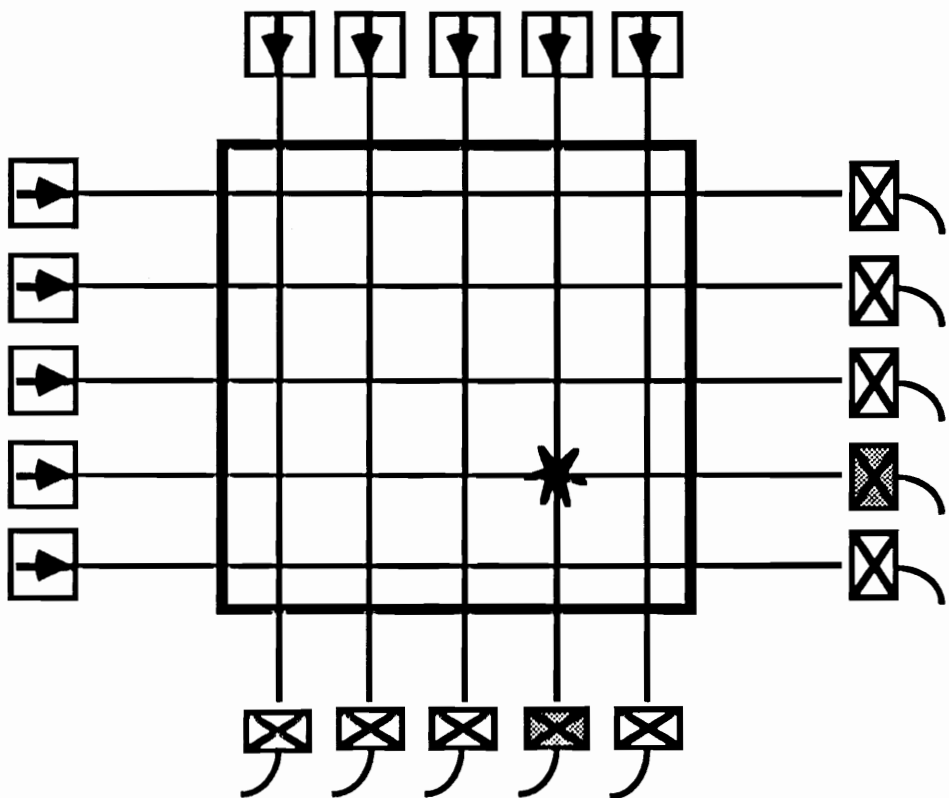
Figure 2.11b). Frequency spectrum of a fiber sensor attached to a vibrating space structure type beam [27].

Figure 2.12. a) Simple transmission interrupt sensor. b) Extension to two dimensions.
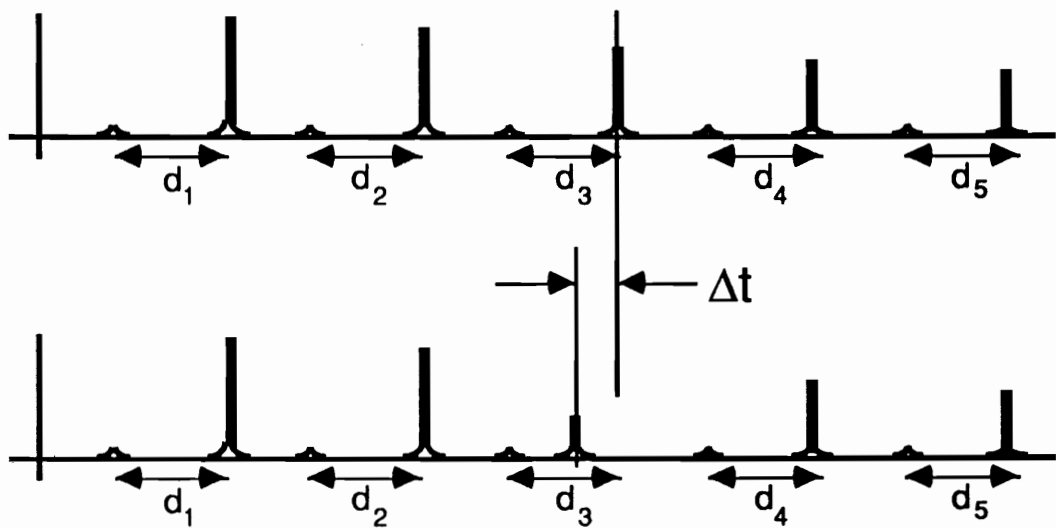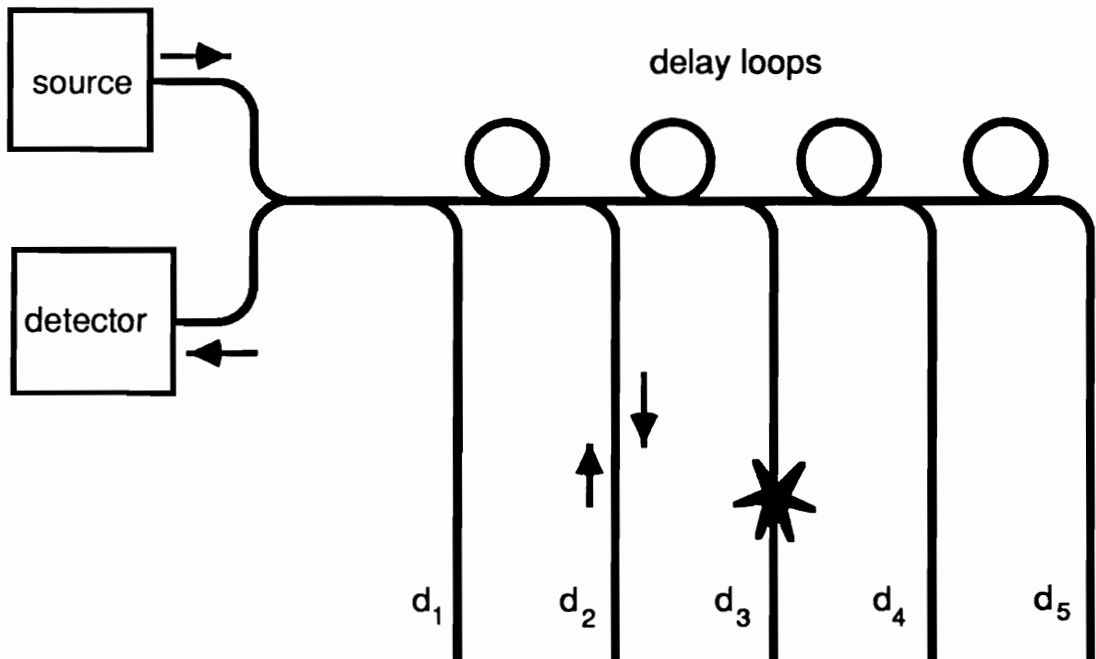
Figure 2.13. Scheme for using OTDR for detection of damage in structures. The location and severity of damage to the fibers could be inferred from the position in time and the amplitude of the backscattered trace.
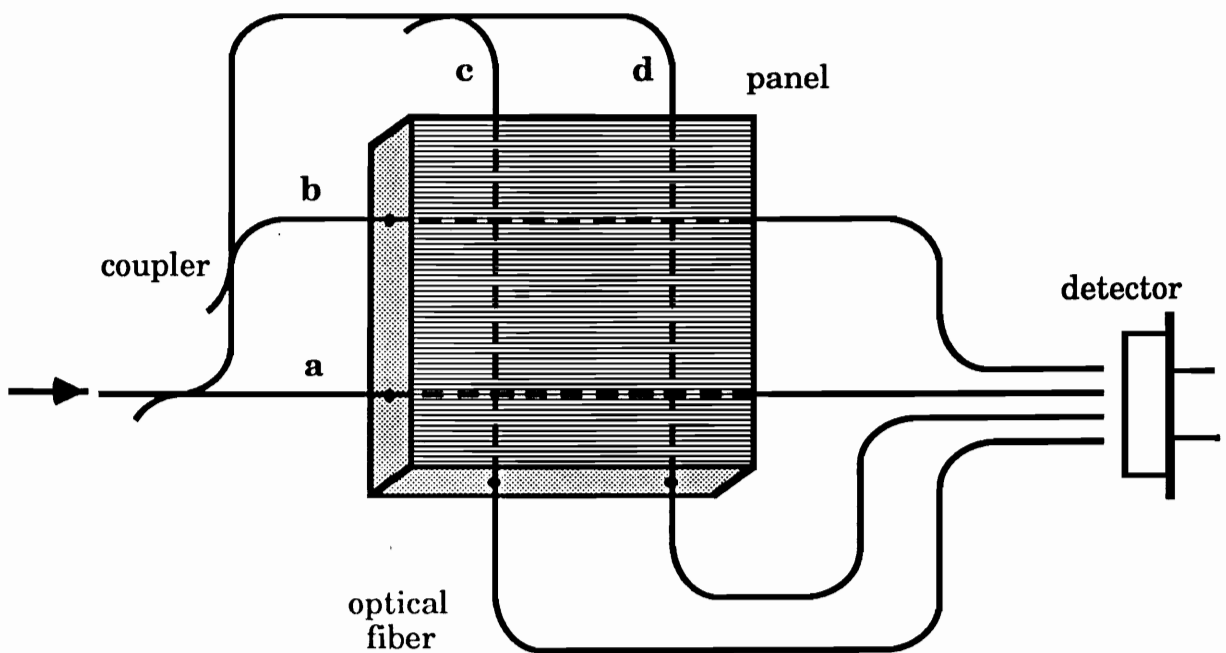
Figure 2.14a. Example of a scheme to optically process damage signals.
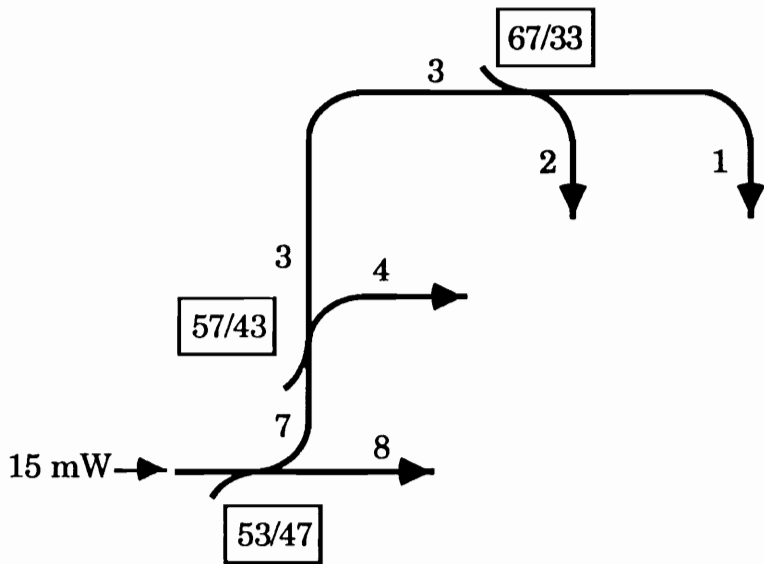
Figure 2.14b. Required coupling ratios in percent, and resulting output power of each fiber, assuming 15 mW input [81].

Table 2.1. Total detector output for each of the possible sixteen combinations of damaged fibers. Here, 0 means no through transmission, 1 means normal light transmission [81].

fibers				output
d	c	b	a	(mW)
0	0	0	0	0
0	0	0	1	1
0	0	1	0	2
0	0	1	1	3
0	1	0	0	4
0	1	0	1	5
0	1	1	0	6
0	1	1	1	7
1	0	0	0	8
1	0	0	1	9
1	0	1	0	10
1	0	1	1	11
1	1	0	0	12
1	1	0	1	13
1	1	1	0	14
1	1	1	1	15
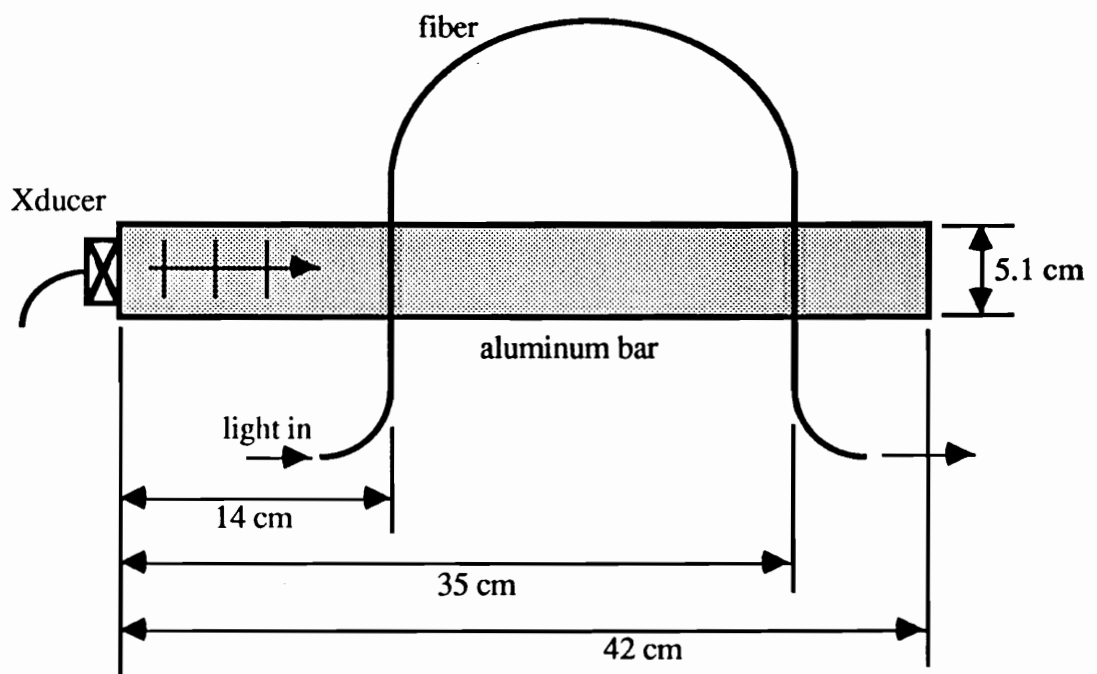
Figure 2.15. Set-up for detecting 2.25 MHz acoustic waves traveling through a metal bar, using a single mode fiber interferometer.
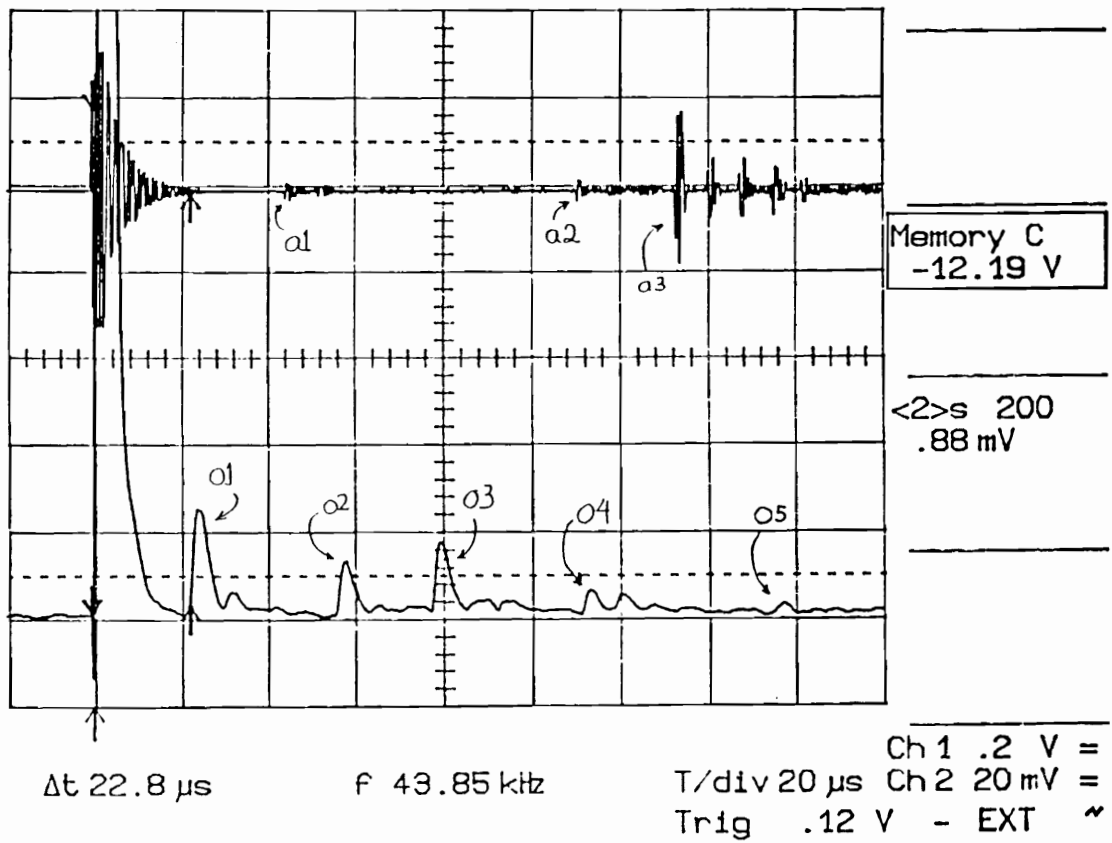
Figure 2.16. Piezoelectric (upper trace) and optical (lower trace) response to applied acoustic energy in the metal bar of Figure 2.15.

3.0 Principles of Modal Domain Sensing

In this section the necessary theoretical background for the use of optical fiber waveguides as phase sensing elements is developed. We begin with a brief review of the existence of modes in fibers, including basic fiber optic quantities and nomenclature. Next the expressions describing the interference of modes in fibers are developed. Interference between two single mode fiber outputs is described first, as a foundation for dual mode sensors. A discussion of the latter follows, with a treatment of both the LP_{01}/LP_{11} and the LP_{01}/LP_{02} mode combinations. Interference in highly multimode fibers is considered next, and a new expression for the output intensity distribution is derived.

3.1 Modes in Fibers

In the discussion which follows, we will consider exclusively the use of step index optical fibers, such as depicted in Figure 3.1. The fiber consists of a core of glass of radius a, having a refractive index n_1, surrounded by a cladding of glass of radius b, with index n_2; note from the figure that $n_1 > n_2$. These glasses are in intimate contact, and are generally inseparable and indistinguishable without special equipment. Their difference in index of refraction is finely controlled by the deposition of trace amounts of dopants to pure fused silica, either in the core or in the cladding. The degree of difference in indices is characterized by the parameter Δ, important in determining fiber performance, where Δ is defined such that

$$\Delta = \frac{n_1^2 - n_2^2}{2n_1^2} \approx \frac{n_1 - n_2}{n_1} , \qquad (3.1)$$

where the approximation applies when $n_1 \approx n_2$.

Though not shown, optical fibers are generally coated with a polymer jacketing. These coatings are designed to add mechanical stability to the fiber, and protect them from dirt and nicks which may act as crack initiation sites. However, as will be mentioned in the next section, they also may insulate the fiber from any straining mechanism, reducing its effectiveness.

The standard approach to describing the phenomenon of modes in a step index cylindrical fiber is outlined below. We start with the modified wave equation for the axial components of the electromagnetic field propagating in a fiber oriented along the positive z axis:

$$\frac{\partial^2 \psi_z}{\partial r^2} + \frac{1}{r}\frac{\partial \psi_z}{\partial r} + \frac{1}{r^2}\frac{\partial^2 \psi_z}{\partial \phi^2} + q^2 \psi_z = 0 . \tag{3.2}$$

Here ψ_z could be either E_z or H_z, and the cylindrical coordinates r, ϕ, and z have already been incorporated. The transverse components of E and H are determined directly once E_z and H_z are found, and will require that

$$q^2 = (k_0^2 n^2 - \beta^2) . \tag{3.3}$$

Here k_0 is the free space wave number, determined by $2\pi/\lambda_0$, where λ_0 is the free space wavelength of the optical radiation; $n = n_1$ in the core and $n = n_2$ in the cladding, and β is the modal propagation constant. At the outset we will note that β is restricted in its value by the wave number in the core and cladding; that is,

$$n_1 k_0 \geq \beta \geq n_2 k_0 . \tag{3.4}$$

Throughout the analysis, the dependance of ψ on z and time take the form $e^{j(\omega t - \beta z)}$, where ω is the angular frequency in the hundreds of terahertz.

Following the standard technique for solving (3.2), we apply the method of separation of variables, and assume that independent solutions can be written for ψ_z in terms of r and ϕ. Thus,

$$\psi_z(r,\phi) = R(r)\,\Phi(\phi) \ . \tag{3.5}$$

Applying this to (3.2), we arrive after some algebraic manipulation at two separate ordinary differential equations for ψ_z coupled by a constant ℓ. For ϕ we have

$$\frac{d^2\Phi(\phi)}{d\phi^2} + \ell^2\,\Phi(\phi) = 0 \ , \tag{3.6}$$

while for r we obtain

$$\frac{d^2R(r)}{dr^2} + \frac{1}{r}\frac{d\,R(r)}{dr} + \left[q^2 - \frac{\ell^2}{r^2}\right]R(r) = 0 \ . \tag{3.7}$$

If both sides of (3.6) are divided by r^2 and added to (3.7), agreement with (3.2) is reached as necessary.

Equations such as (3.6) have standard solutions of the form

$$\Phi(\phi) = A \sin \ell\phi + B \cos \ell\phi \ . \tag{3.8}$$

Noting that the cylindrical symmetry of the waveguide demands that $\Phi(\phi) = \Phi(\phi + 2\pi)$, then it becomes clear that ℓ is restricted to integer values.

Equation (3.7) is a form of Bessel's equation, having several independent solutions. The choice of which solutions apply is dictated by the fact that fields must be finite everywhere and must die to zero as r goes to infinity. The outcome of these physical arguments for the cases where $q^2 > 0$ (core) and $q^2 < 0$ (cladding) results in the combined solution of (3.2):

$$E_z = \begin{cases} A\,J_\ell(ur/a) \begin{pmatrix} \sin \ell\phi \\ \cos \ell\phi \end{pmatrix} & r < a \\[2em] B\,K_\ell(wr/a) \begin{pmatrix} \sin \ell\phi \\ \cos \ell\phi \end{pmatrix} & r > a \ , \end{cases} \tag{3.9}$$

where

$$u = k_0 a \sqrt{n_1^2 - (\beta/k_0)^2}$$

$$w = k_0 a \sqrt{(\beta/k_0)^2 - n_2^2}$$

(3.10)

and a is the fiber core radius. J_ℓ is the Bessel function of the first kind, and K_ℓ is the modified Bessel function of the second kind, both of order ℓ. Either the sine or the cosine term can be chosen in conjunction with the other factors as a solution, with other azimuthal possibilities being decomposed into these components.

Similarly, for H_z we have

$$H_z = \begin{cases} C\, J_\ell(ur/a) \begin{pmatrix} -\cos \ell\phi \\ \sin \ell\phi \end{pmatrix} & r < a \\[2em] D\, K_\ell(wr/a) \begin{pmatrix} -\cos \ell\phi \\ \sin \ell\phi \end{pmatrix} & r > a \;. \end{cases}$$

(3.11)

It can be shown that the signs of the ϕ dependent terms which appear in (3.11) are demanded by boundary conditions and the orthogonal relation between E_z and H_z. We are left with unknown amplitude coefficients A, B, C, D, and unknown β, the latter of which is determined in terms of a single constant by application of the boundary conditions. Final determination of the remaining constant can be made given specifications on the source power and input conditions.

Boundary conditions require that the tangential components of the electric and magnetic fields be continuous at r = a. For this geometry, it means

r < a		r > a
$E_z \big|_{r=a}$	$=$	$E_z \big|_{r=a}$
$E_\phi \big|_{r=a}$	$=$	$E_\phi \big|_{r=a}$
$H_z \big|_{r=a}$	$=$	$H_z \big|_{r=a}$
$H_\phi \big|_{r=a}$	$=$	$H_\phi \big|_{r=a}$

(3.12)

E_ϕ and H_ϕ are evaluated using the relations

$$E_\phi = \frac{-j}{q^2} \left(\frac{\beta}{r} \frac{\partial E_z}{\partial \phi} - \omega\mu_0 \frac{\partial H_z}{\partial r} \right) \tag{3.13}$$

and

$$H_\phi = \frac{-j}{q^2} \left(\omega\varepsilon_0 n^2 \frac{\partial E_z}{\partial r} + \frac{\beta}{r} \frac{\partial H_z}{\partial \phi} \right) , \tag{3.14}$$

which result from Maxwell's equations. Here ε_0 and μ_0 are the free space permittivity and permeability, respectively.

Equations (3.12) comprise a set of four simultaneous equations, which have a nontrivial solution provided that the system determinant equals zero. This determinant is usually expanded to form the characteristic or eigenvalue equation. For the exact formulation, the characteristic equation is complicated. Solutions are expressed in terms of the "vector" modes (so called since we are seeking solutions to the vector wave equation), that is, circularly symmetric TE and TM modes, and hybrid EH and HE modes. If the approximation of weak guidance is made, matters simplify considerably. Specifically, if it is assumed that core and cladding indices $n_1 \approx n_2$, or equivalently $\Delta \ll 1$, then the characteristic equation takes the form

$$\frac{J_\ell(u)}{u \, J_{\ell-1}(u)} + \frac{K_\ell(w)}{w \, K_{\ell-1}(w)} = 0 \qquad \ell = 0, 1, 2, \ldots \tag{3.15}$$

Solutions to (3.15) for β are generally derived numerically, with multiple values of β satisfying the equation for a given value of ℓ and a given set of fiber parameters n_1, n_2, a, and λ. That is, for specific values of the principal mode number ℓ, then m unique solutions result, where the mth solution will be referred to as the propagation constant of the $LP_{\ell m}$ mode. Evidently then, m is simply an integer greater than zero. For each of these values of ℓ and m, the value of β which solves the characteristic equation (3.15) is typically plotted against the normalized frequency V, where

$$V = k_0 a \sqrt{n_1^2 - n_2^2} \ . \tag{3.16}$$

As shown in Figure 3.2, it is also useful to plot the normalized propagation constant b along the ordinate, where

$$b = \frac{(\beta/k_0)^2 - n_2^2}{n_1^2 - n_2^2} \ . \tag{3.17}$$

With β determined, it is also possible to investigate the behavior of u and w, useful for later calculations. Figure 3.3 shows u and w normalized with respect to V, and plotted as a function of b. Note that the maximum value of both u and w is in fact V, while the minimum is zero. Furthermore, it can be shown analytically that at the median value of possible propagation constants, or when b = 0.5, u and w intersect, both taking the value of $V/\sqrt{2}$.

When the fields which result from the solution of equation (3.15) are expressed in rectangular components, it is seen that the electric field is either directed along x or along y, meaning they are linearly polarized. For this reason, these modes are generally referred to as $LP_{\ell m}$ modes. Furthermore, in addition to their counting and naming utility, the subscripts ℓ and m also carry geometrical significance; that is, the final intensity pattern of the mode will display 2ℓ peaks in the azimuthal direction (around ϕ), while the number of peaks in the radial direction in the core will be given by m.

Finally then, general field expressions for the transverse components x and y can be written as

$$\vec{E}_t = \begin{cases} A_{\ell m} \left[\dfrac{J_\ell\left(\dfrac{u_{\ell m} r}{a}\right)}{J_\ell(u_{\ell m})} \right] \begin{pmatrix} \sin \ell\phi \\ \cos \ell\phi \end{pmatrix} \exp\left[j(\omega t - \beta_{\ell m} z + \psi_{\ell m}) \right] \begin{pmatrix} \hat{a}_x \\ \hat{a}_y \end{pmatrix} & r < a \\[30pt] A_{\ell m} \left[\dfrac{K_\ell\left(\dfrac{w_{\ell m} r}{a}\right)}{K_\ell(w_{\ell m})} \right] \begin{pmatrix} \sin \ell\phi \\ \cos \ell\phi \end{pmatrix} \exp\left[j(\omega t - \beta_{\ell m} z + \psi_{\ell m}) \right] \begin{pmatrix} \hat{a}_x \\ \hat{a}_y \end{pmatrix} & r > a \end{cases} \tag{3.18a}$$

and

$$\vec{H}_x = Y_{\ell m} |\vec{E}_y| \hat{a}_x \ ,$$

$$\vec{H}_y = Y_{\ell m} |\vec{E}_x| \hat{a}_y \ ,$$

(3.18b)

where the subscript t refers to either x or y, $A_{\ell m}$ is the generalized amplitude coefficient (different from the A in equation (3.9) above), the propagation constant for each mode has been distinguished, and a random phase factor $\psi_{\ell m}$ for each mode has been included for the sake of generalization. Also, $\hat{a}_x$ and $\hat{a}_y$ are unit vectors in the x and y directions, and $Y = (\beta/k_0) \sqrt{\varepsilon_0/\mu_0}$ is the admittance of the guide,

Modes involving $\cos(\ell\phi)$ are often referred to as even modes, while those involving $\sin(\ell\phi)$ are called odd modes. Thus, for values of ℓ and m, four distinct cases result from the four possible combinations of even, odd, x-polarized, and y-polarized choices. Being all solutions to the same characteristic equation, these modes are deemed degenerate, though it is important to note that this does not imply their field distributions are equal. Also, it is clear that when $\ell = 0$, azimuthal dependence is eliminated, so that LP_{0m} modes have only a two-fold degeneracy arising from the two orthogonal polarization states.

It might be noted that it is possible to derive the characteristic equation (3.15) directly, by starting with the scalar wave equation. The resulting LP modes are thus referred to as "scalar" modes. These differ from the modes which result from the exact characteristic equation, sometimes called "vector" modes, in that they are based on an approximation, namely that $\Delta \ll 1$. It has been shown that equations (3.15) and (3.18) lead, respectively, to propagation constants and field solutions which are within one percent of the exact solutions when $\Delta < 0.1$ [92], which is commonly true.

The LP modes above can also be considered as approximately equal to linear combinations of the exact modes. That is, it can be shown that the characteristic equations for $HE_{\ell+1,m}$ modes ($\ell > 0$) and $EH_{\ell-1,m}$ modes have the same form as equation (3.15). Similarly, TE_{0m}, TM_{0m}, and HE_{2m} modes

are seen to have the same characteristic equations, again meaning that these two groups of modes are degenerate to within the approximation of $\Delta \ll 1$. In fact, the four-fold degeneracy seen in the case of these vector modes is merely an alternate explanation for the four-fold degeneracy in the LP modes.

It is vital to realize that the various exact modes in each group above are not precisely degenerate. Thus they have slightly different propagation constants and phase velocities, leading to an evolving phase difference as they travel down the guide. The intensity of a single LP mode then appears to change periodically as the constituent vector modes move in and out of phase. Not maintaining a constant power distribution along z, these modes defy the definition of a mode, and so the LP modes are often called "pseudo-modes." In fact, it is not the total intensity which changes along z (in which case conservation of energy may be violated), but rather energy oscillates between the two orthogonal polarization states. This does not apply to the LP_{0m} modes however, which are true modes since they consist only of HE_{1m} modes. The relationship between the vector modes and the scalar modes is also shown schematically on the plot of β versus V in Figure 3.2.

3.2 Interference of Modes -- Two Single Mode Fiber Outputs

We now turn to the interference between two propagating modes. In this section we treat the case where interference occurs between the outputs of two single mode fibers. In the following section, expressions for the interference between the modes propagating in a dual mode fiber are derived. Once this formalism is established, an understanding of the interference between modes in a highly multimode fiber is pursued.

Single mode fiber interferometers may take one of several forms, including the Mach-Zehnder, Fabry-Perot, Michelson, and Sagnac interferometers. Because of its relative ease in application, the Mach-Zehnder form is often used to investigate strain in structures, and will be

the sensor which is analyzed here. As described in Figure 3.4, the most basic set-up in a practical situation consists of two single mode fiber optic couplers (usually fused biconical taper types) and a specimen containing a length of embedded or attached single mode fiber. Monochromatic light is injected into one of the input ports of the first coupler, and is split into two portions. One of these passes into the sensor fiber, used to measure the disturbance under investigation, while the other traverses a reference arm.

The coherence length of the optical source is assumed long enough to ensure that interference will occur between these two portions when they are recombined in the second coupler. Light reaching the output ports is proportional in intensity to the phase difference between the two portions entering the coupler. It is amplitude modulated by any disturbance which strains either of the fibers, implying that the output may be used to monitor the perturbation. The modulation depth depends on the amplitudes of the waves input to 1 and 2, with the maximum occurring when the amplitudes are equal. In practical sensors, phase compensation measures are often taken to hold the interferometer in quadrature, since the output tends to drift due to random thermal fluctuations, etc. However, such procedures are not essential to the analysis, and so will not be considered here.

We consider the optical fields propagating in segments 1 and 2 above as having a single polarization state, and without loss of generality, we assign it such that the electric field is directed along x. (Recall that no interference occurs between orthogonal polarizations, and that any field vector may be broken into two orthogonal polarizations.) Taking the $e^{-j\omega t}$ dependence to be common to all fields, we may write the electric field distributions for fibers 1 and 2 as

$$\vec{E}_1 = A_1 f_0 e^{-j(\beta_1 z_1 - \psi_1)} \hat{a}_x = E_1 \hat{a}_x$$

$$\vec{E}_2 = A_2 f_0 e^{-j(\beta_2 z_2 - \psi_2)} \hat{a}_x = E_2 \hat{a}_x \ ,$$

(3.19)

where in general,

$$
f_{\ell m} =
\begin{cases}
\dfrac{J_\ell\left(\dfrac{u_{\ell m} r}{a}\right)}{J_\ell(u_{\ell m})} & r < a \\[2em]
\dfrac{K_\ell\left(\dfrac{w_{\ell m} r}{a}\right)}{K_\ell(w_{\ell m})} & r > a
\end{cases}
\tag{3.20}
$$

Here again it is implicit that u and w, as defined in (3.10), are functions of either β_1 or β_2 (more formally termed β_{01} and β_{11}), and the orthogonal H components are related as in (3.18). Also, z_1 and z_2 are the propagation distances, while ψ_1 and ψ_2 are the initial random phase angles of the two single propagating modes. Although it is not strictly necessary to the formulation to assume equal propagation constants, we do so by noting that for identical single mode fibers $\beta_1 = \beta_2$. Specifically then, a single value of u and w result. After combining in the second coupler, the total fields can then be expressed as

$$
\begin{aligned}
\vec{E}_x &= (E_1 + E_2)\,\hat{a}_x \\
\vec{H}_y &= (Y_1 E_1 + Y_2 E_2)\,\hat{a}_y \; .
\end{aligned}
\tag{3.21}
$$

The intensity resulting from the combination of these two modes is calculated as the time average of the real part of the z component of the complex Poynting vector. That is,

$$
I = \frac{1}{2} \operatorname{Re}\left\{ (\vec{E}_x \times \vec{H}_y^{\,*}) \cdot \hat{a}_z \right\} \; .
\tag{3.22}
$$

Because of the mutual orthogonality of $\vec{E}_x$, $\vec{H}_y$, and $\hat{a}_z$, the intensity becomes

$$
\begin{aligned}
I &= \frac{1}{2} \operatorname{Re}\left\{ Y(E_1 + E_2)(E_1^{\,*} + E_2^{\,*}) \right\} \\
&= \frac{1}{2} \operatorname{Re}\left\{ Y(E_1 E_1^{\,*} + E_2 E_2^{\,*} + E_1 E_2^{\,*} + E_2 E_1^{\,*}) \right\} \; .
\end{aligned}
\tag{3.23}
$$

In this expression, it has been assumed for simplicity that the admittances are equal since it can be shown that $Y_1 \approx Y_2$ even for fibers with slightly different propagation constants. Substituting the field distributions from (3.19) we have,

$$I = \frac{1}{2} \text{Re} \{ Y [A_1^2 f_0^2 + A_2^2 f_0^2 + A_1 A_2 f_0^2 e^{-j(\beta_1 z_1 - \psi_1)} e^{+j(\beta_2 z_2 - \psi_2)} \qquad (3.24)$$
$$+ A_1 A_2 f_0^2 e^{+j(\beta_1 z_1 - \psi_1)} e^{-j(\beta_2 z_2 - \psi_2)} \} \ .$$

Next we combine terms and rearrange the exponentials of the cross term. If we consider that fiber 2 is a reference and therefore does not change with perturbations applied to fiber 1, then $\beta_2 z_2$ is a constant which can be added to $\psi_1 - \psi_2$ to form a composite phase term ψ. Thus

$$I = \frac{1}{2} \text{Re} \{ Y [A_1^2 f_0^2 + A_2^2 f_0^2 + A_1 A_2 f_0^2 [e^{-j(\beta_1 z_1 - \psi)} + e^{+j(\beta_1 z_1 - \psi)}] \} \ .$$
$$(3.25)$$

Applying Euler's identity and taking the real part,

$$I = \frac{1}{2} Y f_0^2 [A_1^2 + A_2^2 + 2A_1 A_2 \cos (\beta_1 z_1 - \psi)] \ . \qquad (3.26)$$

As mentioned above, the maximum amplitude modulation occurs if $A_1 = A_2 = A$, in which case (3.26) becomes

$$I = \begin{cases} YA^2 \left[\dfrac{J_0^2(ur/a)}{J_0^2(u)} \right] [1 + \cos (\beta_1 z_1 - \psi)] & r < a \\[4mm] YA^2 \left[\dfrac{K_0^2(wr/a)}{K_0^2(w)} \right] [1 + \cos (\beta_1 z_1 - \psi)] & r > a \ . \end{cases} \qquad (3.27)$$

From equation (3.27) we can gain an understanding of the type of output one might expect from a single mode fiber interferometer. First we notice that the intensity has a spatial dependence proportional to the first order Bessel function, that is, a single, azimuthally symmetric lobe which is

centrally located. The peak intensity varies between $2YA^2/J_0{}^2(u)$ and 0, depending on the value of the phase term in parentheses, and is static in the event that no perturbation occurs. On the other hand, if a disturbance is experienced by fiber 1 such that either β_1 or z_1 change, then the total intensity changes accordingly (note that ψ is set by initial conditions and does not vary with disturbance).

Finally, defining the phase term $\theta = \beta_1 z_1 - \psi$ and consolidating the amplitude coefficient to I_0 , where I_0 is half the total optical power entering the sensor, we have

$$I = I_0 [\, 1 + \cos\theta\,] \ . \tag{3.28}$$

The intensity distribution for the static case is represented in Figure 3.5, and a plot of the intensity at $r = 0$ as a function of θ appears in Figure 3.6.

3.3 Interference in Dual Mode Sensors

Next we consider the case of a single mode fiber being operated below its cut-off wavelength so that the two lowest order modes propagate. For most fibers, this limits the analysis to focus on the LP_{01} and LP_{11} modes, though this will be extended later to include other scalar modes. In the sensor formed with such dual mode fiber, a single strand of optical fiber propagating coherent light is made to interact with a parameter of interest. As the two modes traverse the fiber, it will be seen that their differing propagation constants give rise to an accumulating phase difference which is again related to the distance traveled, as well as the difference in their values of β. After deriving an expression for the output intensity for the dual mode sensor, its advantages and disadvantages with respect to the single mode interferometer will be discussed. Also, a few remarks will be made on the effect on the analysis of approximating nondegenerate vector mode combinations with pseudo-modes.

3.3.1 The LP_{01} and LP_{11} Mode Combination

Following the same line of reasoning as for the single mode case, we write the electric field expressions for the two modes:

$$LP_{01}: \qquad \vec{E}_0 \;=\; A_0 f_0 \, e^{-j(\beta_0 z - \psi_0)} \, \hat{a}_x$$

$$LP_{11}: \quad \left\{ \begin{array}{l} \vec{E}_1^{\,e} \;=\; A_1 f_1 \cos\phi \; e^{-j(\beta_1 z - \psi_1)} \, \hat{a}_x \\[2ex] \vec{E}_1^{\,o} \;=\; B_1 f_1 \sin\phi \; e^{-j(\beta_1 z - \psi_1)} \, \hat{a}_x \;\; . \end{array} \right. \qquad (3.29)$$

In this case we must account for both the even and odd LP_{11} modes, both being valid solutions to the characteristic equation (3.15). Note that the only difference between them is the possibility of a different amplitude coefficient, and the starting point for the oscillating azimuthal dependence. As before, the corresponding modes polarized along y will not be considered here. Again the total fields can be expressed as the sum of the individual mode fields, or

$$\vec{E}_x \;=\; \{\, E_0 + E_1^{\,c} + E_1^{\,o} \,\} \, \hat{a}_x$$

$$\vec{H}_y \;=\; \{\, Y_0 E_0 + Y_1 E_1^{\,c} + Y_1 E_1^{\,o} \,\} \, \hat{a}_y \;\; . \qquad (3.30)$$

At all points along the fiber the modes interfere. The z component of their combined intensity is calculated as

$$I \;=\; \tfrac{1}{2} \, \mathrm{Re}\,\{\, Y\,(E_0 + E_1^{\,c} + E_1^{\,o})\,(E_0^{\;*} + E_1^{\,c*} + E_1^{\,o*}) \,\}$$

$$=\; \tfrac{1}{2} \, \mathrm{Re}\,\{\, Y\,[\, E_0 E_0^{\;*} + E_1^{\,c} E_1^{\,c*} + E_1^{\,o} E_1^{\,o*} \qquad\qquad (3.31)$$

$$+\; E_1^{\,o} E_1^{\,c*} + E_1^{\,c} E_1^{\,o*} + E_0^{\;*} E_1^{\,c} + E_0 E_1^{\,c*} + E_0^{\;*} E_1^{\,o} + E_0 E_1^{\,o*} \,]\,\} \;\; .$$

In this expression, it has been assumed that $Y_0 = Y_1 = Y$. Although this is not strictly true, since Y_0 and Y_1 contain different propagation constants β_0 and β_1 respectively, because of the bounds on $\beta_{\ell m}$ expressed by the relation of equation (3.4), we assume that $Y_{\ell m}$ varies little from mode to mode, especially with respect to other factors contributing to the change in mode amplitude. Thus we will take $Y_{\ell m} = Y = n\sqrt{\varepsilon_0/\mu_0}$ where n is given as the average value of the refractive index. Substituting the field distributions from (3.29) we have,

$$I = \frac{1}{2} \text{Re} \{ Y [A_0^2 f_0^2 + A_1^2 f_1^2 \cos^2\phi + B_1^2 f_1^2 \sin^2\phi + 2A_1 B_1 f_1^2 \sin\phi \cos\phi$$
$$+ A_0 A_1 f_0 f_1 \cos\phi (e^{-j(\tilde{\beta}z - \tilde{\psi})} + e^{+j(\tilde{\beta}z - \tilde{\psi})}) \qquad (3.32)$$
$$+ A_0 B_1 f_0 f_1 \sin\phi (e^{-j(\tilde{\beta}z - \tilde{\psi})} + e^{+j(\tilde{\beta}z - \tilde{\psi})})] \} \; ,$$

where the difference between the two mode propagation constants is defined as $\tilde{\beta} = \beta_0 - \beta_1$ and the initial phase difference is $\tilde{\psi} = \psi_0 - \psi_1$. Here the tilda is reserved to designate "the static difference between" for the modes involved. If the Euler identity is applied, and the real part taken, a simpler form results, making the r and ϕ dependence more obvious:

$$I = \frac{Y}{2} \{ |A_0|^2 f_0^2 + |A_1|^2 f_1^2 \cos^2\phi + |B_1|^2 f_1^2 \sin^2\phi$$
$$+ 2 |A_1| |B_1| f_1^2 \sin\phi \cos\phi \qquad (3.33)$$
$$+ 2 |A_0| |A_1| f_0 f_1 \cos\phi \cos(\tilde{\beta}z - \tilde{\psi})$$
$$+ 2 |A_0| |B_1| f_0 f_1 \sin\phi \cos(\tilde{\beta}z - \tilde{\psi}) \} \; .$$

The first three terms are the self-interference intensities in the LP_{01} and the even and odd LP_{11} modes, respectively. It is clear that the LP_{01} mode intensity is azimuthally symmetric, leading to a central lobe, while the LP_{11} modes give rise to lobe peaks at $\phi = n\pi/2$ for integer n. The remaining terms arise directly as a consequence of interference between modes. The fourth term can be rewritten as $|A_1| |B_1| f_1^2 \sin(2\phi)$, showing

that the intensity contains a contribution which reaches maxima at $\pi/4$ and $5\pi/4$, and minima at $3\pi/4$ and $7\pi/4$. These terms are all static with respect to disturbances.

The last two terms above are especially important for the performance of a sensor based on modal interference. We see again an antisymmetric contribution to intensity in the azimuthal direction, this time with maxima for the two terms at 0 and $\pi/2$, and minima at π and $3\pi/2$. Note in addition, that the strength of these contributions is modulated by the common $\cos(\tilde{\beta}z - \tilde{\psi})$, which significantly contains both $\tilde{\beta}$ and z. For one, it says that disturbances which alter $\tilde{\beta}$, such as bending or pressure on the fiber, cause phase changes in this factor. It follows that the maximum of these terms moves about in the output field with the disturbance. It also says that as power flows along z, the peaks of intensity shift in ϕ around the center axis. The spatial period of this oscillation, $L = \lambda_0/\Delta n$, is known as the beat length between the two modes, and is a direct result of their differing phase velocities or, alternatively, propagation constants. Here Δn is the effective phase index difference between the modes [93]. Furthermore, if the length z through which the modes travel is modulated by elongating or compressing the fiber, or if β changes, it will be manifested as an exchange of power among the output intensity lobes.

Often equation (3.33) is further simplified by making the reasonable assumption that power is injected in such a way that B_1 (or A_1) = 0. When the definition for f in equation (3.20) is applied, the intensity pattern from the fiber core can be described by

$$
I = \frac{Y}{2}\left[A_0^2 \frac{J_0^2(u_0 r/a)}{J_0^2(u_0)} + A_1^2 \frac{J_1^2(u_1 r/a)}{J_1^2(u_1)} \cos^2\phi \right.
$$
$$
\left. + 2 A_0 A_1 \frac{J_0(u_0 r/a)}{J_0(u_0)} \frac{J_1(u_1 r/a)}{J_1(u_1)} \cos\phi \cos(\tilde{\beta}z - \tilde{\psi}) \right] . \tag{3.34}
$$

The pattern in this case consists of two lobes around ϕ instead of four; a representation of what might be seen emerging from a fiber under typical

conditions appears in Figure 3.7. Figure 3.8 shows the individual terms of (3.34), including the sum of the first two, which are unaffected by strain and are therefore considered a background term. For these plots, $\theta = \tilde{\beta}z - \tilde{\psi}$ is taken to be zero, as is the value of ϕ, meaning we are looking along the x-axis as shown in Figure 3.7.

When strain is applied, both β and z change, altering the value of the cross term at every point. The result is that the lobe of intensity appears to shift across the center axis, as seen in Figure 3.9, as recent publication confirms [94]. If a detector is placed at a particular value of r/a, it would record an oscillating intensity as a function of strain. The modulation depth is in part determined by the position of the detector. For example, it can be shown that for the particular values of β_0 and β_1 used in this model, maximum modulation depth occurs at the peak position when $\theta = 0$, or $r/a \approx 0.42$. However, one can guess from equation (3.34) that this position depends on the proportion of power propagating in each mode, as becomes evident in Figure 3.10. Finally, when the value of the intensity is plotted for increasing strain, Figure 3.11 results. The decreasing peak arises from the fact that β_0 and β_1 *change* with strain (as will be discussed at length in the next chapter) and because the propagation constants appear in Y, u, and w.

Laboratory demonstration of equation (3.34), and Figures 3.9 and 3.11 is extremely straightforward to perform. Experimental confirmation of the usefulness of strain sensors based on LP_{01} and LP_{11} interference was demonstrated first by Layton and Bucaro, who used a dual mode fiber sensor to detect acoustic waves in water [8]. As will be shown, sensors based on this mechanism are predictably two to three orders of magnitude less sensitive than conventional two fiber interferometers, but they offer the advantages of stability and simplicity, while retaining high sensitivity relative to many other fiber optic sensor types. That is, because modal sensing is a differential technique where the two light paths are within the same fiber, random disturbances to the fiber such as thermal fluctuations affect both modes, unlike the two-fiber interferometer. Though the degree to which they influence the modes is different, the net effect can generally be considered small, resulting in a high degree of common mode rejection.

Also, since only a single fiber is used, the need for optical fiber couplers is avoided, increasing the optical throughput and simplifying implementation.

3.3.2 Other Dual Mode Combinations

The above analysis considers only one of many possible mode combinations. It is clear that varying the modal content will lead to changes in the output pattern. As first pointed out by Layton and Bucaro for optimum sensor performance, the modes chosen for interference should exhibit a large difference in β, possess a large cross term in the interference expression, and have a relatively simple spatial variation in the output plane. From Figure 3.2, one can see that for a V of approximately 3, the LP_{01} and LP_{11} modes have a large difference in β, and the slope of the LP_{11} mode at that point is reasonably large. It was shown before that the output pattern could consist of as many as four lobes which exchange power, but often contains only two. Also, Safaai-Jazi has shown that a rotating, one-lobe pattern is possible with these two modes by setting $B_1 = jA_1$ in equation (3.33) above [95]. It is noted that rotation of the lobes is only possible if both the even and the odd contributions are included.

Again referring to Figure 3.2, if $V \approx 4-5$, the difference in β is also large for the LP_{01} and LP_{02} modes. The spatial distribution of the interference between these modes is independent of ϕ, and can be calculated as a circularly symmetric pattern with either a central bright or dark circle. To show this, we write the field expressions for the two modes:

$$
\begin{aligned}
LP_{01}: \quad & \vec{E}_1 = A_1 f_1 e^{-j(\beta_1 z - \psi_1)} \hat{a}_x \\
\\
LP_{02}: \quad & \vec{E}_2 = A_2 f_2 e^{-j(\beta_2 z - \psi_2)} \hat{a}_x \; .
\end{aligned}
\tag{3.35}
$$

Following the same procedure as with the other mode combinations, we arrive at an expression for the output intensity,

$$I = \frac{Y}{2} [A_1{}^2 f_1{}^2 + A_2{}^2 f_2{}^2 + 2 A_1 A_2 f_1 f_2 \cos \theta] \quad . \tag{3.36}$$

More formally, we could write,

$$I = \frac{Y}{2} \left[A_{01}{}^2 \frac{J_0{}^2 (u_{01}r/a)}{J_0{}^2 (u_{01})} + A_{02}{}^2 \frac{J_0{}^2 (u_{02}r/a)}{J_0{}^2 (u_{02})} \right.$$

$$\left. + 2 A_{01} A_{02} \frac{J_0(u_{01}r/a)}{J_0(u_{01})} \frac{J_0(u_{02}r/a)}{J_0(u_{02})} \cos (\tilde{\beta}z - \tilde{\psi}) \right] \quad . \tag{3.37}$$

The individual terms appear graphed in Figure 3.12 as a function of r/a. Note that the criterion for a large cross term is apparently met. The total output intensity for the cases of maximum and minimum cross term is shown in Figure 3.13. The form of equation (3,37) and Figure 3.13 can be readily verified in the laboratory by aligning a fiber intended for single mode operation at 1300 nm axially in a He-Ne laser beam without the use of an objective lens, since the latter tends to launch light into the unwanted LP_{11} and LP_{21} modes. Figure 3.14 demonstrates the effect of strain on such a fiber as seen by a CCD camera. A fiber sensor based on the interference of these modes has recently been reported [96], which makes use of a mask in the output plane imaged onto a set of spatial filters to overcome problems with polarization instabilities. Interestingly, it is also pointed out that in quadruple-clad fibers, the LP_{02} cutoff frequency is lower than that of the LP_{11} and LP_{21} modes, meaning such a fiber could easily be operated with the LP_{01} and LP_{02} modes in a truly dual mode arrangement.

Selective interference between the LP_{11} and LP_{21} modes has also been analyzed [95]. If the amplitude coefficients are properly chosen in magnitude and phase, a three-lobe pattern may result. This pattern rotates with the application of axial strain on the fiber, as was demonstrated by Duncan et. al. [16]. It is unfortunate however, that while the output is simple, it is not unique to this mode pair, and other three-lobe patterns do not necessarily rotate with applied strain. Thus achieving this pattern in

the lab is generally difficult, and requires off-axis injection to avoid launching of the fundamental mode. These factors limit the usefulness of this mode pair in sensor applications.

3.4 Interference in Multimode Optical Fibers

In contrast to the simple output patterns obtained with single and dual mode optical fibers, few mode, and especially highly multimode fibers display much more complicated outputs. To understand why, we need only to consider that each of the propagating modes has its own spatial distribution which simultaneously interferes with all other modes all along the guide and in the output plane. If we also recall that most LP modes consist of four nearly, but not exactly degenerate vector modes, it becomes clear that even when only a "few" LP modes propagate, many distinct modes actually exist in the fiber. For V numbers below 5 or 6, patterns usually appear as a number of lobes of intensity randomly located in the output. When the fiber is disturbed, the various βs associated with each propagating mode are altered, changing their differential phase, and therefore their interference pattern.

If the geometry of the fiber is such that the diameter of the core is much greater than the wavelength of the light traveling inside, then an explanation based on geometrical optics is often useful in understanding the nature of the output pattern from multimode fibers. This is often the case in typical multimode fibers, where the diameter is from 50-200 μm, and the optical wavelength is nominally 1 μm. Referring to Figure 3.15a, we may then consider low order modes as those rays which make small angles with respect to the fiber axis. Their propagation constant β is taken as the z component of the k vector corresponding to that angle. Higher modes make larger angles, and so have smaller values of β, in keeping with the β-V diagram of Figure 3.2.

With any two rays are associated wavefronts, roughly plane waves in a homogeneous, isotropic core, represented in Figure 3.15b. Total internal reflection at the core-cladding boundary ensures that these waves arrive at

the end face, and after propagating to a screen, produce intensity fringes typical of any two interfering plane waves. Interference from other pairs of rays occurs simultaneously, and fill the same space on the output screen. When now rays in the y dimension are considered, and skew rays are included in addition to the meridional rays shown, the many overlapping interference fringes appear as a pattern of numerous speckles. As one would expect, the number of speckles increases with the number of modes in the fiber, while the individual speckle size decreases. For highly multimode fibers, the number of modes propagating in a step index fiber N, can be calculated as approximately [97]

$$N \approx \frac{4\,V^2}{\pi^2} \;.$$

(3.38)

Recalling the definition of the V number in equation (3.16), we note that the number of modes, and therefore the number and size of the speckles in the output pattern depends on the static and dynamic values of the core radius, indices of refraction, and propagation wavelength. This can be seen qualitatively in Figure 3.16, where the speckle patterns from a typical 50/140 (core/cladding diameter) fiber can be seen. In one case the fiber is excited with a standard He-Ne laser, $\lambda_0 = 633$ nm, in the other, the laser is a He-Cd with $\lambda_0 = 482$ nm. As expected, the latter shows a higher number of smaller speckles. However, we note that the exact relationship between the number of modes and the number of speckles has not been stated here. This will be taken up in the last chapter.

It remains to obtain an expression for the intensity distribution of the speckle pattern output. As we have seen, in the case where only a few modes propagate, the resulting interference pattern is relatively straightforward to describe. As more and more modes are included, we are forced to express the result in terms of a summation of terms, as described in a recent paper by Spillman, et. al. [18]. That is, if we wish to find the total electric field in the fiber, we must sum contributions from all modes in the general field expression of equation (3.18) over all values of ℓ and m. We have already established the lower bounds on ℓ and m, yielding $\ell_{min} = 0$ and

$m_{min} = 1$. To determine the upper bounds for these integers, we note that far from cutoff, it can be shown that the total number of modes can be approximated by estimating the number of roots of the equation [97]

$$J_l(u_{lm}) = 0 \ .$$

(3.39)

Noting that the definition of u and w in equation (3.10) applies for each mode, and recalling the bounds on β set in equation (3.4), it can be seen that the upper limit on u_{lm} occurs when $\beta_{lm} = n_2 k_0$; in that case $u_{lm} = V$. However, from the large argument approximation of the Bessel function, it can also be shown that [98]

$$u_{lm} \approx (l + 2m)\frac{\pi}{2} \ .$$

(3.40)

Equating these, we arrive at the conclusion that

$$l_{max} \approx \frac{2V}{\pi} \qquad \text{and} \qquad m_{max} \approx \frac{V}{\pi} \ .$$

(3.41)

By calculating the area in l-m space representing the number of possible modes as approximately $\frac{1}{2} l_{max} m_{max}$, and recalling the fourfold degeneracy for LP modes having $l > 0$, we arrive at the approximate number of bound modes in the fiber given in equation (3.38).

Having established the boundaries on l and m, we express the total electric field for the x-polarized even modes as

$$\vec{E}_X = \sum_{l=0}^{l_{max}} \sum_{m=1}^{m_{max}} A_{lm} \ f_{lm} \ \cos l\phi \ \exp\left[-j(\beta_{lm}z - \psi_{lm})\right] \hat{a}_x$$

(3.42)

$$= \sum_l \sum_m E_{lm} \hat{a}_x$$

(3.43)

while the total magnetic field for the y-polarized even modes is

$$\vec{H}_Y = Y\,|\vec{E}_X|\,\hat{a}_y = Y \sum_\ell \sum_m E_{\ell m}\hat{a}_y \;. \tag{3.44}$$

Again $Y_{\ell m}$ has been approximated by the average admittance Y. Computing the Poynting vector relation of equation (3.22) as before, the intensity becomes

$$I = \frac{Y}{2}\,\mathrm{Re}\left\{\left(\sum_\ell \sum_m E_{\ell m}\right)\left(\sum_{\ell'} \sum_{m'} E^*_{\ell'm'}\right)\right\} \tag{3.45}$$

$$= \frac{Y}{2}\,\mathrm{Re}\left\{\left(\sum_\ell \sum_m \sum_{\ell'} \sum_{m'}\left(E_{\ell m}E^*_{\ell'm'}\right)\right\}\right. \tag{3.46}$$

where the primed dummy variables are introduced to account for the interference between each combination of modes. The summation limits for ℓ' and m' are the same as those for ℓ and m, respectively. Substituting the field distributions in from equation (3.18) and taking the real part, we have

$$I = \frac{Y}{2}\sum_{\ell=0}^{\ell_{max}}\sum_{m=1}^{m_{max}}\sum_{\ell'=0}^{\ell'_{max}}\sum_{m'=1}^{m'_{max}}\Big(A_{\ell m}\,A_{\ell'm'}\,f_{\ell m}\,f_{\ell'm'} \tag{3.47}$$

$$\times\,\cos\ell(\phi+\phi_0)\,\cos\ell'(\phi+\phi_0)\,\cos\big[\tilde{\beta}_{\ell m\ell'm'}\cdot z - \tilde{\psi}_{\ell m\ell'm'}\big]\Big)$$

where the difference between modal propagation constants and initial phases is again represented by a tilda:

$$\tilde{\beta}_{\ell m\ell'm'} = \beta_{\ell m} - \beta_{\ell'm'} \qquad \text{and} \qquad \tilde{\psi}_{\ell m\ell'm'} = \psi_{\ell m} - \psi_{\ell'm'}\;. \tag{3.48}$$

Also, the odd modes have been re-introduced by virtue of the added factor of ϕ_0, which in principle could take on any value, including $-\pi/2$.

When the multimode fiber experiences mechanical perturbations, strain is imparted either along the axis, radially, or both. The simultaneous changes in fiber length, refractive index, and diameter act to

alter the differential phase of each mode, dictated by the fiber parameters of the fiber. Again, it can be seen qualitatively from equation (3.47) that changes in z, the fiber length, affect the phase of the last cosine factor, as do changes in fiber radius and index through β. These changes all tend to modulate the intensity of the output speckle pattern, though it does not change the general *shape* of the interference pattern from each mode pair. Certain types of fiber motion produce a rather regular composite motion of the speckles; for example, the speckles may appear to rotate clockwise about in ϕ when the fiber is swung clockwise in a sweeping arc. However, for most disturbances the changes appear rather random.

A number of terms in (3.47) are stable with respect to perturbations. Specifically, terms arising from mode self-interaction, which in (3.48) means that $\tilde{\beta} = 0$, are invarient with respect to z. It is not strictly true that they are unaffected by mechanically induced changes in β however, since A depends on β by virtue of its dependence on Y, while f depends on β through u and w. It is generally believed that for practical variations in β, changes in intensity because of these mechanisms are much smaller than due to the phase change noted above, though Figure 3.11 suggests that this may not be completely accurate. Nevertheless, considering that the total intensity distribution consists of overlapping contributions from many mode pairs, each with its own sensitivity, as well as from d.c. term, it becomes more clear why disturbing the fiber results in some speckles shifting wildly, some only moderately, some hardly at all .

Thus we have in equation (3.47) a relatively simple, closed form expression for the speckle pattern intensity distribution. Such a form lends itself well to computer simulation, though to be sure, modelling the output of a typical multimode fiber would involve a relatively extensive calculation, especially if the determination of individual propagation constants were first required. However, this novel form does add physical insight into the nature of modal interference in a general situation. For example, it can be easily shown that the intensity distribution of the LP_{01} / LP_{11} or LP_{01} / LP_{02} sensors of equations (3.34) and (3.37) result when the appropriate choice of ℓ_{max} and m_{max} are inserted into (3.47).

The observation of speckle modulation offers a number of advantages to strain sensing. For one, multimode fiber is cheaper and easier to work with than single mode round or elliptical core fiber used for single or few mode sensors. Also, fewer components are necessary to construct a sensor, and rigid injection requirements, as well as source stability and power requirements can often be relaxed significantly. At the same time, it will be shown that highly multimode sensors can retain strain sensitivities which are competitive with single mode interferometers. However, to date only a relatively small number of authors have reported the use of modal interference phenomena in large core fibers for sensing purposes, and even fewer of those in the last five years [9-11,17-19,22].

Nearly all the early demonstrations concentrated on acoustic wave sensors, apparently aimed hydrophone applications. One notable example, described by Culshaw, Kingsley, et. al., clearly shows the flexibility of the technique, as well as the high sensitivity afforded by multimode fibers over a broad acoustic frequency range. Originally conceived for a data telemetry system, their method was termed "fiberdyne" for "fiber-optic self-homodyne" [99]. Piezoelectric transducers clamped to the injection end of an optical fiber cable were FSK modulated by information signals; the local fiber geometry was altered accordingly, rearranging the mode structure of helium-neon light propagating in the fiber. At the far end, demodulation of the modal signal was performed to recover the transmitted information. Such systems have been found to operate acceptably for acoustic modulation frequencies between 100 kHz and 10 MHz. At the same time, detection of acoustic waves from near d.c. to over 100 kHz has been demonstrated by several other authors, thus revealing the wide operating range of the sensor.

Having covered the basic theoretical foundation for the existence of modes in fibers, and gained an understanding of their interference, it is necessary to investigate the degree to which these phenomena can be used for practical sensing. Accordingly, in the next chapter, we turn to calculations of the intrinsic sensitivity of single mode, few mode, and multimode fibers to applied strain.
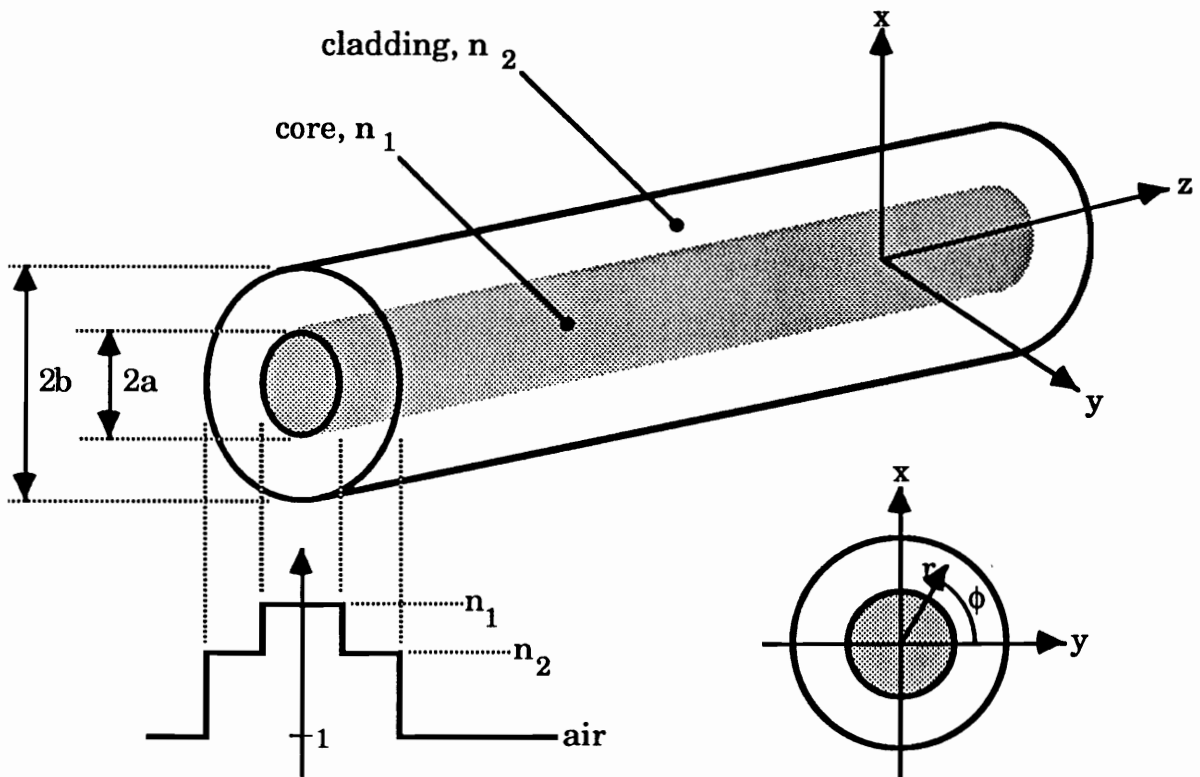
Figure 3.1. The refractive index profile and geometry of the step index fiber, showing the coordinate system used in the present analysis.
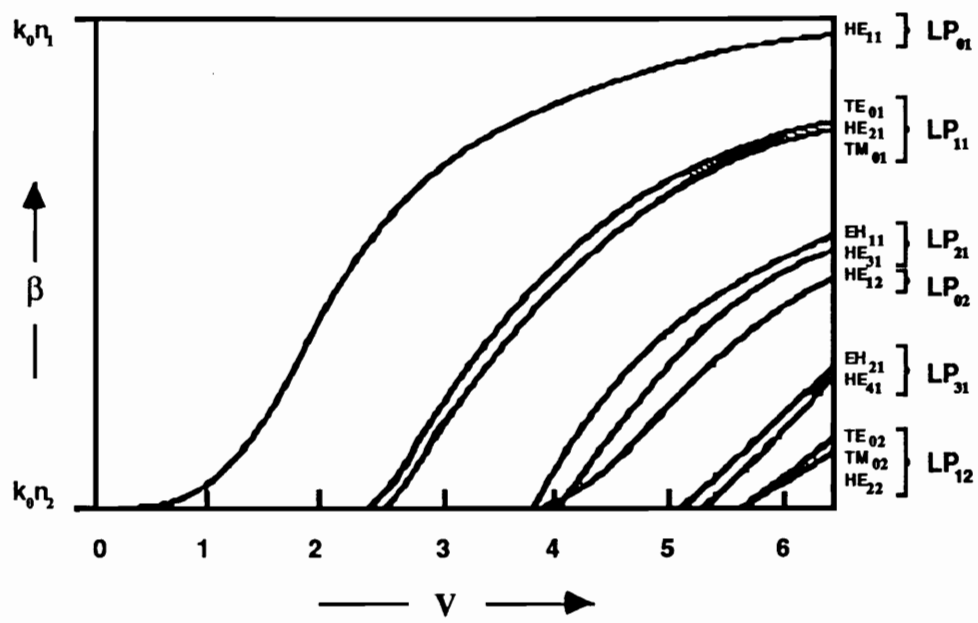
Figure 3.2. Propagation constant versus the normalized frequency V for the first several modes. Shown are the vector modes and their corresponding LP mode designations (after [91]).

Normalized Value of u and w vs. b
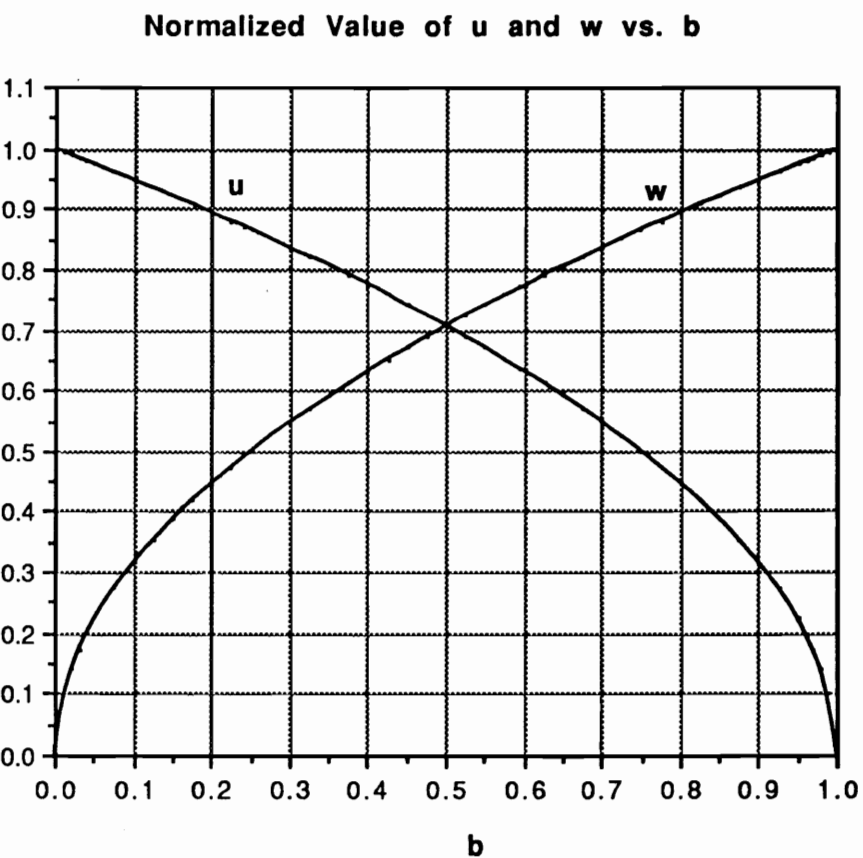
Figure 3.3. Values of u and w (equation (3.10)) as a function of the normalized propagation constant b. Vanues themselves are normalized with respect to V, the normalized frequency of the guide.
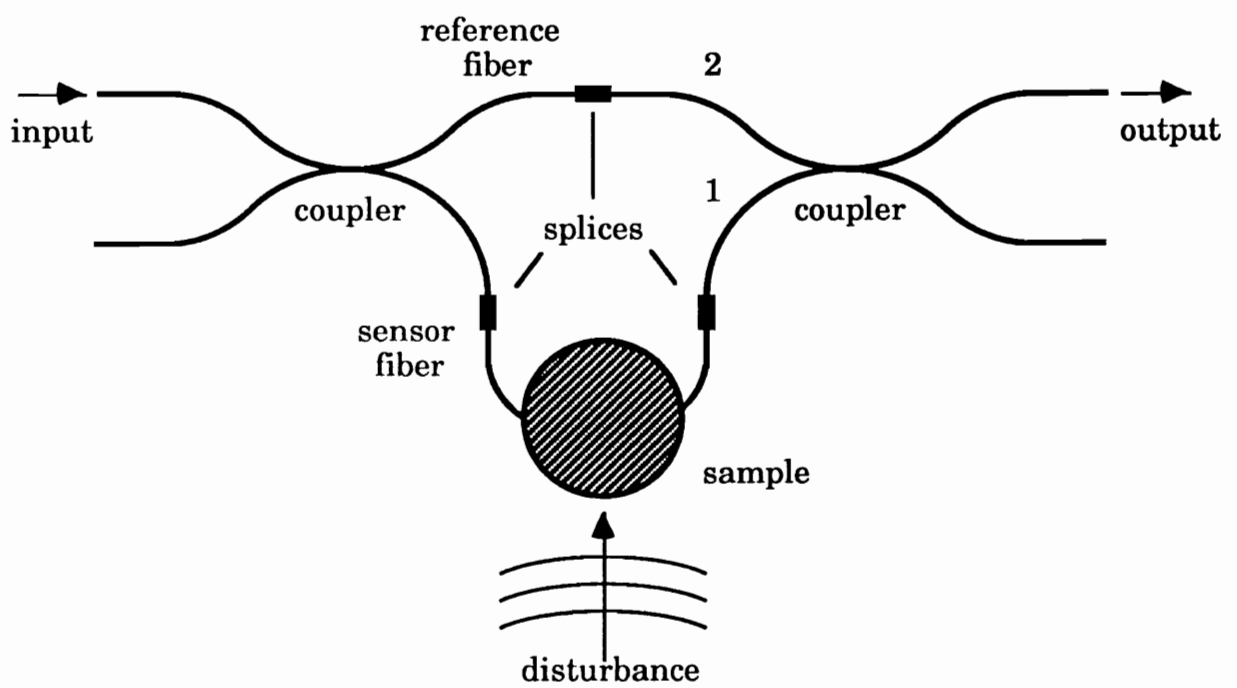
Figure 3.4. A typical Mach-Zender interferometer applied to the measurement of strain in a fiber embedded in or attached to a sample.

Single Mode Interferometer
Normalized Intensity vs. r/a
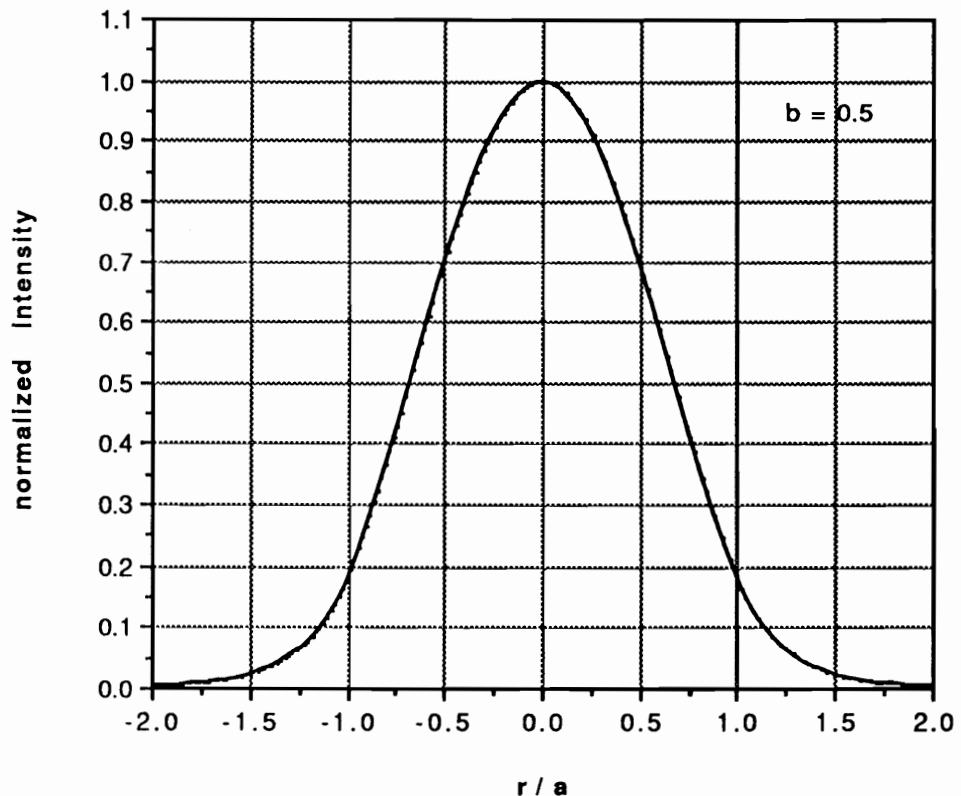
Figure 3.5. Intensity distribution for the single mode fiber interferometer output as a function of the normalized radial position r/a.
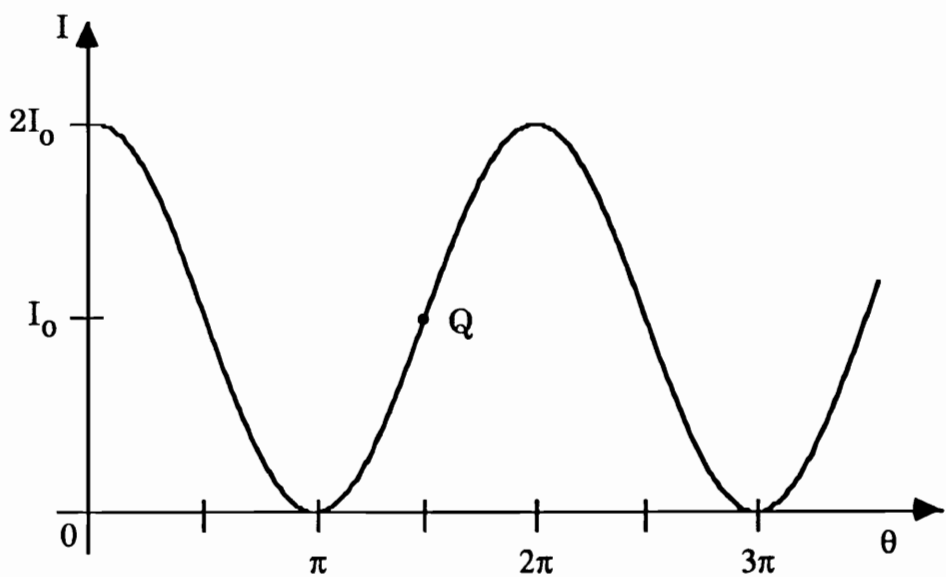
Figure 3.6. Plot of equation (3.28), single mode interferometer output intensity as a function of total phase θ, which is itself affected by external perturbations. Equal amplitudes of the incoming waves is assumed.
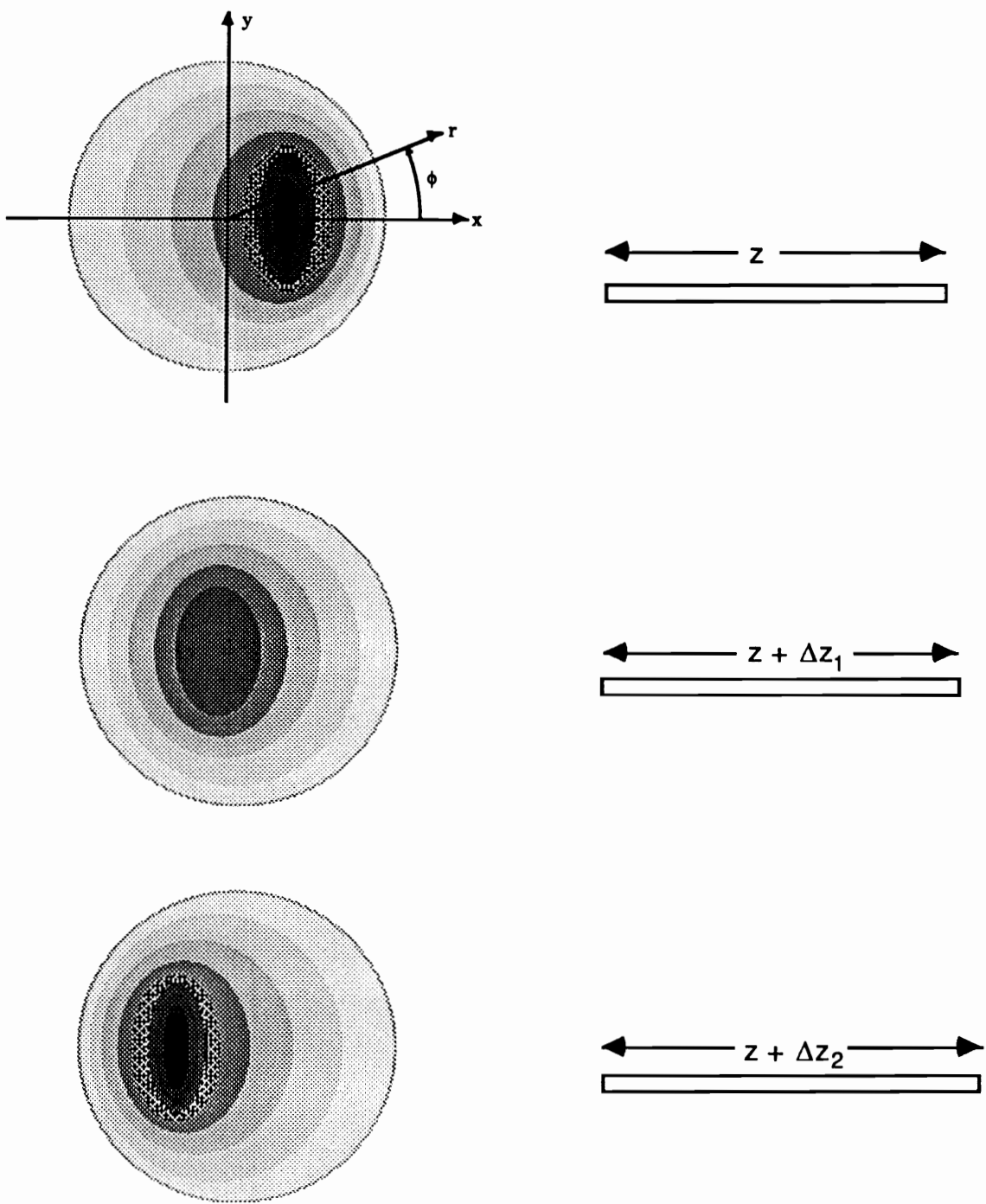
Figure 3.7. Representation of the output pattern observed when a fiber propagates the LP_{01} and LP_{11} modes, for three different values of strain.

LP01/LP11 Terms:
Intensity vs. r/a
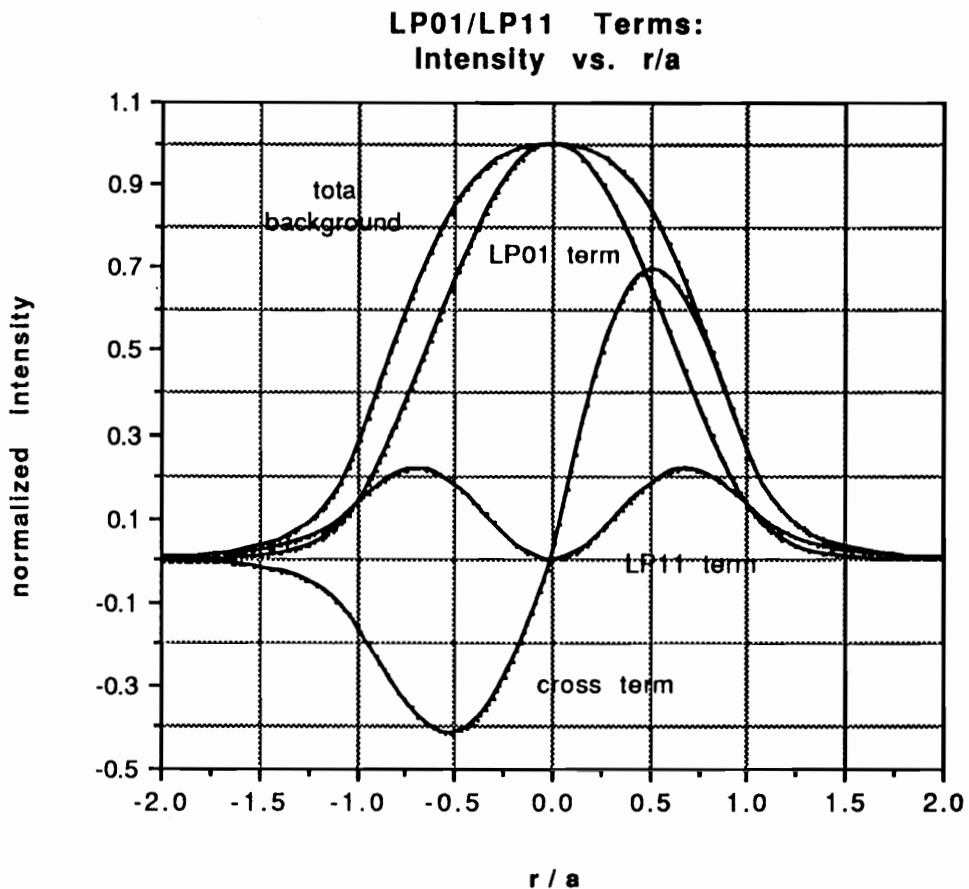
Figure 3.8. Terms of equation (3.34) describing the interference between the LP_{01} and LP_{11} modes. The self-interference terms and their sum are shown; these are all static with strain and therefore considered a background term. On the other hand, the cross term changes with strain.
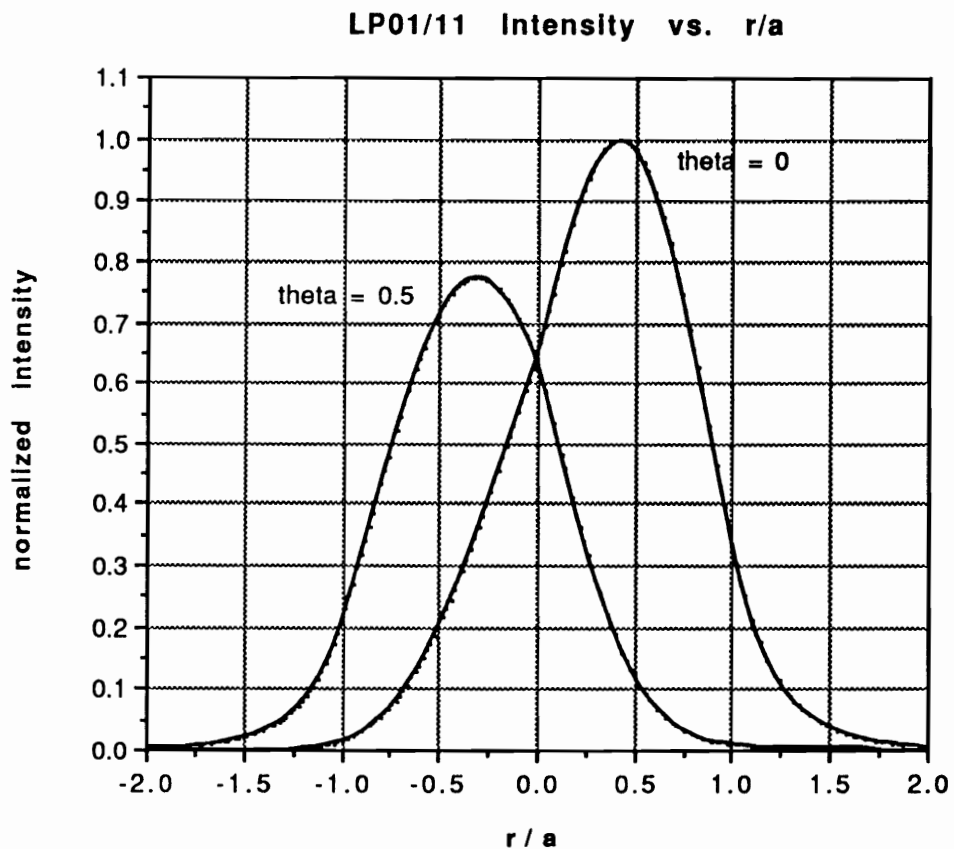
Figure 3.9. Intensity distribution of the LP_{01} / LP_{11} modal domain sensor at two different values of θ, or equivalently, strain. In this plot, it is assumed that the two modes carry equal power.

LP01/11 Intensity vs. Strain
at r/a = 0.42

normalized output

strain units (1 unit = 2 ustrain)
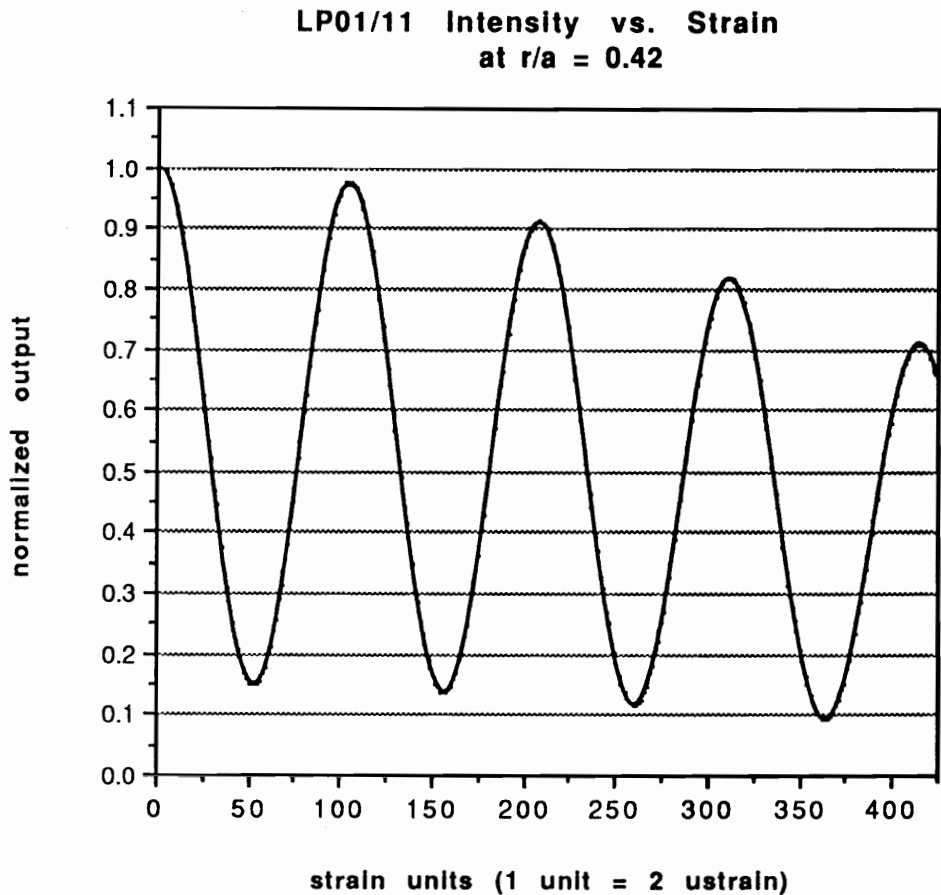
Figure 3.11. LP_{01} / LP_{11} sensor output as a function of strain. In this plot, it is again assumed that the two modes carry equal power.
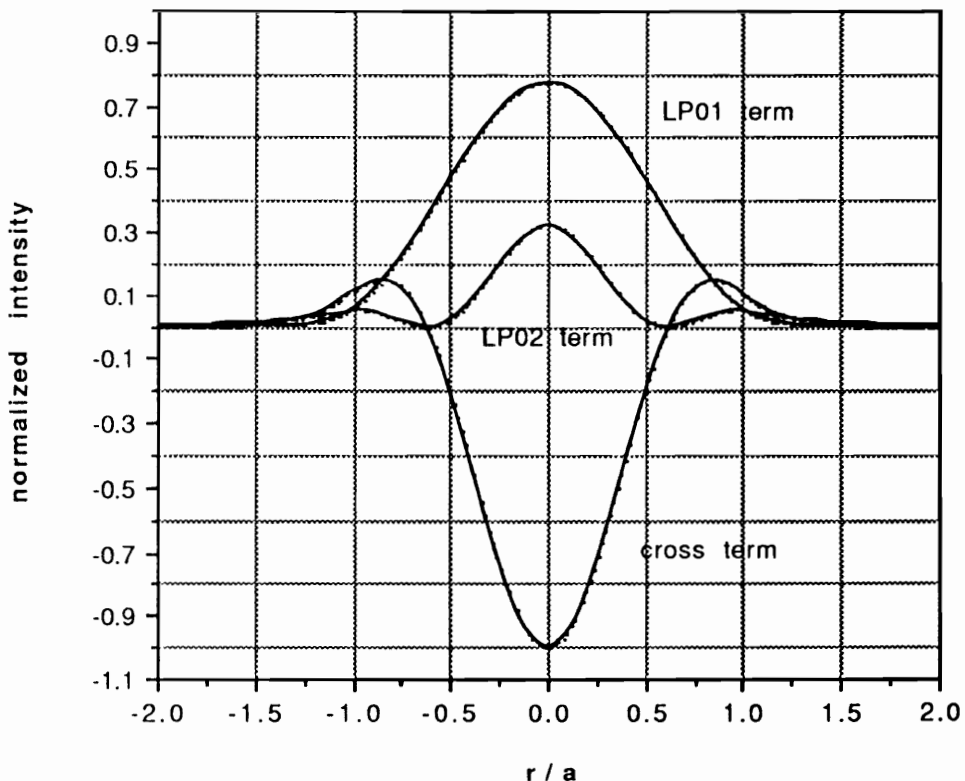
Figure 3.12. LP_{01} / LP_{02} sensor output distribution. Shown are the individual self-interference terms and their sum, which constitute the background intensity. Also shown is the interference cross term.

LP01/02   Intensity   vs.   r/a
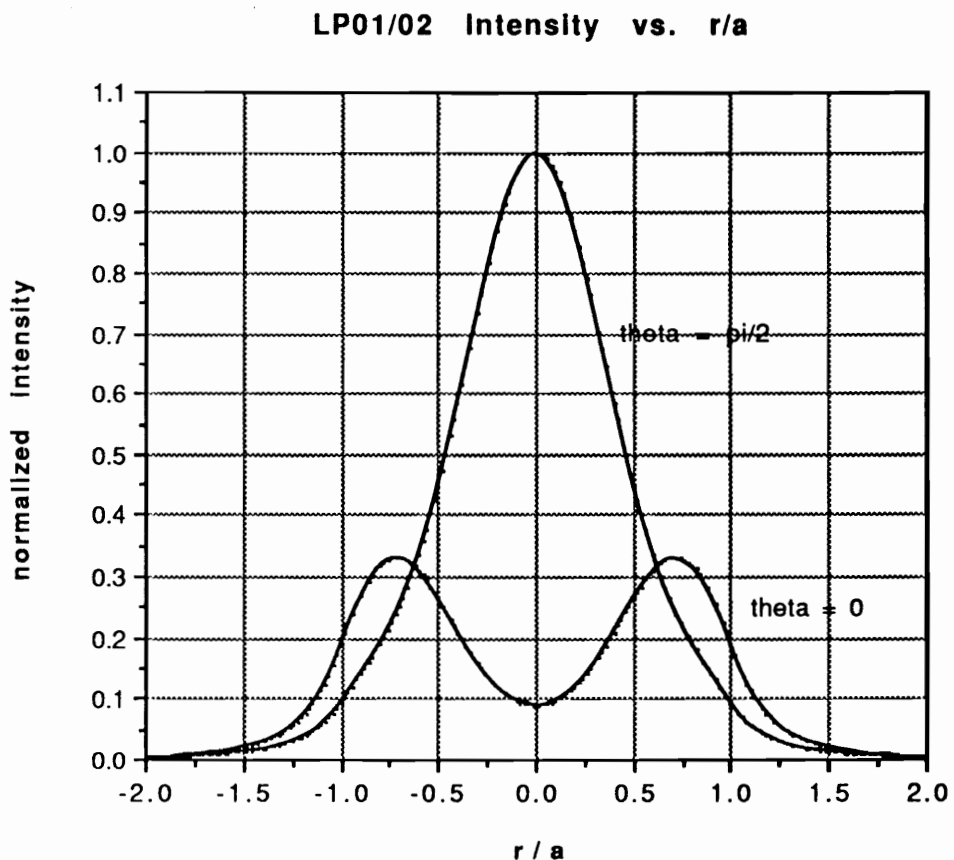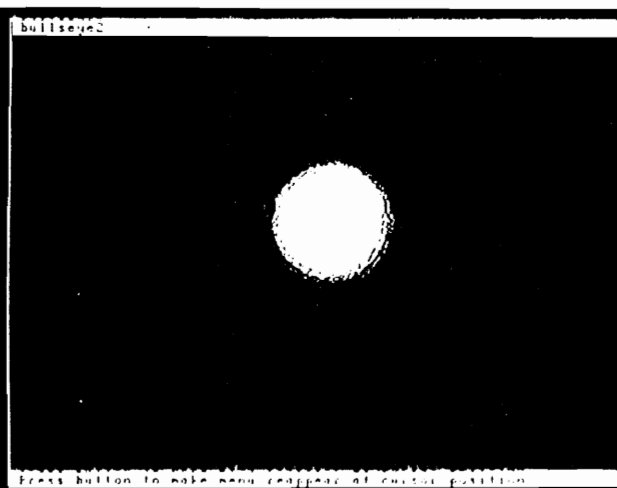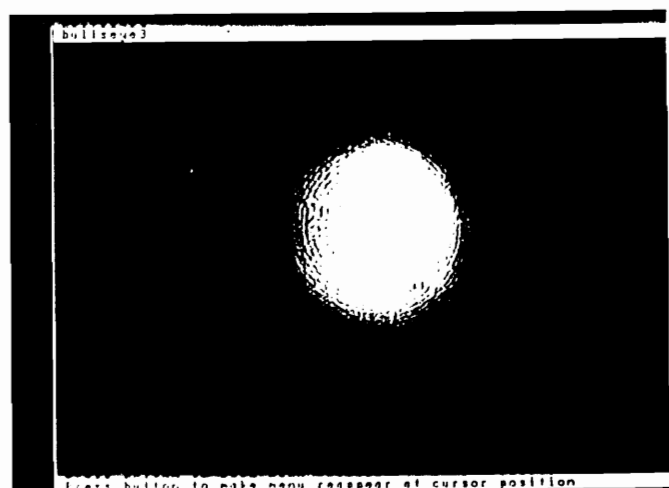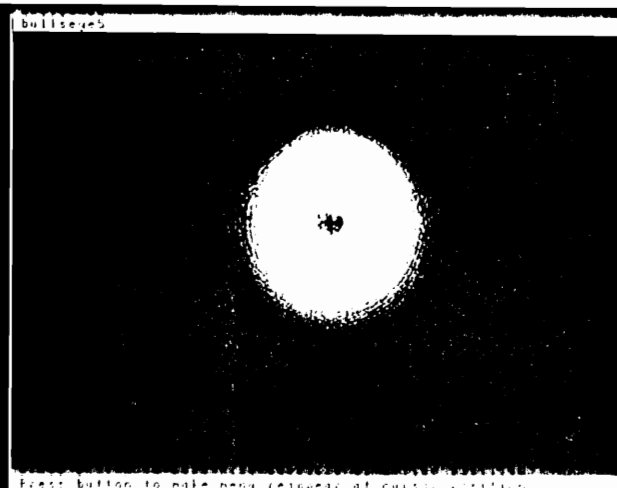
Figure 3.13. Total intensity distribution for the LP_{01} / LP_{02} sensor for two values of θ, or equivalently, strain. The case of $\theta = 0$ corresponds to maximizing the value of the cross term, while for $\theta = \pi/2$, the cross term is eliminated.
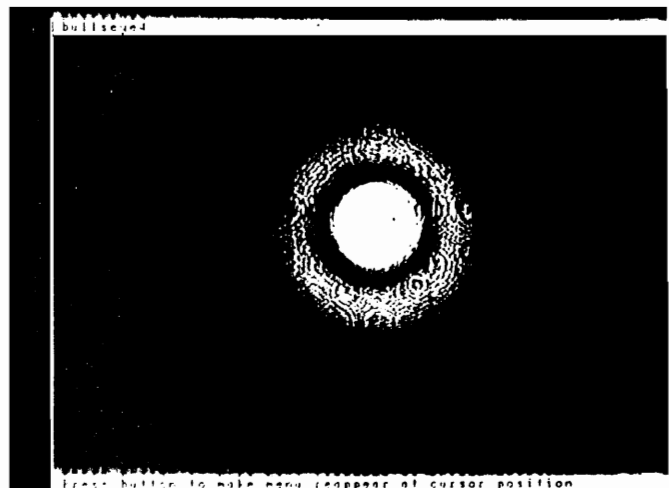
(a)

(b)

(c)

(d)

Figure 3.14. Modulation of the LP_{01}/LP_{02} mode combination intensity is seen for four increasing values of axial strain applied to the fiber. The appearance of fringe-like details occurs due to multiple reflections in the cover glass of the CCD processing array used to record the images.
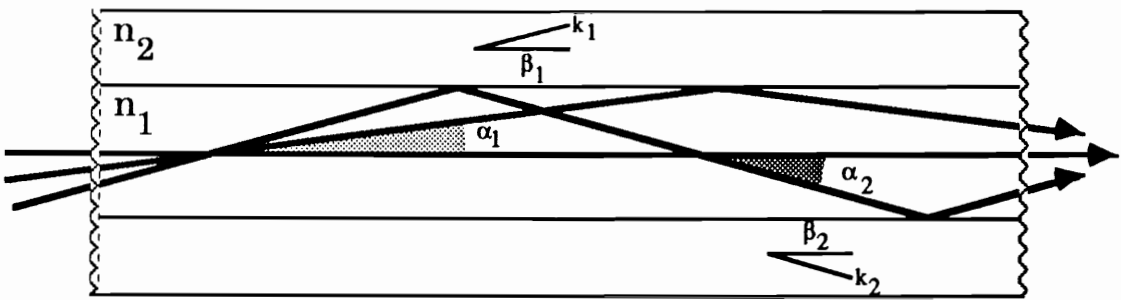
Figure 3.15a. Optical fiber modes in a multimode fiber from a ray optics point of view. Higher modes are represented as those propagating at higher angles with respect to the fiber axis.
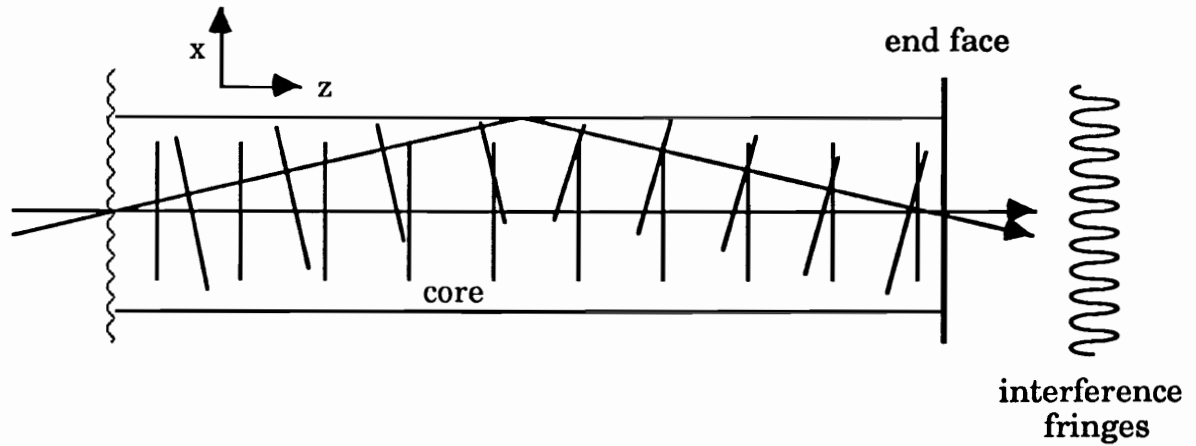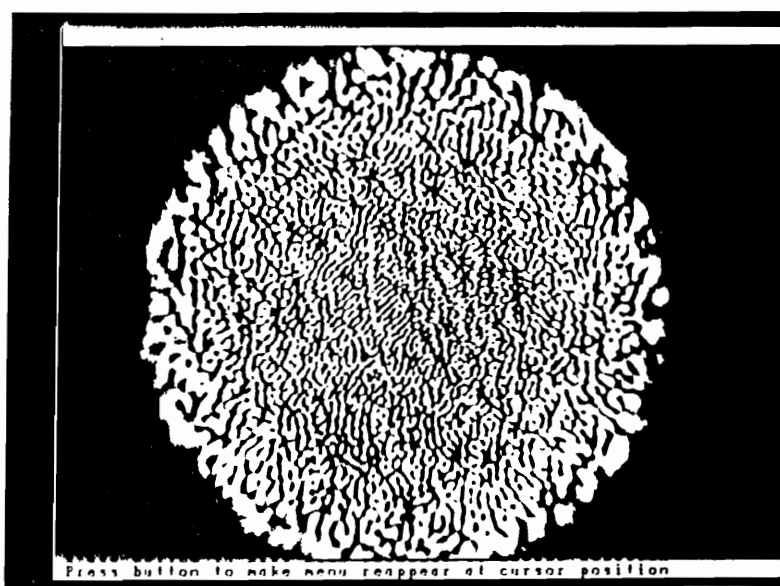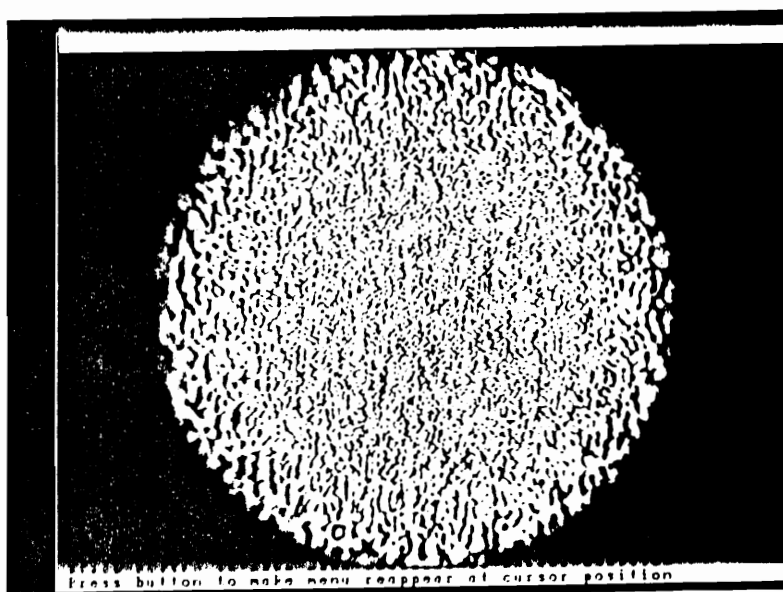
Figure 3.15b. A simplistic representation of modal interference. Two coherent meridonal rays with nearly planar wavefronts interfere in the output to produce ordinary interference fringes. When multiple modes and skew rays are included, the result is a speckle pattern such as seen in Figure 8.

Figure 3.16. Typical speckle patterns emerging from a 50 μm core multimode fiber. The upper figure resulted when 633 nm light from a He-Ne laser was injected into the fiber, while in the lower figure the fiber transmitted 482 nm light from a He-Cd laser.

4.0 STRAIN SENSITIVITY

Up to this point, we have claimed that single mode interferometers, as well as dual and multimode differential interferometers, are well suited for the measurement of induced strain in materials and structures. It has been stated that they offer high sensitivity, in fact greater sensitivity than all other optical fiber sensors. In this section, we address the issue of calculating the absolute sensitivity of fiber optic phase sensors to applied strain.

The analysis will be divided into five sections. In the first, the basic strain mechanics will be discussed, especially with regard to optical fiber strain sensors. The next section will consider the change in phase per unit strain for single mode fibers. These calculations involve a number of differences with the generally accepted procedure first set forth by Butter and Hocker in 1978 [54], and will be discussed in detail. With that foundation laid, the next two sections go on to calculate the phase sensitivity of dual mode, and highly multimode fiber sensors. Applied axial strain, important for many sensing applications, will be treated first for each fiber type. Also addressed for each type is the case of radially applied strain, such as occurs when a fiber is subjected to longitudinal sound waves crossing transverse to its axis. Comments relevant to this application will be mentioned throughout, as it was a primary motivation for the study. A discussion of the assumptions made along the way, and some intermediate results will close the chapter.

4.1 Strain Mechanisms in Optical Fiber Sensors

In many applications of optical fiber sensors, and especially those involving structural measurements, the quantity which is actually sensed is strain, regardless of the particular observable which may have caused it,

such as temperature changes or acoustic emissions. As mentioned earlier, the strain may affect one or more of the basic properties of the light within the waveguide. Theses include the optical phase, intensity, wavelength, polarization, modal power distribution, and propagation time. In this section we outline the basic strain mechanisms to which a fiber may be subject, and set the stage for a more quantitative discussion of the sensitivity of the phase in a fiber to strain.

The general strain tensor, applied to a small body in a Cartesian coordinate system such as appears in Figure 4.1 may be expressed as

$$\varepsilon_{ij} = \begin{pmatrix} \varepsilon_{11} & \varepsilon_{12} & \varepsilon_{13} \\ \varepsilon_{21} & \varepsilon_{22} & \varepsilon_{23} \\ \varepsilon_{31} & \varepsilon_{32} & \varepsilon_{33} \end{pmatrix}. \tag{4.1}$$

Throughout the analysis, we assume that from a mechanical point of view, the fiber is homogeneous and isotropic. That is, though clearly the optical properties of the core and cladding differ, the mechanical properties such as the Young's modulus and Poisson's ratio do not change with respect to position and direction in the fiber. In that case, the tensor is immediately reduced to six independent quantities due to symmetry:

$$\varepsilon_{ij} = \begin{pmatrix} \varepsilon_{11} & \varepsilon_{12} & \varepsilon_{13} \\ \varepsilon_{12} & \varepsilon_{22} & \varepsilon_{23} \\ \varepsilon_{13} & \varepsilon_{23} & \varepsilon_{33} \end{pmatrix}. \tag{4.2}$$

Finally, modelling the fiber as a right, circular cylinder and considering the directions 1 and 2 equivalent, the tensor further reduces to

$$\varepsilon_{ij} = \begin{pmatrix} \varepsilon_{11} & \varepsilon_{12} & \varepsilon_{13} \\ \varepsilon_{12} & \varepsilon_{11} & \varepsilon_{13} \\ \varepsilon_{13} & \varepsilon_{13} & \varepsilon_{33} \end{pmatrix}. \tag{4.3}$$

The four independent strains which result are

ε_{11} – the radial strain

ε_{12} – the torsional or rotational strain

ε_{13} – the shear strain along the axis

ε_{33} – the axial strain

These strains are illustrated in Figure 4.2.

It is instructive to note that all possible deformations of the fiber are included in the strain tensor. For example, bending the fiber may be considered as comprised of a pure bending term, which amounts to pure axial strain ε_{33}, and a moment, which is shear strain ε_{13}. Likewise other strain geometries could be accounted for with the four terms above.

In the general case, we assume that imposing each of these strains on the fiber affect the basic optical properties differently. For example, radial pressure on the fiber may alter the polarization state of the light within it, though the overall intensity may be little affected, while on the other hand, all the strain geometries will simultaneously affect the phase or modal power distribution. In the ideal case, the coupling between all the mechanical and optical effects would be known for several representative fiber types, such as single mode, few mode, polarization preserving, highly multimode step index, and highly multimode graded index. Theoretical models exist for a number of the different relations, and many experiments performed, but to date there appears to be no comprehensive model for opto-mechanical interaction in optical fibers. A general formulation describing how changes in strain affect the six optical quantities mentioned above might appear as

$$
\begin{pmatrix} \Delta I \\ \Delta \theta \\ \Delta P \\ \Delta \lambda \\ \Delta M \\ \Delta t \end{pmatrix}_k = \begin{bmatrix} & T_{ij} & \end{bmatrix}_k \begin{pmatrix} \varepsilon_{11} \\ \varepsilon_{12} \\ \varepsilon_{13} \\ \varepsilon_{33} \end{pmatrix}_k \qquad (4.4)
$$

where

$$
\begin{array}{lcl}
I & = & \text{intensity} \\
\theta & = & \text{phase} \\
\mathcal{P} & = & \text{polarization state} \\
\lambda & = & \text{wavelength} \\
M & = & \text{modal power distribution} \\
t & = & \text{optical pulse time delay} \\
k & = & \text{optical fiber type subscript}
\end{array}
$$

and T_{ij} , $i = 1,...,4$; $j = 1,...,6$, is chosen to represent the transformation tensor coupling the mechanical and optical properties. It is assumed that simple linear superposition applies, allowing the matrix representation above. Whether or not this assumption is valid has yet to be confirmed.

In the following sections, our attention will be restricted to only two of the twenty-four terms in T, namely T_{21} and T_{24}, which relate radial and axial strain in a fiber to the phase change of coherent light propagating within the fiber. Specifically, we seek to determine the absolute sensitivity of the phase to strain; this will be referred to as the "phase sensitivity" to distinguish the results from the other possibilities implied by (4.4). It is important to realize however, that regardless of the optical parameter which is employed for sensing, the final signal is most often formatted in terms of an electrical current proportional to the intensity of light striking a photodiode. Therefore, although phase sensitivity is the focus of the discussion, it will be necessary to begin by examining how the interference intensity pattern changes with the application of strain. Comments regarding several other terms will be interjected where relevant. Single mode, dual mode, and three cases of multimode fibers are considered, though the analysis applies only to step index, round core fibers. Graded index and elliptical core fibers will necessarily be relegated to future work. We begin with the most standard case, that of single mode fibers subject to axial strain.

4.2 Strain in Single Mode Fiber Sensors

The general approach for finding the inherent phase sensitivity an interferometer is outlined as follows. We start by recalling the expression for the peak intensity of the interference distribution, (3.28), repeated here:

$$I = I_0 [1 + \cos\theta] \quad . \tag{4.5}$$

We seek to discover how the intensity I changes with the application of strain to the fiber. That is, we wish to find

$$\Delta I = \left[\frac{\partial I}{\partial \varepsilon} \right] \varepsilon \quad , \tag{4.6}$$

where ε is the applied strain, and the initial strain is taken to be zero. In order to evaluate this, it will be necessary to break up the derivative several times until we can write closed form expressions for all the factors which contribute to change I when strain is applied. Using the chain rule, differentiation with respect to θ is introduced:

$$
\begin{aligned}
\Delta I &= \left[\frac{\partial I}{\partial \theta} \right]\left[\frac{\partial \theta}{\partial \varepsilon} \right] \varepsilon \\
&= -I_0 \sin\theta \left[\frac{\partial \theta}{\partial \varepsilon} \right] \varepsilon \quad .
\end{aligned}
\tag{4.7}
$$

Obviously the signal is maximized for any given level of strain when the phase $\theta = -\pi/2$ (or odd multiples thereof), which corresponds to setting the sensor at the quadrature point, marked Q on Figure 3.6. At this point the slope of the I-θ curve is steepest and the curve is nearly linear, meaning small changes in θ produce maximum change in I. This condition is accomplished in practice by properly choosing or setting ψ_1 and ψ_2 in equation (3.19). In that case,

$$\Delta I = I_0 \left[\frac{\partial \theta}{\partial \varepsilon} \right] \varepsilon \ . \tag{4.8}$$

We first investigate the case of strain applied along the axis of the fiber, the z axis. It is useful to consider a simple mechanical model, such as the section of single mode fiber illustrated in Figure 4.2. The phase of an optical wave moving between points A and B advances by an amount

$$\theta = \beta L - \psi \ . \tag{4.9}$$

When the fiber is strained, not only does L change, but through the Poisson relationship, the fiber radius (or diameter) also changes. Furthermore, not shown in the diagram is the strain-optic effect, to be discussed later, which states that when an optical material is strained, its index of refraction also changes. That a change in L will affect θ and therefore the output intensity is obvious from (4.9). Also, again referring to the definition of the normalized frequency V in equation (3.16), it becomes clear that any change in the fiber radius or refractive index will likewise affect θ. With this intuitive argument in mind then, we state that strain acting on an optical fiber can change the phase of the light within the fiber by three means:

    1)   change in fiber length, L,

    2)   change in fiber radius, a,

    3)   change in fiber refractive index, n.

It is important to realize at the outset that all of these changes occur simultaneously regardless of how strain is applied, though the magnitude and the sign of the individual contributions differ. Thus we can write

$$\Delta I = \left[\frac{\partial I}{\partial L} \right] \Delta L + \left[\frac{\partial I}{\partial a} \right] \Delta a + \left[\frac{\partial I}{\partial n} \right] \Delta n \tag{4.10}$$

$$= \left[\frac{\partial I}{\partial \theta}\right]\left[\frac{\partial \theta}{\partial L}\right]\Delta L \; + \; \left[\frac{\partial I}{\partial \theta}\right]\left[\frac{\partial \theta}{\partial a}\right]\Delta a \; + \; \left[\frac{\partial I}{\partial \theta}\right]\left[\frac{\partial \theta}{\partial n}\right]\Delta n \qquad (4.11)$$

$$= -I_0 \sin\theta \left\{\left[\frac{\partial \theta}{\partial L}\right]\Delta L \; + \; \left[\frac{\partial \theta}{\partial a}\right]\Delta a \; + \; \left[\frac{\partial \theta}{\partial n}\right]\Delta n\right\} \; , \qquad (4.12)$$

and again assuming quadrature,

$$\Delta I \; = \; I_0 \left\{\left[\frac{\partial \theta}{\partial L}\right]\Delta L \; + \; \left[\frac{\partial \theta}{\partial a}\right]\Delta a \; + \; \left[\frac{\partial \theta}{\partial n}\right]\Delta n\right\} \; . \qquad (4.13)$$

Each of the terms in brackets will be discussed individually. To simplify the notation, we define the total change in phase $\Delta\theta$ such that (4.13) can be rewritten in terms of the individual phase change contributions:

$$\Delta I \; = \; I_0 \left\{\Delta\theta_L \; + \; \Delta\theta_a \; + \; \Delta\theta_n\right\} = I_0 \, \Delta\theta \; . \qquad (4.14)$$

4.2.1 Change in Length

Consider first the phase change due to a change in the fiber length,

$$\Delta\theta_L \; = \; \left[\frac{\partial \theta}{\partial L}\right]\Delta L \; . \qquad (4.15)$$

From the definition of θ in equation (4.9), it clear that the derivative is simply β. We note for later use that for uniform strain ε_z applied along the fiber axis, $\Delta L = \varepsilon_z L$. Thus we state simply that

$$\Delta\theta_L \; = \; \beta \, \Delta L \; . \qquad (4.16)$$

Immediately it can be recognized that in order to maximize the change in phase and therefore the change in peak output intensity for a given strain, the sensor should be operated with the highest β possible, or with the V number as close to the cut-in of the second mode as possible. This can be accomplished for a given fiber by altering the propagation wavelength, or for a fixed source, by either increasing a, making the fiber easier to work with, or by increasing the parameter Δ, making the fiber easier to fabricate.

It should be noted that a more general expression for ΔL is preferable when dealing with actual measurements of strain in physical structures. That is,

$$\Delta L = \int_0^L \varepsilon(z,t)\,dz \quad , \tag{4.17}$$

where this form allows for changes in strain along the length of the fiber as a function of time [73]. For the present analysis of sensitivity however, the integral relationship of strain is secondary, and uniform strain will be assumed throughout.

4.2.2 Change in Radius

Next we consider the effect on the phase of changing the radius, noting

$$\Delta\theta_a = \left[\frac{\partial\theta}{\partial a}\right]\Delta a \quad . \tag{4.18}$$

Breaking the derivative up into three terms using the chain rule,

$$\Delta\theta_a = \left[\frac{\partial\theta}{\partial\beta}\right]\cdot\left[\frac{\partial\beta}{\partial V}\right]\cdot\left[\frac{\partial V}{\partial a}\right]\Delta a \quad . \tag{4.19}$$

As before, the first term is merely L. The second term is exactly the slope of the β-V curve. In practice however, it is much more convenient to work

with the normalized parameter b, as defined in equation (3.17), since it varies from 0 to 1, rather than from $n_2 k_0$ to $n_1 k_0$. This term could then be further broken into two terms expressing the change of β with respect to b, and the change of b with respect to V, the latter now being the slope of the b-V curve. From the definition of b, it can be shown that

$$\frac{\partial \beta}{\partial b} = \frac{(n_1^2 - n_2^2)\, k_0^2}{2\beta} \approx (n_1 - n_2)\, k_0 \qquad (4.20)$$

where the approximation arises from the fact that for a weakly guiding fiber $\beta \approx k_0(n_1+n_2)/2$; for typical fiber parameters this introduces an error of less than 0.006%, and the maximum error that could be incurred can be shown to be $(n_1-n_2)\times100$ percent, or about 0.5%. This increases to as much as 3% for multimode fibers since their index difference is generally larger, indicating that the exact formula should be used in this case. For small changes in V due to strain, the b-V curve can be considered linear near the point of operation. Thus, referring to Figure 4.3, we can define the value for the slope of the β-V curve as

$$S \equiv \frac{\Delta \beta}{\Delta V} \approx (n_1 - n_2)\, k_0 \left(\frac{b - b'}{V - V'}\right) = (n_1 - n_2)\, k_0 \, S_b \ , \qquad (4.21)$$

where the primed variables refer to their values after the application of strain, and S_b is the slope of the b-V curve, defined for future use. Note that the values of b, b', V, and V' could all be obtained numerically to any precision desired, though for this argument it suffices to estimate them from the plots.

The third term in equation (4.19) is clearly just $k_0 \sqrt{n_1^2 - n_2^2}$. The last term, Δa, is found from basic strain relations using ν, the Poisson ratio of the fiber material:

$$\Delta a = a\, \varepsilon_r \qquad ; \qquad \varepsilon_r = -\nu\, \varepsilon_z \ , \qquad (4.22)$$

which leads to

$$\Delta a = -a \, \nu \, \varepsilon_z \, . \tag{4.23}$$

Finally, combining the expressions from above,

$$\Delta\theta_a = -\nu \, S \, V \, \Delta L \, . \tag{4.24}$$

4.2.3 Change in Refractive Index

When an optical material is strained, a change in its refractive index may be observed. This change, of foundational importance in the operation of many acousto-optic devices, is due to two principal mechanisms: a change in the spacing of the crystal lattice planes normal to the direction of the applied strain, and a distortion of the orbits of the outermost electrons in the oxygen atoms in the glass [100]. It has been shown that for low refractive index glasses, the latter effect dominates [101].

When calculating the phase change due to the change in refractive index, it is important to realize that although in a ray optics model light is considered as confined to the core of an optical fiber, for single and few mode fibers, much of the transmitted power actually propagates in the cladding. Furthermore, as we have seen, the exact value of the propagation constant for a given mode may very much depend on the operation frequency, V, which is itself dependent on n_1 *and* n_2, or alternatively on Δ. Finally we note that for an ordinary fiber, it is virtually impossible to impart a strain that does not involve an index change in both the core and the cladding. Because of the fiber geometry, the strain in these regions may be considered the same. Thus, when expressing the phase change as

$$\Delta\theta_n = \left[\frac{\partial\theta}{\partial n} \right] \Delta n \, , \tag{4.25}$$

it is evident that the term Δn should be broken up so as to include the effects of changing both n_1 and n_2. That is,

$$\Delta\theta_n = \left[\frac{\partial\theta}{\partial\beta}\right] \cdot \left[\frac{\partial\beta}{\partial V}\right] \cdot \left(\frac{\partial V}{\partial n_1}\Delta n_1 + \frac{\partial V}{\partial n_2}\Delta n_2\right) . \qquad (4.26)$$

As before, the first two partial derivatives are L and S, respectively. The derivatives of V with respect to n_1 and n_2 are

$$\frac{\partial V}{\partial n_1} = \frac{k_0\, a\, n_1}{\sqrt{n_1^2 - n_2^2}}$$

$$\qquad (4.27)$$

$$\frac{\partial V}{\partial n_2} = \frac{-k_0\, a\, n_2}{\sqrt{n_1^2 - n_2^2}} .$$

The change in indices Δn_1 and Δn_2 are expressed in terms of the photoelastic constants of the two glass types, and of the strain level. Because n_1 and n_2 are homogeneous and isotropic, and because of the strain geometry, the strain-optic tensor reduces to only two values, p_{11} and p_{12}, and the Poisson ratio is introduced [54]. Again, it is assumed that the Poisson ratio for the core and cladding can be considered equal. The resulting expression for axial strain is then,

$$\Delta n_1 = \varepsilon_z\left\{-\frac{1}{2}n_1^{\,3}\left[(1-\nu)\,p_{12} - \nu\,p_{11}\right]\right\}$$

and $\qquad (4.28)$

$$\Delta n_2 = \varepsilon_z\left\{-\frac{1}{2}n_2^{\,3}\left[(1-\nu)\,p_{12} - \nu\,p_{11}\right]\right\} .$$

For ease of notation, these will be simplified using the following definitions:

$$p_{\text{eff}} \equiv (1-\nu)\,p_{12} - \nu\,p_{11} \qquad (4.29)$$

and

$$\alpha_1 \equiv -\frac{1}{2}n_1^{\,3}\,p_{\text{eff}} ; \qquad \alpha_2 \equiv -\frac{1}{2}n_2^{\,3}\,p_{\text{eff}} . \qquad (4.30)$$

Combining terms from above, we find the total phase change due to refractive index change can be written as

$$\Delta\theta_n = L S \left(\frac{k_0\, a\, n_1}{\sqrt{n_1^2 - n_2^2}}\, \epsilon_z \alpha_1 - \frac{k_0\, a\, n_2}{\sqrt{n_1^2 - n_2^2}}\, \epsilon_z \alpha_2 \right) \quad (4.31)$$

$$= S\, V \left(\frac{n_1 \alpha_1 - n_2 \alpha_2}{n_1^2 - n_2^2} \right) \Delta L \quad . \quad (4.32)$$

If we further define an effective strain-index coupling coefficient:

$$\alpha_{\text{eff}} \equiv \frac{n_1 \alpha_1 - n_2 \alpha_2}{n_1^2 - n_2^2} \quad , \quad (4.33)$$

we finally arrive at a simple expression for the change in phase due to refractive index changes:

$$\Delta\theta_n = \alpha_{\text{eff}}\, S\, V\, \Delta L \quad . \quad (4.34)$$

4.2.4 Combined Sensitivity

It now remains to gather the results from the previous sub-sections and substitute them into $\Delta\theta$ of equation (4.14) to find the total phase sensitivity of the single mode interferometer per unit axial strain per unit fiber length. Combining (4.16), (4.14), and (4.34) yields the expression

$$\frac{\Delta\theta}{\epsilon_z L} = \left[\beta - \nu S V + \alpha_{\text{eff}} S V \right] \quad . \quad (4.35)$$

In order to assess the meaning of this relation, we substitute realistic values of the associated fiber parameters into the expression. Table 4.1 presents a list of the values used for this study. This gives approximately

$$\frac{\Delta\theta}{\varepsilon_z L} \approx [\, 14{,}500{,}000 - 5{,}000 - 13{,}000 \,] = 1.44 \times 10^7 \text{ m}^{-1} . \qquad (4.36)$$

First note that the contribution due to the change in length is three orders of magnitude larger than that due to the change in index, which is itself twice as large as that due to radius change. Thus for the case of axial strain, one may approximate the phase sensitivity per unit strain per unit length by β, which here is roughly equal to $n_2 k_0$. Second, we observe that the second and third terms are negative, meaning that the change in radius and the change in index tend to partially offset the effect of axial elongation. That is, whereas elongation leads to a delay in the phase of the signal, decreasing the radius and the differential refractive index create phase advance. Qualitatively, elongation means that there is a longer length of fiber to traverse; on the other hand, a decrease in radius results in a slight improvement in waveguide dispersion delay, and the net *de*compression which occurs when combining the elongation and radius decrease leads to a decreased effective index for the fiber, thus reducing the optical path length.

It should also be noted that although most of the values in Table 4.1 are widely accepted for single mode fiber operation, as pointed out by Bertholds and Dändliker [102], those for the strain optic coefficients may not be typical. They empirically determine ν, p_{11}, and p_{12} to be 0.16, 0.113, and 0.252, respectively. Using these values, the last term above is reduced in magnitude by about five percent. Although this is not significant here, it might become so in the case of multimode fiber sensors, where the change in index makes a much higher contribution to the overall phase sensitivity.

Finally we note by way of example, that for a relatively short sensor length of 1 cm experiencing 1 microstrain, we could expect to see a phase change of 0.144 radians, or 8.3 degrees. For transmitted optical powers and detector sensitivities typical in fiber optic sensor laboratories, such a signal change would be readily discernable. It can be shown that for a 1 Hz system bandwidth, SNR's of up to 100 dB can be achieved [100].

4.2.5 Previous Calculations for Single Mode Fiber Sensitivity

Before moving on to the case of radially applied strain, it is appropriate to digress and emphasize where the present investigation departs from and enhances previous models. The first paper to discuss the optical fiber interferometer was authored by Butter and Hocker in 1978, and virtually pioneered the way for the advent of fiber optic sensors [54], having now been referenced thousands of times in the literature. In that paper, the interferometer phase sensitivity is derived in a manner similar to that presented above. To our knowledge, the results of that paper have not been criticized in the literature, except to extend them to a more general case of strain geometry [58], although the results have been used and repeated over and over. However, it is believed that those previous calculations contain minor errors in both their determination of the change in phase due to radius as well as refractive index changes. For the single mode fiber case, the magnitude of the errors introduced are not serious from a numerical point of view, but for both dual mode and multimode fiber sensors, they become significant.

Consider the term due to the change in the fiber radius. The first difference is that Butter and Hocker present their discussion in terms of diameter rather than radius, so for the moment, we follow their convention. Next we note that in equation (4.20), they do not choose to use the approximation, which as noted before, makes little difference for single mode fibers, but should lead to a more precise answer. However they express the change in diameter as $\Delta D = + D \nu \varepsilon_z$ rather than as $- D \nu \varepsilon_z$ (see equation (4.23) above). It is clear from the rest of their paper that they are aware of the negative proportionality between axial and radial strain, and its not being included here appears to be an oversight. Carrying their method through correctly, if we substitute the values listed in section 4.2.2 into

$$\Delta\theta_a = \left[\frac{\partial\theta}{\partial\beta}\right] \cdot \left[\frac{\partial\beta}{\partial b}\right] \cdot \left[\frac{\partial b}{\partial V}\right] \cdot \left[\frac{\partial V}{\partial D}\right] \Delta D \tag{4.37}$$

and further note that

$$\frac{\partial V}{\partial D} = \frac{k_0}{2}\sqrt{n_1^2 - n_2^2} \ , \tag{4.38}$$

then we arrive at an expression for the sensitivity due to radius change:

$$\Delta\theta_a = -\frac{2 \nu V^3 S_b}{\beta D^2} \Delta L \ . \tag{4.39}$$

Butter and Hocker list their result as

$$\Delta\theta_a \bigg|_{BH} = +\frac{\nu V^3 S_b}{2 \beta D^2} \Delta L \ , \tag{4.40}$$

which obviously differs from (4.39) by the sign term noted above, as well as a factor of four. The sign difference indicates that they predict a phase delay rather than an advance, as explained above. For this single mode case, the magnitude of the error is inconsequential, and would be impossible to detect in the laboratory. This probably accounts for why their calculation has gone uncontested all these years (that is, it is likely that others have noticed this discrepancy, but being of little or no consequence in single mode fibers, it has not been reported). Because of its small magnitude, made even smaller by their factor of four reduction, Butter and Hocker, drop this term from the final expression. Those following in their footsteps simply do not bother to calculate it. Lastly, we note that when parameters from Table 4.1 are substituted into (3.39), we find $\Delta\theta_a = 5{,}056$, as compared to $5{,}055$ from (4.24), which was obtained somewhat more simply.

Butter and Hocker's calculation of the phase change due to index changes involves a more serious difference than that for the term above. Initially, they state that

$$\Delta\theta_a = L \left[\frac{\partial \beta}{\partial n}\right] \Delta n \ , \tag{4.41}$$

in agreement with equation (55) above. However, nowhere in their analysis do they differentiate between the core and cladding glasses, nor account for the fact that the strains effect on each tend to partially cancel. Rather, they argue that since $\beta \approx k_0 n$ (where n is always taken in the literature to be n_1), then $\partial\beta/\partial n_1 = k_0 = \beta/n_1$. Though this appears to be a justified assumption according to the words of weak guidance, it violates the spirit. That is, it is well understood that the approximation can be made, in the words of Marcuse, "whenever the exact value of β is not important" [103]. However, in this case, we are specifically investigating β and the way it changes with a change in index, the fine structure of which is masked by this treatment.

Replacing Δn with $\alpha_1 \epsilon_z$ from above, their formulation then yields for the parameter values used above

$$\frac{\Delta\theta_n}{\epsilon_z L} = \frac{\alpha_1 \beta}{n_1} = -3.13 \times 10^6 \text{ m}^{-1} , \qquad (4.42)$$

which is a factor of nearly 250 larger than the value calculated earlier. Thus in their work, they estimate the change in index term to be down by less than an order of magnitude from the length change term, suggesting that it plays a much more significant role in single mode interferometers than is true in reality.

A final comment about Butter and Hocker's work regards the experiment they performed, and their statement that the results stood in excellent comparison with the expected value. It is noted that when they added the respective phase terms to get the total sensitivity, all of the constituent factors were approximated. Compared to the fiber that was actually used, a number of the approximations were too high: $n = 1.5$, $V = 2.5$ (the cut-off frequency to ensure single mode operation is 2.405), $v = 0.25$, $P_{11} = P_{12} = 0.3$. Furthermore, a number of assumptions were made concerning the experimental conditions and parameters such as the fiber length, the most questionable being that the strain in the cantilever beam to which the fiber was adhered was entirely transferred to the fiber. No account for the strain in the fiber jacket or cement is offered, though

extensive experience demonstrates that these elements are important in effecting an incomplete strain transfer, thereby reducing the detected strain. Thus, while none of these approximations or assumptions are unreasonable in themselves, the exact value of neither the predicted nor the empirical value should be taken as an absolute number. Their agreement should then be taken in terms of order of magnitude only.

To summarize the previous work then, it is observed that the bulk of what is reported in the literature rests on the conceptual foundation laid by Butter and Hocker. Recognizing the importance of their calculations, we nevertheless note that they appear to be flawed in that they

- reverse the sign of $\Delta\theta_a$,

- reduce $\Delta\theta_a$ by a factor of four,

- suggest that $\partial\beta/\partial n$ can be approximated by a constant k_0, and

- do not account for differential changes between n_1 and n_2.

Despite the tone of this section, it is meant only to be instructional and not critical. It is well worth recognizing that the errors introduced above were numerically small, so that the order of magnitude for the total phase sensitivity was correctly arrived upon, while their basic procedure provided an important stepping stone for a plethora of further work.

4.2.6 Radial Strain

We now turn our attention to the case where strain is applied along the fiber radius rather than the fiber axis. In this model, we will assume that the fiber is subject to uniform radial strain ε_r, that is, it is the same at every point around the radius, and that the ends are free to contract or expand accordingly. This corresponds to a fiber length through which an acoustic wave passes, assuming the fiber diameter is much less than the acoustic wavelength.

All of the general comments in the beginning of Section 4.2 still apply, with the result that we are trying to evaluate

$$\Delta\theta = \Delta\theta_L + \Delta\theta_a + \Delta\theta_n \ , \tag{4.43}$$

again with $\theta = \beta L - \psi$. For the change in length, we have

$$\Delta\theta_L = \left[\frac{\partial\theta}{\partial L}\right]\Delta L = \beta L \varepsilon_z \ . \tag{4.44}$$

From the basic laws of mechanics and by considering the fiber geometry, it can readily be shown that

$$\varepsilon_z = -\frac{2\nu}{1-\nu}\varepsilon_r \ . \tag{4.45}$$

Thus,

$$\Delta\theta_L = -\left(\frac{2\nu}{1-\nu}\right)\beta L \varepsilon_r \ . \tag{4.46}$$

Notice that the length change contribution has been reduced with respect to the axial strain case by a factor of $2\nu / (1-\nu) \approx 0.4$. The negative sign merely reflects that as the fiber is squeezed radially by the sound, the fiber elongates in response; that is, compression in r leads to tension in z.

The next term in equation (4.43) is derived in the same manner as for axial strain, with the difference that Δa is left expressed in terms of ε_r. So,

$$\Delta\theta_a = S V L \varepsilon_r \ . \tag{4.47}$$

The phase sensitivity for changes in index again proceeds as for axial strain, though for this case the definitions for Δn_1 and Δn_2 must be altered. From reference 100, we find the fundamental definitions of the optical indicatrix terms quoted in simplified form. Repeating them here,

$$\Delta n_x = -\frac{1}{2}n^3 [p_{11}\,\varepsilon_x + p_{12}\,\varepsilon_y + p_{12}\,\varepsilon_z] \tag{4.48}$$

$$\Delta n_y = -\frac{1}{2}n^3 [p_{12}\,\varepsilon_x + p_{11}\,\varepsilon_y + p_{12}\,\varepsilon_z] \tag{4.49}$$

$$\Delta n_z = -\frac{1}{2}n^3 [p_{12}\,\varepsilon_x + p_{12}\,\varepsilon_y + p_{11}\,\varepsilon_z] \quad . \tag{4.50}$$

For the fiber geometry given earlier in Figure 3.1, radial strain implies that $\varepsilon_x = \varepsilon_y = \varepsilon_r$, while the expression for ε_z is given in equation (4.45). Hence

$$\Delta n_x = -\frac{1}{2}n^3 \left[(p_{11} + p_{12}) - \left(\frac{2\nu}{1-\nu}\right)p_{12} \right]\varepsilon_r \tag{4.51}$$

$$\Delta n_y = -\frac{1}{2}n^3 \left[(p_{11} + p_{12}) - \left(\frac{2\nu}{1-\nu}\right)p_{12} \right]\varepsilon_r \tag{4.52}$$

$$\Delta n_z = -\frac{1}{2}n^3 \left[2\,p_{12} - \left(\frac{2\nu}{1-\nu}\right)p_{11} \right]\varepsilon_r \quad . \tag{4.53}$$

The modes in a weakly guiding fiber are predominantly transverse, meaning that refractive index variations in the direction of propagation may be ignored. Rearranging the bracketed terms in (4.51) and (4.52), and noting that x and y are both radial directions, we find

$$\Delta n_r = -\frac{1}{2}n^3 \left[p_{11} + \left(\frac{1-3\nu}{1-\nu}\right)p_{12} \right]\varepsilon_r \quad . \tag{4.54}$$

If simplifying definitions are again made such that

$$p_{eff}' \equiv p_{11} + \left(\frac{1-3\nu}{1-\nu}\right)p_{12} \quad , \tag{4.55}$$

where the prime is added to distinguish p_{eff}' from its value under axial strain. Finally then

$$\Delta n_1 = -\frac{1}{2} n_1^3 p_{eff}' \varepsilon_r = \alpha_1' \varepsilon_r$$

$$\Delta n_2 = -\frac{1}{2} n_2^3 p_{eff}' \varepsilon_r = \alpha_2' \varepsilon_r \; . \tag{4.56}$$

When these values are substituted into equation (4.26) to find the phase change due to index change, an equation of the same form as previously derived results, where primed quantities replace the unprimed. That is,

$$\Delta \theta_n = \alpha_{eff}' \, S \, V \, L \, \varepsilon_r \; . \tag{4.57}$$

Combining the individual terms from equations (4.46), (4.47), and (4.57), we arrive at the total phase sensitivity of a single mode interferometer undergoing radially applied strain per unit strain per unit length. This yields

$$\frac{\Delta \theta}{\varepsilon_r L} = \left[-\left(\frac{2\nu}{1-\nu} \right) \beta + S \, V + \alpha_{eff}' \, S \, V \right] \; . \tag{4.58}$$

If the new values from Table 4.2 are applied,

$$\frac{\Delta \theta}{\varepsilon_r L} = [\, -5,900,000 + 30,000 - 18,000 \,] \; . \tag{4.59}$$

Emphasizing the obvious, we first observe that despite the strain direction, the length of the sensor and its change with strain still dominate its sensitivity. Also, it is clear that to make these expressions useful for predicting the absolute sensitivity to acoustic wave disturbances, the waves must be specified in terms of the actual radial strain level imparted to the fiber. Unlike the normal applications for the axial strain expression, this requires further and often complicated models for acoustic wave propagation in the material surrounding the fiber.

Secondly, we are struck by the fact that the signs in front of the terms in (4.58) look unfamiliar. This is because in the case of axial strain, a tensile strain was assumed as positive, so that elongation led to a positive phase retardation in the $\Delta\theta_L$ term. In the radial case, we have assumed a positive compressive strain. If for the sake of comparison we rather specify tensile loading as imparting positive strain in the load direction, or alternatively simply consider fiber elongation as positive, we may write

$$\frac{\Delta\theta}{\varepsilon_r L} = [\,5{,}900{,}000 - 30{,}000 + 18{,}000\,] \approx 5.9 \times 10^6 \text{ m}^{-1} \, . \qquad (4.60)$$

Note that as in the previous situation, the decrease in radius leads to a phase advance (the wave arrives at the end a little faster), but now the radial strain affects the photoelastic coefficients in such a way as to cause a phase retardation, adding to the elongation term. Also observe that now the radius term is somewhat larger than the index term, and both are relatively larger with respect to the total than before, though both are still down by a factor of 200 or more from the length term.

A further comment is in order to compare the single mode phase sensitivity for axially and radially applied strain:

$$\left.\frac{\Delta\theta}{\varepsilon_r L}\right|_{\text{axial}} \approx 1.5 \times 10^7 \text{ m}^{-1} \, ,$$

whereas

$$\left.\frac{\Delta\theta}{\varepsilon_r L}\right|_{\text{radial}} \approx 0.6 \times 10^7 \text{ m}^{-1} \, .$$

This says that for single mode fiber, the change of phase is approximately two and a half times less sensitive to radially applied strain as compared to axially applied strain. This should be kept in mind whenever the objective is to sense a uniform sound wave traversing an optical fiber. In that case, it is often assumed that since it is the fiber elongation term which most

significantly leads to phase change, one may write the equations assuming applied axial strain and expect to achieve the resulting level of sensitivity. The analysis above predicts a smaller phase shift than derived in such a manner, and therefore lower sensitivity. With this foundation laid for the single mode fiber interferometer, we are ready to move on to investigate the sensitivity of dual mode fiber sensors.

4.3 Dual Mode Fiber Sensitivity

To derive the sensitivity of the dual mode fiber, we first consider the expression for the output intensity from the core of the LP_{01}/LP_{11} sensor, which from (3.34) can be rewritten as

$$I = A_0'^2 J_0^2 + A_1'^2 J_1^2 \cos^2\phi + 2 A_0' A_1' J_0 J_1 \cos\phi \cos\theta , \qquad (4.61)$$

where the arguments of the Bessel functions have been momentarily dropped, and $\theta = \tilde{\beta}z - \tilde{\psi}$. Also, the factors in the dominator of (3.34) are considered constant for small strain levels and are thus absorbed into the new amplitude coefficients A_0' and A_1', as is the factor of Y/2. Recall that the first two terms are static with respect to disturbances, so that in order to increase sensitivity, the last term must be maximized, implying that we should set $\phi = 0$. This is equivalent to placing the detector in the output field along the x axis. Given this condition,

$$I = [A_0'^2 J_0^2(u_0 \frac{r}{a}) + A_1'^2 J_1^2(u_1 \frac{r}{a})]$$

$$+ 2 A_0' A_1' J_0(u_0 \frac{r}{a}) J_1(u_1 \frac{r}{a}) \cos\theta . \qquad (4.62)$$

Again we seek to maximize the coefficients of the last term. Noting the difference in u_0 and u_1, for realistic fiber parameters, the Bessel function product is maximized when $r/a \approx 0.42$. This implies that the detector should be set in the output field so as to intercept radiation from the point

$(x,y) = (0.42 \frac{r}{a}, 0)$, which is simply the rough location of the peak intensity, as indicated on Figure 3.9. In that case the coefficients become roughly

$$I = [0.6 A_0'^2 + 0.3 A_1'^2] + 0.9 A_0' A_1' \cos\theta . \qquad (4.63)$$

Furthermore, for typical injection conditions, it is not unreasonable that the two modes may be powered equally, that is, we assume $A_0 = A_1 = A$. Combining the numerical values into a single constant, we again arrive at

$$I = I_0 [1 + \cos(\tilde{\beta}L - \tilde{\psi})] . \qquad (4.64)$$

A sensor length of L has again been assumed, and the case of axially applied strain will be treated first. Recall that $\tilde{\beta}$ is defined as the difference between the propagation constants of the two modes, or $\tilde{\beta} = \beta_0 - \beta_1$. This is a simple, fixed number before the application of axial strain, and may change only slightly when strain is applied.

To find the strain sensitivity for the dual mode fiber, we proceed as with the single mode fiber, and similar expressions result. Thus in a manner similar to equation (4.7) for single mode fiber,

$$\Delta I = - I_0 \sin(\tilde{\beta}L - \tilde{\psi}) \left[\frac{\partial\theta}{\partial\varepsilon}\right] \varepsilon . \qquad (4.65)$$

Again, the sensitivity is maximized when the output is set at quadrature, generally accomplished for the two mode fiber sensor by adding a bias strain, or conceivably by changing the launch conditions. If quadrature is not achieved, the principle of the sensor operation remains the same, but the local, small strain sensitivity will be reduced. Assuming an optimized situation, we finally arrive at an equation of the exact form as equation (4.13) before, though with a different definition for θ, as emphasized here,

$$\Delta I = I_0 \left\{ \left[\frac{\partial(\tilde{\beta}L)}{\partial L}\right] \Delta L + \left[\frac{\partial(\tilde{\beta}L)}{\partial a}\right] \Delta a + \left[\frac{\partial(\tilde{\beta}L)}{\partial n}\right] \Delta n \right\} , \qquad (4.66)$$

where the constant phase offset is dropped from the derivative. As before, we solve for the three phase change terms, again defining them as $\Delta\theta_L$, $\Delta\theta_a$, and $\Delta\theta_n$.

4.3.1 Axial Strain for the LP_{01} and LP_{11} Mode Pair

Considering first the case of applied axial strain, it is clear by inspection that the first term in the parentheses, the change in phase due to elongation, is merely $\tilde{\beta} \, \Delta L$. To evaluate $\Delta\theta_a$, we break it into several factors, similar to equation (4.19):

$$\Delta\theta_a = \left[\frac{\partial\theta}{\partial\tilde{\beta}}\right] \cdot \left[\frac{\partial\tilde{\beta}}{\partial V}\right] \cdot \left[\frac{\partial V}{\partial a}\right] \Delta a \quad . \tag{4.67}$$

The first term in (4.67) is simply L. The second term expresses the difference in the values of the slopes of the β-V curves for the two modes at the operating frequency V. These are defined as S_0 and S_1, and correspond to the associated values on the b-V curves, S_{b_0} and S_{b_1} . Therefore,

$$\left[\frac{\partial\tilde{\beta}}{\partial V}\right] = \frac{\Delta\beta}{\Delta V} = S_1 - S_2$$

$$= (n_1 - n_2) \, k_0 \, (S_{b_0} - S_{b_1}) \equiv \tilde{S} \quad . \tag{4.68}$$

As before, the third term in (4.66) can be shown to be $k_0 \sqrt{n_1^2 - n_2^2}$, while the last term is $-a v \, \varepsilon_z$. Combining factors, we find

$$\Delta\theta_a = -v \, \tilde{S} \, V \, \Delta L \quad . \tag{4.69}$$

Similarly, we suggest that

$$\Delta\theta_n \quad = \quad \left[\frac{\partial\theta}{\partial\tilde{\beta}}\right] \cdot \left[\frac{\partial\tilde{\beta}}{\partial V}\right] \cdot \left(\frac{\partial V}{\partial n_1}\Delta n_1 + \frac{\partial V}{\partial n_2}\Delta n_2\right) \ , \qquad (4.70)$$

which by (4.67), leads to

$$\Delta\theta_n \quad = \quad \alpha_{\text{eff}} \, \tilde{S} \, V \, \Delta L \ . \qquad (4.71)$$

Here, α_{eff} is defined exactly as in (4.33).

Collecting terms, we arrive at an expression for the phase sensitivity of the dual mode sensor under axial strain per unit strain per unit length:

$$\frac{\Delta\theta}{\varepsilon_z L} \quad = \quad \left[\tilde{\beta} - \nu\,\tilde{S}\,V + \alpha_{\text{eff}}\,\tilde{S}\,V\right] \ . \qquad (4.72)$$

Table 4.3a presents the fiber parameters assumed for the dual mode fiber. The major difference with the values in Table 4.1 for single mode fiber is that the fiber diameter has been increased by 1 µm, raising the V number enough to allow a second mode to propagate and optimize (4.72). The values in Table 4.3a have therefore assumed the two modes propagating are the LP_{01} and LP_{11} modes. It is also noteworthy that with the sign convention that we have established, $\tilde{S}$ will be a negative number. Since α_{eff} has also been defined as a negative constant, both the phase change due to radius change and due to index change are now positive, *contributing* to the phase retardation created by the change in length, rather than detracting from it, as in the single mode case. Computing the sensitivity for these example numbers, we have

$$\frac{\Delta\theta}{\varepsilon_z L}\bigg|_{LP_{01}/LP_{11}} \quad \approx \quad [\, 22{,}000 + 2{,}000 + 6{,}000 \,] \quad = \quad 3\times10^4 \ \text{m}^{-1} \ . \quad (4.73)$$

Several points should be noticed here. Most importantly, the dual mode fiber sensor can be seen to be approximately 500 times less sensitive than

the single mode interferometer. Thus for the advantages of simplicity and stability, nearly three orders of magnitude are lost in sensitivity. Also, observe that the radius and index terms now make up a much larger percent of the total phase change than before, about 8% for the radius term instead of 0.03%, and about 20% instead of 0.08% for the index term. This arises because of the fact that the difference in the propagation constants for the two modes is quite small compared to b itself, where that is much less true for the slope of the curves. That is,

$$\frac{\tilde{S}}{S} \; = \; 0.38 \; >> \; 0.0015 \; = \; \frac{\tilde{\beta}}{\beta} \, . \tag{4.74}$$

The relative size of the radius term is thus large enough that it should not be neglected, as has been done in previous analyses.

We note that the V number in Table 4.3a was specified somewhat arbitrarily, and that it could have been chosen to be larger. This would have the effect of decreasing the difference in propagation constants, $\tilde{\beta}$, though $\tilde{S}$ would increase. With a larger $\tilde{S}$ and V, the radius and index terms would increase relative to the elongation term. This should be kept in mind when optimizing the sensor for acoustic waves transverse to the fiber, where these terms are more significant.

4.3.2   The LP_{01} and LP_{02} Mode Combination

Next we consider the dual mode combination of the LP_{01} and LP_{02} modes. As stated in section 3.4.2, the interference of this mode pair results in an azimuthally symmetric output pattern, the expression for which appears in equation (3.37). As noted, the interference cross term also contains a factor of $\cos\theta$ such as appears in the other mode pairs, and the functional dependence on $\Delta\theta$ is the same. Here however, gains are made in that both $\tilde{\beta}$ and $\tilde{S}$ are larger than before. To show this, we obtain the parameters for a fiber which allows the propagation of the LP_{02} mode,

recalculate constituent factors, and substitute them into equation (4.71). The values appear in Table 4.3b, and they yield

$$\frac{\Delta\theta}{\varepsilon_z L}\bigg|_{LP_{01}/LP_{02}} \approx [\,98{,}000 + 26{,}000 + 66{,}000\,] = 1.9 \times 10^5 \text{ m}^{-1}, \qquad (4.75)$$

which shows a phase sensitivity more than six times greater than the interference between the first two modes, and now 75 times less sensitive than the single mode interferometer. In addition to the increased sensitivity, further advantage is gained from the symmetric output. For one, it is evidence of the fact that these modes do not exist as being even or odd; thus there is no fear of the even/odd mode coupling which tends to rotate the output pattern of the LP_{01}/LP_{11} sensor, confusing the magnitude of the strain. For another, because the point of maximum sensitivity is in the center of the output pattern, placement of the detector is made more simple, especially if a miniaturized, enclosed receiver is employed. The major disadvantage of this mode combination is the need for specialized quadruple-clad fiber in order to avoid launching of unwanted modes.

4.3.3 Dual Mode Fibers Under Radial Strain

With the groundwork which has gone before, it is straightforward to extend the analysis to cover the case of radial strain in dual mode fibers. By analogy to the axial strain case, we may go to equation (4.58) (recalling the sign convention established thereafter) and write directly

$$\frac{\Delta\theta}{\varepsilon_r L} = \left[\left(\frac{2\nu}{1-\nu}\right)\tilde{\beta} - \tilde{S}V - \alpha'_{\text{eff}}\tilde{S}V\right] . \qquad (4.76)$$

With the values prescribed in Tables 4.2 and 4.3a,

$$\frac{\Delta\theta}{\varepsilon_r L}\bigg|_{LP_{01}/LP_{11}} = [\,9{,}000 + 14{,}000 - 8{,}300\,] = 1.5 \times 10^4 \text{ m}^{-1} . \qquad (4.77)$$

Of interest in this expression is the fact that the sign of $\tilde{S}$ now leads to the radius term working in conjunction with the length term to create phase retardation, while the index term acts against these two. Obviously the sensitivity is most influenced by the radius term, which is now up from its value under axial strain by a factor of seven. The length term is reduced because of the nature of the way in which the strain is applied, whereas the radius is greater by a factor of $1/\nu$ for the same reason. Again, however, note that for the dual mode LP_{01}/LP_{11} case, the phase change due to axial strain is twice as large as that due to radial strain. Also, the latter is down by a factor of approximately 400 as compared to the single mode interferometer under radial strain, being 20 percent better for the radial strain sensor than for the axial.

Finally we consider the LP_{01}/LP_{02} sensor experiencing radial strain. The only differences with the preceding sensor arise due to the fact that V, α'_{eff}, $\tilde{\beta}$ and $\tilde{S}$ take on altered values for this mode combination. Substituting the numbers gives

$$\frac{\Delta\theta}{\varepsilon_r L}\bigg|_{LP_{01}/LP_{02}} = [\, 40{,}000 + 152{,}000 - 89{,}000 \,] = 1.0 \times 10^5 \text{ m}^{-1} \ . \tag{4.78}$$

Clearly a sensitivity advantage exists over the LP_{01}/LP_{11} sensor, being up from it by a factor of more than six. It is also interesting to note how large a role the change in radius term plays, giving a hint of what is to come with the multimode sensor. It is to this case that we turn next.

4.4 Sensitivity of Multimode Modal Domain Sensors

It remains to calculate the phase sensitivity of multimode fibers experiencing strain. We begin with several preliminary remarks. First, it has been shown in equation (3.47) that the interference between any two modes in a multimode fiber have a phase term which contains $\tilde{\beta}z$, where again $\tilde{\beta}$ is the static difference between the propagation constants for the

two modes. In general the amplitude coefficients in front of the phase terms will differ for different mode pairs, where these express the spatial distribution of the output, and the modulation depth of the interference terms. Though equal amplitudes were assumed for the light in the two fibers of the single mode interferometer and in the two mode LP_{01}/LP_{11} sensor. it should be kept in mind that in general the power in the fiber will not be equally distributed among the modes. Thus the modulation depth will vary for different mode combinations.

Second, though the phase of any particular mode can be calculated as a function of V, there is no general rule about individual mode combinations and their value of $\tilde{\beta}$. Neighboring modes do not necessarily have a small $\tilde{\beta}$, though this is usually the case, depending on how "neighboring" is defined. However, the magnitude of the interference term between any two modes will change with perturbation; thus any two modes can be employed for sensing. Nevertheless, it will not usually be possible to separate out the interference between two particular discrete modes in a multimode fiber. All of the modes which coexist will simultaneously and mutually interfere, giving the complicated, pseudo-random speckle pattern. It is noted that in some cases it might be possible to monitor the interference between particular mode pairs, especially if it is only those modes which are excited. Specifically we cite the work of Kapany and Burke [104] and Berdague and Facq [105], who photographed outputs from individual modes by placing masks at the input specifically targeted to launch specific modes. On the other hand, Spajer used a filter at the output modes to distinguish the LP_{01}/LP_{02} combination [96]. However, these methods introduce many new unknowns, and so will not be further discussed.

Third, it could be said that the fiber sensitivity will generally be as sensitive as the most sensitive mode combination, especially since each mode intensity distribution fills the whole fiber, even if only weakly in some cases. A perturbation will cause the most sensitive mode combinations to change their differential phase, which will lead to a speckle rearrangement in at least some part of the output field. The modulation depth will again be reduced, depending on the particular modes and their power levels. The

situation could be further complicated if the sensitive spot overlaps in the output plane with a less sensitive spot, which will in effect amplitude modulate the spot of interest.

The most sensitive mode pairs will be those for which $\tilde{\beta} = \beta_1 - \beta_2$ and $\tilde{S} = S_1 - S_2$ are maximized. For the propagation constant, this implies a low order mode whose value of β is already near $n_1 k_0$ for the given V of the fiber, and a high order mode just beyond its cut-in frequency, having β near $n_2 k_0$. To show this, we make use of the WKB method for analyzing a multimode fiber having a power-law profile [106,107]. An eigenvalue equation is derived, for which a "pseudo-solution" for β is arrived upon. The result is

$$\beta = n_1 k_0 \left[1 - 2\Delta \left(\frac{M(\beta)}{\left(\frac{\alpha}{\alpha+2} \right) n_1^2 k_0^2 a^2 \Delta} \right)^{\frac{\alpha}{\alpha+2}} \right]^{\frac{1}{2}} \qquad (4.79)$$

where the denominator

$$N = \left(\frac{\alpha}{\alpha+2} \right) n_1^2 k_0^2 a^2 \Delta = \left(\frac{\alpha}{\alpha+2} \right) \frac{V^2}{2} \qquad (4.80)$$

is the total number of modes, and $M(\beta) = (2\ell + m + 1)^2$ is the compound mode number squared, and defined to be the number of modes with values of the propagation constant that are larger than β. Because the solution for β actually depends on β, it can be seen why this is referred to as a pseudo-solution; nevertheless it is useful for many practical purposes. Also, though the WKB method is generally discussed in regard to graded index fibers, the step index profile is included by setting $\alpha = \infty$. In that case,

$$\beta = n_1 k_0 \left[1 - 2\Delta \left(\frac{M(\beta)}{n_1^2 k_0^2 a^2 \Delta} \right) \right]^{\frac{1}{2}} . \qquad (4.81)$$

Rather than multiplying the Δ through in the second term in brackets, and thereby imply that β is independent of n_2, we note that for any particular mode, the fraction in parentheses will always be less than 1. For low order modes, it will approach $1/N$, which may be as low as $1/5000$ for a normal multimode step index fiber. In stating this, we note that though this expression was derived for a fiber with a large number of modes, that is not to say that it is invalid for low order modes in such a fiber. Rather, it implies that for a normal fiber Δ of 0.01, then on the β-V curve, β will take a value of 0.999998 $n_1 k_0$ at a typical value of V. This corresponds to the asymptotic value of low order mode propagation constants far out in V, such as observed in Figure 3.2. On the other hand, for a large order mode, $M(\beta) \to N$, or $\dfrac{M(\beta)}{N} \to 1$. Thus the limiting values of β from this analysis are

$$\beta_{hi} \approx n_1 k_0 [1 - 2\Delta]^{1/2} = n_2 k_0$$

$$\beta_{lo} \approx n_1 k_0 \tag{4.82}$$

confirming what has been previously stated.

Thus the maximum difference between the static propagation constants of two modes is simply

$$\tilde{\beta}_{max} = (n_1 - n_2) k_0 . \tag{4.83}$$

Meanwhile, for low order modes at high V, the slope $S_{b_1} \approx 0$, while we assume from the curves (Figure 3.2), that $S_{b_2} \approx 0.1$, meaning

$$\tilde{S}_{max} \approx -0.1 (n_1 - n_2) k_0 = \dfrac{-\tilde{\beta}_{max}}{10} , \tag{4.84}$$

where both $\tilde{\beta}_{max}$ and $\tilde{S}_{max}$ have units of m^{-1}.

It is clear from expression for $\Delta\theta$ in equation (4.72) that besides $\tilde{\beta}$ and $\tilde{S}$, the most important factor for determining total phase sensitivity is V. This

means that in general, fibers with high V will be more sensitive than low-V fibers. From the definition of V, this might suggest lowering the source wavelength, enlarging the fiber radius, or increasing the quantity $n_1 - n_2$. The latter also works to increase $\tilde{\beta}_{max}$ and $\tilde{S}_{max}$ through (4.83) and (4.84).

We will consider the interference of modes in three cases. In the first example, typical step index, multimode fiber such as often used for short-haul communications will be addressed. In the second case, we examine the sensitivity of a commercially available fiber which has been used for the detection of ultrasound, to be reported later, and which has the unusual property that it is a simple, unclad silica thread, 25 μm in diameter. The final case to be treated is the "optimized" sensor, in which fiber parameters are all manipulated so as to obtain the highest sensitivity possible. The values of the assumed fiber parameters for all three cases appears in Table 4.4. We note at the outset that all values are meant to be representative, and calculations are all approximate so as to appreciate only their order of magnitude.

Typical Step Index Multimode Fiber

Using the values in the first column of Table 4.4 in equation (4.72), we have in the case of axially applied strain

$$\frac{\Delta\theta}{\epsilon_z L}\bigg|_{typical} = [\ 290{,}000\ +\ 710{,}000\ +\ 1{,}770{,}000\ ]$$
$$= 2.8 \times 10^6\ . \tag{4.85}$$

We are first struck by the fact that the sensitivity is now only a factor of five down from the single mode interferometer. Also we note that the values of $\tilde{\beta}$ and $\tilde{S}$ are significantly higher than for low mode fibers. When combined with the large V, this means that $\Delta\theta_a$ and $\Delta\theta_n$ now make a much larger contribution to the total than in the single mode case, even outweighing the elongation term. The total sensitivity can be seen to be greater than that of the LP_{01}/LP_{11} sensor by nearly two orders of magnitude.

In the case of radial strain, we use all of the prior reasoning and substitute values into equation (4.76), and arrive at

$$\frac{\Delta\theta}{\epsilon_r L}\bigg|_{\text{typical}} = [\,119{,}000 + 4{,}180{,}000 - 2{,}430{,}000\,]$$
$$= 1.9 \times 10^6 \ . \tag{4.86}$$

This now appears to be a factor of roughly three less sensitive than the single mode interferometer under radial strain. Also we note that the gain from single mode to multimode is twice as good for the radial strain case as the axial strain case, though the actual sensitivity itself is down somewhat.

Unclad Silica Fiber

For this sensor and the next, the analysis above must be modified. The fiber under consideration is unclad glass rod which has been drawn down into very fine fiber. We assume for the moment that the fiber is surrounded by air of index 1, so that when the fiber is strained axially, the "cladding" itself is not under stress. So while $\Delta\theta_L$ and $\Delta\theta_a$ remain the same, $\Delta\theta_n$ does not include a contribution due to a changing n_2. This will be true of any liquid or gas clad fiber. Thus,

$$\Delta\theta_n = \left[\frac{\partial\theta}{\partial\tilde\beta}\right] \cdot \left[\frac{\partial\tilde\beta}{\partial V}\right] \cdot \left[\frac{\partial V}{\partial n_1}\right] \cdot \Delta n_1 \tag{4.87}$$

$$= \tilde S \ V \left(\frac{n_1\,\alpha_1}{n_1^{\,2} - n_2^{\,2}}\right) \Delta L \ . \tag{4.88}$$

Hence for the fiber parameters at hand,

$$\alpha_{\text{eff}} = -\frac{\frac{1}{2}n_1^{\,4}\,P_{\text{eff}}}{n_1^{\,2} - n_2^{\,2}} \approx -0.4088 \ . \tag{4.89}$$

Interestingly, had n_2 been included as a changing quantity, then α_{eff} would have been reduced by a factor of 25%, in turn reducing $\Delta\theta_n$ and thus the overall sensitivity. Since here n_2 does not enter the calculations, α_{eff} is on par with that for the typical fiber, leading to a higher sensitivity. It is possible to understand this qualitatively due to the fact that we have no compensating n_2 change to counteract the n_1 change.

Substituting the remaining parameters from Table 4.4, we find

$$\left.\frac{\Delta\theta}{\varepsilon_z L}\right|_{\substack{\text{unclad} \\ \text{fiber}}} = [\, 4{,}500{,}000 + 10{,}200{,}000 + 24{,}600{,}000\,]$$

$$= 3.9 \times 10^7 \, , \tag{4.90}$$

which is well over twice as sensitive as the single mode interferometer under axial strain.

This fiber under radial strain yields a sensitivity calculated as

$$\left.\frac{\Delta\theta}{\varepsilon_r L}\right|_{\substack{\text{unclad} \\ \text{fiber}}} = [\, 1{,}900{,}000 + 59{,}900{,}000 - 33{,}700{,}000\,]$$

$$= 2.8 \times 10^7 \, . \tag{4.91}$$

Now the sensitivity is nearly five times more than for the radially strained single mode fiber, and is slightly less than the axially strained case in terms of absolute sensitivity.

Optimized Sensor

Finally, we consider an optical fiber whose parameters have been chosen so as to optimize its phase sensitivity. It is recognized that the parameters appearing in Table 4.4 do not represent any commercially available fiber, nor are they necessarily convenient; it is believed however, that they are not unreasonable for the present argument. Furthermore, it

is assumed that the Poisson's ratio and the photoelastic constants remain the same as in previous cases, which may not be true for an optimal sensor. Using the numbers, we have

$$\frac{\Delta\theta}{\varepsilon_z L}\bigg|_{optimized} = [\,9{,}000{,}000 + 248{,}000{,}000 + 657{,}000{,}000\,]$$
$$= 9.1 \times 10^8 \ . \tag{4.92}$$

Most significantly, this displays an intrinsic phase sensitivity of more than 60 times that of the single mode interferometer.

If radial strain is applied to this fiber, we conclude the phase sensitivity is given by

$$\frac{\Delta\theta}{\varepsilon_r L}\bigg|_{optimized} = [\,3{,}500{,}000 + 1{,}461{,}000{,}000 - 902{,}000{,}000\,]$$
$$= 5.6 \times 10^8 \ . \tag{4.93}$$

This is almost two orders of magnitude more sensitive than the radially strained single mode interferometer, and is again nearly as sensitive as the axially strained optimized sensor.

4.5 Discussion

The basic theory for the existence of discrete modes in optical fibers has been presented in Chapter 3. The number of modes which are allowed to propagate in a fiber is determined by the frequency of operation, the refractive index profile, and the fiber geometry, summarized in the normalized frequency, V. On the other hand, the particular modes which exist in a waveguide depend on the injection conditions and on mode coupling mechanisms which exist along its length. When more than one mode is present and the light is coherent, the modes interfere along the fiber, as well as in the output plane. The nature of the interference pattern,

its spatial description, as well as its response to perturbations along the fiber, depends on the particular modes in question.

It has been shown that when these fibers are subjected to strain, the phase of the one or more constituent modes changes in direct proportion to the disturbance. If the outputs from two single mode fibers are brought together, an absolute interferometer can be constructed to monitor the perturbation in one of the fibers. Alternatively, differential phase changes between coherent modes of a multimode fiber can also be employed to infer strain. It is generally accepted that whereas single mode interferometers display the highest strain sensitivity, modal domain sensors offer the advantage of greater stability and simplicity.

In this study, the absolute phase sensitivity of both sensor types has been derived. Corrections were made to previous models, and the case of radially applied strain was treated in addition to the standard case of axially applied strain. These calculations can be summarized in tabular form, as seen in Table 4.5. Perhaps the most striking conclusion is that for the phase sensitivity of highly multimode fibers is seen to rival that of single mode interferometers, and in some cases, even surpass it by as much as nearly two orders of magnitude. Also, note that any gains made by using the specialized multimode fibers are only increased for the case of applied radial strain, which for the case of acoustic detection is the primary straining mechanism.

To those with much experience handling highly multimode modal domain sensors, the mathematical results obtained may not come as a complete surprise, despite the general impression that the single mode interferometer is the most sensitive of all optical fiber sensors. For example, in an early MDS paper, T.J. Hall reports that his multimode modal domain hydrophone "was found to have a sensitivity, in terms of phase change per unit pressure, similar to that of a monomode optical fiber hydrophone of similar construction" [11].

Recent experiments at Virginia Tech confirm these findings [108]. In one test, plastic clad silica fiber (PCS) was embedded in graphite-epoxy panels and subject to ultrasonic wave excitation of modal modulation. The PCS, characterized by a high core-cladding index difference and a large

core, was seen to show considerable sensitivity improvement over normal 50/125 step index fiber in a similar acoustic environment. Not only does PCS have a large V number, but also has a compliant polymer coating which efficiently transfers strain. Analysis similar to the last section suggests that in the case of radial strain, PCS should be between five and ten times more sensitive than the single mode fiber interferometer. In another test, 25 micron, unclad silica fiber such as previously described was attached to the same panel and insonified. Similar fibers have also been reported being laid in composite pre-preg for use as damage sensors after cure of the laminate [75]. Again a sensitivity improvement was noticed over the PCS, and though not fully quantified, lend agreement with the analysis summarized in Table 4.5.

Finally, in work recently reported by Indebetouw, et. al., holographic matched filters were applied to the outputs of both dual and multimode fibers in an effort to provide full-field signal processing of sensor outputs [109]. By comparing the plots of the intensity versus strain of the filtered output, one can again see an increased sensitivity for the multimode fiber, though not as much as perhaps expected from the prior analysis. It does, however, give credence to the notion that multimode modal sensors are in fact more sensitive than their few mode counterparts.

It is vital to bear in mind that the numbers quoted above express, as has been said so many times, the absolute *phase* sensitivity of interferometrically-based optical fiber sensors. We have said nothing about whether or not it would ever be possible to take advantage of this sensitivity to make a practical sensor, or what kind of inconveniences doing so might require. Furthermore, several steps are still needed in order to completely predict the response of such a sensor to say, ultrasonic waves in a material. First, and most simply, if we specify detector parameters such as responsivity and size, a detection bandwidth, and input laser power, a number for the strain sensitivity can be derived. For values typical in an ordinary laboratory, such calculations yield a strain sensitivity of roughly 10^{-12} for a centimeter of single mode fiber stained axially with no constraints [5]. This incredibly high strain sensitivity is rarely achieved in practice because of the "no constraints" assumption, which is violated in

most real world situations. In addition, these calculations assume that the fiber is at the quadrature point at all times. The degree to which the fiber drifts from the Q point will also determine final sensitivity.

The numbers above are however useful for purposes of comparison. We note that if any of the assumed parameters were changed, this would clearly affect the final strain sensitivity. Specifically, if the laser power or the detector sensitivity were increased, the final signal to noise ratio would be enhanced accordingly. This may be particularly important in the case of multimode sensors which require at least some power in the high order modes. Nevertheless, to make the jump from strain sensitivity to acoustic wave sensitivity, a number of material parameters, interface conditions, and geometrical considerations must be accurately specified. As noted early in this report, while that may possibly be done for a particular case, this in general would be an extremely cumbersome task, and would be difficult to generalize. However, it is believed that a deeper investigation of the material properties may show that some of the parameters fall within a particular range, and that some assumptions may be made to give a band of expected response for a given input.
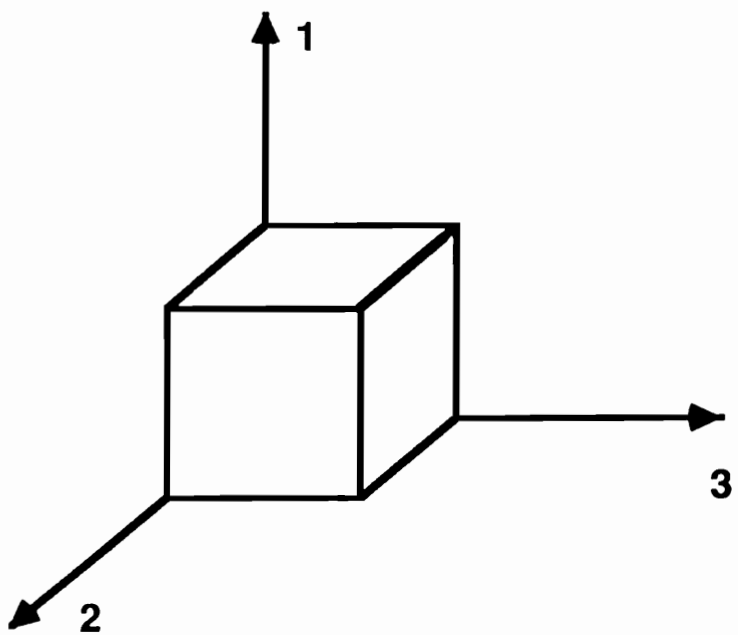
Figure 4.1a. Cartisian coordinate system used in equation (4.1) describing the general strain tensor.
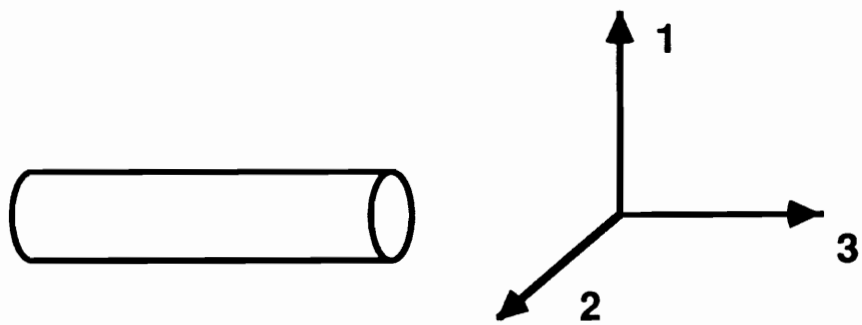
Figure 4.1b. Geometry of an optical fiber modelled as a right, circular cylinder in the above system.
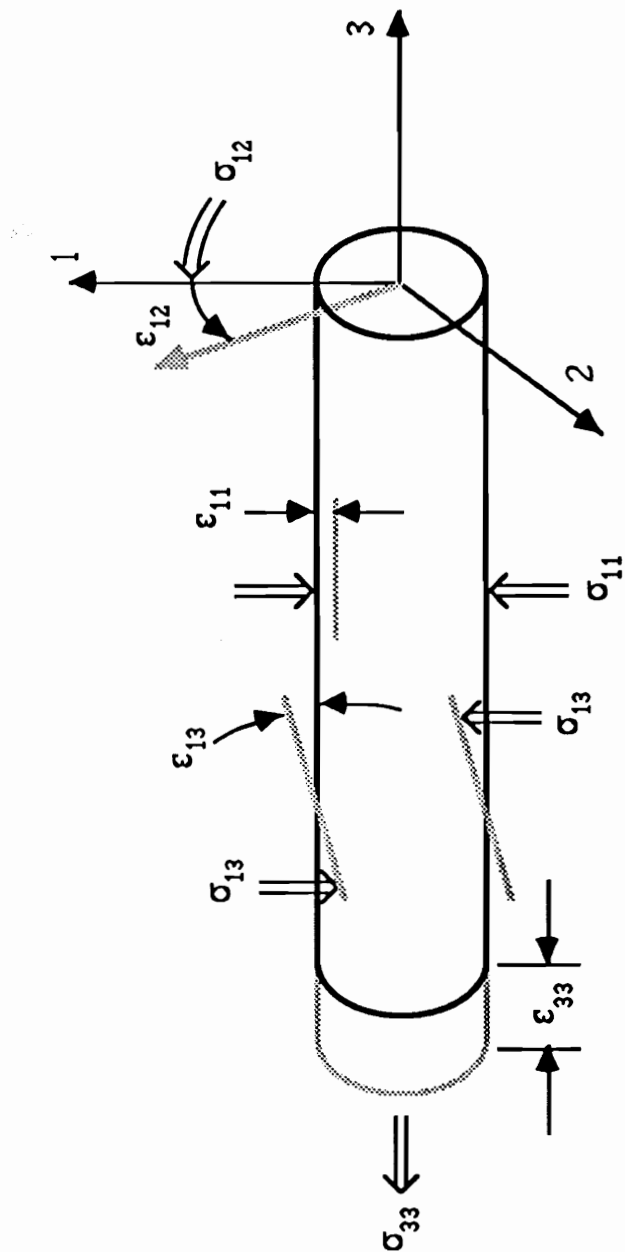
Figure 4.2. Possible strain mechanisms in an optical fiber.
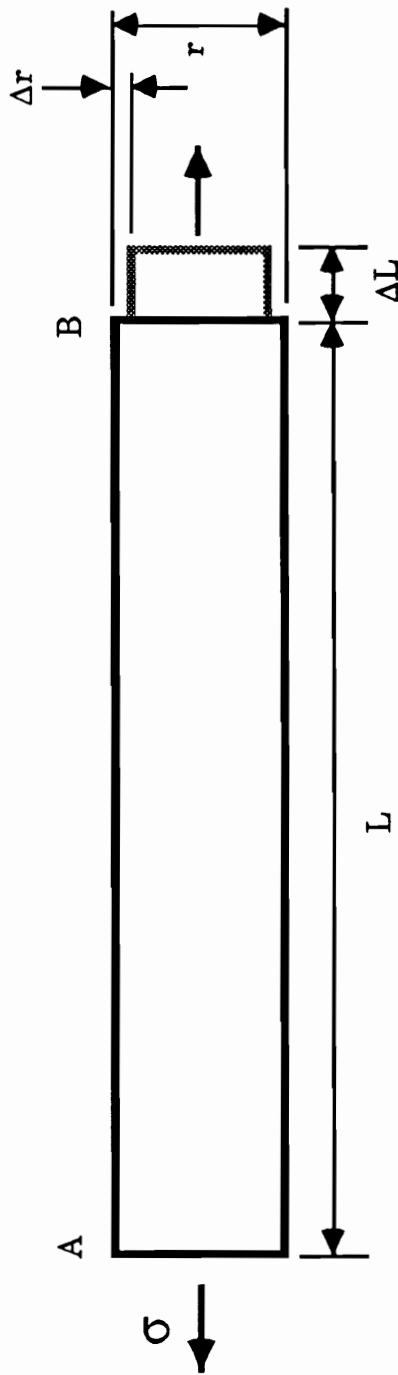
Figure 4.3. When fiber segment AB experiences an axial stress σ, an axial strain of $\varepsilon = \Delta L/L$ results, where σ and ε are related by the Young's modulus of the fiber. Due to the Poisson effect, the radius of the fiber also changes by a predictable amount. Not shown is the strain-optic effect relating changes in refractive index to strain.
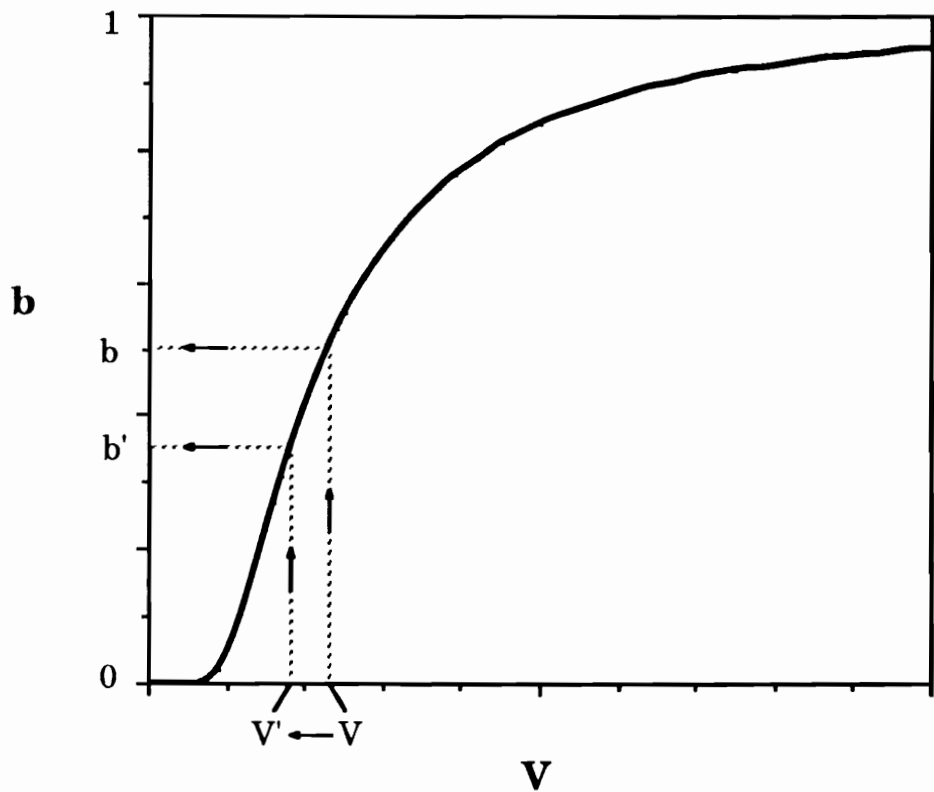
Figure 4.4. Calculating the slope of the b-V curve at a particular value of V can either be done numerically, or simply approximated from the curve by estimating the change in b for a given change in V.

Table 4.1. Typical parameters for single mode optical fibers.

| Parameter	Definition	Value
n_1	core refractive index	1.458
n_2	cladding refractive index	1.4532
Δ	fractional index difference $\dfrac{n_1^2 - n_2^2}{2n_1^2} \approx \dfrac{n_1 - n_2}{n_1}$	0.0033
a	core radius	$2.0\ \mu m$
λ_0	free space wavelength (He-Ne)	$0.6328\ \mu m$
k_0	free space wavenumber $2\pi/\lambda_0$	$9.929 \times 10^6\,m^{-1}$
V	normalized frequency $k_0\, a\, \sqrt{n_1^2 - n_2^2}$	2.35
β	propagation constant at V	$14.45 \times 10^6\,m^{-1}$
b	normalized propagation constant $\dfrac{(\beta/k_0)^2 - n_2^2}{n_1^2 - n_2^2}$	0.5172
S_b	slope of b-V curve at V	0.265
S	slope of β-V curve at V $(n_1 - n_2)\, k_0\, S_b$	$12{,}650\ m^{-1}$
ν	Poisson's ratio for fused silica	0.17
p_{11} p_{12}	strain-optic coefficients	0.12 0.27
p_{eff}	effective strain-optic coefficient $(1-\nu)\, p_{12} - \nu\, p_{11}$	0.2037
α_i	strain-index coupling coefficient $-\dfrac{1}{2}n_i^3\, p_{eff}$	-0.3157 i = 1 -0.3126 i = 2
α_{eff}	effective strain-index coupling $\dfrac{n_1\, \alpha_1 - n_2\, \alpha_2}{n_1^2 - n_2^2}$	-0.4316

Table 4.2. Typical single mode fiber parameters for the case of radial strain.

Parameter	Definition	Value
$\dfrac{2\,\nu}{1-\nu}$	coupling coefficient between radial and axial strain	0.4096
p'_{eff}	$p_{11} + \left(\dfrac{1-3\,\nu}{1-\nu}\right)p_{12}$	0.2794
α'_1	core strain-index coupling $-\dfrac{1}{2}n_1{}^3\,p'_{eff}$	-0.4330
α'_2	cladding strain-index coupling $-\dfrac{1}{2}n_2{}^3\,p'_{eff}$	-0.4287
α'_{eff}	effective strain-index coupling $\dfrac{n_1\,\alpha'_1 - n_2\,\alpha'_2}{n_1{}^2 - n_2{}^2}$	-0.5920

Table 4.3a. Parameters used for evaluating the LP_{01}/LP_{11} sensor.

Parameter	Definition	Value
n_1	core refractive index	1.458
n_2	cladding refractive index	1.4532
a	core radius	2.5 μm
V	normalized frequency	2.94
u_0	$k_0\, a\, [(n_1{}^2 - (\beta_0/k_0)^2]^{1/2}$	1.76
u_1	$k_0\, a\, [(n_1{}^2 - (\beta_1/k_0)^2]^{1/2}$	2.76
$\tilde{\beta}$	propagation difference at V	$22{,}000\,\mathrm{m}^{-1}$
$\tilde{S}$	slope difference of β-V curve at V	$-4{,}750$
α_1	core strain-index coupling	-0.3157
α_2	cladding strain-index coupling	-0.3126
α_{eff}	effective strain-index coupling	-0.4316
α'_{eff}	radial strain-index coupling	-0.5920

Table 4.3b. Parameters used for evaluating the LP_{01}/LP_{02} sensor.

Parameter	Definition	Value
n_1	core refractive index	1.458
n_2	cladding refractive index	1.444
a	core radius	2.0 μm
V	normalized frequency	4
$\tilde{\beta}$	propagation difference at V	$98{,}000\,\mathrm{m}^{-1}$
$\tilde{S}$	slope difference of β-V curve at V	$-38{,}000$
α_1	core strain-index coupling	-0.3157
α_2	cladding strain-index coupling	-0.3067
α_{eff}	effective strain-index coupling	-0.4289
α'_{eff}	radial strain-index coupling	-0.5883

Table 4.4. Parameters for three multimode optical fiber cases examined.

Parameter		typical	thread	optimized
n_1		1.458	1.458	1.7
n_2		1.429	1	1
Δ		0.01	0.5	0.5
a		50 µm	12.5 µm	100 µm
λ_0		0.6328 µm	0.6328 µm	0.51 µm
V		144	132	1694
$\tilde{\beta}$		290,000	4,500,000	8,600,000
$\tilde{S}$		− 29,000	− 450,000	− 860,000
α_1	axial	− 0.316	− 0.316	− 0.500
α'_1	radial	− 0.433	− 0.433	− 0.686
α_2	axial	− 0.297	--	--
α'_2	radial	− 0.408	--	--
α_{eff}	axial	− 0.425	− 0.409	− 0.450
	radial	− 0.582	− 0.561	− 0.617

Table 4.5. Comparison of phase sensitivity for various sensor types and configurations taken up in this report. Numbers in parentheses represent comparative values with the single mode fiber case taken as the reference for each direction of applied strain.

| Fiber/Sensor Type | Sensitivity in radians/strain·length | |
	Axial	Radial
Single Mode	1.4×10^7 (1)	0.6×10^7 (1)
Dual Mode		
LP_{01}/LP_{11}	3.0×10^4 ($1/500$)	1.5×10^4 ($1/400$)
LP_{01}/LP_{02}	1.9×10^5 ($1/75$)	1.0×10^5 ($1/60$)
Multimode		
Typical	2.8×10^6 ($1/5$)	1.9×10^6 ($1/3$)
Unclad Fiber	3.9×10^7 (2.7)	2.8×10^7 (4.7)
Optimized	9.1×10^8 (65)	5.6×10^8 (93)

5.0 APPLICATIONS OF MDS TO ACOUSTIC WAVE DETECTION

In this chapter we review two applications of modal domain sensing to NDE, both involving the detection of acoustic waves. In the first section, fiber optic transduction of acoustic emission signals is discussed. Following that, the subject of real-time impact monitoring is raised. In the last section, we outline some of the areas in which modal domain sensors fall short of either ideal conditions or other sensing methods, and suggest possible solutions.

5.1 Acoustic Emission Detection

The monitoring of acoustic emission (AE) is an important technique for nondestructive characterization in strained materials because time and frequency domain analyses of AE events may yield information about the type, geometry and location of defects, as well as how material failure may occur. The quantitative interpretation of AE event signatures is critically dependent upon the faithfulness of the acoustic transduction and signal processing system in reproducing localized stress wave amplitude as a function of time. The usual sensor for acoustic emission is the piezoelectric transducer, and though they are sensitive and reasonably broadband, these sensors are not suited for embedded measurements and are highly susceptible to electrical noise.

As an alternative, several researchers have considered the application of bulk optical interferometric optical sensing techniques, which offer good spatial resolution and frequency response [110,111]. A non-intrusive fiber optic version of this type of probe has also been implemented to detect a traveling surface acoustic wave [112]. These techniques focus one beam of a modified Michelson interferometer to a small spot on the surface of a specimen and measure the time-dependent normal component of surface

displacement at the location of that spot. However, the similarity in size of an optical fiber with a graphite fiber tow used in many composite materials offered incentive to investigate embedding fibers in materials to detect AE.

Experiments

In the first series of tests, optical fiber was embedded between the two center plies in eight-ply symmetric cross-ply graphite/epoxy laminates and cured under pressure in a standard heated-platen press [12]. The edges from which the fibers emerged were insulated with scrim paper during cure to reduce the embrittlement of the adjacent fiber coating, and protective quick-cure polymer tabs were applied to the fiber-matrix joints soon after cure to minimize fiber breakage. The specimens were then saw-trimmed to approximately 6.5 cm. The optical fiber, intended for single mode operation at 1300 nm, was excited with He-Ne laser light, yielding a few mode fiber. A photodetector was placed in the output field so as to intercept only a portion of the total intensity when the lobe-pattern modulated due to localized strain.

The specimens were tensile loaded in a computer-controlled load frame, with the fibers aligned in the direction of the applied stress. Special grips designed to securely hold the specimen without cracking the embedded fiber sensors. As the specimens were loaded, the optical output was monitored using a digital storage oscilloscope. The detection system recorded burst events at the same times that audible cracking events were noted, as well as smaller amplitude events which were inaudible. Each of the four specimens tested failed at about 65,000 pounds of load, and before the internal fiber sensors failed due to load. This may have been due to partial slippage of the specimen around the fiber.

Typical events recorded for the same composite sample at different times during loading are shown in Figures 5.1a and 5.1b. Analysis of this data indicates that the acoustic emission event in Figure 5.1a is very likely due to the cracking of the composite matrix material. This is evidenced by the fast initial rise time of less than twenty microseconds (the distance between two pixels on the digital scope at this sweep rate), a primary

emission followed by induced plate mode vibrations, and cascading emissions related to subsequent strain release. The very different signature shown in Figure 5.1b is typical of an event occurring near the end of the load cycle, caused by graphite fiber breakage. It consists of a single relatively long and highly energetic pulse of slow rise time, and does not exhibit following events.

Events recorded simultaneously using both the optical fiber and a conventional piezoelectric transducer, manufactured specifically for detecting AE, were also compared. The piezoelectric transducer was attached to the specimen in the center of one side, directly above the embedded fiber. Typical comparison data is shown in Figure 5.2. In some cases the acoustic pulse reached the fiber before the piezoelectric, while in others, the sound waves reached the piezoelectric sensor first. Also, we see that the modal domain sensor exhibits a very large bandwidth ranging from d.c. up to at least tens of megahertz. (Recall that previously discussed experiments by Meltz and Dunphy demonstrate optical fiber detection of waves in the gigahertz frequency range [89].) This stands in contrast with the piezoelectric, which though termed "broadband" by the manufacturer, apparently passes only a fairly narrow range of frequencies. It is noted that the fiber response is in part due to the fact that it is actually a line sensor, integrating strain all along its length.

In subsequent tests, samples were prepared with optical fiber laid across the direction of applied load, allowing for the use of conventional grips, although requiring some care during cure [113]. Also, the use of two fibers for the location of acoustic events was investigated. A representative signal arising from a single acoustic event (the standard pencil-lead break) appears in Figure 5.3. On the other hand, Figure 5.4 compares the output of two embedded fibers embedded with a distance of approximately 10 cm between them. Acoustic waves excited above one sensor are detected immediately, triggering the scope to produce the lower trace. The upper trace shows the arrival of the pulse at a time later, buried in the response of the fiber to plate vibrations. In other work, acoustic emissions in composite cylinders, plywood panels and low-fusion metal alloys have also been detected using embedded modal domain sensors, with similar results.

The measurements reported here indicate that acoustic emission events may in fact be observed and located using optical fiber sensors applied directly to modern engineering materials. It is known from private conversations with scientists in the AE field that in the early 1980's, a certain company conceived the idea of using single mode interferometers to detect AE. It seems that the project was abandoned because of the impracticality of making field measurements, owing to instability problems. Modal domain sensors have much to offer in this regard, since it is a differential method demonstrating high common mode rejection, while retaining high sensitivity. Recent calculations presented in the last chapter suggest that the use of highly multimode fibers might offer even greater sensitivity. Thus, though fiber optic detection of AE is far from perfected, prospects for future work are promising.

5.2 Impact Monitoring

In this section, experiments are reported in which ultrasonic shock waves generated by impacts were detected using optical fiber modal domain sensors. Such measurements are important in that it may be possible to predict the amount of damage a structure such as an aircraft will incur based on the measured accumulation of impact energy. Furthermore, in many materials, and especially carbon-based composites, impacts from stones on a runway or even some high speed projectiles may leave no obvious visible sign of damage on the outside surface, while the interior surface has suffered serious degradation due to the propagation of the resulting shock wave [75,114]. Thus great advantage could be gained by having an on-board, real-time monitor of impacts, which has the ability to assess the energy and power spectrum associated with each event. As mentioned in the first chapter, a broad base of knowledge regarding the behavior of the materials in question must proceed any accurate prediction of properties such as remaining lifetime using fiber optic impact sensors. On the other hand, the monitoring tool itself must also be developed and characterized.

In the case of a continuous modal domain sensor embedded inside or on the surface of an impacted specimen, at least three different sound/light interactions occur. Rigid body motion of the specimen is generally low frequency, and may be detected as motion of the lead-in and lead-out fiber portions. The specimen may also vibrate in both linear and nonlinear combinations of its natural modes. Furthermore, high frequency surface, shear, and bulk waves may be coupled through the fiber, affecting a change in the index of refraction of the core, and thus a change in the output. Again, it might be noted that in comparison to most transducers capable of in-service measurement of acoustic waves, these fiber sensors are extremely broadband.

In order to be useful, it is necessary for impacts to be reliably and repeatably characterized by the signal disturbance they cause. This in turn may be related to the type and degree of damage that occurs. Integrating the work done on the specimen in a given time period has been found to be a more accurate method of estimating impact magnitude than simply relying on the peak voltage associated with any output. Furthermore, if a basic knowledge exists as to the geometry, loading, and type of material in question, frequency analysis of the signal can lead to a meaningful characterization of the type of impact. Finally, time domain analysis of the output of two or more sensors can yield impact location information.

The experiments to be discussed in the following section involve the use of both embedded and attached modal domain sensors, and are applied to both composites and aluminum samples. In many ways the results showed surprisingly similar results.

Experiments

In the first experiment to be described, depicted in Figure 5.5, a 1.5 cm portion in the middle of a two meter length of 1300 nm single mode fiber was stripped of its polymer jacketing. This was bonded with a small amount of rigid epoxy to an aluminum panel measuring 40.6 cm wide, 61 cm long, and 1.9 cm thick. Portions of the fiber which were not bonded were elevated away from the panel and padded to avoid unwanted coupling

of sound energy to the nonsensitized region. The panel was inverted with the fiber on the underside, and supported by vibration absorbing foam.

The fiber was operated at 633 nm, yielding a V number of approximately 4.5 and a four lobe output interference pattern. The output was spatially filtered and detected by a standard Si photodiode. Acoustic waves generated in the panel by the impact of a 250 gram stainless steel sphere interacted with the fiber, causing a modulation of the output modal domain pattern. Signal changes were collected over the course of an impact by a digital waveform analyzer and transferred to a micro-computer for storage.

Six impacts at each of five different heights ranging from one foot to five feet were performed. In each case the time domain voltage from the detector was recorded, and the energy measured in the output signal was calculated as proportional to $\int [v(t)]^2 dt$. A typical output appears in Figure 5.6. The output voltage, shown as $E(t)$ for $0<t<100$ ms was evaluated for each trial and values for the six trials were averaged and plotted against drop height, as seen in Figure 5.7.

For the next part of the work, a second fiber was attached 30.5 cm from the first. Simultaneous detection was performed and monitored using the two traces of the waveform analyzer. The steel mass was dropped at several locations between the two fibers, and the arrival time delay was analyzed for each case. With the aid of a simple algebraic relation, explained in Figure 5.8, the position of the impact could be determined. A sample trace appears in Figure 5.9, where the time scale has been expanded by a factor of 20 from Figure 5.6 in order to resolve the time delay. It should be noted that considering the plate geometry, it was assumed that the first wave to arrive at the sensor was the longitudinal wave; accordingly, the longitudinal wave velocity was used in the calculations. It was understood, however, that the actual situation was somewhat more complex because of the surface wave propagation, the multiple reflections and mode conversions between the longitudinal and shear waves, and the frequency dependent attenuation of the material. Also, it was determined that the sensor system was far more capable of resolving impact location

than were the experimenters trying to accurately position the drop tube over the plate.

Finally, several impacts were conducted using a blunt-ended projectile. This allowed for a number of different types of impacts, depending on how squarely either the flat or the corner of the projectile struck the panel. Time varying voltages were collected as described above, and a Fourier transform was performed. Low frequency components less than a few hundred Hertz resulted in response to what appears to be rigid body motion of the plate on the supporting foam. Midrange frequencies corresponding to calculated harmonic plate mode vibrations of the panel also appeared. Both these and the low frequency vibrations were reasonably insensitive in frequency content to the type of impact. However, the high frequency content and power distribution varied widely with impact type. As expected, the more that the sharp corner struck the panel, the greater the share of power in the high frequency components.

A second test was conducted which involved impacting a composite panel containing optical fiber sensors. A 900 μm o.d. plastic clad silica fiber (core, cladding, and buffer) was embedded in a serpentine fashion 5 plies deep in a graphite/epoxy crossply laminate consisting of 30 plies. The laminate was cut down so as to fit into the restraining fixture of a General Research Dyn730-I impact test unit, and was clamped on all four sides. This unit is capable of measuring load, energy, impact time and sample deflection. However, none are determined from the sample side, that is, all require measurements of time and strain in the impacting tup, external to the laminate itself. Embedded optical fiber sensors thus present the advantage of being able to monitor response from inside the material. An overview of the set-up appears in Figure 5.10.

Several impacts were conducted, and both the optically and mechanically generated data were collected and analyzed. A typical optical signal is seen in Figure 5.11, while Figure 5.12 gives a typical load and energy versus time trace. It should be noted that the signal in Figure 5.11 corresponds to the initial peak, which was always under 10 ms in duration, and which was followed by a series of oscillations similar to those observed

with the aluminum panel. Impacts were conducted from various heights, representing different input energies. Also, 30 one inch impacts and 10 two inch impacts were performed towards making a brief analysis of the sensor response to repetitive impacts. Optical fiber outputs were examined with respect to impact duration, signal rise time, peak voltage, signal shape, the detected energy (related to the time integral of the voltage squared), and the Fourier spectrum of the signal.

Unlike the previous experiment, the detected energy did not correlate well, or even monotonically with the input energy. This was true regardless of the time period used for the calculation. It is believed that the sensor response was saturated by the high input energies imparted by the heavy tup. Time measurements, both duration and rise time, showed more repeatable trends, and correlated with the independent measurements made by the DYN730-I. In both cases, there was a clear downward trend with increasing energy input, as seen in Figure 5.13. Related to these, the signal shape also showed a clear tendency to sharpen at the corners with increasing input energy as the system saturated. The Fourier spectrum seemed to yield little usable information, but it should be kept in mind that in this case, only a single type of tup shape was employed. Further tests should be performed to investigate the effects of changing the shape of the impact surface.

In the case of the repeated impacts, both the detected energy and the signal duration increased gradually during the course of the tests. It is speculated that the rising tendency and the increasingly wide spread in values were related to damage occurring in the material. At this point in the test, the composite panel was obviously incurring significant damage in the form of cracks and delaminations. This suggests that fiber optic sensors may be able to yield in-situ information about material degradation.

A third experiment was performed which combined the previous two. A new panel, also measuring six by six inches and containing PCS optical fibers was subject to relatively low energy impacts. A special impact test frame was constructed to allow for the greatest flexibility with regard to drop height, position, sample size, clamping boundaries, and impacting

projectile mass and shape. An optical interrupt was implemented in order to measure the projectile velocity directly before impact, as well as trigger the detection system. A simple spatial filter, photodetector, and digital oscilloscope were used to record the data as before.

The results of this test appear in Figure 5.14. Most noteworthy is that the detected energy again takes on a monotonic curve, of similar shape to that obtained with the aluminum panel. This lends credence to idea that the non-monotonic curve obtained in the second experiment (not shown) was more a consequence of the manner in which the sample was impacted than the nature of the material or the detection system itself. Of further significance is the fact that the first experiment made use of few-mode fiber, whereas the third employed highly multimode PCS; nevertheless the curve shapes were similar. It should be noted however, that nothing can be said about the sensitivity of the measurements, since different detectors, amplifier gains, and spatial filter methods were used.
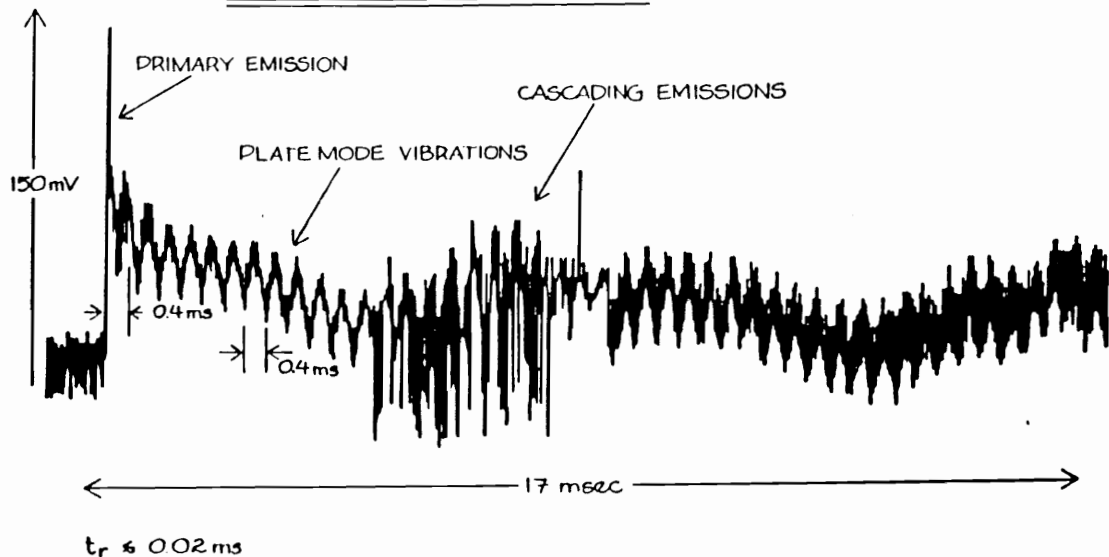

5.3 Conclusions

Optical fiber sensors show considerable promise for detecting and quantifying impact damage in advanced materials. These sensors may be either embedded or attached, and display a number of highly desirable characteristics as an NDE tool. Single sensors may be constructed simply and inexpensively to monitor catastrophic failure in materials, may be networked together to locate damage in complicated structures. Modal domain sensors show particular promise for characterizing impact energy and related features.

A number of concerns still need to be addressed in the proposed sensing scheme. For one, as with any interferometric sensor, the dynamic range for linear operation is fairly limited. Extending the range requires fringe counting techniques, which tend to be complex. Also, care must be taken to avoid the introduction of spurious frequency components in the speckle motion, which can result from irregular strain induced birefringence. Isolating the lead-in/ lead-out portions of the sensor from noise sources

external to the workpiece is also essential for accurate signal analysis. In addition, geometry and frequency dependent effects of the material under test must be take into account. More work is needed to quantify the requirements for identifying unknown signals on the basis of their frequency spectra. In addition, reliable and repeatable methods for nondestructively quantifying damage still require much investigation, as does the more difficult task of predicting performance based on the information obtained. The work spans a broad range of fields from materials characterization to NDE to sensor technology to signal analysis and statistics.

EMISSION DUE TO MATRIX CRACK

PRIMARY EMISSION

CASCADING EMISSIONS

PLATE MODE VIBRATIONS

150 mV

0.4 ms

0.4 ms

17 msec

$t_r \leq 0.02\,ms$

EMISSION DUE TO COMPOSITE FIBER BREAKAGE

100 mV

230 ms

$t_r < 0.5\,ms$
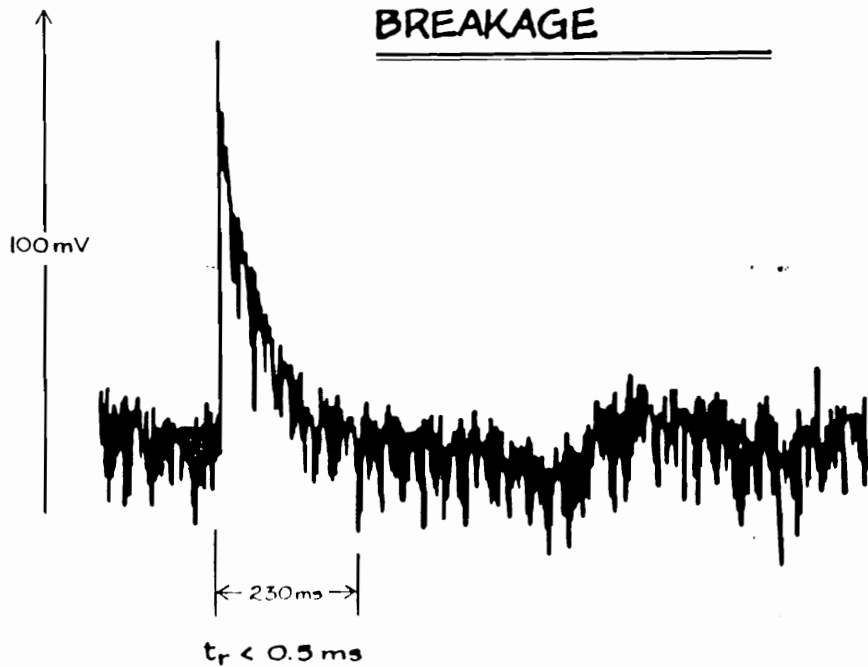
Figure 5.1. Acoustic emission traces output by a modal domain sensor embedded in a graphite/epoxy composite coupon under tensile loading: a) emission due to a crack in the matrix material, b) emission resulting from the breakage of an axially directed graphite fiber [12].
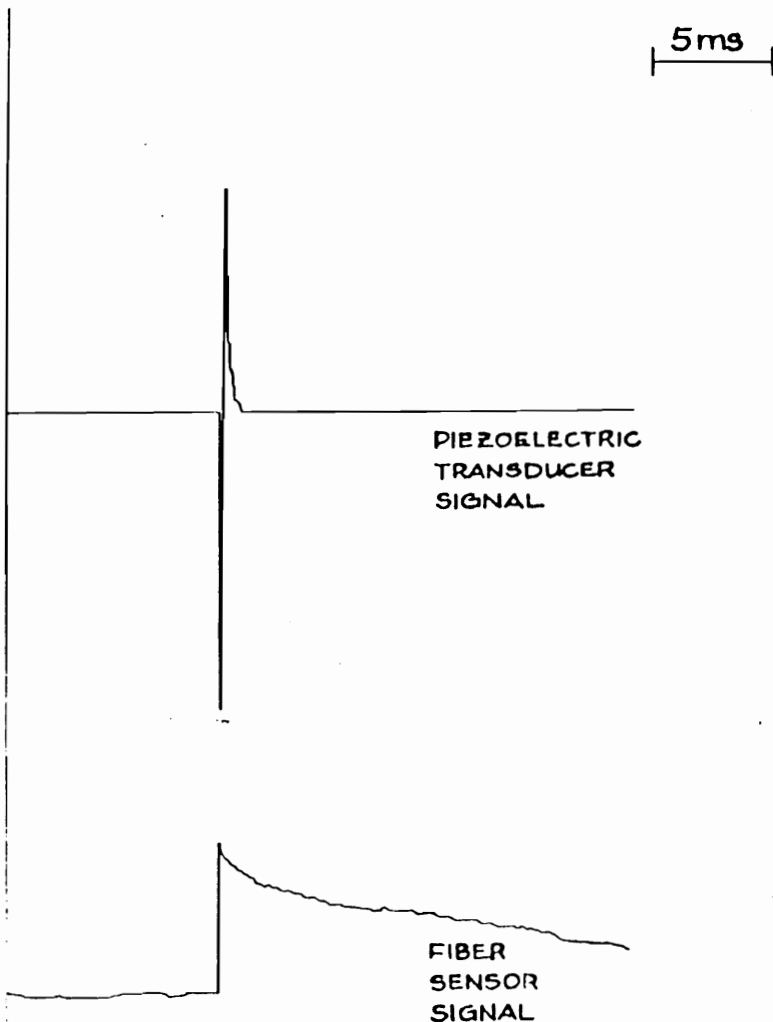
Figure 5.2. Comparison of acoustic emission events detected by piezoelectric (top) and optical fiber sensor (bottom) [12].
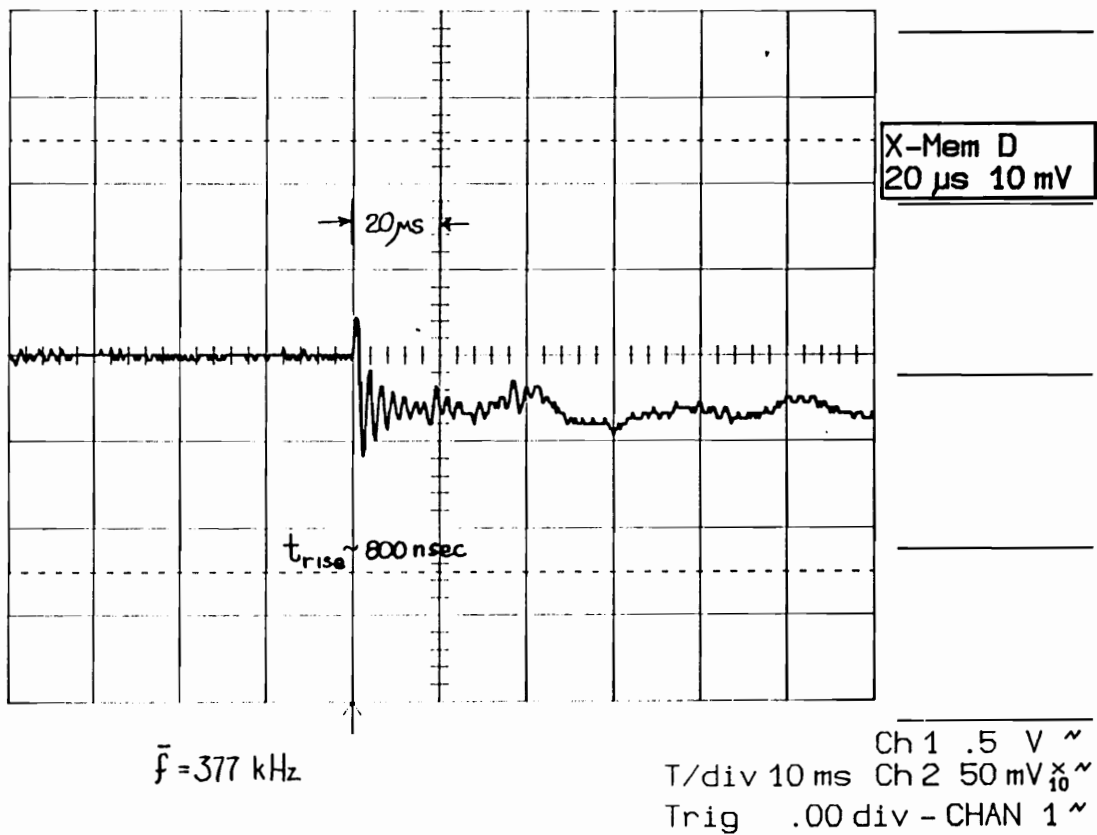
Figure 5.3. Signal resulting from fiber optic transduction of a standard pencil lead break, simulating an acoustic emission [113].

X–Mem C
29.7 mV

X–Mem D
–1.3 mV

Δt 248 μs   f 4.032 kHz   T/div 10 ms

Ch 1 .5 V ~
Ch 2 50 mV ×10 ~
Trig .36 div – CHAN 1 ~
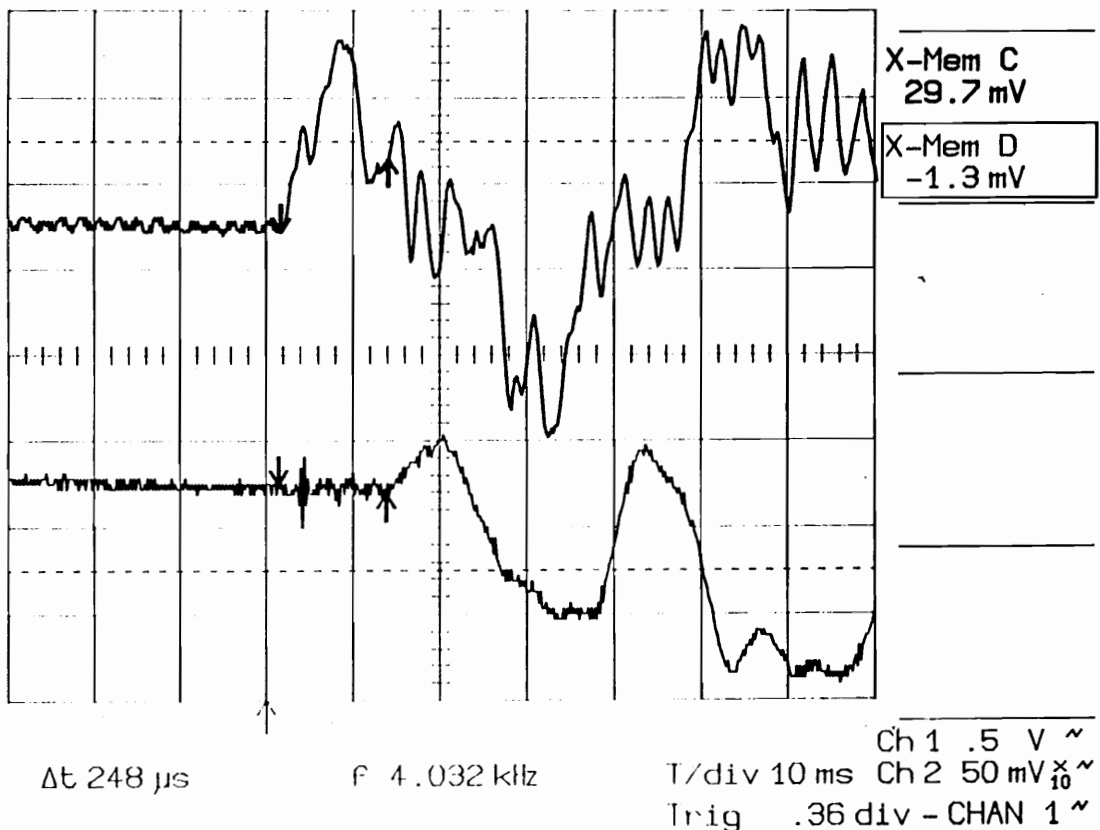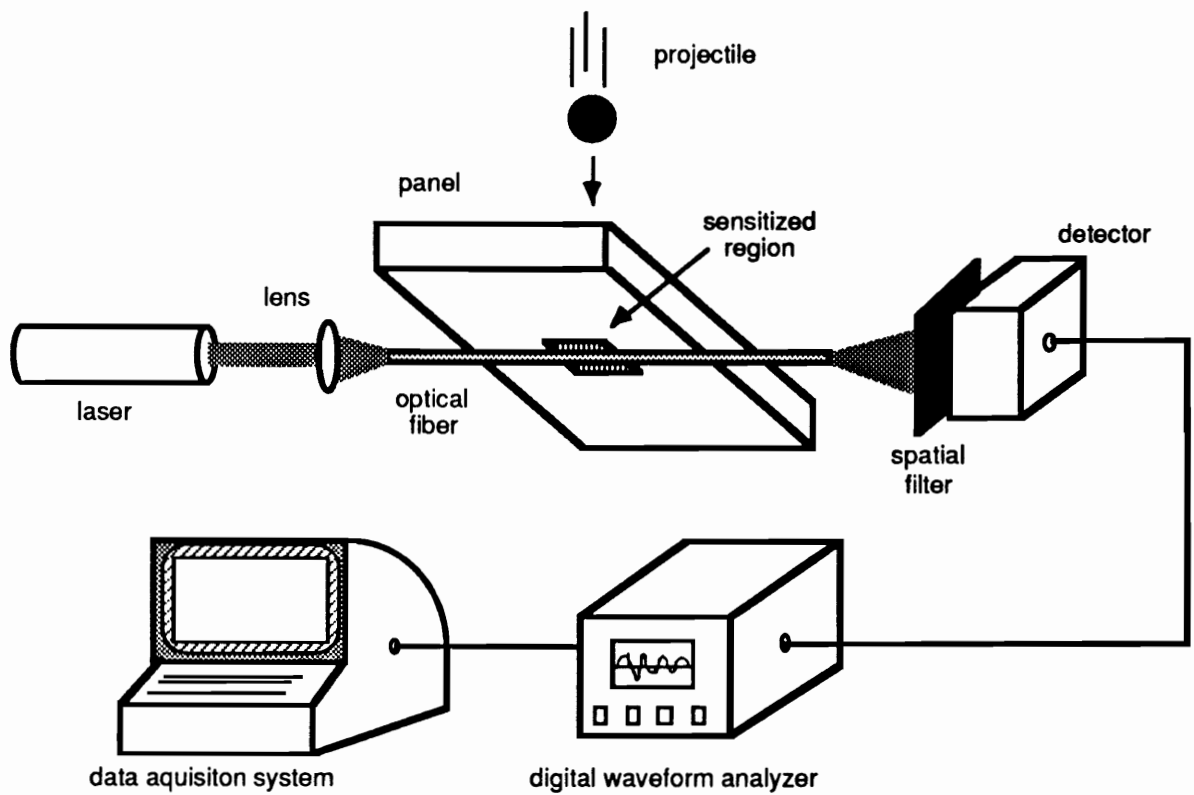
Figure 5.4. A standard pencil lead break was initiated directly above one fiber; the resulting plate mode vibration signal in the upper trace triggered the scope. Some 37 μs later, a second fiber located 4 inches away recorded the arrival of the small acoustic wave from the break, and 248 μs sensed the arrival of the vibrations [113].

Figure 5.5. Experimental set-up for monitoring impacts to an aluminum panel using attached modal domain sensors [13].
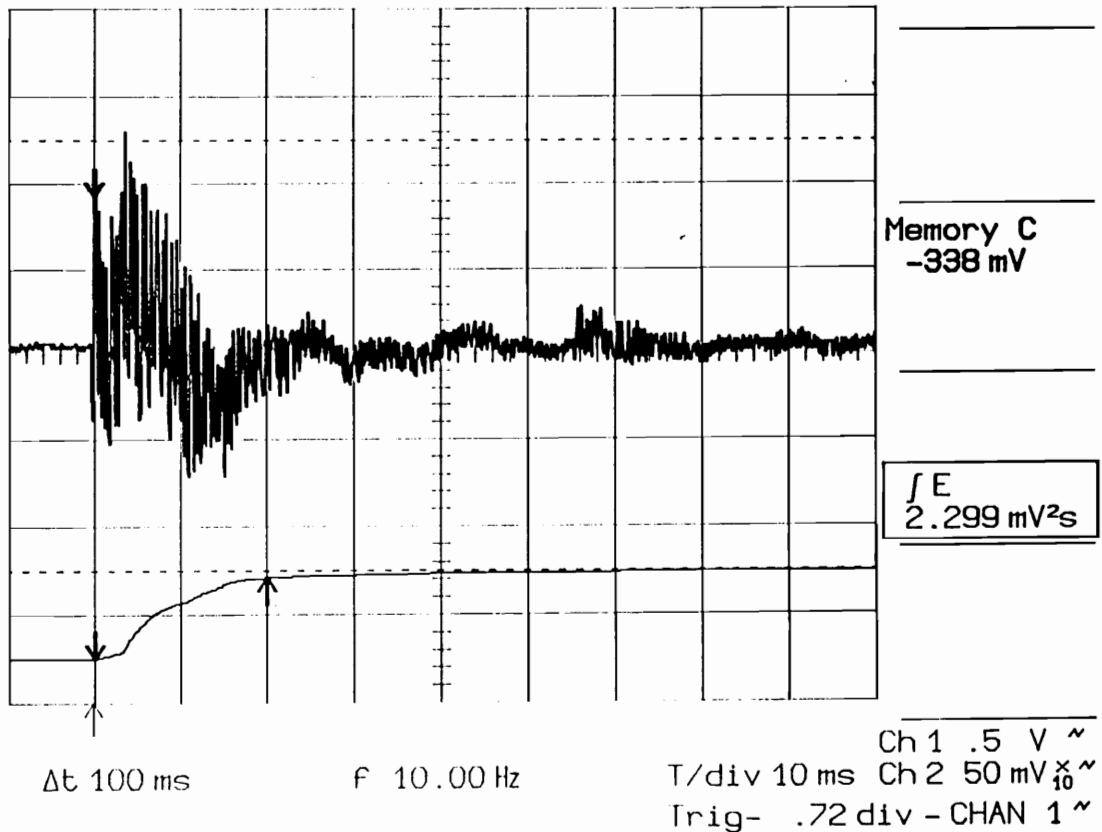
Figure 5.6. The time domain output from a typical impact [13].

Detected vs. Impact Energy
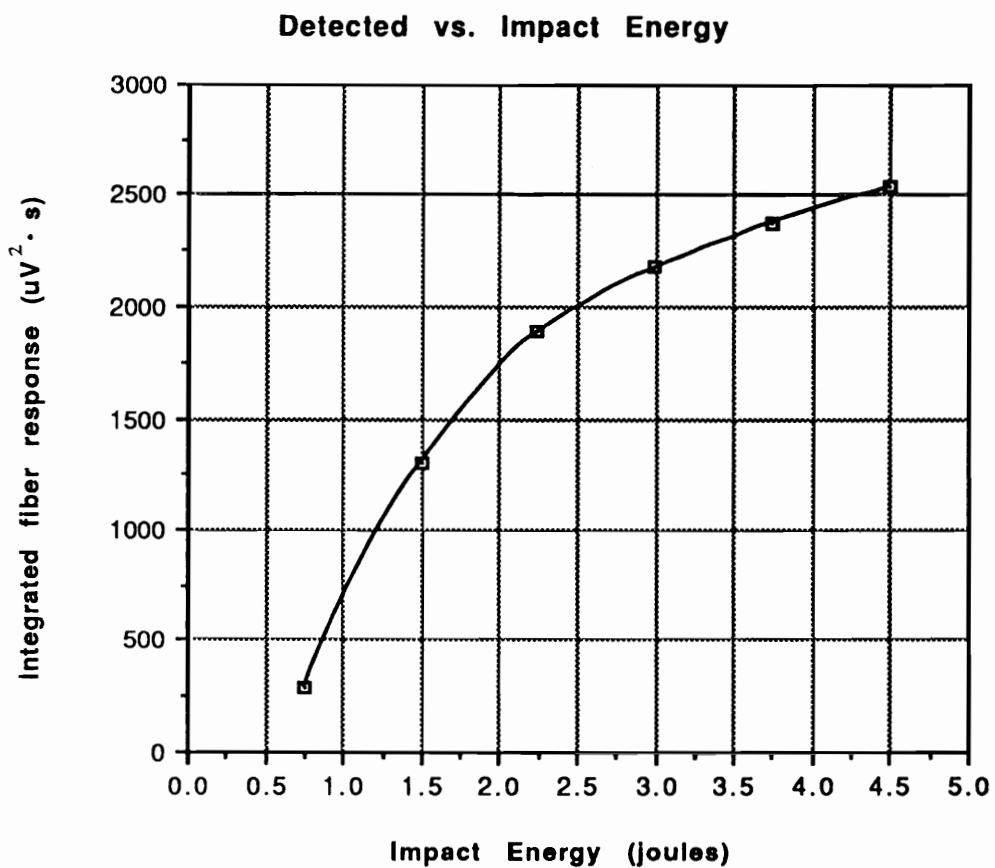
Figure 5.7. Integrated response of the attached optical fiber sensor versus impact energy, calculated as $E = mgh$ [13].

a. IMPACT

X_1 X_2

impact
location

**b. CAPTURE TIME
DOMAIN SIGNAL**

c. FIND Δt:

Δt

d. CALCULATE Δd: $\Delta d = v_L \times \Delta t$; $v_L = 6420$ m/sec (aluminum)

e. SOLVE $\left\{ \begin{array}{l} X_1 + X_2 = 30.5 \text{ cm} \\ X_2 - X_1 = \Delta d \end{array} \right.$ **TO DETERMINE** X_1 **AND** X_2
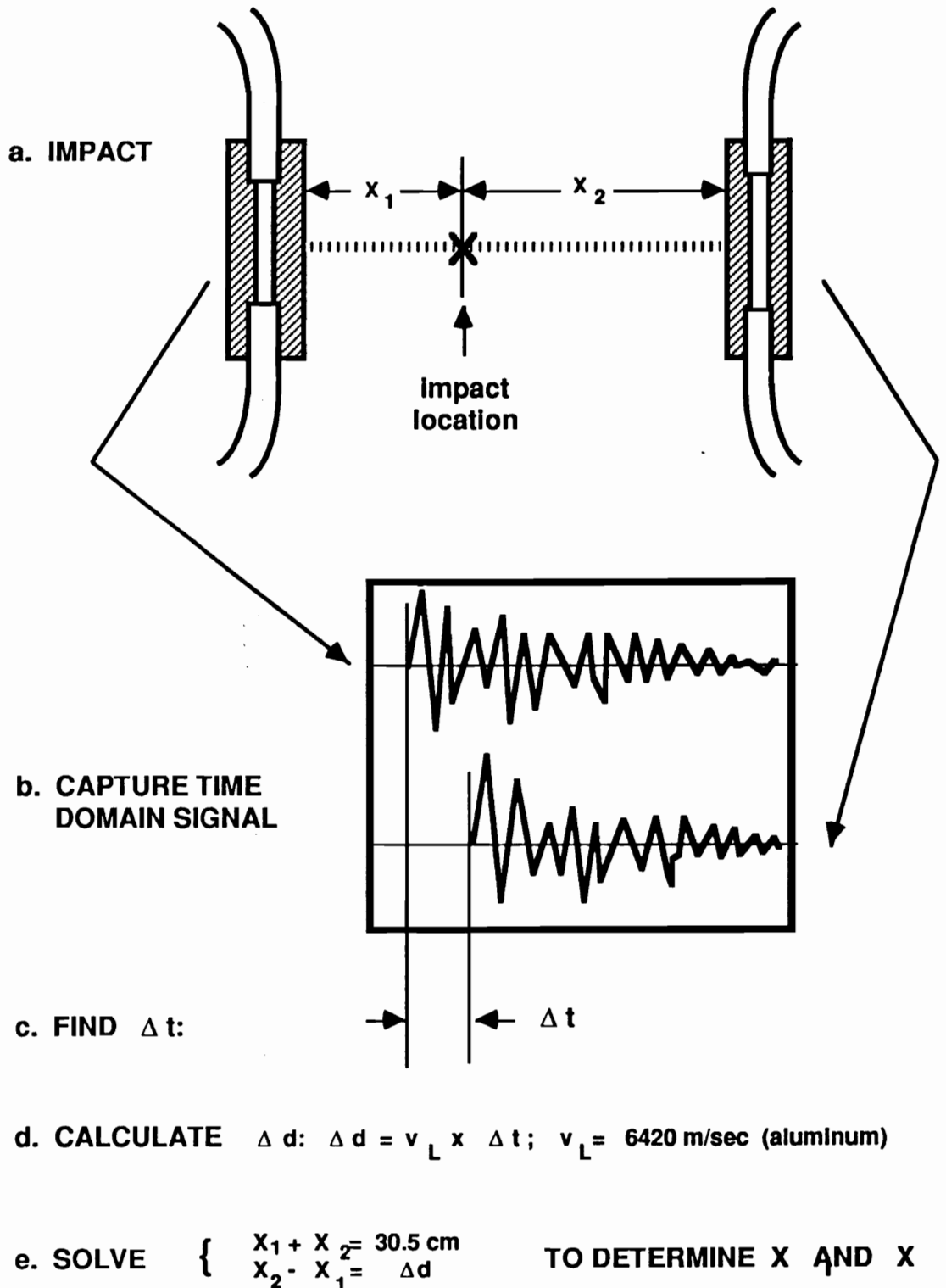
Figure 5.8. Procedure for determining impact location [13].
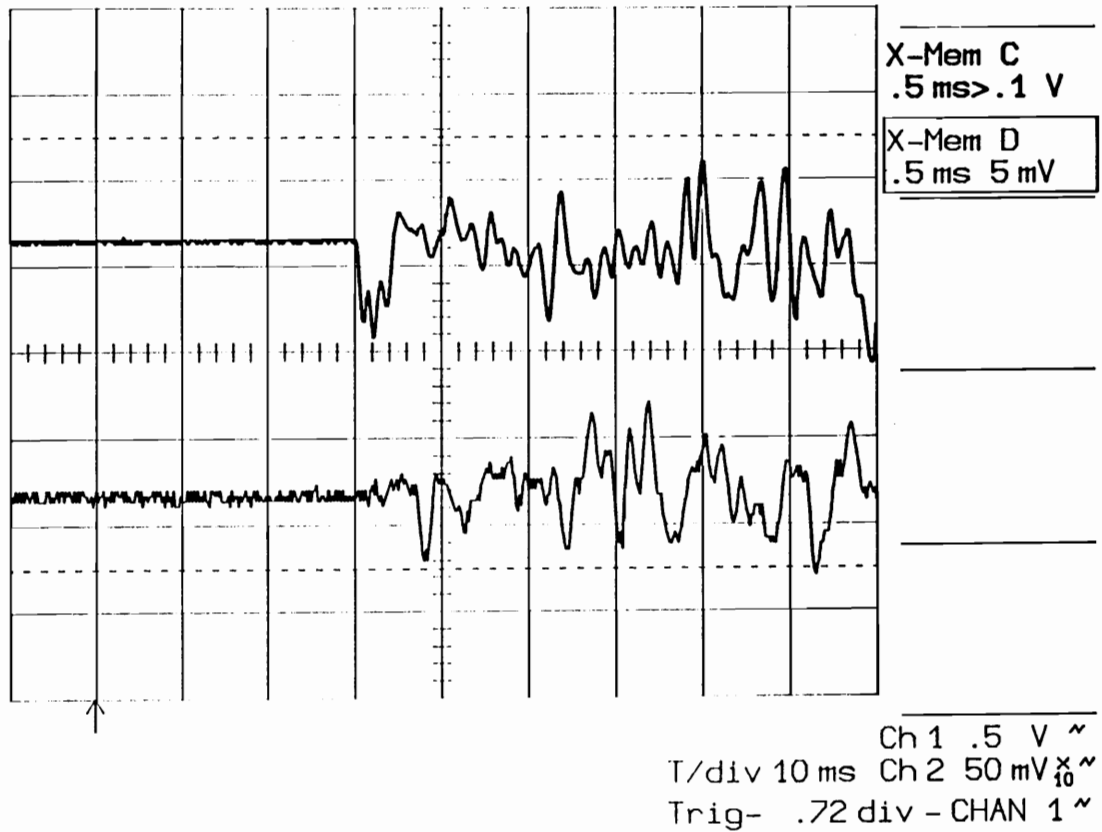
Figure 5.9. Typical output for two attached sensors responding to small level impacts. The scope triggered on the upper trace, the output of the left fiber, also capturing the right fiber output on the lower trace [13].
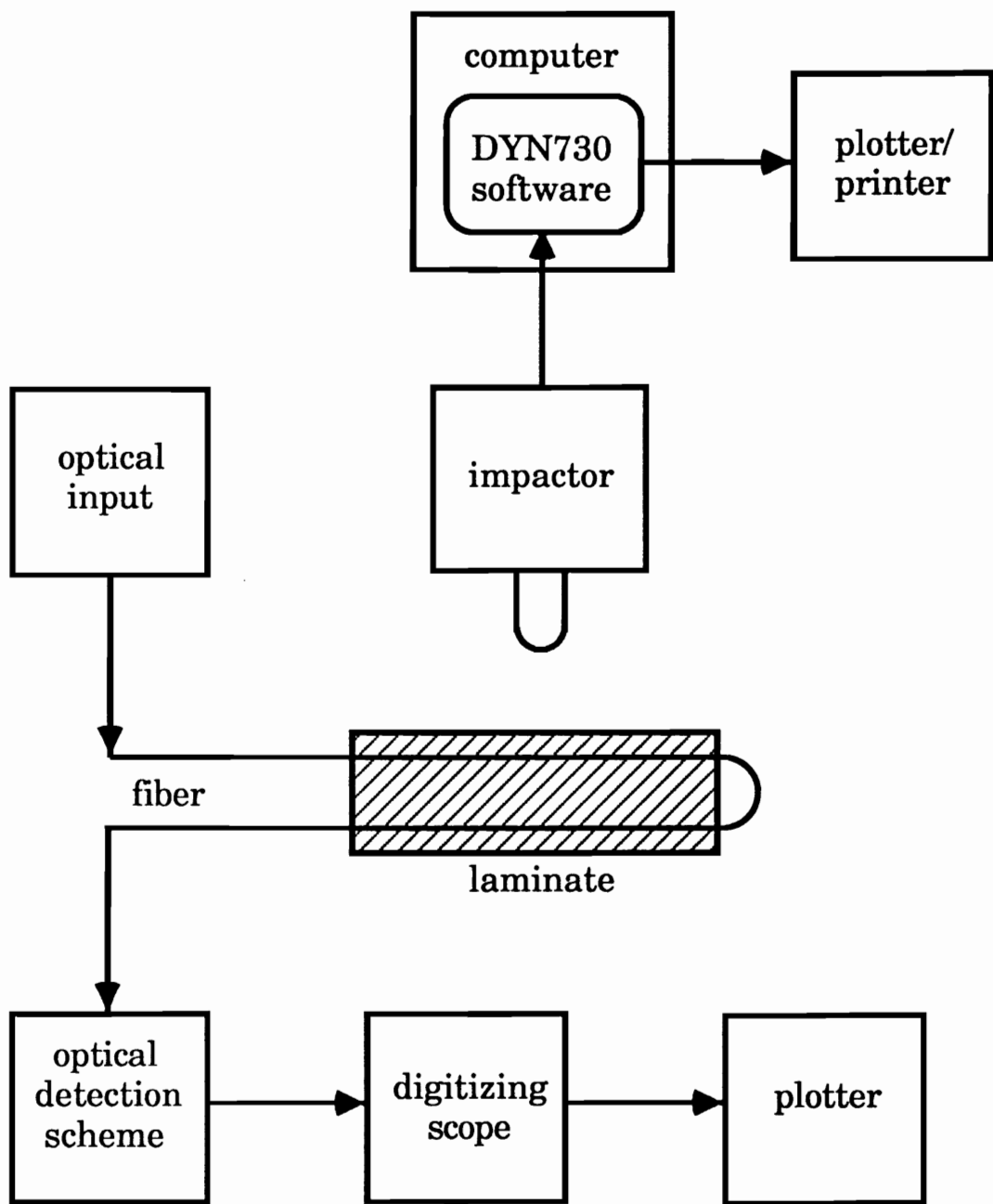
Figure 5.10. Block diagram of the set-up used to test fiber sensors embedded in a composite panel [14].

X–Mem C
−.25 V

X–(∫E)
13.27 V²s

Time 7.04 ms

Ch 1 1 V ~
T/div 10 ms Ch 2 .1 V ~
Trig .20 div + CHAN 1 ~
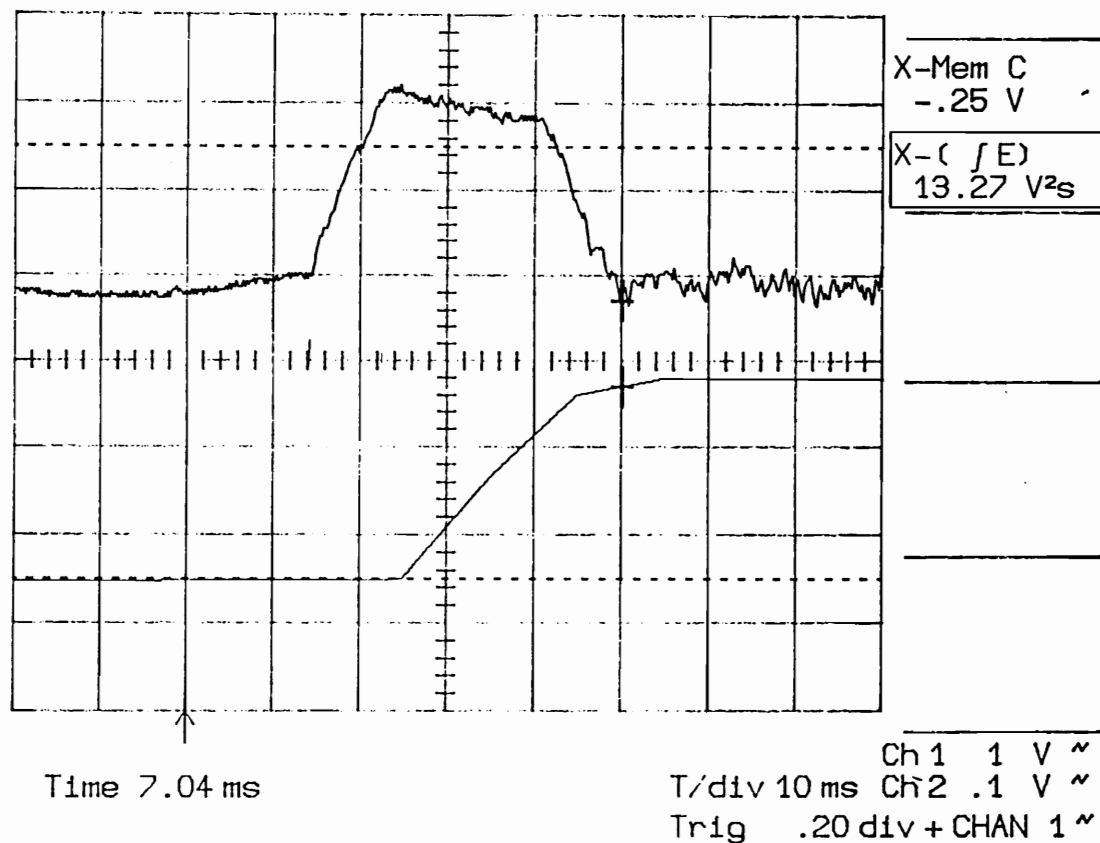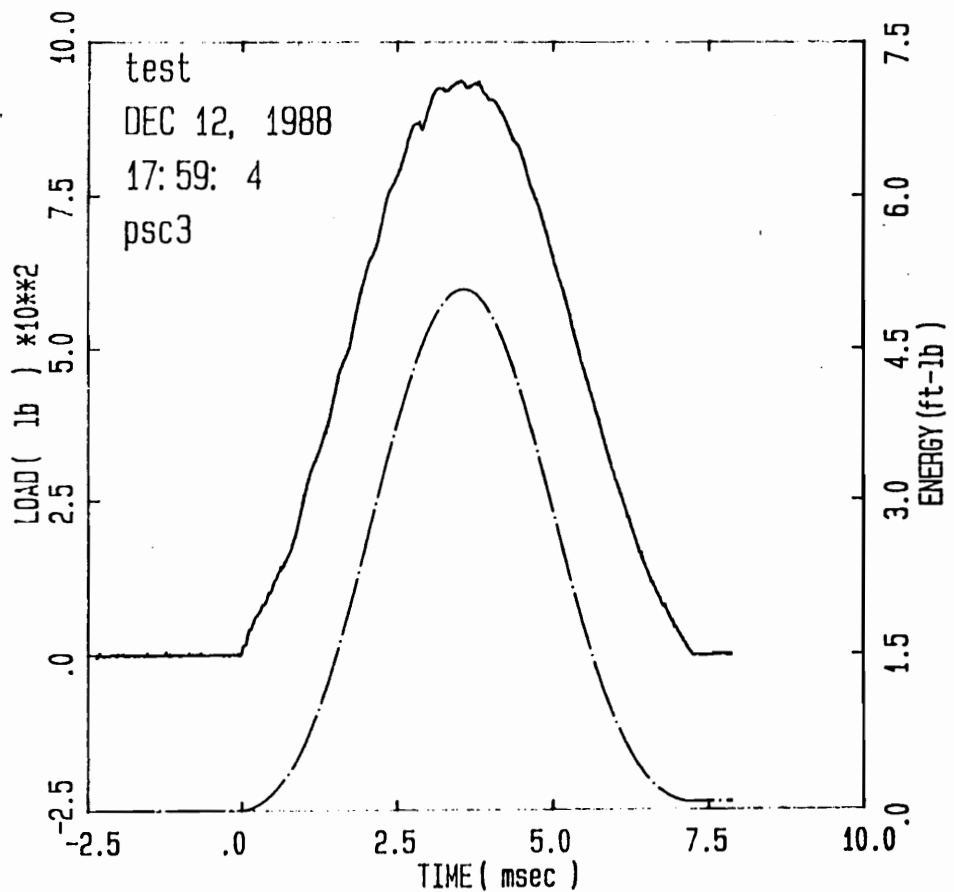
Figure 5.10. Typical response of an embedded optical fiber modal domain sensor to heavy impacts to the host composite; shown are the initial peak in the upper trace and the associated energy [14].

Figure 5.11. Typical load and energy curves generated by the DYN730-I.

Signal Duration and Rise Time vs. Impact Energy
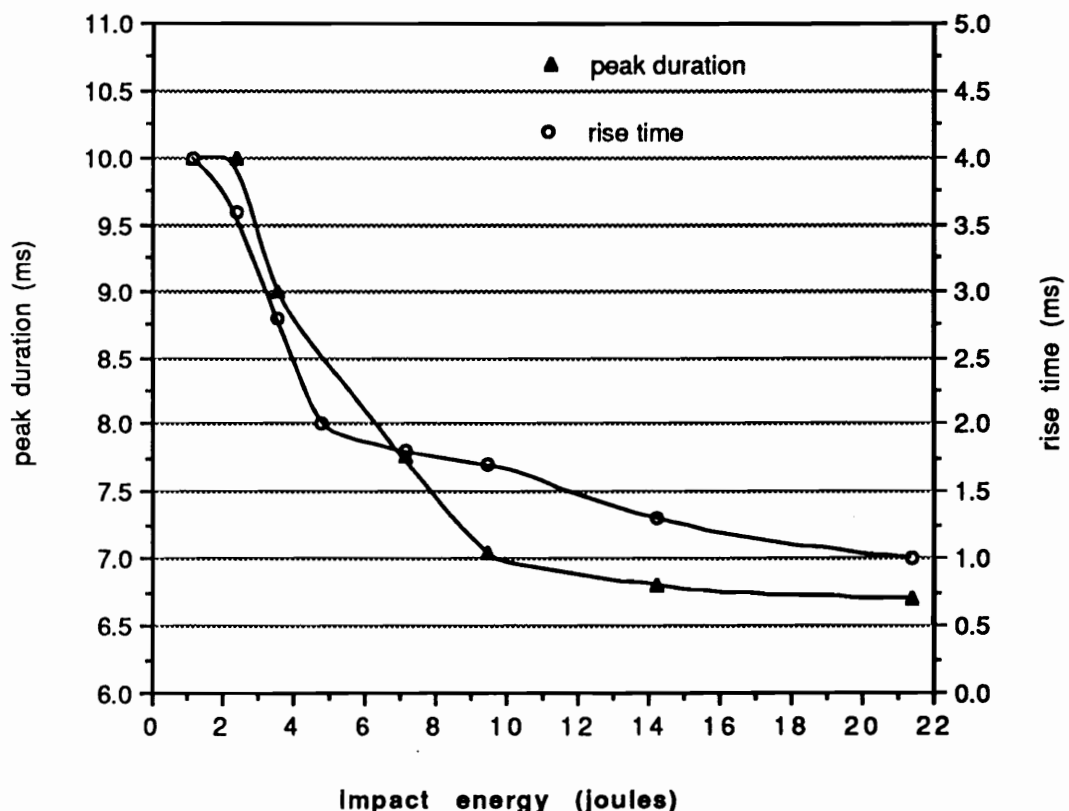
Figure 5.12. Signal duration and rise time versus input energy.

Detected Energy vs. Input Energy
**200 ms Integration**
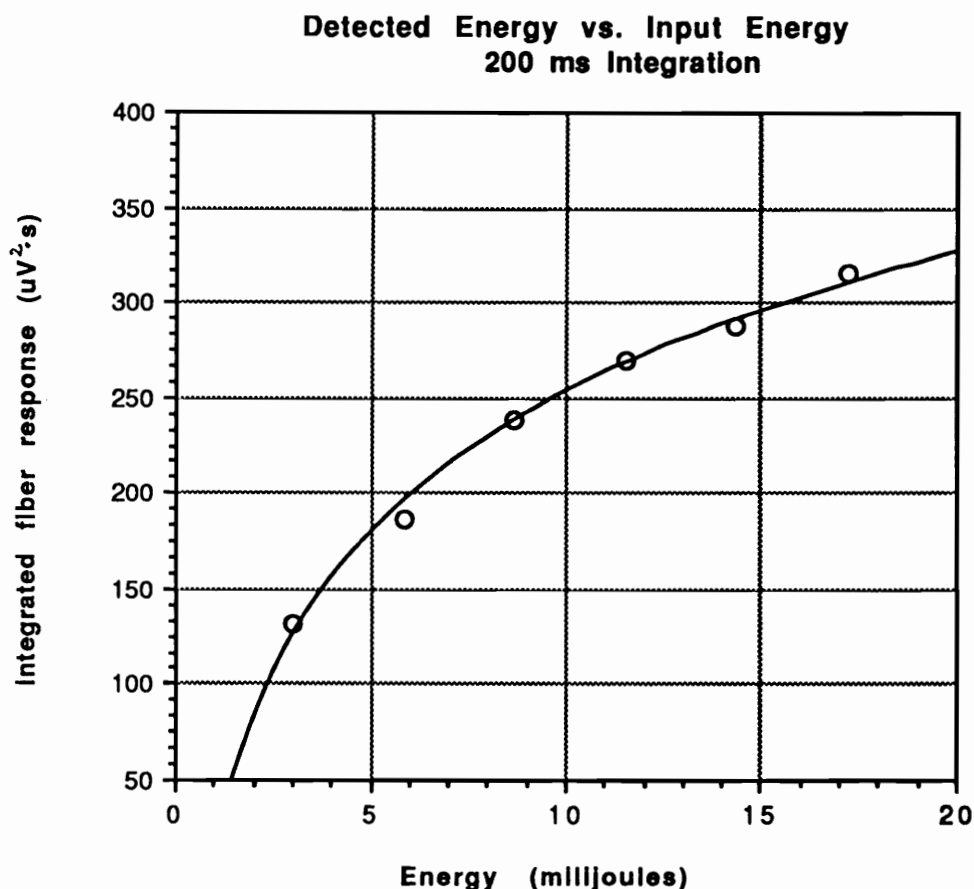
Figure 5.13. Results of low energy impacts on composite panel containing embedded PCS optical fiber. Compare general shape with Figure 5.7 [14].

6.0 OPTIMIZATION ISSUES FOR MODAL DOMAIN SENSORS

It has been stated throughout this report that modal domain sensing still cannot be considered a mature method for transducing physical observables. Despite the advantages of this technique, a number of difficulties still exist which would ultimately limit its deployment in many mission-critical situations. The primary shortcoming of modal domain sensing is simply that not enough is known about it. Fortunately, as displayed in the previous two chapters, because of its many inherent similarities to single mode interferometry, much of the body of knowledge acquired in that discipline can almost certainly be modified or extended, and applied to modal sensors. Furthermore, a large number of factors play a role in determining their final sensitivity and practical utility in various contexts. Thus hope exists that the "right" combination of variables for particular measurement situations can be found.

Considerations for enhancing or optimizing modal domain sensors can be broken into three categories: source characteristics, fiber characteristics, and detection scheme characteristics. Implicit in all of these is a fourth category, that of the target observable and the environment in which it is to be measured. A brief discussion of each of these areas follows.

6.1 Source Characteristics

It is evident from what has been said before, that the optical light source determines in large part the operating features of a modal domain sensor. For one, it must be coherent, though coherence length requirements are much smaller than necessary for single mode interferometers, unless the latter strictly maintain equal path lengths between the two arms. For few mode sensors, which have lower sensitivity, source stability requirements

can also be relaxed somewhat, though at obvious expense. These point to the conclusion that semiconductor laser diodes, which are sometimes unstable and display shorter coherence lengths, should offer improved performance to MDS over conventional interferometry.

Another factor is the source wavelength. It was seen in Chapter 4 that operation of dual mode and multimode fiber sensors at a particular V number in part determined their phase sensitivity. For a given fiber, adjusting the V number is in practice accomplished by altering the operation wavelength of the laser source. This may mean using a different source altogether, or using a different line from a multi-line laser. Also, as shown in Chapter 3, the source wavelength affects the number of speckles visible in the output pattern from a multimode fiber. As will be discussed, it may be possible to use this very mechanism as a means for sensing.

The manner in which source radiation is injected into the fiber is also important in determining the output pattern. For ordinary dual mode fibers in which the amount of power in the two modes is roughly equal, we showed that the output consists of a single, off-centered lobe which oscillates back and forth with the application of strain. However, experience relates that when off-axis launching occurs, particularly in round core fibers (as opposed to elliptical core dual mode fibers), significant power can be excited in the LP_{11} mode over the circularly symmetric LP_{01} mode. The result is that two lobes appear which exchange power with strain; quadrature is reached when power in the lobes is equal. Depending on the detection scheme, either one of these options could be preferable.

In the case of multimode fibers, maximum sensitivity occurs when interference takes place between the lowest and highest order modes. In order to enhance the power in the higher modes, which usually carry less power, off-axis launching may again be employed. Figure 6.1 illustrates the type of changes in output pattern which may be expected in this case. As an alternative, one could imagine a mask to be placed before the input end of the fiber which consists of an annular ring surrounding a centrally located hole, which could be used to increase the relative amount of power injected into the extreme order modes.

6.2 Fiber Characteristics

One of the major problems with interferometrically based fiber sensors arises due to their extreme sensitivity, not only to the observable of interest, but also to the environment. In any practical situation, fluctuations in the sensor temperature or surrounding air currents must be accounted for. At a very minimum, these fiber sensors must be carefully designed to be somewhat insensitive to environmental changes, while simultaneously retaining sensitivity to the parameter under study.

To demonstrate the sensitivity of an optical fiber interferometer to temperature fluctuations, we can lean on the expressions in Chapter 4 to calculate the amount of phase change one might expect when the fiber undergoes a temperature change. We start with the single mode fiber sensor. Specifically, when the fiber experiences a hydrostatic expansion or contraction due to changes in temperature, as a first approximation we take the corresponding change in phase to be due to a combination of both axial and radial strain as expressed by equations (4.35) and (4.58). Furthermore, in order to account for strain in both the x and y directions, we double the contribution due to radial strain. That is, working through the previous derivation term by term, it can be shown that $\Delta\theta_T$,the change in phase due to temperature changes, can be expressed as

$$
\begin{aligned}
\Delta\theta_T \;=\;& \left[\, \beta - v\,S\,V + \alpha_{\text{eff}}\,S\,V \,\right] L\,\varepsilon_z \\[6pt]
+\;& \left[\, -\left(\tfrac{4\,v}{1-v}\right)\beta + 2\,S\,V + 2\,\alpha'_{\text{eff}}\,S\,V \,\right] L\,\varepsilon_r
\end{aligned}
\tag{6.1}
$$

This form can be abbreviated so that the final sensitivity values from Table 4.5 can be substituted directly:

$$
\Delta\theta_T \;=\; \Delta\theta_{\text{axial}}\,L\,\varepsilon_z \;+\; 2\,\Delta\theta_{\text{radial}}\,L\,\varepsilon_r
\tag{6.2}
$$

The change in dimension due to the application of a temperature change ΔT is given in simplified for by

$$\Delta L = \gamma L \Delta T \tag{6.3}$$

for the axial direction, while for the radial direction,

$$\Delta a = \gamma a \Delta T , \tag{6.4}$$

where γ is the coefficient of thermal expansion (CTE) for the glass fiber material. Recalling that from the definition of the strain ε_z and ε_r , we may write $\Delta L = L\varepsilon_z$ and $\Delta a = a\varepsilon_r$. Equating these different expressions for length and radius change, we conclude that

$$\varepsilon_z = \gamma \Delta T = \varepsilon_r , \tag{6.5}$$

which when substituted into (6.2), leads to

$$\Delta\theta_T = (\Delta\theta_{axial} + 2 \Delta\theta_{radial}) L \gamma \Delta T . \tag{6.6}$$

This expression then applies to both single and multimode fibers, as long as the correct expression for $\Delta\theta_{axial}$ and $\Delta\theta_{radial}$ are employed.

Assuming a unit fiber length and a one degree centigrade temperature change, and a CTE for fused silica of roughly 5×10^{-6} /°C, we have for the single mode fiber,

$$\frac{\Delta\theta_T}{L \Delta T}\bigg|_{sm} = 130 \text{ radians} / \text{m} °C , \tag{6.7}$$

while for the typical multimode fiber, the numbers yield,

$$\frac{\Delta\theta_T}{L \Delta T}\bigg|_{mm} = 32 \text{ radians} / \text{m} °C , \tag{6.8}$$

These values demonstrate the extreme sensitivity of both single and multimode fibers to temperature changes. It should be kept in mind that since fractions of a degree of phase change in a fiber sensor can be resolved

with ordinary electronics, then temperature fluctuations of roughly 10^{-4} degrees should be detectable.

Several effects tend to at least partially negate this high sensitivity to temperature. For one, the time constants associated with heat diffusion will cause much of the random temperature fluctuation to be averaged over time, meaning that each minute variation will not necessarily be detected. In addition, this effect will be enhanced with the addition of jacketing material to the fiber, and naturally, one would expect different materials to have different heat diffusivities. Specifically, if δ is the diffusivity of heat, s is the specific heat, and ρ is the density of the coating material, then the rate of heat dH/dt passing an additional radial distance due to the jacketing t_j is given by

$$\frac{dH}{dt} = \delta s \rho \frac{\Delta T}{t_j} d\phi \, dz \quad , \tag{6.9}$$

where ΔT is the temperature differential over the jacketing thickness. This suggests that in order to slow the rate of heat transfer across the jacket, one could apply a softer, thicker coating material.

In addition to time averaging effects, spatial averaging also tends to decrease the practical sensitivity of a fiber phase sensor to temperature changes. That is, whereas random fluctuations may cause elongation in one portion of fiber, it may cause contraction in another. The net effect will be at least a partial cancellation of phase change, though observation of a sensor operating in a practical environment suggests that time-varying temperature effects still lead to a fair amount of signal instability. Also, by comparison with temperature variations, which even in laboratory environments may swing several degrees in a several hour period, normal atmospheric pressure variations are in the millibar range. Thus, with a sensitivity of approximately 10 radians/m/bar [100], the dominant environmental effect can be seen to be temperature variations.

Perhaps the most common temperature compensation scheme applied primarily to single mode interferometers involves the use of a piezoelectric cylinder around which the reference fiber is wound [84]. The cylinder acts

to stretch the reference fiber in response to very low frequency signal variations such as associated with environmental changes, through a feedback circuit. It is envisioned that a similar arrangement could be employed to compensate for fades in multimode fiber outputs, though the lack of a strictly periodic output may lead to complications. However, it is interesting to note that for relatively short lengths of fiber, signal fading is much less problematic than for long lengths, as verified by Crossley [100]. In addition, he reports that increased environmental disturbance (in his case the application of heat to a fiber using a heat gun) produced more frequent signal oscillations or fades, as opposed to deeper fades. This suggests that signal variations could be quantified for a fixed length of fiber.

In this discussion, it is presumed that the signal of interest, such as that due to an acoustic wave, varies at a frequency much faster than that due to environmental perturbations. This allows for the ability to separate the signal responses using standard electronics. In situations where the "noise" and desired signal are similar in frequency, more sophisticated techniques must be employed, such as to intentionally measure strain and temperature effects separately. This may be performed using two different sensors, or as mentioned earlier in the report, with a single sensor operating at two different wavelengths, as outlined by Duncan.

Another concern with modal domain sensors which has basically been ignored so far in this presentation regards the sensitivity to perturbations of portions of the fiber leading to and from the workpiece under study. For example, if we are seeking to measure acoustically induced strain in a section of fiber in a water tank using a multimode fiber, then the sections of fiber leading to and from the water tank must be isolated from any environmental effects which could increase the noise floor of the measurements in the tank, or lead to signals which could be confused with the acoustic waves of interest. This concern is not unique to modal domain sensors, in fact all intrinsic sensors need to face this question, but modal domain sensors do offer some unique solutions.

Since the sensor operates on the principle of differential modulation of the phases associated with the various modes in the section of interest, it is

natural to suggest that the lead-in fiber be one that supports only one mode, thereby defeating noise mechanisms in that section. A single mode fiber then acts only as a pipe to carry light from the laser to the section of dual or multimode fiber in the sample; small perturbations in this section can be tolerated, though that is not meant to imply that the MDS will be totally insensitive to phase changes in the lead-in fiber. Rather, for small perturbations, changes in the initial phase ψ_n will be seen in all the modes supported by the MDS, but large disturbances such as macrobending could shift the position and shape of the mode field radius [115], and affect the amount of power which is injected into the various modes in the sensor portion. The amplitude modulation which occurs is in general indistinguishable from the signal of interest.

A single mode fiber could be employed in a similar manner to carry the sensor signal away to the receiving detector. Instead of placing a spatial filter in the output field, or allowing the photodetector surface itself limit the extent of the radiation from the sensor, a single mode fiber in the near field could perform the same function. Similarly, a smaller core or off-set multimode fiber could be used to collect even more of the signal light, provided the receiving detector collects all the radiation from the lead-out fiber. The use of lead-in and lead-out fibers for multimode sensors was first reported by Bennett and co-workers [108], and later improved by Murphy et. al. [116]. In the latter paper, the authors report the use of elliptical core single mode fiber lead-in, an elliptical core dual mode fiber section for sensing, and a round core single mode fiber used to collect signal information. In their method, the use of a fusion splicer in-line proved invaluable for connecting the fiber sections, while good insensitivity to noise signals on the lead-in and lead-out portions was demonstrated.

Related to the above discussion is the problem of mode coupling effects, especially in dual mode fibers. Instabilities due to coupling between modes lead to fluctuations and rotation of the output intensity pattern, and are especially troublesome when higher order modes are desired at the exclusion of lower order modes which are allowed in the waveguide. One solution to unwanted polarization coupling has been to employ elliptical core or highly birefringent fiber, as discussed in references 117 and 118.

These fibers split the degeneracy between the different polarizations (reducing the possibility of mode coupling), or even disallow one state, but both involve complications of their own, and do not prevent coupling between even and odd modes. For an in-depth analysis of mode coupling mechanisms, see references 93, 119, and 120.

Another possible solution to the problem of rotating lobes is simply to measure the effect rather than trying to prevent it. Two detectors properly placed in the output field could make relative power measurements and determine the amount of rotation which has occurred. Such a monitoring scheme might actually add insight to mode coupling mechanisms in real-world applications, as well as compensate for them. Alternatively, a larger portion of the two lobe output field could be imaged onto the detector surface, which would make the signal much less sensitive to slight rotations due to mode coupling. Unfortunately, this would probably lead to a poorer modulation depth, or fringe contrast.

Another very important concern with respect to dual mode fibers is maintaining quadrature during measurements. Nearly all the analysis presented in the previous chapters assumed that the fiber was operated at the Q-point, though it is well known that during any interferometrically based measurement, a certain amount of fading and drifting of the signal will occur due to environmental changes. A great deal of work has been reported on compensation techniques for maintaining Q-point stability in single mode interferometer reference arms. As mentioned earlier, the primary technique has been to sense the drifting signal from the detector, and use it in a feedback loop to drive a piezoelectric cylinder around which part of the fiber is wound. As the drift voltage appears, the cylinder expands or contracts, changing the strain biasing in the fiber and forcing it back into quadrature. Simple d.c. strain biasing has also proven a useful alternative for achieving quadrature in a relatively stable laboratory environment.

When optical fibers are applied to structures for the purpose of strain sensing, it is always assumed the there is perfect mechanical coupling of

the strain from the structure to the fiber. Not only does this imply that intimate contact is maintained between the structure and the fiber the entire interaction length, but says that the shear modulus of any coating on the fiber is capable of entirely transferring strain. As mentioned in the second chapter, it has been observed that this may not always be an accurate description of the mechanics. Although at least one study has been performed to determine the ability of certain epoxies to transfer shear strain, results of a general nature have been lacking in the field. It is suggested that further experimentation be performed to determine which coatings and epoxies, or which alternate technology are best suited for attached and embedded fiber sensors.

A related concern regards the the proper conditioning of fibers to optimize their sensitivity to acoustic waves. Researchers at the Naval Research Laboratory have performed much work to determine that contrary to previous speculation, maximum sensitivity is generally not achieved by stripping the fiber of its coating before use [121]. Rather, a compliant polymer jacketing seems to best transfer acoustic wave energy to fiber strain, as well, of course, as adding protection to the fiber. This result is suggested in the work using plastic clad silica fiber mentioned earlier.

Finally there is the question of optimized fiber placement, geometry, and gage length. All of these factors depend in part on the quantity that is to be measured. For example, if structural vibrations are to be monitored, fibers may be run in lengths so as to maximize the response to certain modes of vibration, while minimizing others. Such is the crux of the patent of Kush and Meffe mentioned earlier [69]; a figure from that document illustrates the idea in Figure 6.2. Placement of a fiber embedded within a material is also important. Any directionality existing in the field to be measured must be accounted for, such as keeping the fiber transverse to the propagation of acoustic waves. Anisotropies of the part geometry must be regarded as well. For example, it has been shown earlier that excessive internal strain concentrations can at least be partially avoided by embedding fibers parallel to surrounding graphite fiber tows in

graphite/epoxy materials. This may require special considerations in part design.

Furthermore, as suggested by the integral relationship of equation (4.17), the optical fiber actually acts to integrate the component of the strain field parallel to the fiber. If the strain is not uniform, the response will not be straightforward to interpret. Figure 5.2, comparing the response of a piezoelectric transducer with that of a modal domain sensor to an acoustic emission, demonstrates this point. Whereas the piezoelectric sensor has a gage length of a few millimeters and was fairly narrowband in its response, the fiber not only was more broadband, but also interacted with the traveling and resonating acoustic wave all along its length of nearly 20 centimeters. Depending on the type of information necessary, this type of response may be sufficient, though certainly not in all cases. Also, the sensor gage length must be tailored for not only the application, but the particular acoustic wavelength or bandwidth of interest as well. Shorter sections of sensitized fiber can localize the wave interaction better, though at the expense of decreased sensitivity due to smaller interaction length. At the same time, decreasing the sensor size also reduces the complicating integration effect over the active sensor section, as well as the convolution of the signal over time.

6.3 Detection Scheme Characteristics

The primary method for monitoring disturbances to modal domain sensors consists of allowing a photodetector to intercept light from one or more sensitive lobes or speckles. One way to do this is to place a spatial filter such as a pinhole between the end of the fiber and a large area detector. The pinhole location is scanned so as to find the point of maximum amplitude modulation, in the case of the LP_{01}/LP_{11} sensor, or for a multimode fiber, a speckle or group of speckles of the desired sensitivity (note that in some applications the highest sensitivity is not always the optimal case). Alternatively, a small area detector could be used, where the extent of the photodiode itself acts to spatially filter the

output pattern, or a small core fiber could be employed for the same purpose. In all cases it is most important that not all of the light is detected. That is, during the course of detecting an event, the lobe, speckle, or group of speckles will vary in intensity, or equivalently, bright speckles will move in and out of the view of the detector. As one may expect, as mentioned above with respect to dual mode fibers, collecting a larger number of speckles in a multimode output effectively adds an increasing d.c. bias, reducing the modulation depth of the signal. On the other hand, individual speckle motion during a periodic perturbation may contain frequency harmonics which are irrelevant to the problem under study (physically meaningful somewhere in the fiber, but not representative of the overall motion of the structure to which the fiber is attached, for example). Furthermore, monitoring of a single speckle necessarily involves relatively low signal amplitude, noisier signals, and a need for better electronics. Thus the "best" number of speckles to monitor, or with dual mode fibers the optimum detector size varies with each particular situation. No comprehensive study is available documenting the effects of pursuing possible trade-offs.

The previous methods all suffer from the fact that in most cases, only a small proportion of the total energy emerging from the fiber is collected to infer perturbations on the fiber. This leads to obvious needs for higher source power and output amplification to maintain signal integrity. Furthermore, as outlined above, a host of choices exist as to where to place the detector in the output field (centered, near an edge), how many speckles to intercept (one, a few, many), and the shape of the detection area (circle, annular ring to try to increase the contribution from higher modes perhaps). Thus, there is no guarantee that maximum sensitivity will be achieved, or having been achieved, that it will remain that way for long periods of time. Thus efforts have been made to employ full field methods, that is, to use the entire speckle pattern to infer changes. Clearly if highly sensitive interference effects are sought rather than microbending, then simply imaging the entire output field onto a single detector would yield no

change with perturbations. A method to interrogate the structure of the speckle pattern while still collecting all the energy is sought.

The first full field method demonstrated to our knowledge, consisted of a 6 x 6 array of discrete photodetectors analog multiplexed into an A/D board resident in an IBM personal computer [122]. Used primarily to process the output from dual mode sensors, this system discretized the light into 36 pixels, and calculated the location of the centroid of intensity. As the fiber experienced strain, the processor tracked the motion of the centroid. It was noted that the number of detector elements could be increased or decreased depending on the trade-off requirements between resolution and speed. Furthermore, depending on the application, a faster, dedicated processing unit could be built inexpensively. Also, low light levels could be used, and a certain amount of microbending or injection losses could be tolerated. However, though well suited to the simple dual mode fiber output, the calculating algorithm would not be expected to perform well with highly multimode fiber patterns.

A related technique demonstrated by Spillman and fellow researchers did in fact make use of a dedicated processor reading the output of a 128 x 128 CCD array having a speckle pattern imaged on it [18]. Their algorithm differed however in that each frame of pixel intensities were first captured, and then compared pixel by pixel to that of the preceding frame. The difference in pixel intensity was calculated, the absolute value was taken, and the sum of these values was computed over the entire array. The absolute value was necessary in order to avoid the signal cancellation such as occurs when a single detector collects the entire speckle pattern. Changes in the computed sum were used to detect both the vibration of a beam and individual events such as sub-surface ground disturbances. It was seen to be much less sensitive to injection variations than a spatially filtered multimode sensor, also tested by the authors. Their sensor also displayed considerably better harmonic distortion characteristics, though it suffered from a low operation bandwidth due to the large number of pixels processed and the frame processing rate of the system.

The only other example of full field detection of modal domain sensor signals is described in a recent paper by Indebetouw, et. al. [109]. Their

method relies on holographic matched filtering concepts. Light from a modal domain sensor output is mixed with mutually coherent light from a single mode fiber on a photographic plate, thereby forming a hologram of the sensor output. When the hologram is developed and repositioned in the output field, the single mode fiber beam is reconstructed to the extent that the sensor output agrees with what it was at the time the hologram was recorded. Thus, by monitoring the correlation beam, one can infer changes to the sensor fiber. This method was applied successfully to both dual mode and multimode fiber sensors, the latter being characterized by enhanced strain sensitivity and a generally monotonic output, though suffering from a small dynamic range and low signal, and required careful repositioning of the holographic filter.

6.4 Sensing Alternatives for Multimode Fibers

In this final section, two alternative methods for using multimode fibers for sensing are discussed. Both techniques depend on tracking the coupling of power from one mode to another, and possess unique advantages over others described in this report. In the first method, bending in a multimode fiber can be seen to cause a change in the modal power distribution (MPD), or the amount of power in each mode. Not being interference-based, it is possible to avoid the use of laser sources, offering a great savings in cost complexity, and stability, at the expense of sensitivity. In the second method, it is changes in the number of speckles with strain which is monitored. Though not fully confirmed, it is believed that this could be the first interferometrically based sensor to yield a truly linear output.

6.4.1 Speckle Migration Due to Modal Power Redistribution

In the sections above, it is assumed that throughout a measurement, the speckle pattern stays roughly confined in numerical aperture, and that

the distribution of energy across the output takes an approximately Gaussian shape, as shown in Figure 6.3a. When a fiber undergoes sharp, or small radius bends however, much more energy is coupled into the higher order and radiation modes, with the effect that the speckles appear to migrate away from the center, drastically altering the energy distribution. This can be seen in Figure 6.3b-h, where a successive amount of bending was applied to a 50/125 step index fiber propagating He-Ne laser light. Similar trends can be seen when fibers are highly strained in the axial direction, though the signal change is not nearly as dramatic as for bending.

Experiments to quantify this change were performed using the set-up appearing in Figure 6.4. Both a He-Ne and a He-Cd laser were available as sources, while detection was performed with a CCD array coupled in an Imagelab image processing system, yielding roughly 500 x 500 pixel resolution. Because of the extreme sensitivity of this device, the laser needed to be signifryantly attenuated to avoid saturation; two variable-angle polarizers were used to continuously tailor the input intensity. Both fiber ends were mounted on 5-axis positioners (not shown), the output side allowing for centering of the speckle pattern on the CCD array, and the fiber was attached or clamped at two points along its length to be able to impart axial strain with a micropositioner.

Both in the case of the bent fiber and the axially strained fiber, the amount of light intensity falling within the circle defined by the unstrained fiber output was calculated as a function of disturbance. Though the figure above clearly shows a difference in intensity in this area, the results as calculated by the computer were somewhat inconclusive. The exact cause for this is not known, though is is noted that no compensation was made for the microbending loss which accompanied the speckle migration. Also not well understood is the clear ring-like features evident with increasing bending, which seem to imply an underlying trend in the mode coupling effects. However, the use of individual photodiodes in a monitoring system using a conventional (A−B)/(A+B) scheme has been reported [24,123].

6.4.2 Speckle Counting

The motivation for investigating the possibility of counting the number of speckles to infer fiber strain has its roots in a paper presented at the Fourth European Conference on Fiber Optics in Genoa, Italy in 1978 by R. Epworth [124]. In that article, reprints of which were of obtained in 1981, the author discusses the topic of modal noise. This phenomenon occurs when multimode fibers carrying coherent light information signals are imperfectly spliced or connected together, or when the output speckle pattern does not completely fall on the optical receiver. Variations in fiber geometry before the splice, etc. result in the modulation of power at the output, similar to the spatially filtered sensing scheme discussed above. In the course of his discussion, Epworth presents a simple model of modes in the fiber resembling Figure 3.15b, and concludes without justification that the number of speckles S at the output is

$$S = \frac{4 \pi a^2 (n_1^2 - n_2^2)}{\lambda^2} \tag{6.10}$$

This relation was accepted at face value by the present writer for some years, until it was conceived recently that counting the number of speckles as a function of strain may provide an alternate full field sensing technique for modal domain sensors.

Upon further thought however, some doubts arise as to the validity of this equation. It is first striking that from the definition of V, (6.1) can be expressed at $S = V^2/\pi$. This corresponds exactly to the number of modes in a fiber as given by some authors, and is nearly equal to that given in equation (3.38); both expressions are recognized to be approximate. Because Epworth's paper was largely experimental (meaning the emphasis was on data rather than derivations), and because of the absence of any discussion of interference, it is believed that he may have confused the number of speckles with the number of modes. Nevertheless, as pointed out earlier, the number of speckles visible *is* surely related to the number modes of

propagating within the fiber, and so is related to the fundamental fiber parameters encapsulated within V. Therefore, it should be possible to construct a sensor based on monitoring the number of speckles in the output field as a fiber undergoes strain.

Investigation of this idea took two approaches, one analytical, to be presented first, and one experimental. Since no better guess was immediately obvious for determining the number of speckles, and since no clear evidence exists that Epworth was mistaken, the analysis starts with equation (6.10) and proceeds to find an expression for the sensitivity of the number of speckles per unit strain. That is, we begin by taking the derivative of S with respect to strain along the axis, ε_z, and by considering the optical wavelength as unaffected by strain, state that

$$\frac{dS}{d\varepsilon_z} = \frac{4\pi}{\lambda^2} \frac{d}{d\varepsilon_z}(a^2 (n_1^2 - n_2^2)) \tag{6.11}$$

Being the product of terms which individually depend on strain, this becomes

$$\frac{dS}{d\varepsilon_z} = \frac{4\pi}{\lambda^2} \left[2a(n_1^2 - n_2^2)\frac{da}{d\varepsilon_z} + a^2(2n_1\frac{dn_1}{d\varepsilon_z} - 2n_2\frac{dn_2}{d\varepsilon_z}) \right] \tag{6.12}$$

$$= \frac{8\pi a}{\lambda^2} \left[(n_1^2 - n_2^2)\frac{da}{d\varepsilon_z} + an_1\frac{dn_1}{d\varepsilon_z} - an_2\frac{dn_2}{d\varepsilon_z} \right] \tag{6.13}$$

The derivatives of a, n_1 and n_2 are available from Chapter 4, and can be expressed as

$$\frac{da}{d\varepsilon_z} = -a\,v \tag{6.14}$$

$$\frac{dn_1}{d\varepsilon_z} = -\frac{1}{2}n_1^3 p_{eff} = -\frac{1}{2}n_1^3 [(1-v)p_{12} - v\,p_{11}] \tag{6.15}$$

$$\frac{dn_2}{d\epsilon_z} = -\frac{1}{2}n_2^3 p_{eff} \tag{6.16}$$

Substituting these into (6.13) and simplifying, we have

$$\frac{dS}{d\epsilon_z} = -\frac{8\pi a^2}{\lambda^2}\left[(n_1^2 - n_2^2)\nu + \frac{1}{2}p_{eff}(n_1^4 - n_2^4)\right] \tag{6.17}$$

Before proceeding, it is interesting to note at this point that (6.17) predicts a decrease in the number of speckles for a value of positive axial strain (tension). Also, if the typical values for the constituent parameters in Table 4.4 are substituted into this relation, it is discovered that the first term in the brackets is lower than the second by a factor of 2.5. The first term can be considered that part due to the change in fiber radius, while the second arises from changes in the refractive index. The base assumption being the same here as in Chapter 4, namely that the change in index n_1 and n_2 must be accounted for separately, it is not surprising that the analysis in that chapter also predicts that the radius change term for phase sensitivity to be greater than the index term by the same factor.

If the factor $(n_1^2 - n_2^2)$ is factored out of (6.17) and terms are combined, the speckle sensitivity per unit strain can finally be expressed as

$$\frac{dS}{d\epsilon_z} = -\frac{2}{\pi}V^2\left[\nu + \frac{1}{2}p_{eff}(n_1^2 + n_2^2)\right] \tag{6.18}$$

Again, it is important to note that this relation is based on an unconfirmed expression for the number of speckles in the fiber.
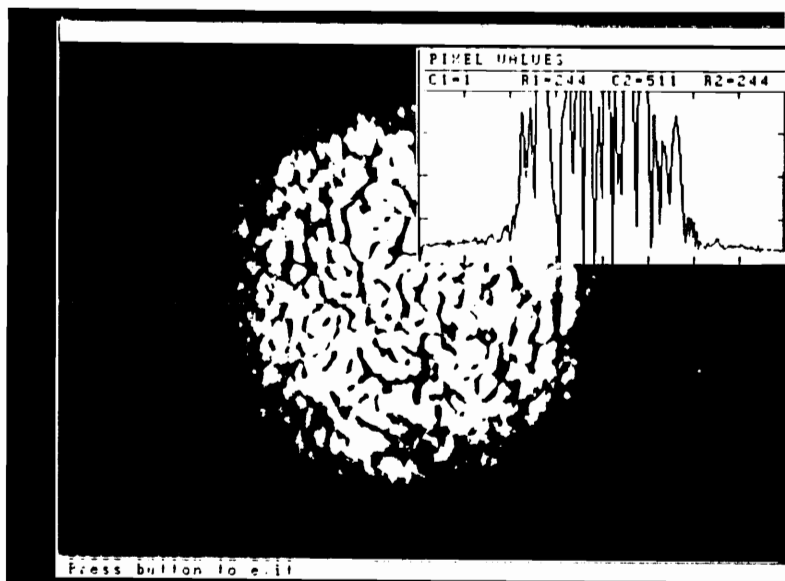
When the same values are substituted into equation (6.18), they suggest that $\Delta S \approx -7,8000\,\epsilon_z$, assuming an initial value of strain equal to zero. This predicts that for a strain of 1%, which is near the breaking point of many commercial fibers, a decrease of 78 speckles will be observed. For the parameters listed, the total numbers of speckles given by our formula is 6,573, meaning that a 1% strain would lead to a 1.2% decrease in the number of speckles.

Several points become immediately obvious here. The first is that at best, this sensing method can be considered quite insensitive relative to many other methods. A 1.2% output change over the total expected range of use is quite small indeed. Second, in order for the sensor to provide useful data, it must provide a stable and repeatable value of the number of speckles at any given moment. The stability should be much better than 1.2%. Finally, (6.18) predicts that the number of speckles is linearly related to strain. If this is true, for this reason alone, the sensor may merit further investigation.
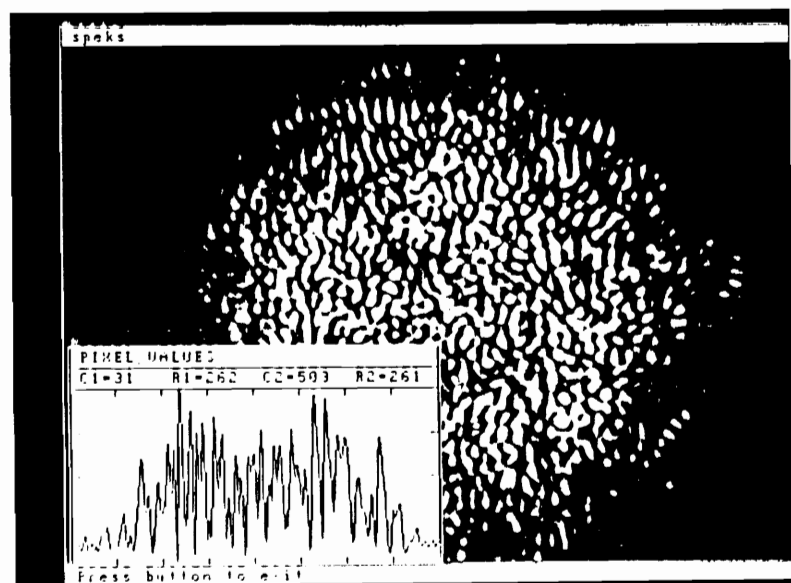
The experimental set-up in Figure 6.4 was again used to try to confirm equation (6.18). Details of the tests will not be given. The first step was deciding what to call a speckle. That is, looking at the typical pattern of Figure 3.16, it becomes uncertain where one speckle stops and the next begins. Clearly a threshold value has to be set, and pixel groups having peaks under that value would not count. Tests were performed to find the threshold value which corresponded most closely with what was observed visibly on the display monitor, and the threshold set at that point. The speckle pattern image was scanned, and the number of times the pixel intensity crossed the threshold setting (rising) were counted. The outcome for seven horizontal and seven vertical lines from near the center of the circular image were averaged, and treated as the diameter of circle. The total number of speckles was calculated as the circle area, or at least proportional to the same. Next, a base line pixel number needed to be established; it was found to vary widely, probably due to fluctuating temperature and air currents in the laboratory.

Finally, axial strain was applied to the fiber and the number of speckles recorded for each quarter turn of the micrometer screw. Unfortunately, there was no obvious relationship between the number of speckles and the amount of displacement. For one, the method of applying strain was found to likely be deficient. Also, the ability to take and individually process multiple frames of data was a sorely missed feature of the image processing software, meaning that a lapse of nearly two minutes between recorded images occurred. Lastly, as noted above, because the noise floor

was so unsteady, expected differences of signal change in the 1% range would be totally buried. At this point, conclusions as to the promise of this sensor method are tenuous, but not altogether unfavorable.

(a)

(b)

Figure 6.1a. Typical speckle pattern from a short section of 50/125 fiber with laser light focussed with a roughly NA-matched lens onto the center of the core. Figure 6.1b resulted from slightly off-axis launching. Note that the favored excitation of higher order modes results in more and smaller speckles spread over a larger angle, as qualitatively discernable from equation (3.47).
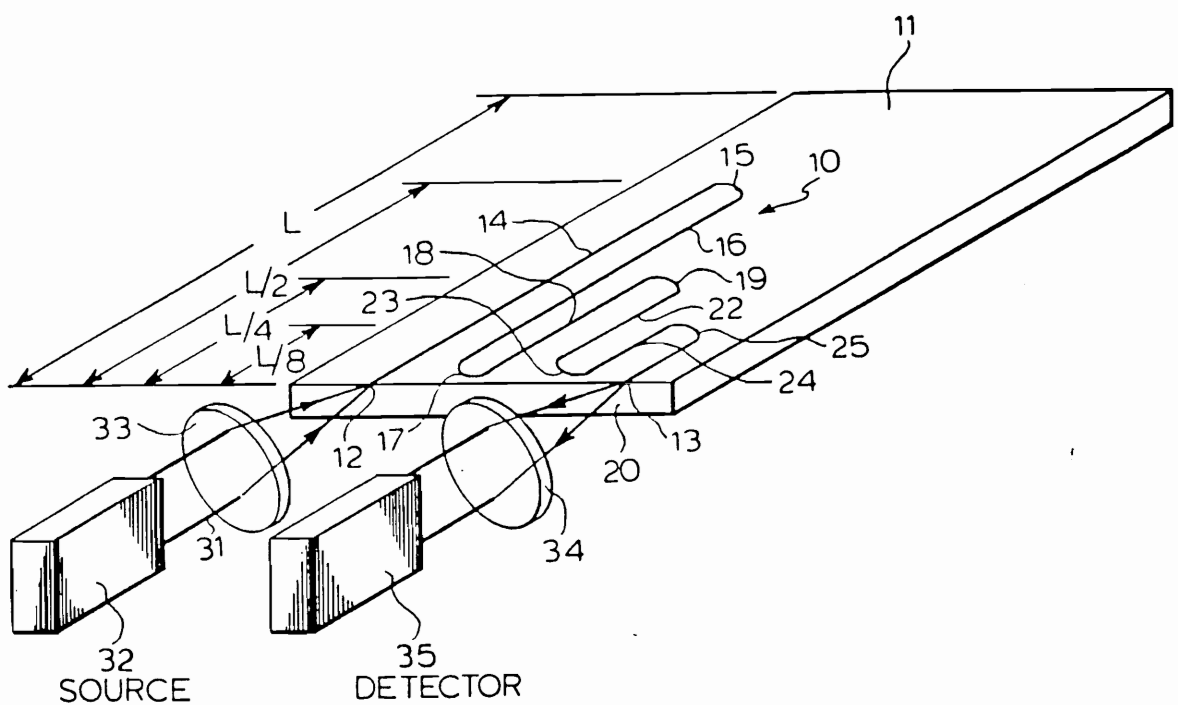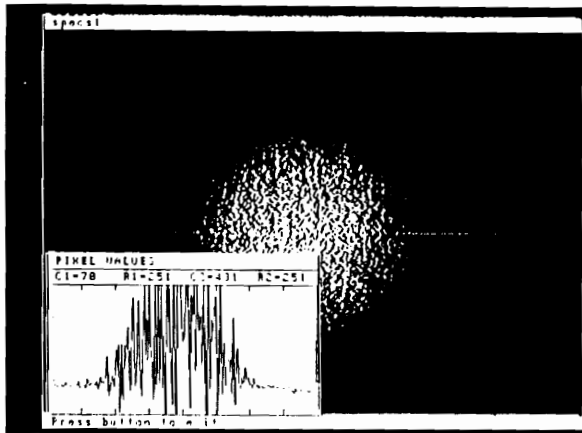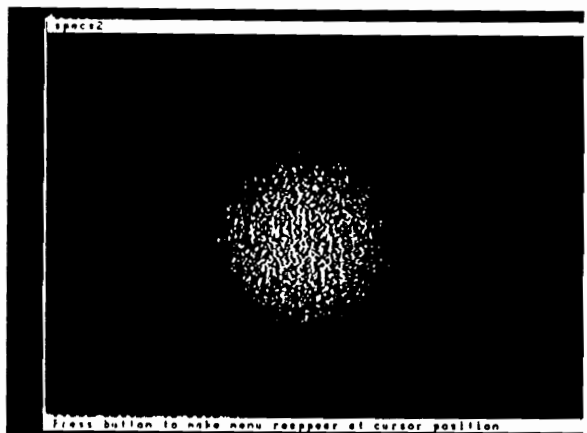
FIG.1.
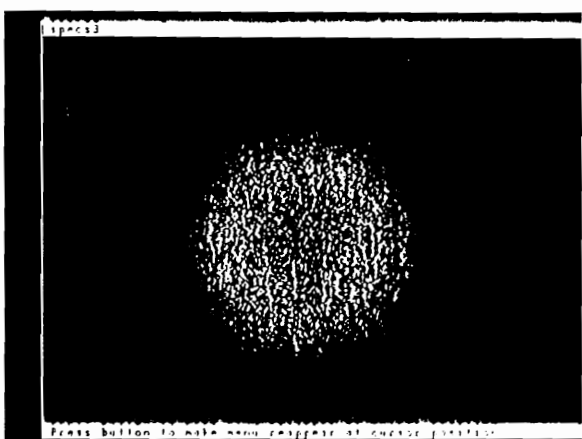
Figure 6.2. Illustration from Kush and Meffe patent [69].
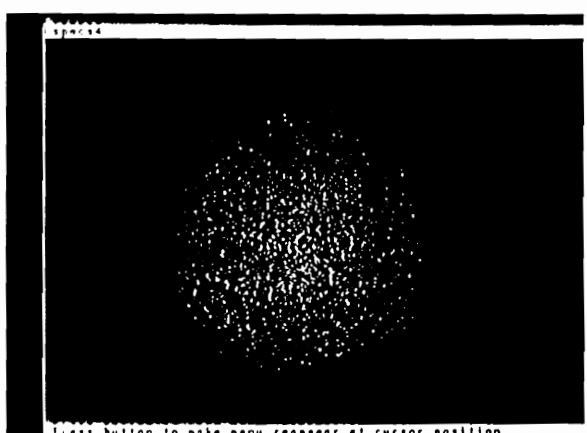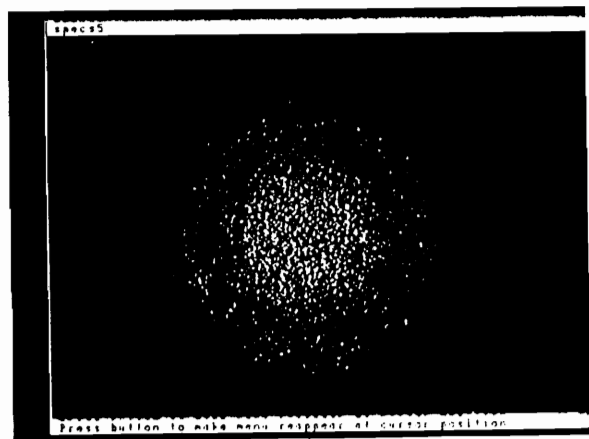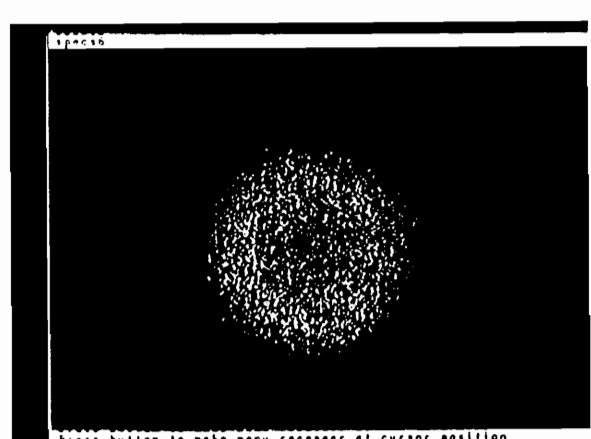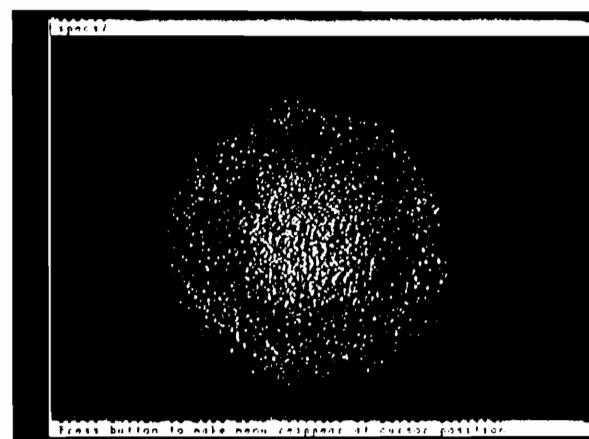
Figure 6.3. Speckle pattern changes as bending pressure increases from image a to h. Image a also shows the distribution of pixel intensities along the line shown on the figure.

Chapter 6 Optimization Issues of Modal Domain Sensors
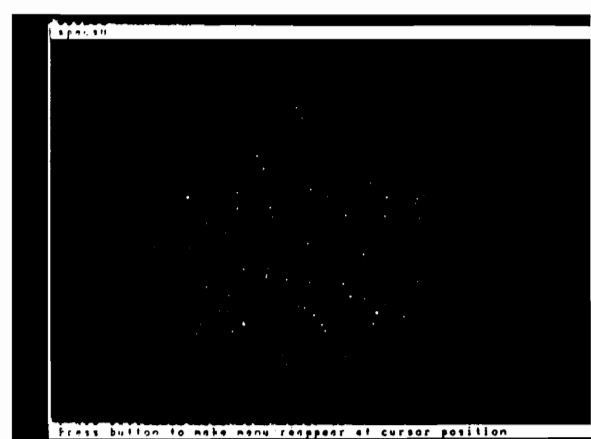
(e)

(f)

(g)

(h)

Figure 6.3 continued.
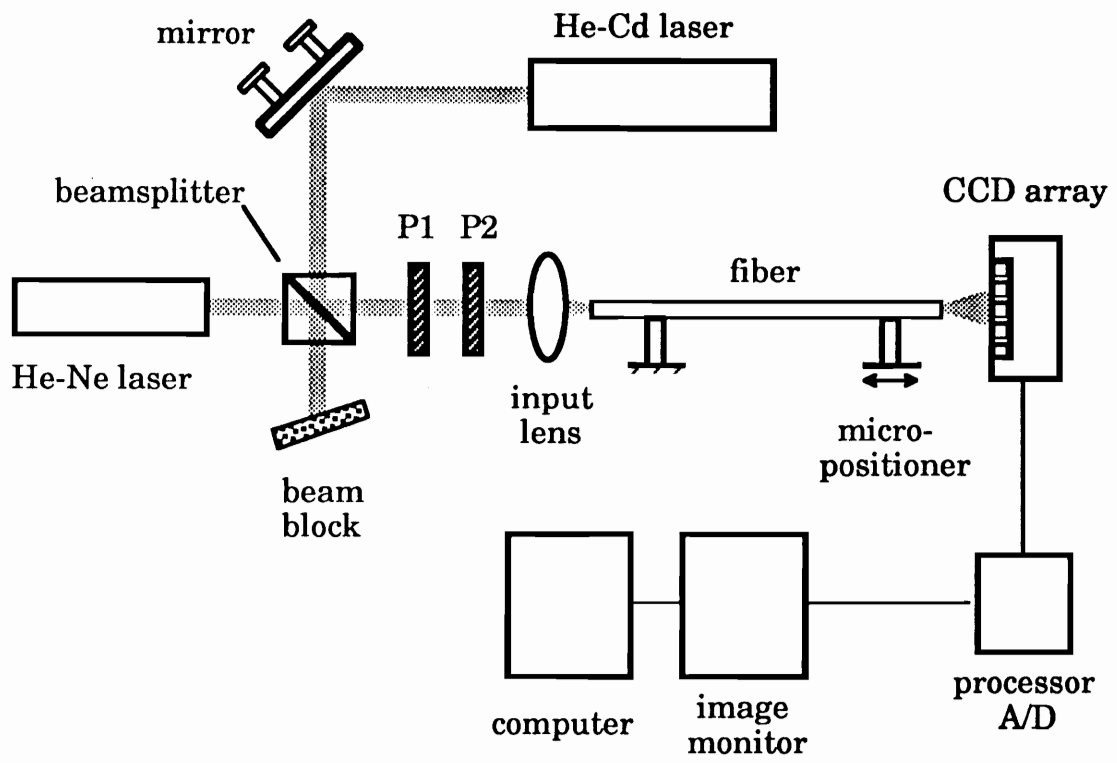
Figure 6.4. The experimental set-up used to test the alternate sensing schemes involving modal power distribution changes and speckle counting.

7.0 CONCLUSIONS

This report has focussed on one particular method of performing nondestructive evaluation, that of modal domain optical fiber sensing. The need for new sensors was justified on the basis of the many new materials being developed, and the increased desire for a variety of information regarding those materials, especially once they are incorporated into engineering structures. It was pointed out that modal domain sensors are only one type of fiber optic sensors that could and have been employed for NDE, particularly for real-time structural monitoring. The use of standard single mode interferometers, intensity or polarimetric based sensors, and optical time domain techniques are reviewed with regard to their application to NDE. It was seen that no one method will provide all the needs being sought by the measurement science community; real world schemes for structural monitoring will likely involve an eclectic combination of both fiber and non-fiber solutions, and perhaps include a number of different fiber sensor types. Nevertheless, modal domain sensors were suggested to offer significant advantages over a number of sensors reported to date.

A theoretical foundation for modal domain sensing was laid, starting with the standard scalar wave equation and proceeding to explain the existence of modes in step-index, circular dielectric waveguides. The nature of the interference between modes was investigated next, beginning with two LP_{01} modes in single mode fibers which are brought together in a Mach-Zehnder configuration. The interference pattern emerging from dual mode fibers was analyzed, and a computer program was written to model its output and performance with the application of strain. Finally, a general expression for the output pattern resulting from the interference of an arbitrary number and combination of modes in a step index multimode fiber was derived.

Next, the sensitivity of the phase of light in an optical fiber to applied strain was investigated. This is the most fundamental step in quantifying

the final sensitivity that one can expect from any fiber device utilizing interference phenomena, preceding discussion of other components in a sensing system, such as detector sensitivity, or electronic detection bandwidth. A new approach was taken to derive the change the index of refraction to strain, one which depends on differentiating between change in the core and cladding indices. These methods were applied to dual and multimode fibers. The LP_{01}/LP_{02} sensor was shown to be as much as seven times more sensitive than the LP_{01}/LP_{11}, with the added enhancement that it avoids problems with the coupling of power between even/odd modes and offers a circularly symmetric output pattern; methods to reliably achieve this sensor were discussed. Analysis of multimode fibers revealed that their absolute phase sensitivity rivals and in some cases can even surpass that of single mode interferometers, especially in the case of radially applied strain. It was seen that in these fibers, the phase change arising from changes in fiber diameter actually dominate the final sensitivity, as opposed to the single mode case, where the waveguide dispersion term is routinely dropped.

The application of modal domain sensing to acoustic wave monitoring in modern structures was described next. Detection of ultrasonic waves in the form of acoustic emissions from cracking graphite/epoxy composite specimens was described, as well as the monitoring of broadband ultrasonic shock waves arising from impacts to both metal and composite materials. These sensors were shown to possess an extremely broad frequency response, especially compared to piezoelectric devices, ranging from d.c. to into the gigahertz. It is believed that the upper frequency limits of fiber optic phase sensors will ultimately depend on factors such as the acoustic spectral attenuation of the host material and sound coupling efficiency, rather than on inherent insensitivity of the fibers themselves. It is noted that a recent U.S. patent awarded to the author and his advisor for the application of modal domain sensors rests largely on their demonstrated ability to perform in-service monitoring of structural vibrations, and acoustic wave events such as discussed here [125]. Finally a few issues were raised regarding the optimization of modal domain sensors, and suggestions for future efforts made.

REFERENCES

1. J.S. Heyman, "NDE In Aerospace--Requirements For Science, Sensors and Sense," IEEE Transactions on Ultrasonics, Ferroelectrics, and Frequency Control, Vol.36, No. 6, p. 581, November 1989.

2. W.J. Rowe, AIAA/SOLE 2nd Aerospace Maintenance Conference (San Antonio, TX) May 1986.

3. T.G. Giallorenzi, J.A. Bucaro, A. Dandridge, G.H. Sigel, J.H. Cole, S.C. Rashleigh, and R.G. Priest, "Optical Fiber Sensor Technology," IEEE J. Quantum Electronics, QE-18, pp. 626-664, 1982.

4. C.M. Davis, "Fiber Optic Sensors: An Overview," Optical Engineering, Vol. 24, No. 2, p. 347, 1985.

5. R.O. Claus, K.D. Bennett, and K.T. Srinivas, "Interferometric optical fiber measurements of internal strain in adhesive joints," Proc. 2nd International Symposium on the Nondestructive Characterization of Materials (Montreal, Canada), July 1986.

6. D.A. Jackson, A. Dandridge, and S.K. Sheen, "Measurement of small phase shifts using a single-mode optical interferometer," Optics Letters, Vol.5, p. 139, 1980.

7. J.D. Weiss, "Fiber-Optic Strain Gauge," J. Lightwave Technology, Vol. 7, No. 9, September 1989.

8. M.R. Layton and J.A. Bucaro, "Optical fiber acoustic sensor utilizing mode-mode interference," Applied Optics, Vol.18, No. 5, p. 666, March 1979.

9. B. Culshaw, D.E.N. Davies, and S.A. Kingsley, "Acoustic sensitivity of optic-fibre waveguides," Electronics Letters, Vol.13, No. 25, p. 760, 1977.

10. S.A. Kingsley, "Fiberdyne systems of passive or semipassive fibre-optic sensors," Electronics Letters, Vol.14, No. 14, p. 419, 1978.

11. D. Howard and T.J. Hall, "Interaction of high-frequency sound with fibre-guided coherent light," Electronics Letters, Vol.14, No. 19, p. 620, 1978.

12. K.D. Bennett, R.O. Claus and M.J. Pindera, "Internal monitoring of acoustic emission in graphite epoxy composites using embedded optical fiber," Proc. Rev of Progress in Quantitative NDE (La Jolla, CA), August 1986.

13. K.D. Bennett, R.O. Claus, and M.D. Dumais, "Impact characterization by optical fiber ultrasonic sensors," IEEE Ultrasonics Symp. (Chicago, IL), October 1988.

14. K.D. Bennett, R.O. Claus, and D.A. Kapp, "Characterization of optical fiber impact sensors for composite materials," Proc. ASNT Meeting on NDE for Life Extension (Charlotte, NC), March 1989.

15. K.D. Bennett and R.O. Claus, "Optical fiber measurement of vibration in graphite-epoxy composites," ASTM Eighth Symposium on Composite Materials Testing and Design (Charleston, SC), April 1986.

16. B.D. Duncan, B.W. Brennan, and R.O. Claus, "Intermodal pattern modulation in optical fiber modal domain sensor systems: experimental results," Proc. SPIE O/E Fiber LASE (Boston, MA), Vol. 986, p. 186, September 1988.

17. C. Leung, I. Chang, and S. Hsu, "Fiberoptic line-sensing system for perimeter protection against intrusion," Technical Digest, Fourth International Conference on Optical Fiber Sensors (Tokyo, Japan), 1986, p. 113.

18. W.B. Spillman, B.R. Kline, L.B. Maurice, and P.L. Fuhr, "Statistical-mode sensor for fiber optic vibration sensing uses," Applied Optics, Vol. 23, No. 15, August 1989.

19. G.L. Tangonan, D.I. Persechini, R.J. Morrison, and J.A. Wysocki, "Current sensing with metal-coated multimode optical fibres," Electronics Letters, Vol.16, No. 25, p. 958, 1980.

20. W. Eickhoff, "Temperature sensing by mode-mode interference in birefringent optical fibers," Optics Letters, Vol.6, No. 4, p. 204, April 1981.

21. J.L. McMillan and S.C. Robertson, "Dual-mode optical-fibre interferometric sensor," Electronics Letters, Vol.20, No. 3, p. 136, February 1984.

22. B. Culshaw and M.J. Hutchings, "Optical-fibre flowmeter," Electronics Letters, Vol.15, No. 18, p. 568, 1979.

23. D. Kreit, R.C. Youngquist, and D.E.N. Davies, "Two-mode fiber interferometer/amplitude modulator," Applied Optics, Vol.25, No. 23, p. 4433, December 1986.

24. K.D. Bennett, "Fiber Optic Techniques for Remote Sensing," M.S.E.E. Thesis, Virginia Polytechnic Institute and State University, August 1985

25. K.D. Bennett, "Optical Fiber Mode Phenomena," Fiber and Electro-Optics Research Center, Internal Research and Development Report, December 1985.

26. A. Sankar, "On-Line Evaluation of Mode Field Distribution in Optical Fibers," M.S.E.E. Thesis, Virginia Polytechnic Institute and State University, August 1986.

27. P.A. Ehrenfeuchter, "Fiber Optic Modal Domain Sensing of Structural Vibrations," M.S.E.E. Thesis, Virginia Polytechnic Institute and State University, December 1986.

28. K.T. Srinivas, "Axial Strain Effects on Optical Fiber Mode Patterns," M.S.E.E. Thesis, Virginia Polytechnic Institute and State University, January 1987.

29. N.K. Shankaranarayanan, "Mode-Mode Interference in Optical Fibers: Analysis and Experiment," M.S.E.E. Thesis, Virginia Polytechnic Institute and State University, March 1987.

30. B.D. Duncan, "Modal Interference Techniques for Strain Detection in Few-Mode Optical Fibers," M.S.E.E. Thesis, Virginia Polytechnic Institute and State University, December 1987.

31. A. Flax, "Micro-Optical Fiber Devices Used with Modal Domain Sensing," M.S.E.E. Thesis, Virginia Polytechnic Institute and State University, June 1988.

32. I. Aeby, "Non-destructive measurements in advanced composite materials and structures using a fiber optic sensing system," Proc. SPIE O/E Fiber Lase (Boston, MA), SPIE Vol. 986, p. 140, September 1988.

33. R.O. Claus and J.H. Cantrell, "Detection of ultrasonic waves in solids by an optical fiber interferometer," Proc. IEEE Ultrasonics Symposium (Boston, MA), October 1980.

34. R.O. Claus, K.D. Bennett, A.M. Vengsarkar, and K.A. Murphy, "Embedded Optical Fiber Sensors for Materials Evaluation," (Invited), Journal of Nondestructive Evaluation, Vol 8., No. 2, pp. 371-381, 1989.

35. K.D. Bennett and R.O. Claus, "Microbending losses of optical fibers imbedded in composite material," Proc. Optical Society of America Annual Meeting (Washington, DC), October 1985.

36. B.S. Jackson, "Optical Time Domain Reflectometry as a Nondestructive Evaluation Technique for Composite Materials," MSEE Thesis Virginia Polytechnic Institute and State University, May 1984.

37. W.B. Spillman, "Fiber optic sensors for composite monitoring," Proc. SPIE O/E Fiber Lase (Boston, MA), Vol. 986, September 1988.

38. R.O. Claus, T. Chandler, K.D. Bennett, D. Kapp, A. Vengsarkar, "Connectorization of Optical Fibers Embedded in Graphite Composites," Patent Disclosure, Virginia Tech, April 1989.

39. S. Jeglinski and T. Rytting, Proc. NASA Workshop on Intelligent Structures, NASA LaRC (Hampton, VA), February 1987.

40. E. Udd, "Overview of fiber optic smart structures for aerospace applications," Proc. SPIE O/E Fiber Lase (Boston, MA), Vol. 986, September 1988.

41. R.O. Claus, B.S. Jackson, and K.D. Bennett, "Nondestructive testing of composite materials by OTDR in imbedded optical fibers," SPIE Vol. 566, pp. 243-248, 1985.

42. R.M. Measures, N.D.W. Glossop, J. Lymer, and R.C. Tennyson, "Structurally integrated fiber optic damage assessment system for composite materials," Proc. SPIE E/O Fiber Lase (Boston, MA), Vol. 986, September 1988.

43. R.M. Measures, N.D.W. Glossop, J. Lymer, J. West, S. DuBois, W. Tsaw, and R.C. Tennyson, "Fiber Optic Impact Damage Detection of Composite Materials" Proc. SPIE E/O Fiber Lase (Boston, MA), Vol. 986, p. 949, September 1988.

44. R. Czarnek, Y. Guo, K.D. Bennett and R.O. Claus, "Interferometric measurements of strain concentrations induced by an optical fiber embedded in fiber reinforced composites," Proc. SPIE O/E Fiber Lase (Boston, MA), Vol. 986, September 1988.

45. R.L. Levy and D.P. Ames, Polymer Science Technology, Vol.29, Adhesion Chemistry, Plenum, pp.245-256, 1984.

46. B. Franconi, F. Wang, D. Hunston, F. Mopsik, "Materials Characterization for Systems Performance and Reliability," J.W. McCauly and V. Weiss (eds.), Plenum.

47. C. DiFrancia, "Development of Fiber Optic Sensors Using an Active Polymer Cladding," MS Thesis in Chemistry, Virginia Polytechnic Institute and State University, February 1988.

48. M. Reddy, K.D. Bennett, and R.O. Claus, "Imbedded optical fiber sensor of differential strain in composites," Proc. Rev. of Progress Quantitative NDE (La Jolla, CA), August 1986.

49. M.A. Drury, "In-situ fiber optic sensors for FTIR monitoring of composite cure cycles," Proc. NASA Workshop on Intelligent Structures, NASA LaRC (Hampton, VA), February 1987.

50. M.A. Aframowitz, "Fiber Optic Polymer Cure Sensor," J. Lightwave Tech., Vol.6, No. 10, pg. 1591, 1988.

51. W.P. Winfree and F.R. Parker, "Measurement of the degree of cure in epoxies with ultrasonic velocity," Rev. of Progress in Quantitative NDE, Vol. 5b, p. 1055, July 1985.

52. F.R. Parker and W.P. Winfree, "Acoustic characterization of composite cure," Rev. of Progress in Quantitative NDE, Vol. 5b, p. 1063, July 1985.

53. W.V.Miller, "Fiber Optic Sensors Embedded in Composites," Virginia Tech Fiber and Electro-Optics Research Center, Final Project Report to McDonnell Douglas Astronautics Co., Huntington Beach, CA, December 1989.

54. C.D. Butter and G.B. Hocker, "Fiber optics strain gage," Applied Optics, Vol.17, No. 18, p. 2867, September 1978.

55. J.C. Wade and R.O. Claus, "Interferometric techniques using embedded optical fibers for the quantitative NDE of composites," Proc. Rev. of Quantitative NDE (La Jolla, CA), August 1982.

56. A.O. Garg and R.O. Claus, "Application of Optical Fibers to Wideband Differential Interferometry," Materials Evaluation, Vol. 41, p. 106, 1983.

57. R.O. Claus and J.C. Wade, "Distributed strain measurement in a rectangular plate using an array of optical fiber sensors," J. Nondestructive Evaluation, Vol.41, p. 106, 1983.

58. J.S. Sirkis, "Interferometric optical fiber strain sensor under biaxial loading," Proc. 5th Conf on Optical Fiber Sensors (New Orleans, LA), p. 203, 1988.

59. W.J. Rowe, E.O. Rausch, and P.D. Dean, "Embedded optical fiber strain sensor for composite structure applications," Proc. SPIE Fiber Optic and Laser Sensors IV, Vol. 718, p. 266, 1986.

60. G. Meltz, J.R. Dunphy, W.W. Morey, and E. Snitzer, "Cross-talk fiber-optic temperature sensor," Applied Optics, Vol.22, No. 3, pg. 464, 1983.

61. K.A. Murphy, A. Vengsarkar and R.O. Claus, "Temperature insensitive fiber optic interferometric sensor," Proc. SPIE O/E Fiber Lase (Boston, MA), Vol. 986, September 1988.

62. R. Kriz, "Optical fiber sensors at NBS," Proc. NASA Workshop on Intelligent Structures, NASA LaRC (Hampton, VA), February 1987.

63. G. Meltz and J.R. Dunphy, "Quantitative fiber-optic techniques for the nondestructive evaluation of composites," Proc. Rev. of Progress in Quantitative NDE (Williamsburg, VA), June 1985.

64. B.W. Brennan, "Embedded fiber optic sensors for compsites," Proc. NASA Workshop on Intelligent Structures, NASA LaRC (Hampton, VA), February 1987.

65. R.O. Claus, K.D. Bennett, and B.S. Jackson, "NDE of composite materials by pulsed optical time domain methods in embedded optical fibers," Proc. of Review of Quantitative NDE (Williamsburg, VA), June 1985 (invited).

66. R.O. Claus, S. Sudeora, K.A. Murphy, and K.D. Bennett, "Low profile optical time domain fiber sensors for materials evaluation," Proc. Rev. of Progress in Quantitative NDE (La Jolla, CA), Vol. 8B, p. 1437 August 1988.

67. B.D. Zimmermann, K.A. Murphy, and R.O. Claus, "Local strain measurements using fiber splices and time domain Reflectomety," Proc. Rev of Progress in Quantitative NDE (Williamsburg, VA), June 1987.

68. B.D. Zimmermann, R.O. Claus, D.A. Kapp, K.A. Murphy, "Optical time domain reflectometry for local strain measurements," Proc. SPIE O/E Fiber Lase (Boston, MA), Vol. 986, September 1989.

69. S.T. Kush and M.E. Meffe, "Fiber Optic Vibration Modal Sensor, " U.S. Patent No. 4,525,626, June 1985

70. K.D. Bennett and R.O. Claus, "Analysis of composite structures using optical fiber modal sensing techniques," IEEE Region 3 Conference (Richmond, VA), March 1986.

71. P.A. Ehrenfeuchter and R.O. Claus. "Optical fiber waveguide methods for advanced materials," Proc. Intnl. Metallagraphic Soc. Conf. (Monterey, CA), July 1987.

72. R.S. Rogowski, "Smart structures for NASA missions," Proc. SPIE O/E Fiber Lase (Boston, MA), Vol. 986, September 1988.

73. D. Cox, D. Thomas, K. Reichard, D. Lindner, and R.O. Claus, "Modal domain fiber optic sensor for closed loop vibration control of a flexible beam," Proc. SPIE O/E Fiber Lase (Boston, MA), September 1989.

74. C.A. Rogers, D.K. Barker, K.D. Bennett, and R.H. Wynn, Jr., "Demonstration of a smart material with embedded actuators and sensors for active control," Proc. SPIE O/E Fiber Lase (Boston, MA), September 1988.

75. B. Hofer, "Fibre optic damage detection in composite structures," Composites, Vol.18, No. 4, pp. 309-316, September 1987.

76. R.M. Crane, A.B. Macander, and J.Gagorik, "Fiber optics for a damage assessment system for fiber reinforced plastic composite structures," AF/DARPA-NAVY/DARPA Rev. of Progress in Quantitative NDE (La Jolla, CA), August 1982.

77. R.M. Measures, N.D.W. Glossop, J. Lymer, R.C. Tennyson, "Structurally integrated fiber optic damage assessment system for composite materials," Proc. SPIE O/E Fiber Lase (Boston, MA), Vol. 986, September 1988.

78. R.M. Measures, N.D.W. Glossop, J. Lymer, M. Leblanc, J. West, S. Dubois, W. Tsai, and R.C. Tennyson, "Damage assessment for composite materials based on structurally imbedded optical fibers and image enhanced backlighting," Proc. Rev. of Progress in Quantitative NDE, Vol.8B, p. 1457, 1988.

79. M. Miller and S. Feth, "DUCkMAT," Fiber and Electro-Optics Research Center Annual Review, (Blacksburg, VA), April 1988.

80. R. Kuhlman, B.D. Duncan, and R.O. Claus, "Fiber optic composite impact monitor," Proc. IEEE Region 3 Conf. (Tampa, FL), April 1987.

81. K.D. Bennett and R.O. Claus, "Optical Signal Processor/Computer," Virginia Tech Patent Disclosure, April 1988.

82. K.D. Bennett and R.O. Claus, "Optical signal processing of spatially distributed sensor data in smart structures," Proc. ASME Technical Design Conference (Montreal, Canada), September 1989.

83. R.O. Claus and J.C. Wade, "Distributed strain measurement in a rectangular plate using an array of optical fiber sensors," J.Nondestructive Evaluation, Vol.41, p. 106 1983.

84. J.A Bucaro, N. Lagakos, H.H. Cole, and T.G. Giallorenzi, "Fiber optic acoustic transduction," in *Physical Acoustics XVI*, W.P. Mason and R.N. Thurston, Eds., Academic Press, New York, 1982.

85. D.A. Danielson and S.L. Garrett, "Fiber-Optic Ellipsoidal Flextensional Hydrophones," J. Lightwave Technology, Vol.7, No. 12, p. 1995, December 1989.

86. Fields et. al., "Fiber optic hydrophone," in *Physics of Fibers, Vol. 2*, Advances in Ceramics, Bendow and Mitra (eds.), American Ceramic Society, pp. 529-538.

87. A.M. Vengsarkar, K.A. Murphy, T.A. Tran, and R.O. Claus, "Microbend loss fiber optic amplitude and direction sensor for underwater applications," Proc. SPIE O/E Fiber Lase (Boston, MA), Vol. 986, September 1988.

88. H.L.W. Chan, K.S. Chiang, and J.L. Gardner, "Polarimetric optical fiber sensor for ultrasonic power measurement," IEEE Ultrasonics Symp. (Chicago, IL), October 1988.

89. J.R. Dunphy and G. Meltz, "Fiber optic sensor for high speed material diagnostics," Proc. Conf. of SEM, Optical methods in composites, November 1986.

90. J.R. Dunphy and G. Meltz, "Optical fiber shock wave sensor for composites," Proc. SPIE O/E Fiber Lase (Boston,MA), Vol. 986, September 1988.

91. W.V. Miller, K.A. Murphy, M.F. Gunther, A.M. Vengsarkar, and R.O. Claus, "Acoustic emission detection in metals with embedded optical fibers," Proc. Rev. of Progress in Quantitative NDE (Brunswick, ME), July 1989.

92. K.D. Bennett, "Investigation of In-Process Cure Control for Automated Composite Processing Using Embedded Optical Fiber Sensors," Virginia Tech Fiber and Electro-Optics Research Center, Final Project Report to General Dynamics Corporation, Convair Division, San Diego, CA, November 1989.

91. P.K. Cheo, *FIBER OPTICS Devices and Systems,* Prentice-Hall, Inc., Englewood Cliffs, New Jersey, 1985, p. 46.

92. A.W. Snyder, "Asymptotic Expressions for Eigenfunctions and Eigenvalues of a Dielectric Optical Waveguide," IEEE Trans. Microwave Theory Tech., MTT-17, p. 1130, December 1969.

93. R.C. Youngquist, J.L. Brooks, and H.J. Shaw, "Two-mode fiber modal coupler," Optics Letters, vol. 9, no. 5, p. 177, May 1984.

94. P. Wysocki, A.G. Kostenbauder, B.Y. Kim, and A.E. Siegman, "Bipolar Optical Modulation and Demodulation Using Dual-Mode Fiber and a Fast Diffusion-Driven Photodetector," J. Lightwave Technology, Vol. 7, No. 12, p. 1964, December 1989.

95. A. Safaai-Jazi and R.O. Claus, "Synthesis of interference patterns in few-mode optical fibers," Proc. SPIE O/E Fiber Lase (Boston, MA), Vol. 986, p. 180, September 1988.

96. M. Spajer, "Linear phase detection for a bimodal fiber sensor," Optics Letters, vol. 18, no. 3, p. 239, March 1988.

97. A.H. Cherin, *An Introduction to Optical Fibers*, McGraw-Hill Book Company, New York, 1983.

98. I.S. Gradshteyn and I.M. Ryzhik, *Table of Integrals, Series, and Products,* Academic Press, Inc, San Diego, CA, 1980, p. 961.

99. B. Culshaw, P.R. Ball, J.C. Pond, and A.A. Sadler, "Fiberdyne data collection system for industrial telemetry application," SPIE Fiber Optics, Vol.355 p. 132, 1982.

100. S.D. Crossley, "Signal Recovery Techniques for a Coherent Optical Fibre Data Telemetry Highway," PhD. Dissertation, University College London, May 1986.

101. W.P. Mason and R.N. Thurston (eds.), *Physical Acoustics*, Vol. VII, Academic Press, 1970.

102. A. Bertholds and R. Dändliker, "Determination of the Individual Strain-Optic Coefficients in Single-Mode Optical Fibers," J. Lightwave Technology, Vol. 6, No. 1, January 1988.

103. D. Marcuse, *Principles of Optical Fiber Measurements*, Academic Press, London, 1981, p. 36.

104. N.S. Kapany and J.J. Burke, *Optical Waveguides*, Academic Press, London, 1972.

105. S. Berdague and P. Facq, "Mode division multiplexing in optical fibers," Applied Optics, vol. 21, no. 11, p. 1950.

106. D. Marcuse, *Principles of Optical Fiber Measurements*, Academic Press, London, 1981, p. 35.

107. J.E. Midwinter, *Optical Fibers for Transmission*, John Wiley and Sons, New York, 1979, p. 84.

108. K.D. Bennett, D.A. Kapp, and R.O. Claus, "Optical Fiber Sensors for Smart Aerospace Structures," Virginia Tech Fiber and Electro-Optics Research Center Final Project Report to General Dynamics Corporation,Fort Worth Division, Fort Worth, TX, May 1989.

109. G. Indebetouw, K.D. Bennett, P.Y. Zhang, and R.G. May, "Holographic Matched Filter for Full Field, In-line Signal Processing of Optical Fiber Sensor Outputs," Jounal of Lightwave Technology, accepted for publication, November 1989.

110. H. Palmer and R.E. Green, Jr., "A Comparison of optically and piezoelectrically sensed acoustic emission signals," App. Opt., Vol.16, p 2333, 1977.

111. R.A. Kline and R.E. Green, Jr., "Optical detection of acoustic emission waves," J. Acoust. Soc. Am., Vol.64, p 1633, 1978.

112. A.M. Vengsarkar, K.A. Murphy, C.J. Chung, and R.O. Claus, "Fiber optic interferometric sensor for surface acoustic wave measurement," Rev. of Progress in Quantative NDE (San Diego, CA), August 1988.

113. K.D. Bennett and K.D. Zehnder, "Acoustic emission detection in smart materials," Fiber and Electro-Optics Research Center Second Annual Review (Blacksburg, VA), April 1988.

114. K.D. Bennett, "Shock Waves in Composite Materials," College of William and Mary Senior Thesis, in conjunction with the NASA Langley Research Center, Hampton, VA, June 1981.

115. D. Marcuse, "Field Deformation and Loss Caused by Curvature in Optical Fibers," J. Optical Society of America, Vol. 66, p. 311, April 1976.

116. K.A. Murphy, M.S. Miller, A.M. Vengsarkar, R.O. Claus, and N.E. Lewis, "Embedded modal domain sensors using elliptical core optical fibers," Proc. SPIE O/E Fiber Lase (Boston, MA) September 1989.

117. B.Y. Kim, J.N. Blake, S.Y. Huang, and H.J. Shaw, "Use of highly elliptical core fibers for two-mode fiber devices," Optics Letters, vol. 12, no. 9, p. 729, September 1987.

118. J.N. Blake, S.Y. Huang, B.Y. Kim, and H.J. Shaw, "Strain effects on highly elliptical core two-mode fibers," Optics Letters, vol. 12, no. 9, p. 732, September 1987.

119. J.N. Blake, B.Y. Kim, and H.J. Shaw, "Fiber-optic modal coupler using periodic microbending," Optics Letters, vol. 11, no. 3, p. 177, March 1986.

120. S. J. Garth, "Intermodal coupling in an optical fiber using periodic stress," Applied Optics, vol. 28, no. 3, p. 581, February 1989.

121. N. Lagakos, P. Ehrenfeuchter, T.R. Hickman, A. Tveten, and J.A. Bucaro, "Planar flexible fiber-optic interferometric acoustic sensor," Optics Letters, Vol. 13, No. 9, p. 788, September 1988.

122. K.D. Bennett, J.C. McKeeman, and R.G. May, "Full field analysis of modal domain sensor signals for structural control," Proc. SPIE O/E Fiber Lase (Boston, MA), Vol. 986, p. 186, September 1988.

123. M. Kieli, "Novel fiber optic sensor based on modal distribution (MPD) modulation," SPIE Vol. 798 Fiber Optic Sensors II, p. 331, 1987.

124. R.E. Epworth, "The Phenomenon of modal noise in analogue and digital optical fibre systems," 4th European Conf. on Optical Communications (Genoa), September 1978.

125. R.O. Claus and K.D. Bennett, "Modal Domain Optical Fiber Sensor," U.S. Patent No. 4,854,706, August 1989.

VITA

K.D. Bennett was born in Alexandria, Virginia in 1959. He received a B.S. degree in Physics from the College of William and Mary, Williamsburg, VA in 1981, and attended Virginia Tech, where he received M.S. and PhD. degrees in Electrical Engineering in 1985 and 1990, respectively. He worked from 1981-82 at the ITT Electro-Optical Products Division in Roanoke, Va, on semiconductor laser testing, and in 1985 consulted for Inland Motor Corporation developing fiber optic sensors for military applications. Between 1986-87, he was a visiting professor at the Sichuan Foreign Language Institute in Chongqing, P.R. China. He returned to Virginia Tech and worked as a Research Associate in the Fiber and Electro-Optics Research Center, before resuming full time graduate work. He now works there as a Research Scientist, with primary research interests in the field of fiber optic sensors applied to smart structures and nondestructive evaluation.